University of Warwick institutional repository: http://go.warwick.ac.uk/wrap

A Thesis Submitted for the Degree of PhD at the University of Warwick

http://go.warwick.ac.uk/wrap/55164

This thesis is made available online and is protected by original copyright.

Please scroll down to view the document itself.

Please refer to the repository record for this item for information to help you to cite it. Our policy information is available from the repository home page.

THE UNIVERSITY OF
WARWICK

Library Declaration and Deposit Agreement

1. STUDENT DETAILS

Please complete the following:

Full name: ………………………………………………………………………………………….

University ID number: ………………………………………………………………………………

2. THESIS DEPOSIT

2.1 I understand that under my registration at the University, I am required to deposit my thesis with the University in BOTH hard copy and in digital format. The digital version should normally be saved as a single pdf file.

2.2 The hard copy will be housed in the University Library. The digital version will be deposited in the University's Institutional Repository (WRAP). Unless otherwise indicated (see 2.3 below) this will be made openly accessible on the Internet and will be supplied to the British Library to be made available online via its Electronic Theses Online Service (EThOS) service.
[At present, theses submitted for a Master's degree by Research (MA, MSc, LLM, MS or MMedSci) are not being deposited in WRAP and not being made available via EthOS. This may change in future.]

2.3 In exceptional circumstances, the Chair of the Board of Graduate Studies may grant permission for an embargo to be placed on public access to the hard copy thesis for a limited period. It is also possible to apply separately for an embargo on the digital version. (Further information is available in the *Guide to Examinations for Higher Degrees by Research*.)

2.4 *If you are depositing a thesis for a Master's degree by Research, please complete section (a) below. For all other research degrees, please complete both sections (a) and (b) below:*

(a) Hard Copy

I hereby deposit a hard copy of my thesis in the University Library to be made publicly available to readers (please delete as appropriate) EITHER immediately OR after an embargo period of ……….................... months/years as agreed by the Chair of the Board of Graduate Studies.

I agree that my thesis may be photocopied. YES / NO (*Please delete as appropriate*)

(b) Digital Copy

I hereby deposit a digital copy of my thesis to be held in WRAP and made available via EThOS.

Please choose one of the following options:

EITHER My thesis can be made publicly available online. YES / NO (*Please delete as appropriate*)

OR My thesis can be made publicly available only after…..[date] (Please give date)
YES / NO (*Please delete as appropriate*)

OR My full thesis cannot be made publicly available online but I am submitting a separately identified additional, abridged version that can be made available online.
YES / NO (*Please delete as appropriate*)

OR My thesis cannot be made publicly available online. YES / NO (*Please delete as appropriate*)

3. GRANTING OF NON-EXCLUSIVE RIGHTS

Whether I deposit my Work personally or through an assistant or other agent, I agree to the following:

Rights granted to the University of Warwick and the British Library and the user of the thesis through this agreement are non-exclusive. I retain all rights in the thesis in its present version or future versions. I agree that the institutional repository administrators and the British Library or their agents may, without changing content, digitise and migrate the thesis to any medium or format for the purpose of future preservation and accessibility.

4. DECLARATIONS

(a) I DECLARE THAT:

- I am the author and owner of the copyright in the thesis and/or I have the authority of the authors and owners of the copyright in the thesis to make this agreement. Reproduction of any part of this thesis for teaching or in academic or other forms of publication is subject to the normal limitations on the use of copyrighted materials and to the proper and full acknowledgement of its source.

- The digital version of the thesis I am supplying is the same version as the final, hard-bound copy submitted in completion of my degree, once any minor corrections have been completed.

- I have exercised reasonable care to ensure that the thesis is original, and does not to the best of my knowledge break any UK law or other Intellectual Property Right, or contain any confidential material.

- I understand that, through the medium of the Internet, files will be available to automated agents, and may be searched and copied by, for example, text mining and plagiarism detection software.

(b) IF I HAVE AGREED (in Section 2 above) TO MAKE MY THESIS PUBLICLY AVAILABLE DIGITALLY, I ALSO DECLARE THAT:

- I grant the University of Warwick and the British Library a licence to make available on the Internet the thesis in digitised format through the Institutional Repository and through the British Library via the EThOS service.

- If my thesis does include any substantial subsidiary material owned by third-party copyright holders, I have sought and obtained permission to include it in any version of my thesis available in digital format and that this permission encompasses the rights that I have granted to the University of Warwick and to the British Library.

5. LEGAL INFRINGEMENTS

I understand that neither the University of Warwick nor the British Library have any obligation to take legal action on behalf of myself, or other rights holders, in the event of infringement of intellectual property rights, breach of contract or of any other right, in the thesis.

Please sign this agreement and return it to the Graduate School Office when you submit your thesis.

Student's signature: ....…… Date: ....

Investigating Materials with Disordered Structures Using Total Neutron Scattering

by

Helen Yvonne Playford

Thesis

Submitted to the University of Warwick

for the degree of

Doctor of Philosophy

Department of Chemistry

September 2012

Contents

Contents i

List of Figures vi

List of Tables xviii

Acknowledgements xxi

Declaration xxiii

Abstract xxv

1. Introduction: Disordered Materials 2
   - 1.1. Ordered Materials 2
   - 1.2. Flavours of Disorder 6
     - 1.2.1. Disordered crystalline materials 6
     - 1.2.2. Nanocrystalline materials 10
     - 1.2.3. Amorphous materials and liquids 13
   - 1.3. Studying Disordered Structures 14
   - 1.4. Aims of the Work Described in this Thesis 22
   - 1.5. References 24
2. Theory and Experimental Techniques 27
   - 2.1. Diffraction 27
     - 2.1.1. X-ray diffraction 27
       - 2.1.1.1. Structure, symmetry and space groups 32
       - 2.1.1.2. Experimental details 36
     - 2.1.2. Neutron diffraction 36
       - 2.1.2.1. Time-of-flight neutron diffraction 41
     - 2.1.3. Rietveld refinement 43
       - 2.1.3.1. The Le Bail method for profile fitting 49
   - 2.2. Total Scattering 51
     - 2.2.1. A total neutron scattering experiment 52
       - 2.2.1.1. Experimental details 53
     - 2.2.2. Data processing 53
       - 2.2.2.1. Gudrun and ATLAS 53
       - 2.2.2.2. Correcting for the presence of hydrogen 55

2.2.2.3. The Fourier transform 56
2.2.2.4. Properties of the correlation function D(r) 58
2.2.3. Pair Distribution Function analysis 59
2.2.4. Reverse Monte Carlo 61
2.2.5. X-ray total scattering 63
2.2.5.1. Experimental details 65
2.3. Hydrothermal and Solvothermal Synthesis 65
2.3.1. Experimental details 66
2.4. Other Techniques 67
2.4.1. Electron microscopy 67
2.4.1.1. Scanning electron microscopy 67
2.4.1.2. Transmission electron microscopy 67
2.4.2. X-ray absorption near-edge spectroscopy 67
2.4.3. SQUID magnetometry 68
2.4.4. Nuclear magnetic resonance 68
2.4.5. Infrared spectroscopy 68
2.4.6. Thermogravimetric analysis 69
2.4.7. Pycnometry 69
2.5. References 70
3. The Polymorphism of Gallium Oxide 73
3.1. Introduction 73
3.1.1. Background 73
3.1.2. Scope of this chapter 77
3.2. Experimental 78
3.2.1. Synthesis 78
3.2.1.1. Alpha- and beta-Ga_2O_3 78
3.2.1.2. Gamma-Ga_2O_3 79
3.2.1.3. A novel gallium oxyhydroxide 80
3.2.1.4. Gallium nitrate nonahydrate 80
3.2.1.5. Delta- and epsilon-Ga_2O_3 82
3.3. Results and Discussion 83
3.3.1. Alpha- and beta-Ga_2O_3 83

3.3.2. Gamma-Ga_2O_3 87
3.3.2.1. General characterisation 87
3.3.2.2. Rietveld refinement 90
3.3.2.3. Pair distribution function analysis 93
3.3.2.4. RMCProfile 97
3.3.2.5. The structure of nanocrystalline γ-Ga_2O_3 from a short solvothermal reaction 103
3.3.2.6. The structure of γ-Ga_2O_3 made by the precipitation method 107
3.3.3. Epsilon-Ga_2O_3 112
3.3.3.1. General characterisation 112
3.3.3.2. Rietveld refinement 113
3.3.3.3. PDF analysis 118
3.3.4. Delta-Ga_2O_3 121
3.3.4.1. General characterisation 121
3.3.4.2. In situ neutron diffraction 122
3.3.5. A novel gallium oxyhydroxide 127
3.3.5.1. General characterisation 127
3.3.5.2. Neutron diffraction 129
3.3.5.3. High resolution powder XRD 131
3.3.6. Kappa-Ga_2O_3 135
3.4. Conclusions 137
3.5. References 141
4. Gallium-containing Mixed Metal Oxides with the Spinel Structure 145
4.1. Introduction 145
4.1.1. Background 145
4.1.2. Scope of this chapter 150
4.2. Results and Discussion 151
4.2.1. Synthetic approach 151
4.2.2. Cobalt gallium oxide 155
4.2.2.1. General characterisation 155
4.2.2.2. Total neutron scattering 158
4.2.2.2.1. Model 1 159

4.2.2.2.2. Model 2 160

4.2.2.2.3. Model 3 161

4.2.2.2.4. Model 4 163

4.2.2.2.5. PDF analysis 164

4.2.2.3. Magnetic behaviour 167

4.2.3. Iron gallium oxide 170

4.2.3.1. General characterisation 170

4.2.3.2. Total neutron scattering 175

4.2.3.3. Magnetic behaviour 181

4.3. Conclusions 184

4.4. References 186

5. The Structures of Fluorite-like Cerium Bismuth Oxides and a Cerium Titanate Pyrochlore 189

5.1. Introduction 189

5.1.1. Background 189

5.1.2. Scope of this chapter 190

5.2. Results and Discussion 192

5.2.1. Cerium bismuth oxide 192

5.2.1.1. Synthesis 192

5.2.1.2. Total neutron scattering 193

5.2.2. Sodium cerium titanate pyrochlore 206

5.2.2.1. Synthesis 206

5.2.2.2. Total neutron scattering 207

5.3. Conclusions 218

5.4. References 220

6. Structural Studies of Amorphous Zeolite Precursors 222

6.1. Introduction 222

6.1.1. Background 222

6.1.2. Scope of this chapter 231

6.2. Experimental 233

6.2.1. Synthesis 233

6.2.2. Neutron scattering measurements 235

6.3. Results and Discussion 239
  6.3.1. NMR 239
  6.3.2. IR spectroscopy 240
  6.3.3. SEM 242
  6.3.4. Neutron scattering experiments 243
    6.3.4.1. SANS 243
    6.3.4.2. Total scattering 246
  6.3.5. Conclusions 266
6.4. References 269
7. Conclusions and Possible Future Work 272
7.1. The Polymorphism of Gallium Oxide 272
  7.1.1. The structure of γ-Ga_2O_3 272
  7.1.2. The structure of ε-Ga_2O_3 and “δ-Ga_2O_3” 274
  7.1.3. A novel gallium oxyhydroxide and κ-Ga_2O_3 274
7.2. Gallium-containing Mixed Metal Oxides with the Spinel Structure 275
  7.2.1. Synthesis 275
  7.2.2. Cobalt gallium spinel 276
  7.2.3. Iron gallium spinel 276
7.3. The Structures of Fluorite-like Cerium Bismuth Oxides and a Cerium Titanate Pyrochlore 277
  7.3.1. Cerium bismuth oxide 277
  7.3.2. Sodium cerium titanate pyrochlore 279
7.4. Structural Studies of Amorphous Zeolite Precursors 279
  7.4.1. Synthesis method and experimental setup 279
  7.4.2. Neutron scattering results 280
7.5. General Concluding Remarks 281
7.6. References 282

List of Figures

Figure 1.1 Schema 7 from Robert Hooke's Micrographia, demonstrating the range of shapes that can be formed by the close packing of spherical objects, and their relation to the crystal habits of shards of flint. (Source: Project Gutenberg). 2

Figure 1.2 An illustration of the symmetry of a simple space group generating multiple equivalent atom positions. Provided with the coordinates of two atoms, the symmetry operators of the cubic space group $Ia\mathbf{3}$ are used to generate the other atom positions within the unit cell. 3

Figure 1.3 Diagram demonstrating Bragg's Law for a rectangular lattice. 4

Figure 1.4 The mineral $MgAl_2O_4$ with the cubic spinel structure.[9] Blue spheres are Al, yellow spheres are Mg and red spheres are O. In Fe_3O_4 the Fe atoms are distributed over all Mg and Al sites. In Fe_2O_3, some of these sites are vacant. 8

Figure 1.5 A representation of a layered material with (a) no stacking faults and (b) severe displacive stacking faults. 9

Figure 1.6 Schematic drawing of the two types of nanocrystalline particle. A: crystalline particles of a few-nanometres in size, and B: larger particles with nano-scale coherent domains separated by (i) normal grain boundaries and (ii) disordered interfaces.[13] 10

Figure 1.7 Simulated XRD patterns for SiO_2 (quartz) for different particle sizes. The nanometric particle exhibits severely broadened peaks. 12

Figure 1.8 (A) The regular arrangement of spheres in a hypothetical crystal (B) The same material as a glass, as per Zachariasen's random network model. 13

Figure 1.9 High resolution TEM image of a nanocrystal of $Ce_{1-x}Bi_xO_{2-0.5x}$ showing that it is highly ordered and has facetted edges.[27] 15

Figure 1.10 An example measured correlation function for liquid carbon tetrachloride, with thanks to Alex Hannon. 18

Figure 2.1 A representation of the diffraction cones produced by an isotropic powder sample. The angle 2θ is the angle between incident and diffracted beams. 28

Figure 2.2 An example X-ray diffractogram, of silicon (λ = 1.54184 Å), showing the *d*-spacings and Miller indices (see below) of the Bragg peaks. 28

Figure 2.3 Illustration of the (100) and (111) Miller planes in a cubic unit cell. 30

Figure 2.4 The arrangement of points in an orthorhombic lattice: (a) primitive, P, (b) body-centred, I, (c) base-centred, C, and (d) face-centred, F. 34

Figure 2.5 A C-centered tetragonal lattice (in black) can always be reduced to a smaller primitive tetragonal lattice (in blue). 34

Figure 2.6 An illustration of the geometry of a neutron scattering experiment. 40

Figure 2.7 The flight path of a neutron in a time-of-flight diffractometer. 41

Figure 2.8 The GEM diffractometer at ISIS, (a) the arrangement of the 8 detector banks and (b) a drawing of GEM with banks 6 & 7 at the lower left and the beamstop at the top right. 42

Figure 2.9 An example of a Rietveld fit to a time-of-flight neutron diffraction pattern from a NBS (National Bureau of Standards) silicon standard sample. 44

Figure 2.10 The constituent parts of a GSAS TOF profile function. A pseudo-Voigt function, the sum of Gaussian and Lorentzian components, is convoluted with an Ikeda-Carpenter function to make the total function. 47

Figure 2.11 A flow chart showing the general procedure used for Rietveld refinement. The refinement of various parameters is enabled (or "switched on") sequentially to minimise the chances of the refinement diverging. 49

Figure 2.12 The steps involved in data analysis with Gudrun and ATLAS. 54

Figure 2.13 An example of fitting a cubic spline to data from GEM bank 6 with a sloping background to correct for the presence of hydrogen in a sample. 56

Figure 2.14 A comparison between (a) $D(r)$ and (b) $T(r)$, emphasising their relationship. $T(r)$ is obtained by adding a function with constant slope, $T_0(r)$, to $D(r)$. 57

Figure 2.15 (a) The scattering data from crystalline Si after application of the step modification function at Q_{max} = 15 Å^{-1} and (b) the result of the Fourier transform. (c) The scattering data after application of the Lorch modification function at Q_{max} = 15 Å^{-1} and (d) the result of the Fourier transform. Note that the application of the Lorch function both greatly reduces the appearance of termination ripples in, and slightly broadens, the resultant $D(r)$. 58

Figure 2.16 An example of PDF analysis using total neutron scattering data from a NBS (National Bureau of Standards) silicon standard sample. 60

Figure 3.1 (a) The structure of α-Ga_2O_3, (b) The structure of β-Ga_2O_3, (c) The structure of γ-Al_2O_3, (d) The bixbyite structure (In_2O_3) and (e) The structure of κ-Al_2O_3. Green spheres are octahedral cation sites, blue spheres are tetrahedral sites and yellow spheres are pseudo-pentahedral sites. 74

Figure 3.2 A flow-chart of the interconversions of the polymorphs of Ga_2O_3 as described by Roy *et al.*[1] 77

Figure 3.3 In black: thermodiffraction of the decomposition of commercial gallium nitrate hydrate. The red trace is the simulated pattern for $Ga(NO_3)_3.9H_2O$ and the blue trace is the simulated pattern for the $[Ga_{13}(\mu_3\text{-}OH)_6(\mu_2\text{-}OH)_{18}(H_2O)_{24}](NO_3)_{15}$ "nanoclusters". 81

Figure 3.4 The measured *i*(*Q*) for β-Ga_2O_3 compared with a simulated *i*(*Q*) for particles of diameter 100 Å. The structure of β-Ga_2O_3 was taken from Ahman *et al.*.[8] 83
Figure 3.5 The results of PDF analysis for β-Ga_2O_3, wRp = 9.67%. 84
Figure 3.6 The measured *i*(*Q*) for α-Ga_2O_3 compared with a simulated *i*(*Q*) for particles of diameter 80 Å. The structure of α-Ga_2O_3 was taken from Marezio *et al.*[10] 85
Figure 3.7 The results of fitting the first peak in the PDFs for (left) α- and (right) β-Ga_2O_3. 86
Figure 3.8 Plot showing XRD patterns for various samples of γ-Ga_2O_3: (a) MEA, 72 hrs (b) MEA, 18 hrs (c) DEA, 30 hrs (d) DEA, 18 hrs (e) DEA, 11 hrs (f) precipitation from aqueous solution. The sharp peaks marked with vertical dotted lines are from the Al sample holder, and the upper panel shows the simulated XRD pattern for the structure determined in Section 3.3.2.2. 87
Figure 3.9 Contour plots of the *in situ* heating of γ-Ga_2O_3 where the Z axis is intensity and the first and last scans are highlighted. Left: heating of poorly crystalline γ-Ga_2O_3 produced *via* precipitation from aqueous solution. Right: heating of crystalline γ-Ga_2O_3 from solvothermal reaction. 89
Figure 3.10 (a) TEM image of precipitation-method γ-Ga_2O_3. (b) TEM images of crystalline solvothermal γ-Ga_2O_3. 89
Figure 3.11 TGA/DSC results for γ-Ga_2O_3. Left: disordered γ-Ga_2O_3 from precipitation method. Right: crystalline solvothermal γ-Ga_2O_3. 90
Figure 3.12 Result of Rietveld refinement for solvothermal γ-Ga_2O_3. Left: data from GEM bank 3 (mean scattering angle 34.9°). Right: data from GEM bank 5 (mean scattering angle 91.3°). 92
Figure 3.13 Result of an attempted Rietveld refinement for γ-Ga_2O_3 on GEM bank 5 data using a model with only the ideal spinel sites occupied. 93
Figure 3.14 The fit of the Rietveld refined structure to the neutron PDF for γ-Ga_2O_3. 94
Figure 3.15 (a) The low-*r* region of the PDF fit to the cubic spinel model (from Rietveld refinement) and (b) the fit using the non-centrosymmetric *F***4**3*m* model. 95
Figure 3.16 Comparison of the octahedral coordination of gallium in various Ga_2O_3 structures. 96
Figure 3.17 (a) The simulated Ga–Ga partial *D*(*r*) for the refined γ-Ga_2O_3 structure; (b) The Ga–Ga partial *D*(*r*)s for models with various cation sites fully occupied. 97
Figure 3.18 Result of RMC refinement of γ-Ga_2O_3: the final fit to the *i*(*Q*). 98

Figure 3.19 Result of RMC refinement of γ-Ga_2O_3: the final fit to the $T(r)$ over (a) the full data range and (b) close up of the low-r region. 99

Figure 3.20 The arrangement of Ga atoms in the cubic $Fd\mathbf{3}m$ spinel model of γ-Ga_2O_3. Colours denote different Ga sites. Note that in these projections, the 16c and 48f sites obscure some of the 8a and 16d sites. 100

Figure 3.21 The results of RMC modelling for γ-Ga_2O_3. Collapsed RMC unit cells are shown on the left with the crystallographic model on the right for comparison. Colour conventions are as in Figure 3.20. 101

Figure 3.22 (a) Refined Ga–O partial correlation functions from RMC for γ-Ga_2O_3 and (b) the Ga–O partial functions from the starting configuration. 103

Figure 3.23 Result of Rietveld refinement for nanocrystalline solvothermal γ-Ga_2O_3. Left: data from GEM bank 3 (mean scattering angle 34.9°). Right: data from GEM bank 5 (mean scattering angle 91.3°). 104

Figure 3.24 The measured PDF of nanocrystalline solvothermal γ-Ga_2O_3 with calculated Ga–O and Ga– –Ga partial functions. Also shown is the feature at 1.5 Å due to C–N and C–C bonds in the residual surface-associated organic species. 105

Figure 3.25 The FT-IR spectrum of liquid DEA (upper panel) compared with the spectra of (a) crystalline solvothermal γ-Ga_2O_3, (b) nanocrystalline solvothermal γ-Ga_2O_3 and (c) disordered precipitation method γ-Ga_2O_3. 106

Figure 3.26 TGA/DSC result for nanocrystalline solvothermal γ-Ga_2O_3. 106

Figure 3.27 The result of PDF analysis using the Rietveld-derived structural model for nanocrystalline solvothermal γ-Ga_2O_3. 107

Figure 3.28 X-ray $i(Q)$s for (a) solvothermal γ-Ga_2O_3 and (b) disordered γ-Ga_2O_3 from the precipitation method. Left panel is full data range, right is close-up of low-Q region. 108

Figure 3.29 Neutron $i(Q)$s for (a) solvothermal γ-Ga_2O_3, (b) solvothermal γ-Ga_2O_3 with a smaller particle size from a shorter reaction and (c) disordered γ-Ga_2O_3 from the precipitation method. Left panel is full data range, right is close-up of low-Q region. 109

Figure 3.30 (a) A comparison of neutron diffraction data (GEM bank 3) from disordered γ-Ga_2O_3 (i) with the simulated and broadened pattern from the modified spinel model (ii). (b) A comparison of the neutron $i(Q)$ from disordered γ-Ga_2O_3 (i) with the $i(Q)$ simulated for the modified spinel model, adjusted for small particle size (diameter 20 Å) using a Mason factor (ii). (c) A comparison of the measured neutron PDF from disordered γ-Ga_2O_3 (i) with the simulated PDF from a mixture of the modified spinel model (90%) and a boehmite-like GaOOH phase (10%) (ii). 111

Figure 3.31 Thermodiffraction of ε-Ga_2O_3. An intermediate phase is formed during the heating process which can be seen *via* peaks at 28, 39, 42. 48 and 50° appearing and then disappearing, and the intensity of the peaks at ~31 and 34° increasing and then decreasing between 625 – 850 °C. 112

Figure 3.32 TEM images of ε-Ga_2O_3. 113

Figure 3.33 The measured XRD pattern for ε-Ga_2O_3 with the simulated pattern from the orthorhombic κ-Al_2O_3/ε-Fe_2O_3 model. 114

Figure 3.34 The results of a Le Bail profile refinement for ε-Ga_2O_3 using space group $Pna2_1$ and with a = 5.1306(4) Å, b = 8.6812(4) Å and c = 9.4006(7) Å. Plots shown are from two different GEM banks, (a) bank 5 (average scattering angle 91.3 °) and (b) bank 3 (average scattering angle 34.9 °). 115

Figure 3.35 The structure of hexagonal ε-Fe_2O_3 as stated by Tronc *et al.*[24] (Left) and the structure after correcting the *x* and *y* coordinates of the Ga atom overlapping the O. (Right). 116

Figure 3.36 The measured XRD pattern for ε-Ga_2O_3 with the simulated pattern from (i) the hexagonal ε-Fe_2O_3 model and (ii) β-Ga_2O_3. 117

Figure 3.37 The result of Rietveld refinement for ε-Ga_2O_3 using two phases (hexagonal "ε-Fe_2O_3" model and β-Ga_2O_3). Phase fractions are ε = 54.43(5)% , β = 45.57(6)%. The data are from GEM bank 3 (mean scattering angle 34.9°). 118

Figure 3.38 The result of PDF refinement of ε-Ga_2O_3 using the Rietveld model as a starting point. Phase fractions are ε = 57.05(5)%, β = 42.95(5)%. 119

Figure 3.39 Thermodiffraction of "δ-Ga_2O_3". It can be seen that the peaks due to β-Ga_2O_3 appear cleanly at around 550 °C. 121

Figure 3.40 TEM images of "δ-Ga_2O_3" 122

Figure 3.41 (a) The powder XRD pattern of "δ-Ga_2O_3" with the simulated patterns for (i) bixbyite model based on the structure of Mn_2O_3 with Mn replaced by Ga and the lattice parameter adjusted to give the closest match, (ii) hexagonal ε-Ga_2O_3 model and (iii) β-Ga_2O_3. (b) The first peaks from the neutron PDFs of (i) "δ-Ga_2O_3", (ii) β-Ga_2O_3 and (iii) α-Ga_2O_3 after Fourier transformation with a Q_{max} = 50 $Å^{-1}$. The dotted lines show the different positions of the peak maxima, at ~1.92 Å for α-Ga_2O_3 and ~1.87 Å for δ- and β-Ga_2O_3. 123

Figure 3.42 The PDFs measured during heating of "δ-Ga_2O_3" at (i) room temperature, (ii) 400 °C, (iii) 600 °C and (iv) 700 °C. 125

Figure 3.43 The fitting of the neutron total scattering data measured during heating of “δ-Ga_2O_3” at (a) 400 °C, (b) 600 °C and (c) 700 °C using $i(Q)$ simulated from a two-phase mixture of ε-Ga_2O_3 and β-Ga_2O_3 and modified for the effects of small particle size using a Mason factor. 126
Figure 3.44 TGA/DSC trace of Ga-tohdite. 128
Figure 3.45 FT-IR spectrum of Ga-tohdite. 128
Figure 3.46 SEM (a) and TEM (b)-(d) microscopy of Ga-tohdite. (c) and (d) are bright and dark-field images of the same particle. 129
Figure 3.47 Results of Rietveld refinement of Ga-tohdite, $Ga_5O_7(OH)$, using neutron diffraction data from GEM bank 5 (average scattering angle 91.3°). Tick marks are allowed reflections for (upper): $Ga_5O_7(OH)$ and (lower): γ-Ga_2O_3. 130
Figure 3.48 The structure of Ga-tohdite as determined from Rietveld refinement of powder neutron diffraction data. Green spheres are octahedral sites, blue are tetrahedral. The left-hand panel shows the layered structure as it extends in the *ab* plane. The right hand panel shows the environment of each hydrogen atom in the structure. 131
Figure 3.49 Initial Rietveld fit of high resolution XRD data for Ga-tohdite, using the structure detemined from neutron diffraction. Lower tickmarks are for Ga-tohdite, upper for β-Ga_2O_3. Rp = 11.0% wRp = 16.41%. 132
Figure 3.50 Plot of FWHM *vs* *d*-spacing for the peaks of Ga-tohdite (upper) and plots of FWHM *vs* Miller index (lower). 133
Figure 3.51 Rietveld fit of high resolution XRD data for Ga-tohdite, using the structure detemined from neutron diffraction and implementing Stephens’ model of anisotropic broadening. Lower tickmarks are for Ga-tohdite, upper for β-Ga_2O_3. Rp = 7.52% , wRp = 10.23%. 134
Figure 3.52 Contour plot of in situ heating XRD on Ga-tohdite, with intensity on the Z axis and the first, last and an illustrative intermediate scan highlighted. Tick-marks in the centre panel are peaks from κ-Ga_2O_3. 136
Figure 3.53 A Le Bail profile refinement of XRD data for a mixture of κ-Ga_2O_3 (upper tickmarks) and β-Ga_2O_3 (lower tickmarks). 137
Figure 3.54 Summary of the synthesis and interconversion of polymorphs of Ga_2O_3 and related phases. Note that “δ-Ga_2O_3” is a nanocrystalline form of ε-Ga_2O_3. 138
Figure 3.55 Idealised cartoon representations of the structures of the polymorphs of Ga_2O_3. Upper row: the polymorphs based on a face centred cubic oxygen lattice and lower row: the polymorphs based on a hexagonal close packed oxygen lattice. Note that in reality the oxide layers may be distorted from planarity, and that not all Ga sites are fully occupied. 140

Figure 4.1 The spinel structure. Left: the unit cell of the spinel structure with cations in tetrahedral sites in yellow and cations in octahedral sites in blue. Right: the spinel structure viewed along the [111] direction showing the positions of cations in the interstices of the cubic close packed oxygen lattice. 146

Figure 4.2 The as-synthesised spinel powders, L-R: M = Zn, Ni, Co and Fe. Note that for M = Fe, the sample is attracted to a magnet at room temperature. 151

Figure 4.3 SEM images of the gallium-zinc spinel. 153

Figure 4.4 SEM images of the gallium-nickel spinel. 153

Figure 4.5 Le Bail fits to X-ray diffraction patterns of the MGa_2O_4 spinels where (a) M = Zn (Rp = 7.68%, wRp = 11.1%) and (b) M = Ni (Rp = 6.58%, wRp = 8.7%). Note: a small peak due to metallic Zn is labelled with an arrow in (a) and peaks due to metallic Ni were included in the fit and shown by the lower set of tick marks in (b). 154

Figure 4.6 Representative TEM images of the Co-Ga spinel. 155

Figure 4.7 XANES at the Co K-edge of $CoGa_2O_4$ with relevant Co(II) and Co(II/III) standards. 156

Figure 4.8 TGA trace of $CoGa_2O_4$. 157

Figure 4.9 (a) Thermodiffraction of $CoGa_2O_4$. (b) Close-up of region showing non-typical thermal expansion behaviour. 158

Figure 4.10 Result of Rietveld refinement for solvothermal $Co_{1.1}Ga_{1.9}O_{3.95}$ using the stoichiometric $CoGa_2O_4$ as a starting model. Left: data from GEM bank 3 (mean scattering angle 34.9°). Right: data from GEM bank 5 (mean scattering angle 91.3°). 159

Figure 4.11 Result of Rietveld refinement for solvothermal cobalt gallate using γ-Ga_2O_3 as a starting model. Left: data from GEM bank 3 (mean scattering angle 34.9°). Right: data from GEM bank 5 (mean scattering angle 91.3°). 161

Figure 4.12 Result of Rietveld refinement for solvothermal $CoGa_{1.56}O_{3.34}$ starting from the defect spinel model. Left: data from GEM bank 3 (mean scattering angle 34.9°). Right: data from GEM bank 5 (mean scattering angle 91.3°). 163

Figure 4.13 Result of Rietveld refinement for solvothermal CoGaO using the partially defect, mixed valence model. Left: data from GEM bank 3 (mean scattering angle 34.9°). Right: data from GEM bank 5 (mean scattering angle 91.3°). 164

Figure 4.14 The measured PDF of the cobalt gallate spinel with the result of peak fitting (red), and the calculated $T_0(r)$ slopes for model 4 (green) and stoichiometric model 1 (blue). 165

Figure 4.15 (a) The result of PDF analysis of $CoGa_2O_4$ using the Rietveld model 4 as a starting point. wRp = 13.3% (b) Close-up view of the low-*r*

region of the fit, emphasising the discrepancy in the position and shape of the first peak. 167
Figure 4.16 Magnetisation *vs* temperature for solvothermal cobalt gallate, with inset showing an enlargement of the low temperature region. 168
Figure 4.17 (a) Magnetisation *vs* applied field curves for the cobalt gallate spinel at three different temperatures and (b) view of the 300 K data showing its linearity. 168
Figure 4.18 Close up of the low-field region of the *M* vs *H* curves for the cobalt gallate spinel at 5 K and 17.5 K 169
Figure 4.19 TEM images of the iron gallium spinel. The numbers in the lower panels correspond to regions used for EDX analysis in Table 4.9. 171
Figure 4.20 Fe K-edge XANES of the iron gallium spinel and relevant standard materials. 172
Figure 4.21 Thermodiffraction of the iron gallium spinel. 173
Figure 4.22 TGA traces of the iron gallium spinel, (a) measured in air and (b) measured in N_2 174
Figure 4.23 The X-ray diffraction pattern of ε-$GaFeO_3$ prepared by the ceramic method with vertical bars denoting the expected peak positions and intensities. Peaks marked with a * are from the aluminium sample holder. 174
Figure 4.24 The result of a Le Bail fit to the neutron diffraction data for the iron gallium spinel using space group *Fd***3***m*. Left: GEM bank 5, Right: GEM bank 3. The cubic lattice parameter, *a* = 8.3043(6) Å, Rp = 2.75%, wRp = 3.36%. 175
Figure 4.25 Close-up view of a region of the Le Bail fit for the iron gallium spinel in space group *Fd***3***m*, with arrows identifying the subtle but significant discrepancies in the fit. 176
Figure 4.26 The powder XRD pattern of the gallium iron spinel. 177
Figure 4.27 The result of a Le Bail fit to the neutron diffraction data for the iron gallium sample using two spinels in space group *Fd***3***m*. Left: GEM bank 5, Right: GEM bank 3. The cubic lattice parameters are, a_1 = 8.3668(9) Å and a_2 = 8.3127(5) Å, Rp = 1.74%, wRp = 2.24%. 177
Figure 4.28 The calculated neutron diffraction patterns for magnetite Fe_3O_4 both with and without magnetic contribution. Panel on the right is a closer view of the region $1 \leq d \leq 2$ Å. 179
Figure 4.29 (a) The result of PDF analysis for the iron gallium spinel and (b) a close-up view of the low-*r* region showing discrepancies in the fit to the first two peaks. 181
Figure 4.30 Upper: the FC and ZFC *M vs T* curves for ε-$FeGaO_3$. Lower: *M* vs *H* hysteresis loop measured at 2K. 182
Figure 4.31 *M vs T* curves for the solvothermal iron gallium spinel. 183

Figure 4.32 Left: M *vs* H loops for the solvothermal iron gallium spinel measured at 5, 100 and 300 K, and Right: close-up view of the low-field region of the hysteresis loops. 184

Figure 5.1 The structure of CeO_2.[12] (a) the unit cell of CeO_2, space group $Fm\mathbf{3}m$ (b) the cubic, 8-coordinate arrangment of oxygen atoms around each cerium atom. Yellow spheres are Ce atoms and red spheres are O atoms. 190

Figure 5.2 The results of Rietveld refinement against neutron diffraction data for (a) Ce75, (b) Ce50 and (c) Ce40. The ticks show allowed reflections for the refined fluorite structure. 194

Figure 5.3 The $i(Q)$ for (a) Ce75, (b) Ce50 and (c) Ce40. 196

Figure 5.4 The $D(r)$ for (a) Ce75, (b) Ce50 and (c) Ce40. The decrease in particle size with increasing Bi content is obvious from the damping of the $D(r)$ at high-r. 197

Figure 5.5 Plot showing the results of PDF analysis of (a) Ce75, (b) Ce50 and (c) Ce40, using the mixed phase CeO_2 + α-Bi_2O_3 model. 198

Figure 5.6 Plot showing the results of PDF analysis of (a) Ce75, (b) Ce50 and (c) Ce40, using the single phase model. 201

Figure 5.7 Comparison of the low-r region of the PDF fitting of (top to bottom) Ce75, Ce50, Ce40, for (a) the single phase model and (b) the distorted β-Bi_2O_3/CeO_2 model. 203

Figure 5.8 The local environment of the "β-Bi_2O_3 like" Bi from the low-r fit of the mixed-phase model for Ce75, Ce50 and Ce25. 205

Figure 5.9 Plot showing the result of PDF analysis for Ce50 using the two phase CeO_2 + β-Bi_2O_3 model. 205

Figure 5.10 Left: $i(Q)$ for the two pyrochlore samples, with inset showing expanded high-Q region. Right: $D(r)$ for the two samples. 208

Figure 5.11 The results of PDF analysis using the simple pyrochlore model for (upper) P700 and (lower) P300. 209

Figure 5.12 Simulated partial correlation functions from the simple pyrochlore model and their comparison with the measured $D(r)$ for P700. 210

Figure 5.13 The results of PDF analysis using the modified pyrochlore model with A-site Ti and CeO_2 as a secondary phase for (upper) P700 and (lower) P300. 211

Figure 5.14 Comparison of (a) simulated diffraction pattern of the PDF analysis model, with (b) the measured diffraction pattern from P700. Tick marks are allowed reflections from the refined pyrochlore model (upper) and CeO_2 (lower). 212

Figure 5.15 The low-r region of the results of PDF analysis using the modified pyrochlore model with A-site Ti and CeO_2 as a secondary phase for (a) P700 and (b) P300. 213

Figure 5.16 Evolution of pyrochlore structure (far left) to defect fluorite structure (far right) *via* relaxation of 48f oxygen towards the ideal fluorite position, occupation of the previously vacant 8a site and subsequent cation mixing. See text and Heremans *et al.*[24] for further explanation. 214

Figure 5.17 The results of fitting the low-*r* region of the PDFs with the $F\mathbf{4}3m$ model for (a) P700 and (b) P300. 216

Figure 5.18 Upper: two views of the geometry of the A site in the $F\mathbf{4}3m$ pyrochlore model. Lower: two views of the geometry of the B site in the $F\mathbf{4}3m$ pyrochlore model. Red spheres are oxygen, yellow are cerium and blue are titanium. 217

Figure 6.1 The structures of (a) zeolite A and (b) zeolite Y. Tetrahedra representing the [TO_4] units are shown without associated water and/or cations. 223

Figure 6.2 Figure illustrating two views of zeolite crystallisation, based on Cundy and Cox,[11] (a) heterogeneous crystallite growth *via* gel releasing reactive species/building units into solution and (b) homogeneous crystallite growth *via* rearrangement and successive ordering of the gel phase. 225

Figure 6.3 Cartoon illustrating a proposed scheme for zeolite crystallisation *via* successive ordering of the gel precursor. Based on Cundy and Cox.[12] 227

Figure 6.4 The framework structure of zeolite A, showing the structural motifs involved. T atoms lie on the points where the wire “bonds” intersect. 231

Figure 6.5 Cartoon representation of the separation of zeolite precursor gels. 234

Figure 6.6 The measured X-ray diffraction pattern of crystalline zeolite A, compared with the allowed reflections generated from Ikeda *et al.*[36] 235

Figure 6.7 A cartoon representation of the zeolite precursor gel and the experimental set-up for neutron diffraction measurements. 236

Figure 6.8 (a) The ^{27}Al NMR spectrum of the liquid layer of a zeolite A precursor gel. Features at (i) and (ii) indicate Q^0 monomeric species and Q^1 dimeric species, respectively. (b) ^{29}Si NMR spectrum of the liquid layer of a zeolite A precursor gel. Features at (iii) and (iv) indicate q^0 monomeric and q^1 dimeric species, respectively. Note that DSS is a sodium salt of 2,2-dimethyl-2-silapentane-5-sulfonate, a common NMR standard used in aqueous solution. The Q/q notation is used to represent complex silicate and aluminosilicate species in solution: the superscript represents the number of T–O–T bridges. 239

Figure 6.9 Infrared spectra of zeolite samples over the full measured range (a) and over the range incorporating the T–O–T asymmetric stretching frequencies (b). 241

Figure 6.10 Upper: SEM micrograph of crystalline zeolite A. Lower: SEM micrograph of quenched and dried precursor gel. 242

Figure 6.11 SANS plot for a gel and liquid layer pair measured on LOQ at ISIS. Inset: Porod plot of the data from the gel layer. 243

Figure 6.12 SANS plots for zeolite precursor gels aged at different temperatures (30, 70 and 90 °C) for 90 minutes, measured on NIMROD. 244

Figure 6.13 Porod plots for the SANS data measured on NIMROD for three differently aged zeolite precursors. 245

Figure 6.14 The measured $i(Q)$ for crystalline zeolite A with the inset showing a close-up of the region $0 \text{ Å}^{-1} \leq Q \leq 6 \text{ Å}^{-1}$. 246

Figure 6.15 (a) The measured $D(r)$ from a sample of crystalline zeolite A compared with the hydrated model from Ikeda *et al.* and (b) The measured $D(r)$ compared with the dehydrated model also from Ikeda *et al.*.[36] 247

Figure 6.16 Comparison of various partial correlation functions that are significantly different in the hydrated and dehydrated models of zeolite A.[36] 249

Figure 6.17 The local environment of sodium ions in the structure of zeolite A.[36] Yellow spheres are Na, red oxygen, light blue aluminium and dark blue silicon. (a) the hydrated zeolite A and (b) the dehydrated zeolite A. 249

Figure 6.18 The measured $i(Q)$ for the quenched and dried precursor gel. 251

Figure 6.19 The measured $D(r)$ from crystalline zeolite A and the dried precursor gel. 251

Figure 6.20 The $i(Q)$s of D_2O and NaOD solution with an inset showing the low Q region. 252

Figure 6.21 The $D(r)$ of D_2O and NaOD solution with an inset showing the low r region. 253

Figure 6.22 The $i(Q)$ of a sample of zeolite A suspended in D_2O compared with that of pure D_2O. 254

Figure 6.23 Plot showing the *i*(Q) from dry crystalline zeolite A compared with that of the D_2O-subtracted “wet” zeolite A. 254

Figure 6.24 A comparison of the $i(Q)$ for a gel aged at 30 °C for 3 hours and its corresponding liquid layer. 256

Figure 6.25 (a) A comparison of the $D(r)$ for a gel aged at 30 °C for 3 hours and its corresponding liquid layer and (b) a close-up of the first peaks of the same two $D(r)$. 256

Figure 6.26 A comparison of the $D(r)$ from the liquid and gel layers with those from the dried gel and crystalline zeolite A. For this plot, all the $i(Q)$ were Fourier transformed with $Q_{\max} = 20 \text{ Å}^{-1}$, to enable direct comparison of the $D(r)$. 257

Figure 6.27 (a) The $D(r)$ obtained after subtracting the $i(Q)$ from the liquid layer from that of the gel layer and Fourier transforming the result with $Q_{\max} = 20 \text{ Å}^{-1}$, and (b) the $D(r)$ measured from the dry gel. 258

Figure 6.28 The liquid and gel layer *D*(*r*) compared with the calculated partial functions from the hydrated zeolite A model. 259

Figure 6.29 (a) *i*(*Q*) for the gel and liquid layers after ageing at 70 °C for 3 hours and (b) *D*(*r*) for the same samples. 261

Figure 6.30 (a) *i*(*Q*) for the gel and liquid layers after ageing at 90 °C for 4 hours and (b) *D*(*r*) for the same samples. 262

Figure 6.31 A comparison of *D*(*r*) from the gel and liquid layers aged at different times and temperatures. Arrows represent features of note, as explained in the text. 263

Figure 6.32 Left: comparison between *i*(*Q*) for the primary gel and the gel aged at 30 °C for 3 hours. Right: comparison between *i*(*Q*) for the primary gel and the liquid layer after aging at 30 °C for 3 hours. 264

Figure 6.33 The first peak in the *i*(*Q*) of the primary gel and the liquid layer. 265

Figure 6.34 Left: comparison between *D*(*r*) for the primary gel and the gel aged at 30 °C for 3 hours. Right: comparison between *D*(*r*) for the primary gel and the liquid layer after aging at 30 °C for 3 hours. 266

List of Tables

Table 2.1 The datasets which must be obtained for a neutron total scattering experiment. 52

Table 2.2 The parameters available for refinement in PDFgui. 61

Table 3.1 Refined parameters from PDF analysis of β-Ga_2O_3 ($Q_{\max}$ = 30 Å^{-1}). Space group $C2/m$. Refined (and initial) cell parameters: a = 12.22530(6) Å (12.214 Å), b = 3.03636(1) Å (3.0371 Å), c = 5.80645(3) Å (5.7981 Å) and β = 103.7540(8)° (103.83°). 84

Table 3.2 The results of fitting the first peak of the PDF for α-Ga_2O_3. According to the crystal structure,[10] the average coordination number of Ga in α-Ga_2O_3 is 6.0. 86

Table 3.3 The results of fitting the first peak of the PDF for β-Ga_2O_3. According to the crystal structure,[8] the average coordination number of Ga in β-Ga_2O_3 is 5.0. 86

Table 3.4 Estimated particle diameters using the Scherrer equation for various samples of γ-Ga_2O_3. 88

Table 3.5 Table 1: Crystal parameters for γ-Ga_2O_3, space group $Fd\mathbf{3}m$, a = 8.23760(9) Å. Rp = 1.23%, wRp = 1.36%. Measured density = 5.7607 gcm^{-3}, calculated density = 5.9376 gcm^{-3}. 92

Table 3.6 Atomic parameters for $F\mathbf{4}3m$ model of γ-Ga_2O_3. Italics designate unrefined parameters. 95

Table 3.7 Crystal parameters from nanocrystalline, solvothermal γ-Ga_2O_3. Space group $Fd\mathbf{3}m$, a = 8.2240(2) Å. Rp = 0.66%, wRp = 0.92%. 104

Table 3.8 The modified spinel model used to describe disordered γ-Ga_2O_3 made by the precipitation method. 109

Table 3.9 Refined crystal parameters for ε-Ga_2O_3 from Rietveld refinement. Space group $P6_3mc$. a = 2.9036(2) Å, c = 9.2554(9) Å, wRp = 1.48%. 118

Table 3.10 Refined crystal parameters for ε-Ga_2O_3 from PDF analysis. Space group $P6_3mc$. a = 2.90726(5) Å, c = 9.2559(3) Å, wRp = 12.7% 119

Table 3.11 Comparison of Ga–O bond lengths in the Rietveld and PDF models for ε-Ga_2O_3. 119

Table 3.12 Crystal parameters for Ga-tohdite, $Ga_5O_7(OH)$. Space group $\boldsymbol{P63mc}$, a = 5.82107(8) Å, c = 9.0662(2) Å. Rp = 2.87%, wRp = 3.48%. 130

Table 3.13 The polymorphs of Ga_2O_3 and the related Al_2O_3 and Fe_2O_3 phases. 139

Table 4.1 The ideal crystal parameters of the spinel structure, in space group $Fd\mathbf{3}m$ and with both origin choices. In this thesis, origin choice 2 is used exclusively. 146

Table 4.2 Synthesis conditions and lattice parameters for solvothermally produced mixed spinels. 152

Table 4.3 Crystal parameters for $Co_{1.106(8)}Ga_{1.893(8)}O_{3.95}$, using the stoichiometric model. Space group $Fd\mathbf{3}m$, a = 8.31393(8) Å. Rp = 1.49%, wRp = 2.38%. Measured density = 5.437 g cm^{-3}, calculated density = 6.019 g cm^{-3}. 159

Table 4.4 Crystal parameters for $Co_{0.756(4)}Ga_{1.495(4)}O_3$, using the model based on γ-Ga_2O_3. Space group $Fd\mathbf{3}m$, a = 8.3133(1) Å. Rp = 1.92%, wRp = 2.87%. Measured density = 5.437 g cm^{-3} , calculated density = 4.841 g cm^{-3}. 161

Table 4.5 Crystal parameters for $Co_{1.000(7)}Ga_{1.562}O_{3.34}$, using the defect model. Space group $Fd\mathbf{3}m$, a = 8.31288(9) Å. Rp = 1.73%, wRp = 2.57%. Measured density = 5.437 g cm^{-3}, calculated density = 5.291 g cm^{-3}. 162

Table 4.6 Crystal parameters for $Co_{0.973(8)}Ga_{1.767(8)}O_{3.752(8)}$, using the partially defect, mixed valence model. Space group $Fd\mathbf{3}m$, a = 8.31282(9) Å. Rp = 1.71%, wRp = 2.54%. Measured density = 5.437 g cm^{-3}, calculated density = 5.563 g cm^{-3}. 163

Table 4.7 Comparison of Co:Ga ratios for the various spinel models for the cobalt gallate spinel. 165

Table 4.8 Comparison of cation distribution in the two spinel models for the cobalt gallate spinel. Numbers given are % cations on each site. 165

Table 4.9 EDX results for gallium iron spinel from the regions labelled in Figure 4.19. 170

Table 4.10 The site occupancies of two spinel models proposed for the iron gallium sample 180

Table 5.1 The crystallographic description of the CeO_2 fluorite structure in space group $Fm\mathbf{3}m$. 190

Table 5.2 Refined structural parameters for Ce-Bi oxides from Rietveld refinement of neutron diffraction data. 195

Table 5.3 Refined structural parameters for Ce-Bi oxides from PDF analysis of neutron diffraction data. 199

Table 5.4 The composition of the cerium bismuth oxides, as determined by various methods. 202

Table 5.5 The Bi–O bond lengths, in Å, found in α-Bi_2O_3,[12] β-Bi_2O_3, [21] and the distorted Bi environment in the $Ce_xBi_{1-x}O_2$ local structure. 204

Table 5.6 The structural parameters for the starting pyrochlore model. Space group $Fd\mathbf{3}m$. 208

Table 5.7 The refined parameters from the modified pyrochlore + CeO_2 model. 212

Table 5.8 The conversion of the $Fd\mathbf{3}m$ pyrochlore model to $F\mathbf{4}3m$. 215

Table 5.9 The refined parameters from the $F\mathbf{4}3m$ model fitting of the low-r (r < 5.8 Å) region of the PDFs. 216

Table 6.1 Results of ICP analysis of representative zeolite precursor gels. 237

Table 6.2 The composition of a zeolite precursor gel, as approximated for analysis of neutron scattering data. 238

Table 6.3 A summary of atomic correlations in the crystalline zeolite A, taken from the structure of Ikeda *et al.*[36] 248
Table 6.4 The coherent neutron scattering lengths of the components of the zeolite gels. 255

Acknowledgements

I would firstly like to thank Richard Walton, for the endless guidance and encouragement so generously given to me over the last four years. Thank you, Richard, for never running out of questions and reminding me to stay positive. I am grateful also to Alex Hannon for many hours spent teaching me about neutron scattering and many more hours providing expertise at the various ISIS beamlines. To Emma Barney I offer my sincere thanks for a great deal of help and support with ISIS experiments and data analysis.

I would also like to thank everybody else with whom I have worked at central facilities: Steve King, Dave Keen, Matt Tucker, Alan Soper and Daniel Bowron at ISIS, and Julia Parker, Chiu Tang, Silvia Ramos and Andy Dent at Diamond. A special thanks goes to Matt Tucker for his assistance with RMCProfile.

I am grateful to Anna Carnerup, Reza Jalilikashtiban and Peter Dunne for providing TEM images. Thanks to Matthew Breeze for assistance with XANES experiments. TGA/DSC data were measured by Peter Dunne and Luke Daniels, and Luke also kindly provided me with some high-resolution XRD. I also thank Mohammed Hilni Harunsani for the high-resolution XRD measurements used in Chapter 4. I am grateful to Craig Hiley for some last-minute SEM imaging. A big thanks goes to Guy Clarkson for single-crystal X-ray diffraction.

I am immensely grateful to all the technical staff at Warwick, ISIS and elsewhere whose expertise has contributed to this work through the provision, maintenance and repair of instruments, equipment and supplies.

I would like to thank Alexis Munn for her friendship, advice, support, companionship in the middle of the night at Diamond and ISIS and, of course, for the tequila. Thanks also to Ben Douglas for his support and encouragement, and for listening to me rant on occasion!

To the rest of the Waltons (sorry Richard), past and present: thank you for being great colleagues and friends, these last few years would not have been the same without you.

To my neutron-scattering family (Jodie, Dean, Dan, Phil, Nix, and the rest): thank you for everything. I have not yet been on an experiment where I have failed to bump into at least one of you (I even managed to find Dan when I went to Grenoble) and it has been fantastic to always know that there's someone there.

Last, but not least, an enormous thank you must go to my parents and to Pete for the amazing amounts of love and encouragement they have given me. This thesis would not have happened without their support and I would therefore like to dedicate it to them.

Declaration

This thesis is submitted to the University of Warwick in support of my application for the degree of Doctor of Philosophy. It has been composed by myself and has not been submitted in any previous application for any degree.

The work presented (including data generated and data analysis) was carried out by the author except in the cases outlined below:

For the work in Chapter 5: samples of the cerium-bismuth oxides were provided by Dr Kripasindhu Sardar. Sample preparation and collection of neutron scattering data for the sodium-cerium-titanate pyrochlore was carried out by Dr Deena Modeshia and corrected neutron scattering data were supplied to the author by Dr Emma Barney.

Parts of this thesis have been published or submitted for publication:

1. “Nanocrystalline Cerium-Bismuth Oxides: Synthesis, Structural Characterization, and Redox Properties” Sardar, K.; Playford, H. Y.; Darton, R. J.; Barney, E. R.; Hannon, A. C.; Tompsett, D.; Fisher, J.; Kashtiban, R. J.; Sloan, J.; Ramos, S.; Cibin, G.; Walton, R. I., *Chem. Mater.* **2010,** *22*, 6191.
2. “Structural Characterization and Redox Catalytic Properties of Cerium(IV) Pyrochlore Oxides” Playford, H. Y.; Modeshia, D. R.; Barney, E. R.; Hannon, A. C.; Wright, C. S.; Fisher, J. M.; Amieiro-Fonseca, A.; Thompsett, D.; O'Dell, L. A.; Rees, G. J.; Smith, M. E.; Hanna, J. V.; Walton, R. I., *Chem. Mater.* **2011,** *23*, 5464.
3. “Controlled Hydrothermal Synthesis of Complex Mixed Oxides Using Solution Redox Chemistry” Walton, R. I.; Sardar, K.; Playford, H. Y.; Modeshia, D. R.; Darton, R. J.; Fisher, J.; Thompsett, D., *Mater. Res. Soc. Symp. Proc.* **2011,** *1309*, 9.
4. “The Disordered Polymorphs of Gallium Oxide” Playford, H. Y.; Hannon, A. C.; Barney, E. R.; Walton, R. I., *manuscript submitted for publication,* **2012**.

In addition, the following paper arose from commissioning experiments performed on the D8 X-ray diffractometer during the course of the work described in the thesis:

1. “$Yb_3O(OH)_6Cl.H_2O$: An Anion-Exchangeable Hydroxide with a Cationic Inorganic Framework Structure” Goulding, H. V.; Hulse, S. E.; Clegg, W.; Harrington, R. W.; Playford, H. Y.; Walton, R. I.; Fogg, A. M., *J. Am. Chem. Soc.* **2010,** *132*, 13618.

Helen Playford
September 2012

Abstract

The structures of a variety of disordered materials were determined using the technique of total neutron scattering.

The synthesis of various polymorphs of Ga_2O_3 and related materials was investigated and the structures of the hitherto uncharacterised polymorphs were examined in detail. The structure of γ-Ga_2O_3 was found to be a cubic defect spinel with four partially occupied Ga sites, however, the octahedral Ga coordination environments were found to be distorted from the average cubic structure. The cation distribution in γ-Ga_2O_3 was found to depend on particle size and synthesis method. Examination of the structure of ε-Ga_2O_3 revealed that it is analogous to a disordered, hexagonal form of ε-Fe_2O_3. The poorly crystalline product of the thermal decomposition of $Ga(NO_3)_3.9H_2O$ was found to be a nanocrystalline modification of ε-Ga_2O_3, rather than a distinct phase with the bixbyite structure, as had been previously reported. The structure of a novel gallium oxyhydroxide, $Ga_5O_7(OH)$, was determined to be analogous to tohdite, $Al_5O_7(OH)$, and in its thermal decomposition pathway was revealed a new Ga_2O_3 polymorph: orthorhombic κ-Ga_2O_3.

A solvothermal synthetic route to spinel structured ternary gallium oxides, of general formula $M_xGa_{3-x}O_{4-y}$, was developed. The structures of the materials where M = Zn or Ni were found to be consistent with those previously published. The materials where M = Co or Fe possess novel, oxygen-deficient compositions and exhibit interesting magnetic behaviour.

A series of cerium bismuth oxides of formula $Ce_{1-x}Bi_xO_{2-1/2x}$ were found to adopt the cubic fluorite structure with significant local distortion due to the preference of Bi^{3+} for an asymmetric coordination environment. A sodium cerium titanate pyrochlore was also structurally characterised and it was determined that, due to the presence of three different cations on the A site, the local structure required a model with reduced symmetry.

In situ neutron scattering experiments were carried out on amorphous zeolite precursor gels in the presence of the reaction liquid. These experiments revealed structural features unique to the gel, and proved that the gel undergoes irreversible structural changes on drying. Preliminary analysis of the gel structure indicated that the Na^+ cations play an important role in the development of the ordered zeolitic framework, and revealed no strong evidence for the existence of discrete structural building units in the gel.

Chapter 1: Introduction

1. Introduction: Disordered Materials

1.1. Ordered Materials

If the atoms in a solid material are arranged in a regular, periodic, three-dimensional array, that material is said to be crystalline.

The relationship between the obvious external order exhibited by many crystalline materials and their internal order began to be understood as far back as the 17th century when Johannes Kepler speculated that the sixfold symmetry of snowflakes could be explained by the close-packing of spherical objects and Robert Hooke observed that many different crystal forms could arise from arrangements of regular spheres (Figure 1.1).[1-2]

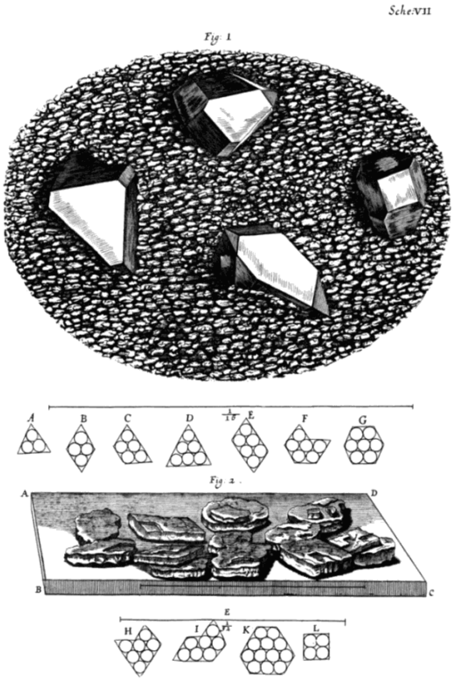

Figure 1.1 Schema 7 from Robert Hooke's Micrographia, demonstrating the range of shapes that can be formed by the close packing of spherical objects, and their relation to the crystal habits of shards of flint. (Source: Project Gutenberg).

It was Haüy, in 1784,[3] who showed that the common crystal habits of the mineral calcite could be described by the packing together of tiny rhombohedral units. This concept, now understood as the packing of repeat units or “unit cells”, forms the basis of the study of crystalline materials. Of course, many crystalline materials do not display any obvious external order; not all single crystals are beautifully facetted, and not all polycrystalline materials reveal intricate crystal habits under a microscope. It is the internal order of a material, rather than its external appearance, which defines it as a crystal (or not a crystal), and modern crystallography is the study of internal order.

The periodic nature of a crystalline structure is crucial to its study. In theory, the entire structure from the local coordination environment of an atom to the arrangement of many millions of atoms needs only one description. The symmetry of the unit cell is assigned to one of the 230 crystallographic space groups which in turn belong to one of the 7 lattice systems. A full structural description of a crystalline material, therefore, requires only a space group, the dimensions of the unit cell, and the locations and identities of atoms within the unit cell.

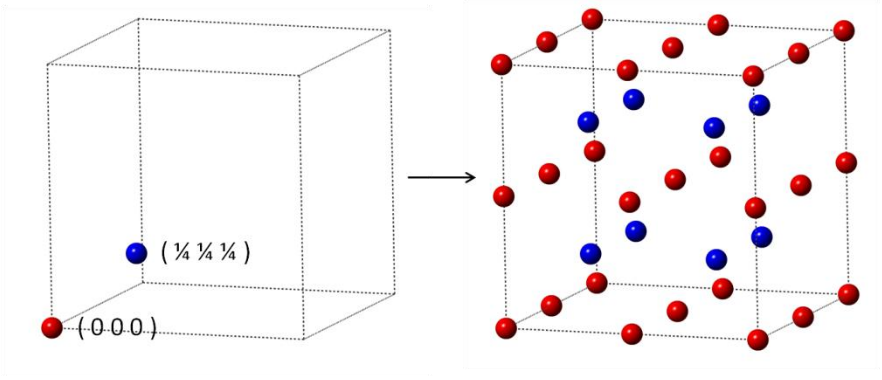

Figure 1.2 An illustration of the symmetry of a simple space group generating multiple equivalent atom positions. Provided with the coordinates of two atoms, the symmetry operators of the cubic space group $Ia\overline{3}$ are used to generate the other atom positions within the unit cell.

Information about the structure of crystalline materials can be obtained relatively easily using techniques such as X-ray diffraction. The diffraction of an incident beam of radiation by a solid crystalline material results in a pattern of spots or lines whose spacing and intensity can be directly related back to the arrangement of atoms in the solid.

The diffraction of X-rays from crystals was first observed a century ago, in 1912, by Laue, Friedrich and Knipping, although there was some controversy surrounding their interpretation of their results.[4] The following year, father and son team W. H. and W. L. Bragg proposed their theory of diffraction.[5] They observed that at certain incident angles, a beam of X-rays directed at a crystal surface produced intense reflected beams. By envisaging the crystal as a collection of planes of atoms separated by a constant distance, they explained this observation in terms of constructive interference of scattered waves. Figure 1.3 demonstrates their explanation.

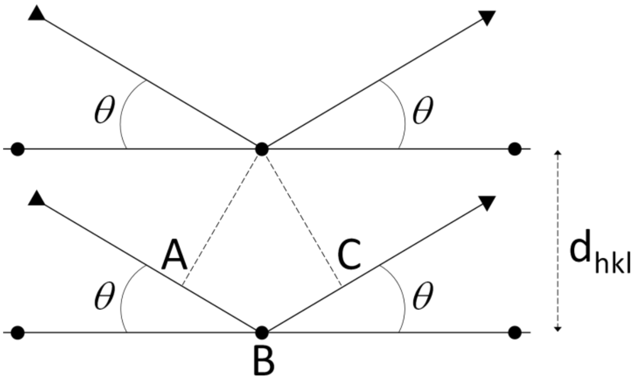

Figure 1.3 Diagram demonstrating Bragg's Law for a rectangular lattice.

The path difference between waves scattered by two adjacent planes of atoms, is given by Equation 1.1.

$$AB + BC = (d_{hkl}\sin\theta + d_{hkl}\sin\theta) = 2d_{hkl}\sin\theta \qquad \textbf{(1.1)}$$

For constructive interference to occur between the two scattered waves, the path difference must be equal to an integer number of wavelengths. This relationship leads to Bragg's Law (Equation 1.2).

$$n\lambda = 2d_{hkl}\sin\theta \tag{1.2}$$

Therefore, for a fixed wavelength, λ, constructive interference of waves scattered by planes with a separation d_{hkl} occurs at a specific incident angle θ.

In a typical powder diffraction experiment, the incident and/or reflected angle is scanned such that the Bragg condition is met for a range of values of *d*. Peaks occur at the values of *d* which correspond to planes of atoms in the crystallites. The amplitude of a diffracted wave is determined by the types and positions of atoms which make up the plane, a complex quantity known as the structure factor, F_{hkl} (Equation 1.3). The measured intensity of a Bragg peak is proportional to the square of the structure factor for that plane. The theory of diffraction is discussed in more detail in Chapter 2.

$$F_{hkl} = \sum_{j=1}^{N} f_j e^{2\pi i(hx_j + ky_j + lz_j)} \tag{1.3}$$

If a suitably large single crystal (0.05 – 0.2 mm is recommended by the Southampton Chemistry Analytical Solutions X-ray diffraction service) can be obtained the elucidation of its structure from diffraction data is now fairly routine and a discussion of single crystal diffraction techniques is beyond the scope of this thesis. For polycrystalline samples, structure determination is sometimes as simple as matching the obtained diffraction pattern with one or more of the thousands catalogued in the International Centre for Diffraction Data (ICDD) database. Techniques such as Rietveld refinement are used routinely to obtain detailed structural information about new materials; provided that a reasonably accurate “guess” at the structure can be made initially, the structural parameters can be refined until the calculated diffraction pattern matches the measured. Techniques for *ab initio* structure solution from powder diffraction data are also becoming increasingly common.[6]

1.2. Flavours of Disorder

Disordered materials are ones whose internal order is, to a greater or lesser extent, reduced from that in a perfectly crystalline material. If “crystalline” is considered a common state of solid matter, “disordered” is more so, because the ways in which order can be reduced are many and varied, as will be discussed in this section.

The first and most ubiquitous type of disorder is caused by thermal vibrations. The atoms in a crystal are constantly in motion due to thermal energy. Therefore, even if their mean positions fall on well defined points within the symmetrical lattice, their instantaneous positions do not. The effect of thermal motion is to reduce intensity of Bragg peaks, and generally speaking, modelling of this is well incorporated into the analysis of crystalline diffraction (see Chapter 2).

Structural order can be viewed as a continuum with perfect order on one end and complete disorder on the other. If a perfect crystal sits on the ordered end, an amorphous material occupies the disordered end, and other flavours of disorder can be placed somewhere between these points.

1.2.1. Disordered crystalline materials

Often it is appropriate to describe a material as crystalline while recognising that it deviates significantly from a ‘perfect’ crystal. The length scale over which the structure is viewed is often crucial to this definition, as in many cases the average or bulk structure (*i.e.* the long-range order) will still be satisfactorily described by the crystal structure when the local structure requires a different description.

One of the most frequently encountered forms of disorder is that of partial occupancy of atomic positions. Depending on the space group of the material involved, the "site" on which an atom sits has a certain multiplicity – the number of equivalent sites that are generated by the symmetry operations applicable to the space group – and in some cases the composition of a material does not allow for the site to be fully occupied. A similar case occurs for mixed occupancy where instead of vacancies, some of the atomic sites are occupied by different elements, as in the case of mixed oxides.

A convenient demonstration of partial occupancy is provided by iron oxide. The same crystal structure is adopted by two forms of iron oxide: magnetite Fe_3O_4 and maghemite γ-Fe_2O_3.[7-8] The structure is known as the spinel structure, named for the mineral $MgAl_2O_4$, and the unit cell contains 32 oxygen sites and 24 metal sites. In Fe_3O_4 (and $MgAl_2O_4$) all of the metal sites are occupied, however to maintain the correct stoichiometry for Fe_2O_3, only 21⅓ of the metal sites are filled. The vacancies are usually considered to be randomly distributed, thus maintaining the same average structure. It is common, however, for vacancy ordering to occur, and this is an important consideration when examining the structures of materials with partial occupancy. It is unlikely that there will be any evidence of this type of disorder in the diffraction data, unless the ordering of vacancies occurs in a concerted manner across many unit cells, creating a "supercell" structure.

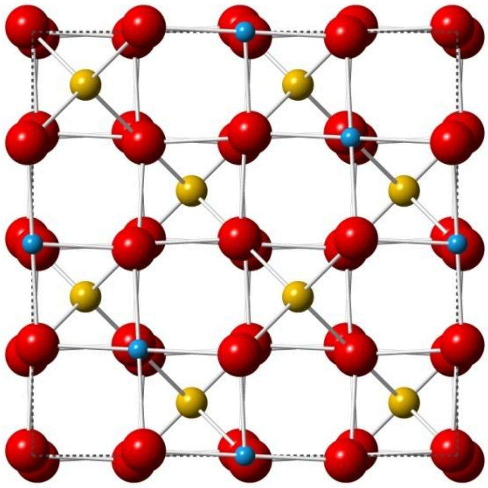

Figure 1.4 The mineral $MgAl_2O_4$ with the cubic spinel structure.[9] Blue spheres are Al, yellow spheres are Mg and red spheres are O. In Fe_3O_4 the Fe atoms are distributed over all Mg and Al sites. In Fe_2O_3, some of these sites are vacant.

The spinel structure also provides an example of mixed occupancy. There are two cation sites, one with a multiplicity of 8 and another with a multiplicity of 16. In $MgAl_2O_4$ the atoms are arranged as might be expected from the formula, with Mg on the 8a site and Al on the 16d site, and this is known as the normal spinel structure. However many spinels exhibit an inverse atomic arrangement, where the 8a site is occupied by the half of the trivalent cations and the 16d site has a disordered mixture of the rest of the trivalent cations and the divalent cations. The vast majority of spinels lie somewhere between these two extremes and exhibit significant cation disorder.

Other common types of disorder in crystals include defects such as twinning, stacking faults and dislocations. Stacking faults are especially common in layered materials such as clays, and can, in general, be categorised into either stacking sequence defects (for example, ABCABCCABCA...) or displacive defects where the layers are rotated around the stacking axis with respect to the ones above and below (see Figure 1.5). These defects manifest as anomalies in the diffraction patterns such as peak shift, broadening or asymmetry. In a well understood system, information about defects can therefore be obtained from careful interpretation of powder diffraction, however the presence of defects also hinders the process of structure refinement.[10]

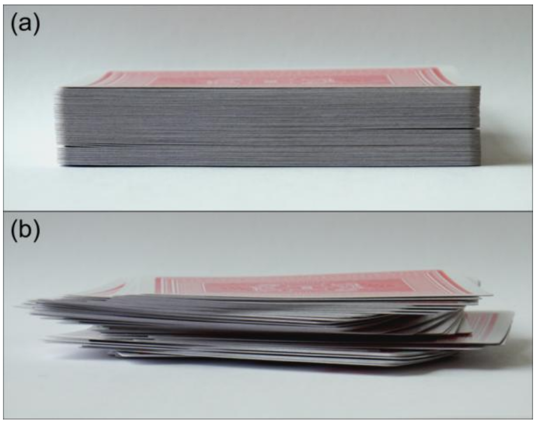

Figure 1.5 A representation of a layered material with (a) no stacking faults and (b) severe displacive stacking faults.

In an ideal crystal, the local coordination environment of an atom (*i.e.* bond lengths and angles) is defined by the crystal structure, however in many disordered crystals the local coordination environment is distorted by the bonding requirements of one of the atoms. Unless this distortion propagates through the material in an ordered way the overall symmetry (and thus, the average structure) is unchanged, but the local structure is very different. It is this kind of situation which leads to the requirement for disordered materials to be studied on multiple length scales.[11]

An illustrative example of the difference between local and average structure is found in the case of $(Ga_{1-x}In_x)As$.[12] The crystallographically measured lattice constant changes linearly with x, as does the (Ga,In)-As distance. In reality it is strongly disfavoured for the Ga-As and In-As bond lengths to deviate much from their values in the pure compounds. Examining the local structure therefore reveals two nearest neighbour bond lengths in $(Ga_{1-x}In_x)As$, neither of which is represented by the crystallographic average.

Yet more forms of disorder in crystals can be found in modulated or incommensurate structures, the inclusion of highly mobile species in interstices, intergrowth materials, and still more, too numerous to attempt to list here. Add to this the fact that types of disorder rarely exist in isolation: a disordered crystalline material will often display a complex mixture of disorder effects, and this level of complexity requires more in-depth study than traditional crystallographic methods alone.

1.2.2. Nanocrystalline materials

The term "nanocrystalline" can mean one of two things: a material which is crystalline but consists of nano-sized particles, or a material which consists of larger particles with nano-sized coherent domains (see Figure 1.6). The definition of "nano-sized" is somewhat arbitrary but generally a material with at least one dimension less than 100 nm is considered to be a nanomaterial. In practise it is usually not possible to be sure which definition of nanocrystalline applies to a particular material unless a technique such as high-resolution transmission electron microscopy (TEM) is used to image the individual particles.

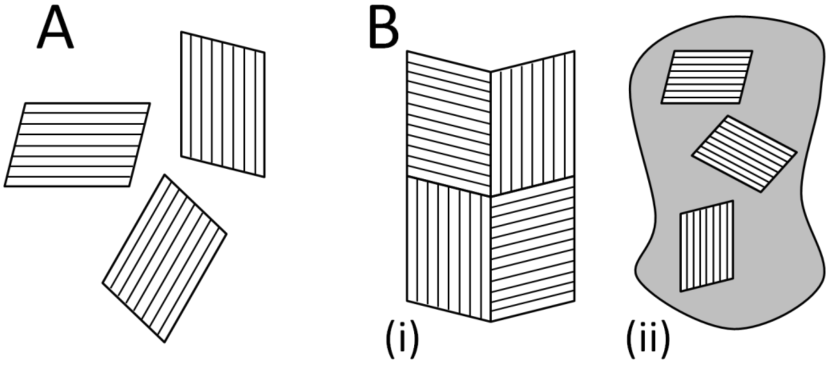

Figure 1.6 Schematic drawing of the two types of nanocrystalline particle. A: crystalline particles of a few-nanometres in size, and B: larger particles with nano-scale coherent domains separated by (i) normal grain boundaries and (ii) disordered interfaces.[13]

Nanocrystalline materials are characterised by their severely broadened diffraction profiles. If the number of crystal planes in the sample is large, any slight deviation from the Bragg angle will lead to strong destructive interference. If the number of crystal planes is small, as in a nanocrystalline material, the conditions for destructive interference are not met until a significant deviation from the Bragg angle is reached, and hence the diffraction peak is broadened. This is illustrated in Equation 1.4, where m = number of planes in the sample.[14]

$$\left(\frac{m}{2}\right)\lambda + \frac{\lambda}{2} = \left(\frac{m}{2}\right) 2d_{hkl}\sin\left(\theta + \delta\theta\right) \tag{1.4}$$

Figure 1.7 shows simulated XRD patterns for bulk and nanocrystalline quartz, demonstrating the effect of particle size broadening. The correlation between particle size and Bragg peak width is given by the Scherrer equation (Equation 1.5, where K = shape factor, λ = wavelength, β = sample contribution to the peak broadening (FWHM) and θ = Bragg angle) and this is often used as a method of estimating an approximate crystallite/domain size. The accuracy of this method is dependent on the assumption that peak broadening from instrumental effects is negligible or well characterised enough to be taken into account.

$$\tau = \frac{K\lambda}{\beta\cos\theta} \tag{1.5}$$

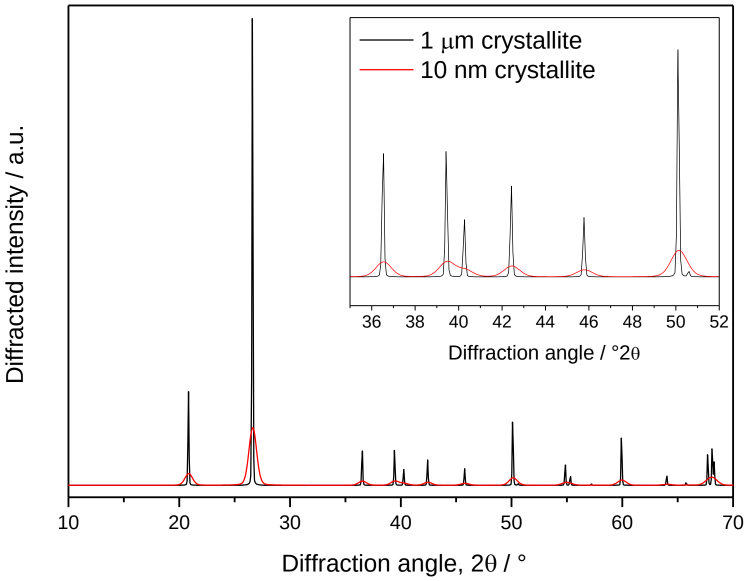

Figure 1.7 Simulated XRD patterns for SiO_2 (quartz) for different particle sizes. The nanometric particle exhibits severely broadened peaks.

Nanocrystalline forms of bulk crystalline structures are very common, and often very sought after for technological applications.[15-17] Nano-sized materials often display size dependent optical and/or electronic effects, and their high surface areas can lead to enhanced activity in catalytic applications. Nanocrystalline materials, and their synthesis and characterisation, are therefore the subject of a vast amount of research.[18]

It is common for nanocrystalline materials to have measurably different structures to their bulk counterparts. As the surface-area-to-volume ratio increases, the bulk structure becomes less important in defining the material, as the deviations in the surface region become dominant. One example is CeO_2 whose unit cell size increases with decreasing particle size once in the region of 10 nm or below.[19-20] There is also the potential for a high degree of surface rearrangement and other surface effects such as adsorption of water or atmospheric gases.

1.2.3. *Amorphous materials and liquids*

The word amorphous is derived from the Greek *amorphos*, which means shapeless or without form. However, even the least structured of materials (*i.e.* monatomic liquids and gases) have a degree of local order simply due to the restrictions on how close the atoms can approach one another, and molecular materials have the additional order arising from intramolecular bonds. As applied to solid matter, the term amorphous is used to describe a material that displays no Bragg peaks, and more generally, an amorphous solid is one which has no long-range order. An amorphous solid generally has a well defined local structure (such as the [SiO_4] tetrahedral units which are largely unchanged between crystalline and glassy silica);[21-22] and an irregular, aperiodic average structure. This description of the structure of an amorphous solid was originally proposed by Zachariasen, who called it the "random network model" (Figure 1.8).[23]

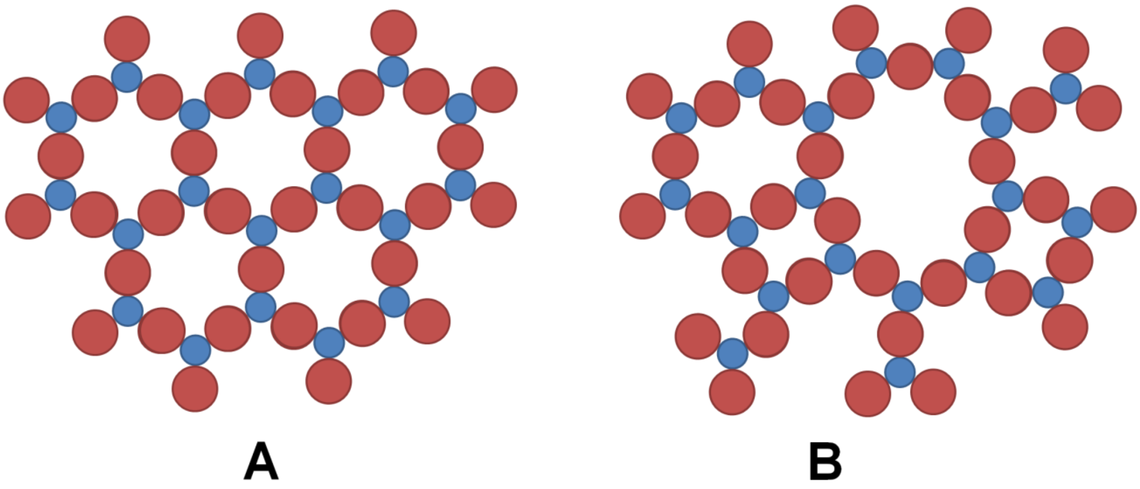

Figure 1.8 (A) The regular arrangement of spheres in a hypothetical crystal (B) The same material as a glass, as per Zachariasen's random network model.

Glasses are perhaps the most well known type of amorphous solid. They are formed by rapidly cooling from a molten state, thereby inducing solidification without crystallisation.[24] Crystalline materials can be made amorphous, or "amorphised", by radiation damage or the application of pressure, and semi-solid materials such as gels are also often amorphous.

The powder diffraction pattern, measured using wavelengths encountered in the laboratory (~ 1 Å), of a truly amorphous material will consist of only a very broad ‘hump’ barely distinguishable from the background. A material which displays Bragg peaks, even very broad ones, is not amorphous and instead exhibits a different flavour of disorder. It is often difficult to distinguish between nanocrystalline and amorphous materials (at least within the limits of available instrumentation), and the terms are often used interchangeably in the literature.

1.3. Studying Disordered Structures.

Traditional crystallographic techniques (*i.e.* diffraction) focus on the information contained in the Bragg scattering only. A disordered material, by definition, contains structural features that produce anomalous and/or reduced intensity Bragg scattering, and/or increased diffuse scattering, and thus requires more in-depth study.

Diffuse scattering from single crystals has been observed since the early days of crystallography, as demonstrated by several papers on the subject appearing in the very first issue of the journal *Acta Crystallographica*, but its analysis has still not become routine. Diffuse scattering is caused by deviations from the average structure and is typically of much lower intensity than Bragg scattering, which makes it hard to analyse. Traditionally, the simulation of diffuse scattering from a model has been compared with the measured data, though recently a great deal of progress has been made with Monte Carlo simulations.[25-26] In powder diffraction experiments, the separation of Bragg and diffuse scattering is far more difficult and the latter has traditionally been treated as part of the background. This is effectively throwing away important structural information, particularly for disordered materials where deviation from the average structure can be the defining characteristic!

As mentioned earlier, transmission electron microscopy (TEM) is a powerful tool for imaging nanoscale materials, and at sufficiently high resolution can prove or disprove the presence of crystalline order in tiny particles (see Figure 1.9).

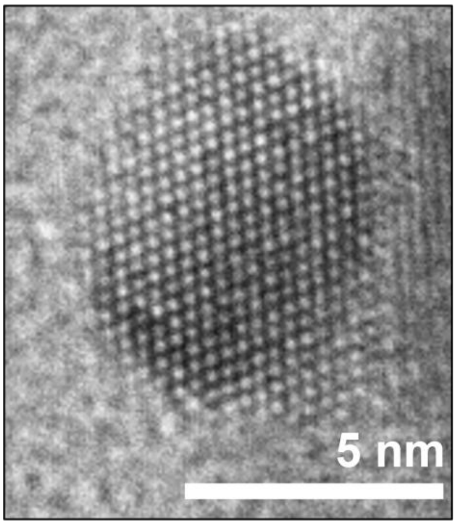

Figure 1.9 High resolution TEM image of a nanocrystal of $Ce_{1-x}Bi_xO_{2-0.5x}$ showing that it is highly ordered and has facetted edges.[27]

It is also important not to discount the potential of electron diffraction (ED) as a structural probe for nanomaterials. A focussed beam of electrons can be incident on and diffract from a single nanoparticle, thus avoiding many of the problems with bulk powder diffraction of nanocrystalline samples. Electron diffraction can be combined with high-resolution imaging to regain the phase information lost in the diffraction pattern and to directly study defects and local structural deviations.[28] Electrons interact with matter much more strongly than do X-rays (or neutrons) which means that the intensities of electron diffraction spots are not straightforward to interpret, and this combined with the relative difficulty of obtaining the diffraction patterns has limited the use of this technique. More recently, advanced techniques such as precession electron diffraction have begun to overcome some of the problems with ED, however, due mainly to the operational expertise required, its potential as a technique for the structural study of nanomaterials has yet to be fully realised.[29-30]

In Section 1.2.1 above, it was noted that disordered materials often exhibit local distortions from an average structure. Experimental techniques designed to probe the local environment in a material can be used to great effect in these cases. X-ray spectroscopic techniques such as X-ray absorption near edge structure (XANES) and extended X-ray absorption fine structure (EXAFS) can reveal element specific information about the oxidation state and coordination geometry of a particular site in a material, and when carefully analysed, the second or even third coordination spheres can be probed.[31] Nuclear magnetic resonance (NMR) spectroscopy can reveal the number of inequivalent atomic sites in a material and the nature of those sites (in terms of coordination and degree of order). A great many different nuclei can be studied by NMR, although NMR of paramagnetic systems may be challenging. Techniques for obtaining high quality NMR data from solid state samples are increasingly available, such as the use of very powerful magnets and the magic angle spinning (MAS) technique which reduces line broadening. Other probes that can reveal local structural information include Raman and Mössbauer spectroscopies, though the latter requires the presence of a suitable nucleus (commonly iron). These techniques, while powerful, do not provide information about how the local structural features relate to the material as a whole.

The study of amorphous materials and liquids has used diffraction as a structural probe for many decades yet these materials possess no long range order and display no Bragg peaks in their diffraction patterns. In a liquid containing only one type of atom, the only well-defined structure is that of closest distances of approach between atoms. This type of structure can be expressed in terms of the number of atoms at a distance *r* from the average atom placed at the origin: a function called the radial distribution function. This function is related by Fourier transform to the measurable scattering intensity from the sample, an extremely important observation which was first made by Zernike and Prins in 1927.[32-33] The first exploitation of this relationship was by Debye and Menke in 1930, studying the structure of liquid mercury. The same relationship can be applied to samples containing more than one type of atom, though the final radial distribution function is a superposition of the various “partial” distribution functions corresponding to the correlations between the different pairs of atoms.

Under the right experimental conditions, it is therefore possible to take the diffraction pattern of any material and obtain *via* Fourier transform a correlation function which reveals real interatomic distances. Even in an amorphous material, a few well defined features corresponding to nearest and next-nearest neighbour distances, will be visible. Treatment of scattering data in this way explicitly includes both Bragg (if present) and diffuse scattering in the one function, and for this reason these experiments are referred to as “total scattering” measurements.[11]

An example correlation function for carbon tetrachloride is shown in Figure 1.10. Two sharp peaks are visible, at distances corresponding to the C–Cl bond length and the Cl–Cl non-bonded nearest neighbour distance. Beyond this, the correlations rapidly decay due to the lack of long range order in the liquid (*i.e.* there are many correlations which overlap due to the absence of a well-defined structure).

It is worth noting here that in addition to the aforementioned radial distribution function, there are many similar correlation functions which reveal subtly different structural information and are referred to by many similar names. The term “correlation function” is here used generally, and specific functions related to the work in this thesis will be introduced in Chapter 2.

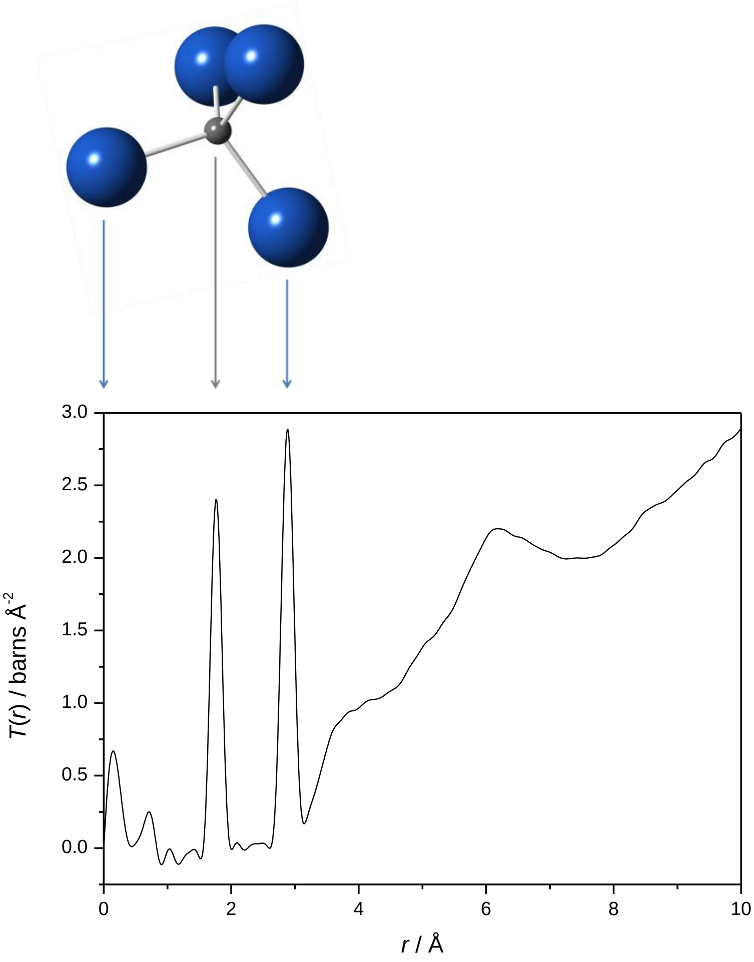

Figure 1.10 An example measured correlation function for liquid carbon tetrachloride, with thanks to Alex Hannon.

Several common approaches are used when analysing total scattering data. Commonly associated with liquid and amorphous diffraction is the extraction of bond lengths and coordination numbers from fitting the first few peaks in the correlation function, and this is equally applicable to other disordered materials. For disordered crystalline materials an approach similar to Rietveld refinement, called Pair Distribution Function (PDF) analysis, has been developed by Billinge, Egami and co-workers whereby a model structure, often based on a crystal structure, is refined by the minimisation of differences between the calculated PDF (a correlation function) and a measured one.[11]

PDF analysis, in its simplest application, can be used to determine whether a crystallographic model adequately describes the local structure of a material, and to refine the model further if required. Continuing the analogy with traditional Rietveld refinement, PDF analysis still requires the definition of a crystal structure and still assumes a periodic structure, although the creation of larger supercells and the lowering of symmetry are both common and straightforward in PDF analysis software.

The correlation function of a crystalline material contains structural information over a range of length scales, which allows the local and mid-to-long range order to be studied simultaneously. There have been examples of correlation functions of highly-crystalline materials revealing subtleties in their structure which were missed in traditional crystallographic investigations.[11] In the case of $LiMoO_2$ the structure was determined using Rietveld refinement of X-ray and neutron diffraction data,[34] and it was not until the PDF was checked almost a decade later that inadequacies were revealed.[35] The Rietveld structure had each Mo atom surrounded by six others at equal distance, while the PDF-derived model revealed short and long Mo–Mo correlations which indicated the presence of metal-metal bonding interactions, as seen in other similar materials.

A different but complementary approach to PDF analysis is to model the total scattering with a large "box" of atoms using Reverse Monte Carlo (RMC) modelling.[36] The arrangement of atoms in the box is initially generated from a refined crystal structure, but the atoms are then moved at random until the calculated and measured total scattering are in agreement. The final configuration of atoms can be studied to gain insight into likely local structural distortions and their relationship to the original unit cell. Knowledge about the structure obtained from other techniques can be easily incorporated into an RMC refinement using chemical restraints (*e.g.* coordination number or bond lengths) or, in some cases, by inclusion of data from other, independent measurements. The analysis of total scattering data is discussed further in Chapter 2.

The applications of total scattering methods are many and varied, and some of the most notable were the subject of a recent review article by Young and Goodwin.[37] Several examples will be briefly discussed here to demonstrate the scope of the technique.

The structure of the important catalytic material, γ-Al_2O_3, was investigated using PDF analysis by Paglia *et al.*.[38] The results on mid-to-long length scales were in agreement with previous studies of its average structure: a tetragonally distorted spinel with multiple partially occupied sites. However, the local structure was found to deviate significantly from this model due to faults in the oxygen sublattice that could be modelled by incorporating nanoscale elements of the structure of the boehmite (AlOOH) precursor.

Corr *et al.* used X-ray total scattering measurements to follow the structural changes in vanadium oxide, VO_2, as a function of temperature. On cooling through 340 K a transition from metallic to insulating behaviour is observed due to a phase change from a tetragonal (rutile) structure to a monoclinic structure. Correlation functions collected near the transition temperature revealed that the two phases exist in equilibrium and that there is no evidence for the existence of an intermediate phase.[39]

Zeolitic imidazolate frameworks (ZIFs) are metal organic frameworks consisting of metal atoms connected by bridging imidazolate ligands whose topology often mimics that of aluminosilicate zeolites due to the similarity in the M–ligand–M and Si–O–Si bond angles. The thermal behaviour of crystalline zinc imidazolate, ZIF-4, is rather unusual. At about 300 °C it becomes amorphous and on further heating to 400 °C a second crystalline phase emerges with the same composition but a different structure to ZIF-4. Neutron and X-ray total scattering measurements were used to constrain a RMC simulation of the structure of the amorphous ZIF.[40] It was found that although the local environment of the Zn atoms was exactly the same as in its two neighbouring crystalline ZIFs, the arrangement of the tetrahedral network was distinct. In fact, the structure of the amorphous ZIF was best modelled using a structure analogous to that of silica glass.

White *et al.*[41] used *in situ* neutron scattering to examine the local structural changes that occurred during the formation of a metakaolin-based geopolymer gel. The use of neutrons allowed the role of water in the structure of the gel to be examined, and the results provided insight into the processes of dissolution, gel formation and stabilisation *via* crosslinking. The work was recently extended using a density functional theory (DFT) simulation to examine the molecular processes responsible for the observed changes.[42]

As these and other examples show, disordered materials are by nature complex, and as such require a variety of techniques to study them. Differences between local and average structure must be examined using techniques that cover a range of length scales. Total scattering is one such technique which is both extremely simple (conceptually) and extremely powerful.

1.4. Aims of the Work Described in this Thesis

The primary aim of the work described in this thesis was to investigate the structures of a variety of complex and/or disordered inorganic materials using the technique of total neutron scattering.

For this work, three groups of materials were identified whose structures were either known to, or considered likely to display various “flavours” of disorder that would therefore benefit from the application of neutron scattering techniques to their characterisation.

Firstly, gallium sesquioxide, Ga_2O_3, displays surprisingly complex polymorphism; behaviour which was first described in the 1950s,[43] but never followed up with a full structural investigation. An initial investigation into the synthesis of the various polymorphs, by solvothermal and other methods, was to be carried out, followed by an investigation into their structures and interconversions using total scattering and *in situ* diffraction techniques. The application of solvothermal methods to the synthesis of structurally related ternary gallium oxides was also to be explored.

Secondly, the determination of the structure of several catalytically active cerium-containing oxides was to be carried out using total scattering techniques, since an accurate description of atomic-scale structure is of considerable importance when attempting to understand the structure-property relationships in functional materials.

Finally, the viability of *in situ* neutron scattering as a technique with which to probe the structure of the amorphous gels which act as precursors to crystalline aluminosilicate zeolites was to be explored.

1.5. References

1. Kepler, J., *The six-cornered snowflake : a new year's gift*. 1st ed.; Paul Dry Books: Philadelphia, 2010.
2. Hooke, R., *Micrographia: or some Physiological Descriptions of Minute Bodies made by Magnifying Glasses with Observations and Inquiries Thereupon*. London, UK, 1665.
3. Haüy, R.-J., *Essai d'une théorie sur la structure des crystaux appliquée à plusieurs genres de substances crystallisées*. Paris, France, 1784.
4. Eckert, M., *Acta Crystallogr. A* **2011,** *68*, 30.
5. Bragg, W. H.; Bragg, W. L., *The Crystalline State*. G. Bell: London, 1933-1965.
6. David, W. I. F.; Shankland, K.; McCusker, L. B.; Baerlocher, C., *Structure determination from powder diffraction data*. Oxford University Press: Oxford, UK, 2002.
7. Fleet, M., *Acta Crystallogr. B* **1981,** *37*, 917.
8. Jørgensen, J.-E.; Mosegaard, L.; Thomsen, L. E.; Jensen, T. R.; Hanson, J. C., *J. Solid State Chem.* **2007,** *180*, 180.
9. Bragg, W. H., *Nature* **1915,** *95*, 561.
10. Neder, R. B.; Proffen, T., *Diffuse Scattering and Defect Structure Simulations: A Cook Book Using the Program DISCUS*. Oxford University Press: Oxford, UK, 2008.
11. Billinge, S. J. L.; Egami, T., *Underneath the Bragg Peaks: Structural Analysis of Complex Materials*. Pergamon: Oxford, UK, 2003; Vol. 7.
12. Petkov, V.; Jeong, I. K.; Chung, J. S.; Thorpe, M. F.; Kycia, S.; Billinge, S. J. L., *Phys. Rev. Lett.* **1999,** *83*, 4089.
13. Chadwick, A. V.; Savin, S. L. P., In *Low-Dimensional Solids*, Bruce, D. W.; O'Hare, D.; Walton, R. I., Eds. John Wiley & Sons, Ltd: 2010.
14. Hammond, C., In *The Basics of Crystallography and Diffraction*, Oxford University Press: Oxford, UK, 1997; pp 145.
15. Gleiter, H., *Prog. Mater Sci.* **1989,** *33*, 223.
16. Siegel, R. W., *Nanostruct. Mater.* **1994,** *4*, 121.
17. Suryanarayana, C., *JOM* **2002,** *54*, 24.
18. Wu, J.; Cao, J.; Han, W.-Q.; Janotti, A.; Kim, H.-C., *Functional Metal Oxide Nanostructures*. Springer: 2012.
19. Deshpande, S.; Patil, S.; Kuchibhatla, S.; Seal, S., *Appl. Phys. Lett.* **2005,** *87*.
20. Hailstone, R. K.; DiFrancesco, A. G.; Leong, J. G.; Allston, T. D.; Reed, K. J., *J. Phys. Chem. C* **2009,** *113*, 15155.
21. Keen, D. A.; Dove, M. T., *J. Phys.: Condens. Matter* **1999,** *11*, 9263.
22. Keen, D. A.; Dove, M. T., *Mineralogical Magazine* **2000,** *64*, 447.
23. Zachariasen, W. H., *J. Am. Chem. Soc.* **1932,** *54*, 3841.
24. Ossi, P. M., *Disordered Materials An Introduction*. 2nd ed.; Springer: Berlin, Germany, 2006.
25. Nield, V. M., *Nucl. Instrum. Methods Phys. Res., Sect. A* **1995,** *354*, 30.
26. Welberry, T. R.; Goossens, D. J., *Acta Crystallogr. A* **2008,** *64*, 23.
27. Sardar, K.; Playford, H. Y.; Darton, R. J.; Barney, E. R.; Hannon, A. C.; Tompsett, D.; Fisher, J.; Kashtiban, R. J.; Sloan, J.; Ramos, S.; Cibin, G.; Walton, R. I., *Chem. Mater.* **2010,** *22*, 6191.

28. Zou, X., In *Electron Crystallography, Novel Approaches for Structure Determination of Nanosized Materials*, Weirich, T. E.; Lábár, J. L.; Zou, X., Eds. Springer: The Netherlands, 2006; pp 3.
29. Vincent, R.; Midgley, P. A., *Ultramicroscopy* **1994,** *53*, 271.
30. Berg, B. S.; Hansen, V.; Midgley, P. A.; Gjonnes, J., *Ultramicroscopy* **1998,** *74*, 147.
31. Rehr, J. J.; Albers, R. C., *Reviews of Modern Physics* **2000,** *72*, 621.
32. Zernike, F.; Prins, J. A., *Z. Phys. A: Hadrons Nucl.* **1927,** *41*, 184.
33. Warren, B. E., In *X-Ray Diffraction*, Addison-Wesley: USA, 1969; pp 116.
34. Aleandri, L. E.; McCarley, R. E., *Inorg. Chem.* **1988,** *27*, 1041.
35. Hibble, S. J.; Fawcett, I. D.; Hannon, A. C., *Inorg. Chem.* **1997,** *36*, 1749.
36. Tucker, M. G.; Keen, D. A.; Dove, M. T.; Goodwin, A. L.; Hui, Q., *J. Phys.: Condens. Matter* **2007,** *19*, 335218.
37. Young, C. A.; Goodwin, A. L., *J. Mater. Chem.* **2011,** *21*, 6464.
38. Paglia, G.; Bozin, E. S.; Billinge, S. J. L., *Chem. Mater.* **2006,** *18*, 3242.
39. Corr, S. A.; Shoemaker, D. P.; Melot, B. C.; Seshadri, R., *Phys. Rev. Lett.* **2010,** *105*.
40. Bennett, T. D.; Goodwin, A. L.; Dove, M. T.; Keen, D. A.; Tucker, M. G.; Barney, E. R.; Soper, A. K.; Bithell, E. G.; Tan, J.-C.; Cheetham, A. K., *Phys. Rev. Lett.* **2010,** *104*, 115503.
41. White, C. E.; Provis, J. L.; Llobet, A.; Proffen, T.; van Deventer, J. S. J., *J. Am. Ceram. Soc.* **2011,** *94*, 3532.
42. White, C. E.; Provis, J. L.; Proffen, T.; van Deventer, J. S. J., *AlChE J.* **2012,** *58*, 2241.
43. Roy, R.; Hill, V. G.; Osborn, E. F., *J. Am. Chem. Soc.* **1952,** *74*, 719.

Chapter 2: Theory and Experimental Techniques

2. Theory and Experimental Techniques

2.1. Diffraction

2.1.1. X-ray diffraction

A basic introduction to the theory of X-ray diffraction will be presented here, much of which is based on books by Clearfield and Hammond.[1-2]

An array of atoms, such as a crystal, can act as a diffraction grating for radiation of an appropriate wavelength. As mentioned in Chapter 1, constructive interference between radiation diffracted from adjacent planes of atoms in a crystal occurs at an angle, 2θ, determined by the wavelength of the radiation and the interplanar separation, as given by the Bragg equation (Equation 2.1).

$$n\lambda = 2d_{hkl}\sin\theta \tag{2.1}$$

Each set of planes in a crystal lattice with a different d_{hkl} (interplanar spacing) value will meet the Bragg condition at a different angle. The orientation of a single crystal relative to an incoming X-ray beam can be adjusted so as to observe all the diffracting planes. The diffraction pattern is therefore a three-dimensional array of "spots". However, the materials whose structures will be discussed in this thesis are not single crystals, but rather polycrystalline powders. Since an ideal powder sample consists of a large number of randomly oriented crystallites, diffraction will occur in all directions but at angles defined by the values of d_{hkl}. This results in diffraction "cones" extending out around the axis of the incident beam (Figure 2.1).

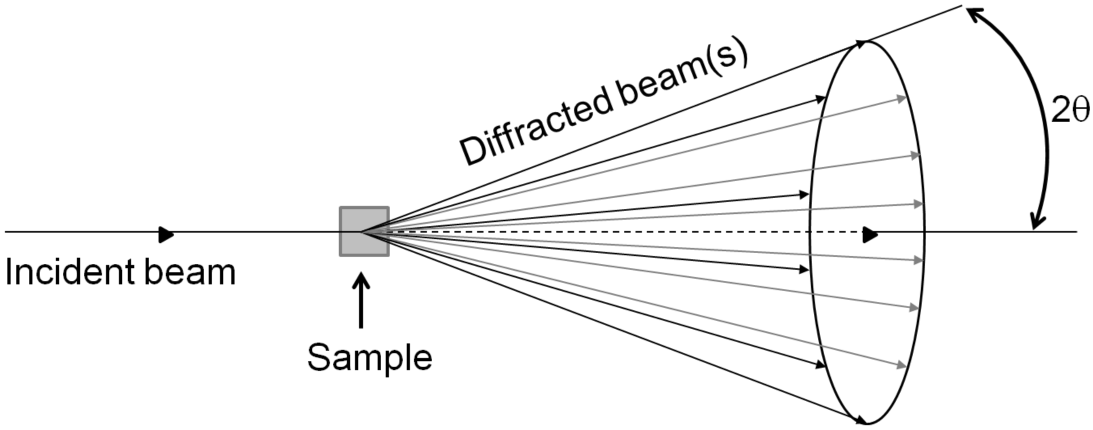

Figure 2.1 A representation of the diffraction cones produced by an isotropic powder sample. The angle 2θ is the angle between incident and diffracted beams.

An X-ray powder diffraction experiment typically records the intensity of diffracted radiation as a function of 2θ, and high intensity peaks are observed at angles which correspond to lattice planes in the sample. An example diffractogram is shown in Figure 2.2.

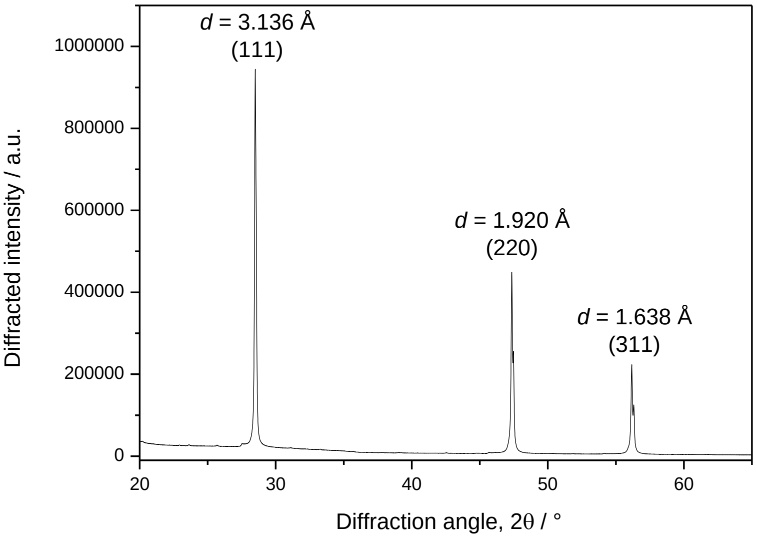

Figure 2.2 An example X-ray diffractogram, of silicon (λ = 1.54184 Å), showing the *d*-spacings and Miller indices (see below) of the Bragg peaks.

Although a set of *d*-spacings can be used to determine the size of the unit cell, a full understanding of a material's structure can only be obtained if the position of the atoms within the unit cell is known. This can be achieved by determining and analysing the intensities of the reflections.

X-rays are scattered by the electron cloud that surrounds a nucleus, which means that the 'strength' of the scattering scales with the number of electrons, Z, and is quantified as the atomic scattering factor, f_j.

$$f_j = \frac{\text{amplitude of the wave scattered by atom } j}{\text{amplitude of the wave scattered by an electron}} \tag{2.2}$$

Since the diameter of the electron cloud is similar to the wavelength of the incident X-ray beam, the angle at which the scattering occurs will change the intensity of the scattered waves. At zero scattering angle, $f_j = Z$, but this rapidly decreases with increasing 2θ.

An ordered array of atoms, *i.e.* a crystalline material, will produce many diffracted waves which interact with each other. To understand this it is first necessary to define the convention used to describe the various different planes of atoms: the concept of Miller indices. The letters h, k and l are known as the Miller indices of a plane and are determined by the position of the plane relative to the axes of the unit cell. The numerical values of h, k and l correspond to the reciprocal of the intercept (in fractions of the unit cell dimensions) of a particular plane with the edges of the unit cell, so for example, the (100) plane intercepts the x-axis at 1 unit cell length, a, and lies parallel to the y and z axes such that the intercept is infinity (Figure 2.3). The (100) plane is, of course, one of a set of equidistant parallel planes, including the one that passes through the origin of the unit cell. The (200) plane lies parallel to the (100), but with an intercept of ½ *a*, and the (111) plane lies diagonally across the body of the unit cell intercepting all three axes at *a*, *b* and *c* respectively.

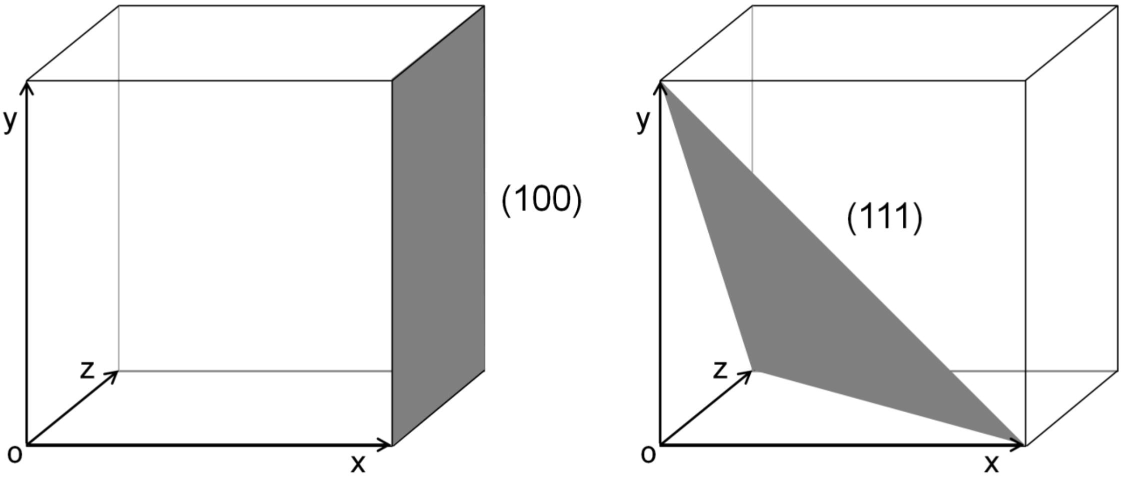

Figure 2.3 Illustration of the (100) and (111) Miller planes in a cubic unit cell.

Every atom in a unit cell will produce a diffracted wave whose amplitude is proportional to f_j. The way in which these contributions combine to produce the observed intensities of diffraction peaks is determined by the position of the atom and the *hkl* plane in which it lies, and the amplitude of diffraction from a particular plane is defined by the structure factor, F_{hkl}.

$$F_{hkl} = \sum_{j=1}^{N} f_j e^{2\pi i(hx_j + ky_j + lz_j)} \qquad \textbf{(2.3)}$$

It will be noted that F_{hkl} is a complex quantity, which reflects the fact that the scattered wave exhibits a phase difference relative to the incident wave. Nevertheless, the structure factor can be used to calculate the diffraction intensity from a particular plane, and can also be applied in reverse, to determine the positions of atoms from measured intensities. This last statement comes with the caveat that measured intensities are proportional to the square of F_{hkl} and thus information inherent to the complex part of the structure factor is lost. This is known as the "phase problem" and although it will not be discussed at length here, more information can be found in any good text on diffraction theory.[2]

The integrated intensity (I_{hkl}) of a diffraction peak is defined as the area under it, and while part of this is due to the structure factor (*i.e.* the positions of the atoms within the crystal), there are several other terms arising from interactions between the electron cloud and the X-rays (Equation 2.4).

$$I_{hkl} = \left(\frac{N^2 e^4 \lambda^3 V}{2m^2 c^4}\right) |F_{hkl}|^2 \left(\frac{TLp}{A}\right) \tag{2.4}$$

Where N = number of unit cells, V = volume, e = charge of an electron, c = speed of light, m = electron mass, T = temperature factor, Lp = Lorentz and polarisation factors and A = absorption factor. The contribution of the Lorentz and polarisation factors and the absorption factor to the X-ray intensity can be accurately calculated as part of structure determination.

A powder X-ray diffraction experiment provides information on the angular spread of diffracted intensities for the sample. To take these intensities and accurately extract the structure factor is the key to structure solution, and is far from a trivial matter due to the difficulty of accurately determining intensities of overlapped peaks and the information lost because of the phase problem. However, the application of powder diffraction data in structure *refinement*, where a known structure is used as a model for an unknown material, is relatively straightforward and can be extremely powerful. This will be discussed in more detail in Section 2.1.3.

2.1.1.1. *Structure, symmetry and space groups*

This section will give a brief overview of the crystallographic concepts of symmetry and space groups which are a necessary part of the interpretation of diffraction data.

In a powder diffraction measurement, the peaks correspond to interplanar spacings, d_{hkl}, and the relationship between plane indices and d is dependent on the shape of the unit cell: *i.e.* which crystal system it is in. For a cubic system, the relationship is of the form shown in Equation 2.5.

$$d_{hkl} = \left[\frac{1}{a^2}\left(h^2 + k^2 + l^2\right)\right]^{-1/2} \tag{2.5}$$

And the general relationship, applicable to any system, is given by Equation 2.6.

$$d_{hkl} = [X/Y]^{-1/2}$$

$$\begin{aligned} X = {} & \frac{h^2}{a^2}\sin^2\alpha + \frac{k^2}{b^2}\sin^2\beta + \frac{l^2}{c^2}\sin^2\gamma \\ & + \frac{2hk}{ab}(\cos\alpha\cos\beta - \cos\gamma) + \frac{2kl}{bc}(\cos\beta\cos\gamma - \cos\alpha) \\ & + \frac{2lh}{ca}(\cos\gamma\cos\alpha - \cos\beta) \end{aligned} \tag{2.6}$$

$$Y = 1 - \cos^2\alpha - \cos^2\beta - \cos^2\gamma + 2\cos\alpha\cos\beta\cos\gamma$$

The relationship between a diffraction pattern and the dimensions of the unit cell is thus clear, and as was established in Section 2.1.1, the intensity of diffraction peaks depends on the atomic contents of the *hkl* planes. With this information it is theoretically possible to assign Miller indices to each observed diffraction peak and thus obtain the dimensions of the unit cell. This procedure, known as “indexing” a powder pattern, can be done manually for a simple cubic system, but more complex systems are intensive enough to require computerised calculations. There are several examples of so-called "autoindexing" computer software which, when provided with an input of accurately measured *d*-spacings, will attempt to identify the smallest, most symmetrical unit cell that could produce that set of peaks. Any indexing carried out in the course of this thesis was done using the Crysfire package,[3] which contains a number of autoindexing routines, and the potential unit cells were evaluated using the program Chekcell.[4]

That there is a finite number of possible arrangements of points in three dimensional periodic arrays is clear when one considers that translational symmetry must be maintained in all directions and that all symmetry elements must be self-consistent. In fact, there are 7 different crystal systems (cubic, tetragonal, orthorhombic, hexagonal, rhombohedral, monoclinic and triclinic) which, when combined with the possible centering of points within the unit cell, produce 14 Bravais lattices. In an orthorhombic Bravais lattice (where $a \neq b \neq c$ and $\alpha = \beta = \gamma = 90°$), there are three mirror planes, one perpendicular to each face, and four different centering choices: P (primitive, lattice points only on the corners of the cell), I (body-centred, a lattice point in the very centre of the cell in addition to the corners), C (base-centred, lattice points in the centre of the top and bottom faces in addition to the corners) and F (face-centred, lattice points in the centre of all faces in addition to the corners), see Figure 2.4. It should be noted that there is no requirement for an atom in a real crystal to fall on all or any of the lattice points.

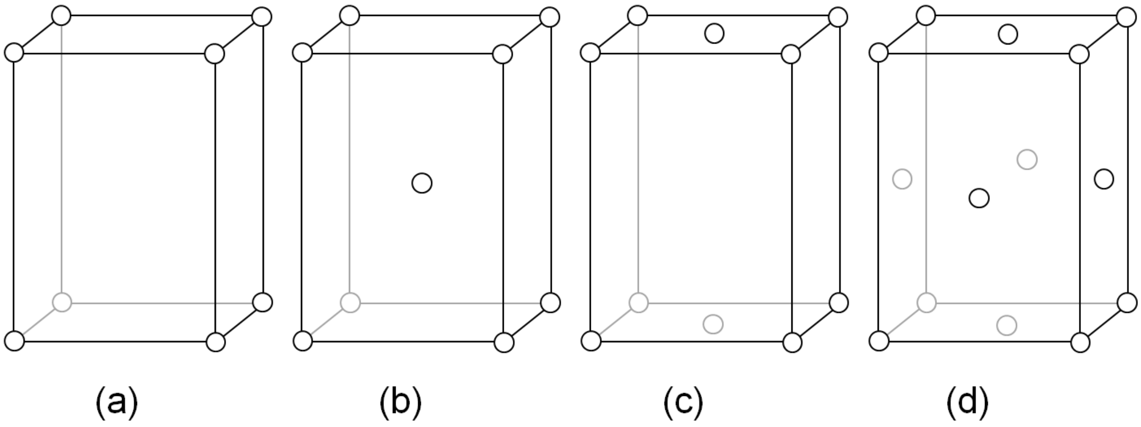

Figure 2.4 The arrangement of points in an orthorhombic lattice: (a) primitive, P, (b) body-centred, I, (c) base-centred, C, and (d) face-centred, F.

It is not immediately obvious why there are not 28 Bravais lattices (7 crystal systems multiplied by 4 centering choices) but in fact, some of these combinations are duplicates. For example, there is no C-centered tetragonal lattice, because this arrangement can be described by a primitive tetragonal lattice with a smaller volume (Figure 2.5).

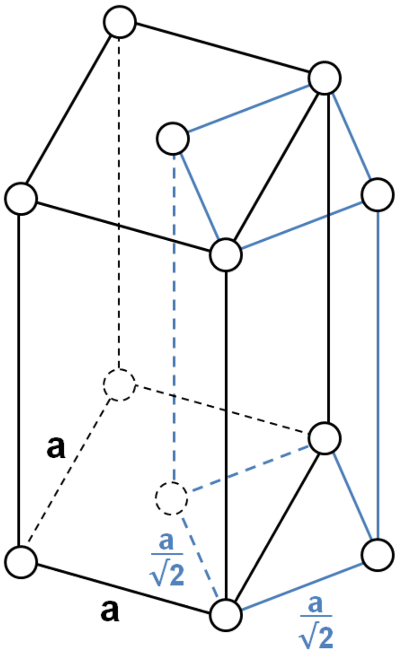

Figure 2.5 A C-centered tetragonal lattice (in black) can always be reduced to a smaller primitive tetragonal lattice (in blue).

From the 14 Bravais lattices, combined with translational symmetry elements such as glide planes and screw axes and with inversion axes, come the 230 space groups. These space groups, their symmetry elements, and the sets of equivalent coordinates within the unit cell that the symmetry elements produce, are detailed in the International Tables for Crystallography, volume I.[5]

Determination of the space group of, or at least of a set of potential space groups for an unknown sample from a powder diffraction pattern is possible due to the phenomenon of systematic absences. This is the situation where a reflection which is technically allowed for a certain crystal system has zero intensity due to the symmetry of the periodic arrangement of atoms. The structure factor equation (Equation 2.3) provides a simple explanation for this. Consider an orthorhombic unit cell with dimensions *a, b, c,* with one atom at the origin, 0*a*, 0*b*, 0*c,* and another in the center of the *ab* face at ½*a*, ½*b*, 0*c* (*i.e.* C centering). The structure factor equation can be used to calculate the expected diffraction intensity from various planes.

$$F_{hkl} = f\left[e^{2\pi i(0h+0k+0l)} + e^{2\pi i\left(\frac{1}{2}h+\frac{1}{2}k+0l\right)}\right]$$

$$F_{hkl} = f\left[e^{2\pi i(0)} + e^{2\pi i\left(\frac{1}{2}h+\frac{1}{2}k\right)}\right] \qquad \textbf{(2.7)}$$

$$F_{hkl} = f + fe^{2\pi i}\left(\frac{h+k}{2}\right)$$

Therefore, if $h + k = 2n$, the exponential term becomes 1 and $F_{hkl} = 2f$, but that if $h + k = 2n + 1$, $F_{hkl} = 0$. Hence, for a peak to appear in the diffraction pattern for a C-centered lattice, $h + k$ must be even.

Once the systematic absences have been examined and rationalised, it is possible to assign a space group to the structure in question. This, along with the unit cell parameters and a set of atomic coordinates provides a complete description of a structure, because the symmetry operators of the space group will generate all of the equivalent atom positions.

2.1.1.2. Experimental details

For the work presented in this thesis, three laboratory X-ray diffractometers were used. For general phase identification purposes and other room temperature measurements, a Bruker D5000 diffractometer equipped with non-monochromated Cu K$\alpha_{1/2}$ radiation (λ_1 = 1.54056 Å, λ_2 = 1.54443 Å) was used. A typical scan was from 2θ = 10 – 70° with a step size of 0.02° and a time-per-step of 1 second.

For non-ambient measurements a Bruker D8 diffractometer, also using Cu K$\alpha_{1/2}$ radiation and equipped with a VÅNTEC solid state detector and an Anton-Paar XRK900 reaction chamber capable of reaching temperatures of up to 900 °C, was used. The step size was 0.008° and the time-per-step was chosen to suit the sample requirements. The heating rate was 0.2 °C/second and samples were held at the desired temperature for at least 10 minutes prior to measurement to allow for thermal equilibration.

For high resolution measurements a Panalytical X-Pert Pro MPD with monochromated Cu Kα_1 radiation and a PiXcel solid-state detector was used. These measurements were carried out by Mohammed Harunsani and Luke Daniels.

2.1.2. Neutron diffraction

This section will offer a brief introduction to the theory of neutron diffraction. The material presented here is partially adapted from books by Squires and Billinge.[6-7]

The neutron was discovered in 1932 by Chadwick, and neutron diffraction was first observed in 1936 in the groups of Mitchell and Powers,[8] and Halban and Preiswerk.[9] Neutron diffraction was then developed throughout the 1940s by Wollan and Shull.[10] That neutron radiation is of the right wavelength to diffract from an array of atoms can be easily seen if we consider that the kinetic energy of a thermal neutron is given by Equation 2.8 , where $T \approx 293$ K, and hence its velocity, $v \approx 2198$ ms^{-1}. Since the de Broglie wavelength, $\lambda = h/mv$, $\lambda \approx 1.8$ Å.

$$E = k_B T = \frac{1}{2} m v^2 \tag{2.8}$$

Modern neutron sources fall into two categories: steady state reactor sources and pulsed spallation sources. An example of the former is the Institut Laue Langevin in Grenoble, France, where neutrons are generated by the fission of uranium nuclei. As a research reactor the ILL uses fuel rods highly enriched with the fissile ^{235}U isotope to produce a high flux of neutrons from a small reactor core. The fast, fission-produced neutrons are slowed down by various “moderators” (water, solid D_2 and graphite) to obtain neutrons with a range of energies suitable for diffraction and many other experimental techniques. An example of the latter type of neutron source is the UK’s ISIS. The first stage of neutron production at ISIS is a linear accelerator which accelerates bunches of negatively charged hydride ions (H^-) before their extra electrons are stripped and they enter a synchrotron accelerator as protons (H^+). Two pulses of roughly 100 ns in length exit the synchrotron and travel towards a tungsten target where neutrons are produced *via* spallation: a process in which heavy nuclei release large numbers of neutrons after impact from a high energy particle. The neutrons are moderated by water, liquid methane or liquid hydrogen. The ISIS proton beam is now directed to two targets: target

1 receives a 150 μA beam at a frequency of 40 Hz and target 2 receives a 38 μA beam at a frequency of 10 Hz. ISIS also produces muons for research purposes by passing the proton beam through a thin carbon target before it reaches neutron target 1. All of the neutron scattering work described in this thesis was carried out at ISIS and therefore the discussion in this section will focus on pulsed neutrons.

Unlike X-rays, which, as mentioned in the previous section, interact with the electron cloud surrounding an atom, neutrons interact with the nucleus itself. The scattering amplitude from a collection of nuclei is given by Equation 2.9.

$$\psi(\mathbf{Q}) = \frac{1}{\langle b \rangle} \sum_{j} b_v e^{i\mathbf{Q}R_j} \tag{2.9}$$

Where b_j = scattering amplitude of atom j, R_j = position of atom j and $\langle b \rangle$ is a compositional average given by Equation 2.10. The equivalence of Equation 2.9 with the structure factor given in Equation 2.3 should be clear, and the terminology used in this section has been chosen to facilitate the future discussion of total neutron scattering.

$$\langle b \rangle = \frac{1}{N} \sum_{j} b_j \tag{2.10}$$

The vector **Q** is referred to as the “diffraction vector” or “scattering vector” and is defined as the difference between the wavevector of the incident beam and the wavevector of the final beam: $\mathbf{Q} = \mathbf{k}_{\mathrm{init}} - \mathbf{k}_{\mathrm{final}}$.

When we are considering only elastic scattering (*i.e.* the case when there is no energy transfer between the neutron and the sample and magnitudes of the initial and final wavevectors are equal) the magnitude of **Q** is given by Equation 2.11, and it is this quantity which is of interest in diffraction measurements.

$$|\mathbf{Q}| = Q = \frac{4\pi \sin\theta}{\lambda} = \frac{2\pi}{d} \tag{2.11}$$

The neutron scattering power of an atom is known as its scattering length, b. Because the neutron interacts with the nucleus, which is extremely small relative to the wavelength of the neutron, the value of b is independent of Q (there is no form factor). This is one of the most practically important features of neutron diffraction because it increases the range of Q over which the diffraction pattern can be usefully measured. Of equal significance is the fact that the neutron-nuclear interactions do not scale with Z, and in fact, elements very close in mass (even different isotopes of the same element) will often have very different neutron scattering lengths. Some scattering lengths are negative, which means that the phase of the scattered wave is the same as the incident wave (a positive scattering length means the incident and scattered waves are 180° out of phase), and some are complex due to absorption effects. It is necessary for this thesis only to keep in mind the relationship between b and the effective “visibility” of different elements in a neutron diffraction experiment.

In a neutron scattering experiment the quantity measured is usually the differential cross section (see Figure 2.6 and Equation 2.12).

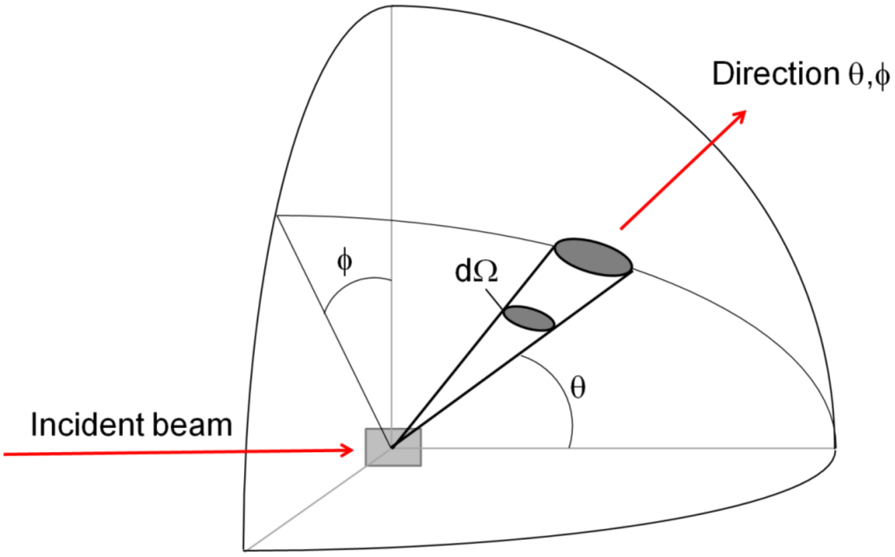

Figure 2.6 An illustration of the geometry of a neutron scattering experiment.

$$\frac{d\sigma}{d\Omega} = \frac{\substack{\text{Number of neutrons of wavelength } \lambda \text{ scattered} \\ \text{into solid angle } d\Omega \text{ at angle } 2\theta, \phi}}{\Phi(\lambda) d\Omega} \tag{2.12}$$

Where $\Phi(\lambda)$ is the incident flux of neutrons of wavelength λ. The formal derivation of the differential cross section will not be covered here, but it is important to note that it is proportional to the square of the scattering amplitude, just as the observed intensity of X-ray diffraction peaks is proportional to the square of the structure factor. The cross section, σ, is related to the scattering length b as $\sigma = 4\pi b^2$, and has two components: coherent and incoherent. Coherent scattering occurs when the incident neutron beam interacts with the sample as a whole, such that the scattered waves from different nuclei are in phase and interference can occur between them. A diffraction experiment measures elastic coherent scattering, but inelastic coherent scattering (where there is an transfer of energy between the neutron and the nucleus) can also be measured to obtain insights into lattice vibrations. Incoherent scattering occurs when the neutrons interact with individual nuclei and results in the scattered waves being out of phase. An example of incoherent scattering is self scattering, caused by the interaction of a nucleus with itself. In a diffraction experiment, incoherent scattering contributes a fairly flat and featureless background to the Bragg peaks, although measurement of incoherent scattering can provide information on atomic dynamics. The relative sizes of the coherent and incoherent cross sections provide information on the suitability of the element/isotope for diffraction measurements.

2.1.2.1. Time-of-flight neutron diffraction

The short, intense pulses of neutrons produced at a spallation source are ideally suited to time-of-flight (TOF) diffraction measurements. As the neutrons travel away from the target they are separated by wavelength due to their different velocities (*i.e.* shorter wavelength neutrons travel faster). After passing through a sample, the neutrons are sorted by their time of flight to the detector. In this manner an entire diffraction pattern can be collected by a fixed-angle detector, and the TOF is directly proportional to *d*-spacing, as shown by Equation 2.13 and Figure 2.7.

$$d = 1.9777\, x\, 10^{-3}\, t\, [(L_1 + L_2)\sin\theta]^{-1} \tag{2.13}$$

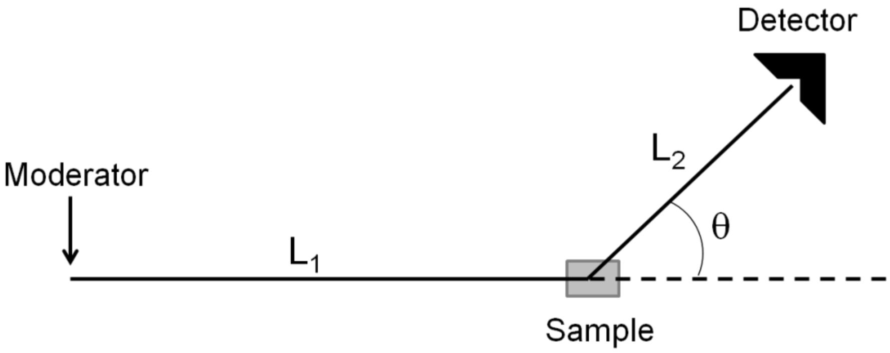

Figure 2.7 The flight path of a neutron in a time-of-flight diffractometer.

The resolution of a TOF instrument is improved by both increasing the total flight path, $L_1 + L_2$, as this improves the wavelength separation, and by increasing the detection angle. Unfortunately, both of these things decrease the count rate, but this can be mitigated by increasing the number of detectors. The GEM diffractometer at ISIS has 7270 individual detectors grouped into 8 banks at different scattering angles (see Figure 2.8),[11] which enables it to make fast, high-resolution diffraction measurements, as well as being extremely well suited to total scattering measurements which will be expanded upon in Section 2.2 below.

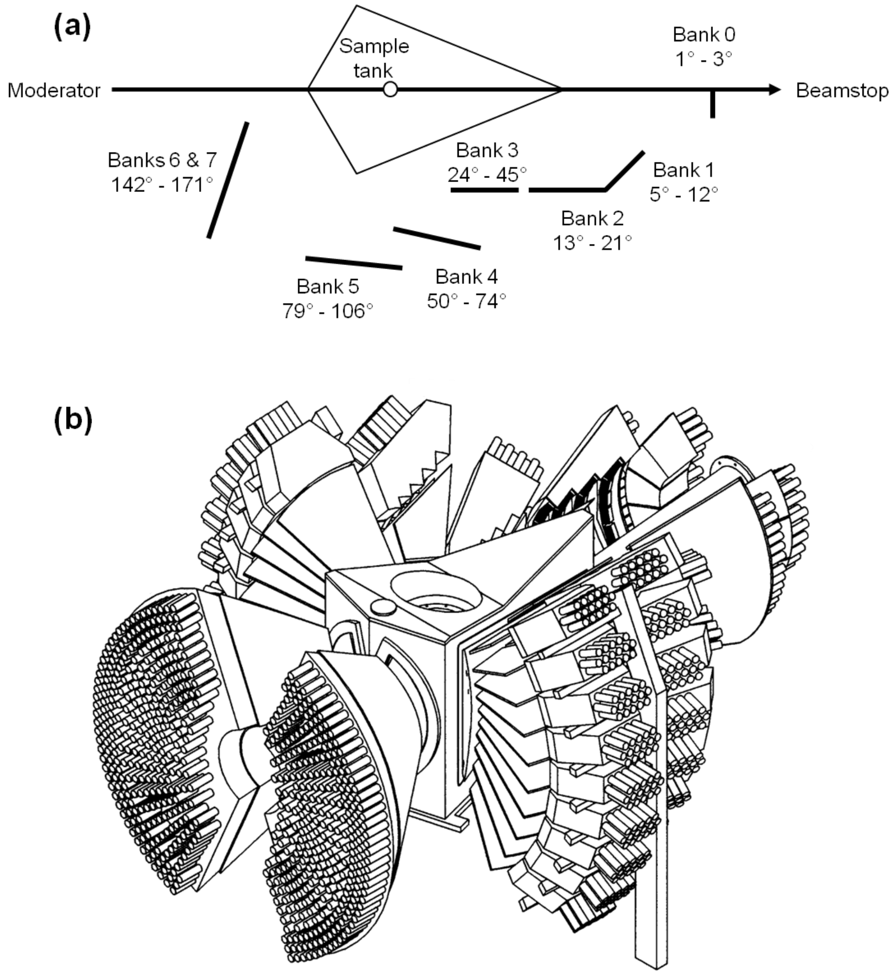
(a)
Sample tank
Bank 0
1° - 3°
Moderator
Beamstop
Banks 6 & 7
142° - 171°
Bank 3
24° - 45°
Bank 1
5° - 12°
Bank 2
13° - 21°
Bank 5
79° - 106°
Bank 4
50° - 74°
(b)

Figure 2.8 The GEM diffractometer at ISIS, (a) the arrangement of the 8 detector banks and (b) a drawing of GEM with banks 6 & 7 at the lower left and the beamstop at the top right.

2.1.3. Rietveld refinement

Faced with a material of unknown atomic arrangement, the task of solving its structure from scratch is a daunting one, particularly if a single crystal cannot be obtained. It is often the case, however, that the structure of an unknown material closely resembles the structure of another, known material. Provided with a description of a crystal structure, it is possible to accurately calculate an expected diffraction pattern, such that it can be compared with the data from an unknown material. The agreement between a calculated and measured pattern depends on two factors: how good the model is and how well the instrument used to measure the data is described. Parameters relating to these two factors require adjustment until good agreement between the calculated and observed profiles is obtained. This is the basis of the procedure of Rietveld refinement. The content of this section is partially based on the book “The Rietveld Method” edited by R. A. Young.[12]

Hugo Rietveld developed the refinement technique which now bears his name in the late 1960s,[13] when powder diffraction was still regarded as infinitely inferior to single crystal methods. Rather than focusing on the relative intensities of individual peaks (which causes problems when the peaks are overlapped), Rietveld realised that every data point in the pattern contained information – whether it was Bragg intensity or the lack thereof. Computer algorithms were developed which could compare the full measured powder pattern with a full calculated powder pattern, adjust model or instrumental parameters, then re-calculate and re-compare, over and over again until the difference between the observed and calculated patterns was minimised (see Figure 2.9).

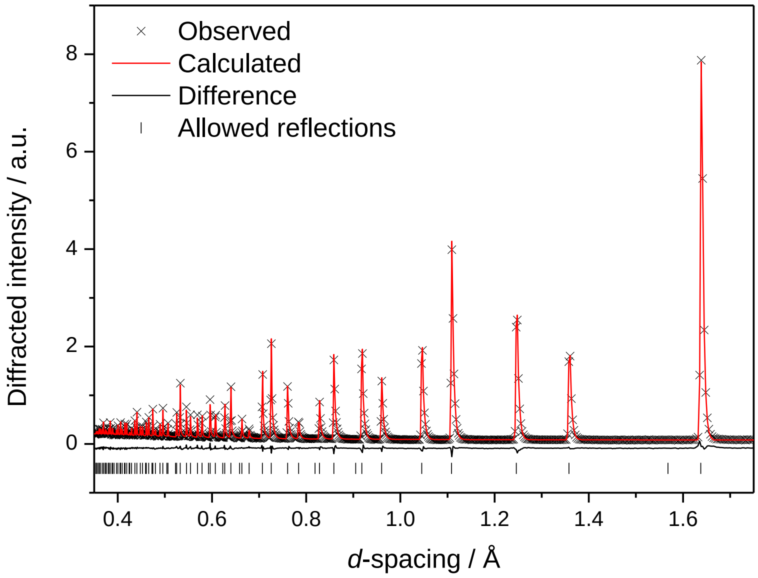

Figure 2.9 An example of a Rietveld fit to a time-of-flight neutron diffraction pattern from a NBS (National Bureau of Standards) silicon standard sample.

In a Rietveld refinement, the quantity whose minimisation drives the least-squares procedure is the residual, S_y.

$$S_y = \sum_i w_i (y_i - y_{ic})^2 \tag{2.14}$$

Where y_i = observed intensity at the *i*th data point, y_{ic} = calculated intensity at the *i*th data point and $w_i = 1/y_i$. In order to monitor the progress of the minimisation procedure, statistical as well as graphical checks are made. The most commonly quoted statistical parameter is the weighted *R*-factor, R_{wp}, which is as defined in Equation 2.15.

$$R_{wp} = \left\{ \frac{\sum w_i (y_i(\text{obs}) - y_i(\text{calc}))^2}{\sum w_i (y_i(\text{obs}))^2} \right\}^{1/2} \tag{2.15}$$

Rietveld refinement is equally applicable to X-ray and neutron diffraction; indeed it can be used for combined refinement with both types of data simultaneously, and there are several distinct sets of parameters which are always part of the refinement process. There are numerous examples of Rietveld refinement software which all perform largely the same function but differ in specific implementation. All the refinement work in this thesis was done using the freely available GSAS package with the EXPGUI graphical interface.[14-15] As such, the following discussion is particularly relevant to the way in which GSAS handles the various sets of parameters.

The first and most important of these are the model parameters: the unit cell, space group, atom types and coordinates, site occupancies and thermal displacement parameters. Reasonably accurate starting values of these parameters are a requirement for the success of the refinement. To illustrate the necessity for good unit cell parameters, consider that if a calculated reflection does not lie at least partially under the corresponding observed Bragg peak, the least squares procedure cannot meaningfully refine its position. The effect of thermal vibrations of atoms in a crystal is to reduce the intensity of the Bragg peaks. This effect is described by the Debye-Waller factor, or *B*-factor, and is strongly dependent on the scattering angle. The scattered intensity can therefore be written as:

$$f = f_0 e^{\left[-B\left(\frac{\sin\theta}{\lambda}\right)^2\right]} \qquad \textbf{(2.16)}$$

Where f_0 is the unattenuated intensity from a static lattice. B is related to the mean displacement of the atom by the equation $B = 8\pi^2 U$ where $U = \langle u^2 \rangle$, the mean-squared displacement of the atom from its equilibrium position. In this thesis, U is referred to either as the thermal displacement parameter, or the average displacement parameter (ADP). Assuming that the thermal vibrations are isotropic the parameter U_{iso} defines a sphere. If the vibrations are anisotropic, 6 U_{ij} terms are required to define each vibrational ellipsoid. In GSAS, either isotropic or anisotropic thermal displacement parameters can be defined and refined for each atom.

The second group consists of the parameters related to instrumental geometry. For X-ray diffraction they include the wavelength (or wavelengths), the zero shift (*i.e.* the deviation from perfect alignment of the diffraction optics) and the Lorentz polarisation factor. For time-of-flight neutron diffraction they consist of several parameters which describe the exact relationship between the d-spacing and TOF. In GSAS, this relationship is given by Equation 2.17.

$$t = \mathrm{DIFC}\, d + \mathrm{DIFA}\, d^2 + \mathrm{ZERO} \tag{2.17}$$

The numerical values of the parameters DIFC, DIFA and ZERO can be determined during instrument calibration by careful refinement using data from a standard sample.

The third group consists of the parameters which describe the shape of the diffraction peaks. These are generally part instrumental and part sample related, and again are different for X-ray and neutron diffraction. X-ray diffraction peaks can generally be described well by a Voigt or pseudo-Voigt function wherein Gaussian and Lorentzian terms are combined formerly by convolution and latterly by summation. For computational reasons, the pseudo-Voigt is often preferred. The contribution of the Gaussian and Lorentzian terms is defined by a mixing parameter, η.

$$pV = \eta L + (1 - \eta) G \tag{2.18}$$

Time-of-flight diffraction peaks have a complex shape with a sharp leading edge and slowly decaying trailing edge. This is caused by the “shape” of the moderated neutron pulse. In GSAS this is modelled by convoluting a pseudo-Voigt function with an Ikeda-Carpenter function to describe the moderator pulse shape.[16]

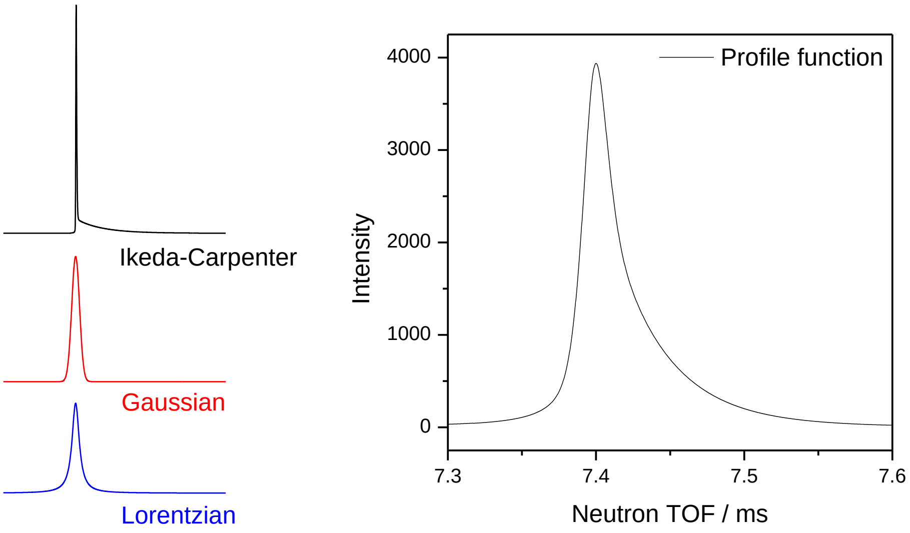

Figure 2.10 The constituent parts of a GSAS TOF profile function. A pseudo-Voigt function, the sum of Gaussian and Lorentzian components, is convoluted with an Ikeda-Carpenter function to make the total function.

Sample specific broadening terms that account for the effects of crystallite size and microstrain are also included amongst the profile parameters.

The remaining parameters include a scale factor which can be used to extract relative amounts of different phases in a mixed/impure sample, corrections for absorption and extinction effects and the background function. A polynomial function is usually used to describe the shape of the background with more complex backgrounds requiring more terms in the polynomial. When a background is particularly complex and there are deficiencies in the starting crystallographic model, the refinement program is likely to struggle to produce a good estimation of it. Within EXPGUI is included the ability to define graphically (and to fit a polynomial to) a series of fixed background points, thus providing a starting point that allows the refinement to proceed to a stage where the peak shapes and intensities are well matched enough that the background can be refined.

Figure 2.11 shows the general procedure used for the refinement of time-of-flight diffraction data as applicable to the work in this thesis. Where possible, refinements were carried out using data from two detector banks of the instrument GEM simultaneously to cover a wider range of *d*-spacing. In these cases different scale factors, background and profile parameters were refined for each bank due to the differences in their scattering angles and resolutions. The various instrument and profile parameters were initially determined *via* a refinement of a NBS (National Bureau of Standards) silicon standard (as shown in Figure 2.9).

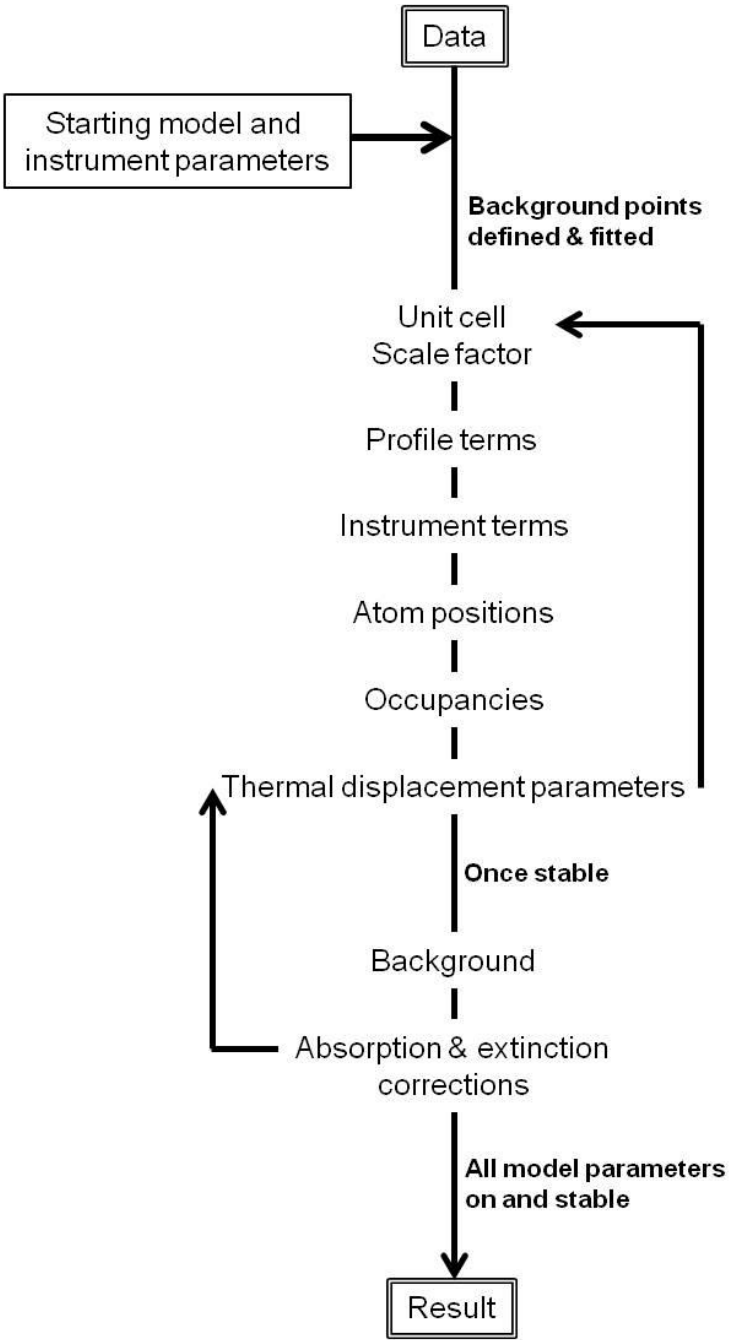
Data
Starting model and instrument parameters
Background points defined & fitted
Unit cell
Scale factor
Profile terms
Instrument terms
Atom positions
Occupancies
Thermal displacement parameters
Once stable
Background
Absorption & extinction corrections
All model parameters on and stable
Result

Figure 2.11 A flow chart showing the general procedure used for Rietveld refinement. The refinement of various parameters is enabled (or "switched on") sequentially to minimise the chances of the refinement diverging.

2.1.3.1. The Le Bail method for profile fitting

As mentioned in the preceding section, a good starting model is a requirement for a successful Rietveld refinement. However, it is rather common to find that a suitable starting model is not available and only a guess at a unit cell and space group have been made *via* autoindexing. To go from this situation to structure solution requires the extraction of accurate $|F_{hkl}|$ values for each reflection. This is not an easy task and is particularly problematic for overlapped reflections. Hugo Rietveld's solution was to take each point in turn, examine the percentage contribution of each overlapped reflection to the calculated intensity of that point and then assign that percentage of the observed intensity to the reflection. The "correctness" of the assignment is strongly biased by the model: if the model is wrong, so too will be the intensity.

Armel le Bail realised that this extraction procedure could also be used without a model.[17] In his profile fitting procedure, the calculated intensities are initially set to an arbitrary value, and from these arbitrary "calculated" intensities are extracted an initial set of "observed" intensities. Obviously this will not be very accurate, but the key part of the method is the subsequent refinement. The arbitrary calculated intensities are replaced by the extracted intensities, the extraction is repeated and so on and so forth. The unit cell, profile, background and instrument parameters can all be refined as part of this process, which leads to a set of highly accurate "observed" intensities which can be used for structure solution.

The Le Bail method is also extremely useful in cases where a model is available, but a sample displays complex peak shapes or background functions and this causes a large discrepancy between the measured diffraction pattern and the model. Under these circumstances, a Le Bail fit can be used to improve the starting parameters before a Rietveld refinement is begun, and it is this approach that has been utilised in the work in the later chapters of this thesis.

2.2. Total Scattering

Total scattering describes an experiment where the diffuse and Bragg scattering are examined together. The preceding sections have focused on the conditions required for Bragg scattering to be observed, however as long as the scattering is coherent, the scattered waves provide information about the relationships between neighbouring atoms, even if those atoms are not arranged in ordered layers as in a crystal. Any measured diffraction pattern contains a great deal of information, even if the Bragg peaks are few or none. Total scattering methods allow this information to be extracted.

It is important to note that whilst in traditional crystallographic analysis, the diffuse scattering is typically treated as part of the "background" to be either fitted with a polynomial function and refined or simply discarded. In total scattering methods, the word "background" quite categorically does **not** include the diffuse scattering.

The differential cross section, as defined in Equation 2.12, is a measure of the total number of neutrons scattered at a certain scattering angle, not just the sample specific scattering. The various non-sample components include: scattering from the inside of the instrument, scattering from the air (if the measurement is not done in a vacuum), and scattering from the sample container. The sample-related part of the differential cross section also requires correction for multiple scattering (where a neutron scatters from more than one nucleus before it leaves the sample, its time-of-flight is meaningless) and consists of two parts (Equation 2.19).

$$\frac{d\sigma}{d\Omega} = I(Q) = i(Q) + I^S(Q) \qquad \textbf{(2.19)}$$

Where $i(Q)$ is the distinct scattering (and the function we desire to extract as accurately as possible) and $I^s(Q)$ is the incoherent self scattering, as given by Equation 2.20.[18]

$$I^S(Q) = \sum_l \frac{n_l \sigma_l^{\text{scatt}}}{4\pi}(1 + P_l(Q,\theta)) \tag{2.20}$$

Where n_l = number of atoms of element l in the sample and σ_l = total scattering cross section for element l. The term $P_l(Q,\theta)$ is a correction for inelasticity effects known as a Placzek correction (named for its originator).[19-20] The apparent complexity of the procedures required to obtain a corrected $i(Q)$ is rather misleading. Computer programs that quickly and accurately perform the required corrections and normalisations are readily available and their use will be discussed below.

2.2.1. A total neutron scattering experiment

A total scattering experiment has more components than a simple diffraction experiment, to allow all of the necessary corrections to be performed accurately.These are described in Table 2.1.

Table 2.1 The datasets which must be obtained for a neutron total scattering experiment.

Dataset required	Purpose
Vanadium rod	Normalisation: to put the data on an absolute scale.
Empty instrument	Background subtraction.
Sample container	Background subtraction. Must be the same as those used for the samples.
Sample environment	Background subtraction if an additional insert such as a furnace was used.
Sample	Structural investigations.

Each of these datasets must be measured as accurately as possible to avoid introducing additional errors into the final $i(Q)$. It is also important to measure the mass and height of the sample in its container and to know how much of the sample is illuminated by the beam. This is so that the number of atoms in the beam can be estimated.

2.2.1.1. Experimental details

The work described in this thesis was carried out using four instruments at ISIS.

For GEM, samples were loaded into cylindrical vanadium cans. Most commonly used were 0.762 cm inner diameter cans with wall thickness 0.013 cm, but 0.500 and 0.830 cm inner diameter foil cans with wall thickness 0.0025 cm were also used. The beam size was 1.5 × 4.0 cm and the vanadium standard was a 0.834 cm diameter rod.

For SANDALS, samples were loaded into specially made, 12 cm long, drawn vanadium cans (inner diameter 0.762 cm, wall thickness 0.013 cm). The beam size was 1.5 cm square and the vanadium standard was a 0.834 cm diameter rod. Further details of SANDALS experiments will form part of Chapter 6.

For NIMROD, samples were placed into flat plate cans made of null scattering TiZr alloy (the coherent scattering lengths of Ti and Zr are of opposite sign and therefore an alloy of the correct composition has an average coherent scattering length of 0 and does not give rise to Bragg peaks). The inner dimensions of the cans were approximately 4.0 × 4.0 × 0.2 cm to allow for a beam size of ~3.0 cm square. The vanadium standard was a solid flat plate of thickness 3 mm.

For LOQ, samples were placed into quartz cuvettes of width 12.5 mm and path length 2 mm. The beam was 8 mm in diameter.

2.2.2. Data processing

2.2.2.1. Gudrun and ATLAS

The programs Gudrun and ATLAS were used for the processing of GEM, SANDALS and NIMROD data. These programs perform the corrections described in Section 2.2, above. The flow chart in Figure 2.12 explains the procedure in simple terms and more detailed explanation can be found in the Gudrun manual,[21] and in a paper by Hannon *et al.*.[18]

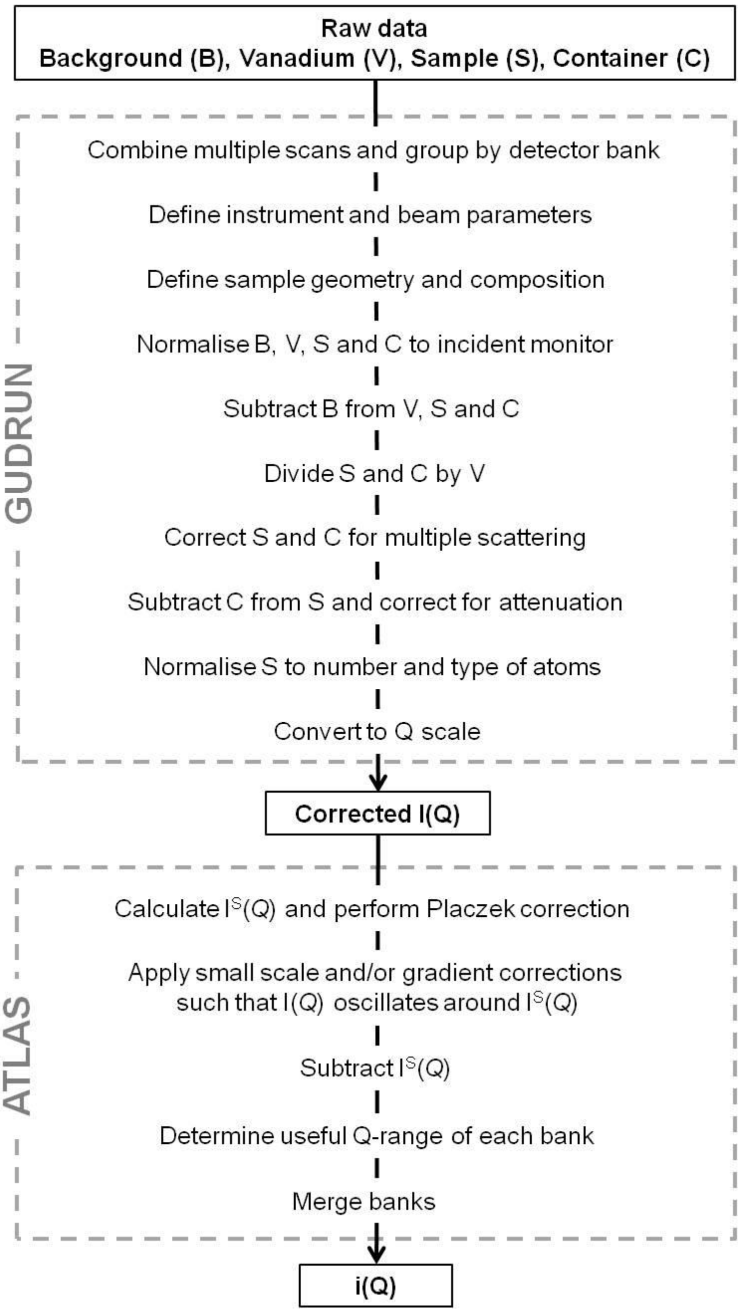
Raw data
Background (B), Vanadium (V), Sample (S), Container (C)
GUDRUN
Combine multiple scans and group by detector bank
Define instrument and beam parameters
Define sample geometry and composition
Normalise B, V, S and C to incident monitor
Subtract B from V, S and C
Divide S and C by V
Correct S and C for multiple scattering
Subtract C from S and correct for attenuation
Normalise S to number and type of atoms
Convert to Q scale
Corrected I(Q)
ATLAS
Calculate I^S(Q) and perform Placzek correction
Apply small scale and/or gradient corrections such that I(Q) oscillates around I^S(Q)
Subtract I^S(Q)
Determine useful Q-range of each bank
Merge banks
i(Q)

Figure 2.12 The steps involved in data analysis with Gudrun and ATLAS.

Although it is possible to use Gudrun to perform all the steps of the analysis up to and including producing a merged $i(Q)$, this was not done (at least for neutron data) so as to take advantage of the extra control offered by determining the merge parameters *via* inspection of the data. The manual process also lends itself more readily to the correction for the presence of hydrogen in the sample, as discussed below.

2.2.2.2. Correcting for the presence of hydrogen

Hydrogen (^{1}H) has a large incoherent scattering length relative to its coherent scattering length (b_{inc} = 25.27 fm, b_{coh} = -3.74 fm). Its presence in samples studied by neutron scattering leads to a high, sloping background. For most materials, the calculation of self-scattering and correction for (slight) inelasticity using the Placzek correction leads to a reasonably accurate calculation of the background level, but for very light atoms the inelasticity effects are significant and the correction cannot be used.

Where possible, samples for neutron studies were deuterated, as deuterium (^{2}H) has a much smaller incoherent scattering length (b_{inc} = 4.04 fm, b_{coh} = 6.67 fm) and the effects of inelasticity are less severe. Where this was not feasible, samples were dried thoroughly in a desiccator or vacuum oven, but in several cases it was not possible to completely remove the hydrogen.

To correct for the presence of hydrogen, the shape of the sloping background was fitted using a smooth function (in this case a cubic spline) and then this background function was subtracted to obtain an $i(Q)$ which oscillated around zero.[22] This is illustrated in Figure 2.13.

The cubic spline fitting was done *via* remote access to the ISIS VMS computers using code written by Alex Hannon.

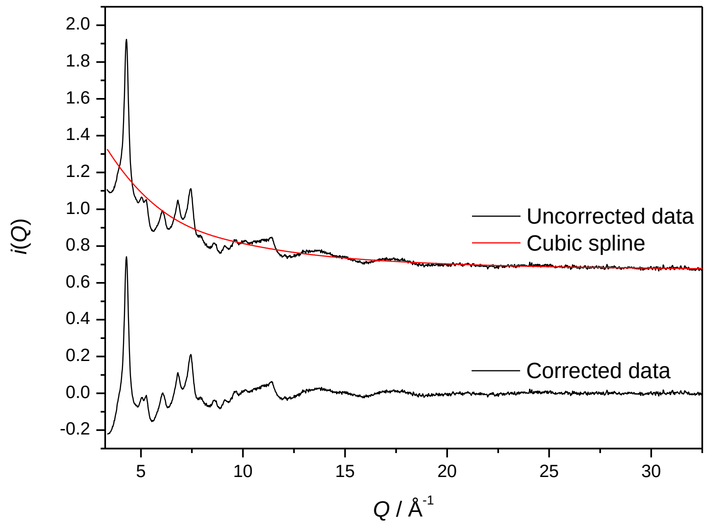

Figure 2.13 An example of fitting a cubic spline to data from GEM bank 6 with a sloping background to correct for the presence of hydrogen in a sample.

2.2.2.3. The Fourier transform

The experimental $i(Q)$, once suitably corrected and normalised, is related by Fourier transform to the differential correlation function, $D(r)$, which reveals the probability of finding a pair of atoms at a certain distance, r, and thus is a direct visualisation of interatomic distances in a sample.

$$D(r) = \frac{2}{\pi}\int_{Q_{\mathrm{min}}}^{Q_{\mathrm{max}}} Qi(Q)\, M(Q) \sin r(Q)\, dQ \qquad \textbf{(2.21)}$$

This correlation function is also known as the pair distribution function (PDF) and will be referred to as such in this thesis. Another common form of the correlation function is the total correlation function, $T(r)$.

$$T(r) = 4\pi\rho^0 r \left(\sum_i c_i \overline{b_\imath}\right)^2 + D(r) = T_0(r) + D(r) \qquad \textbf{(2.22)}$$

Therefore, $T(r)$ and $D(r)$ are related by a constant slope function, $T_0(r)$, which is dependent on the density and composition of the sample. The relationship between $D(r)$ and $T(r)$ is perhaps best understood graphically (Figure 2.14)

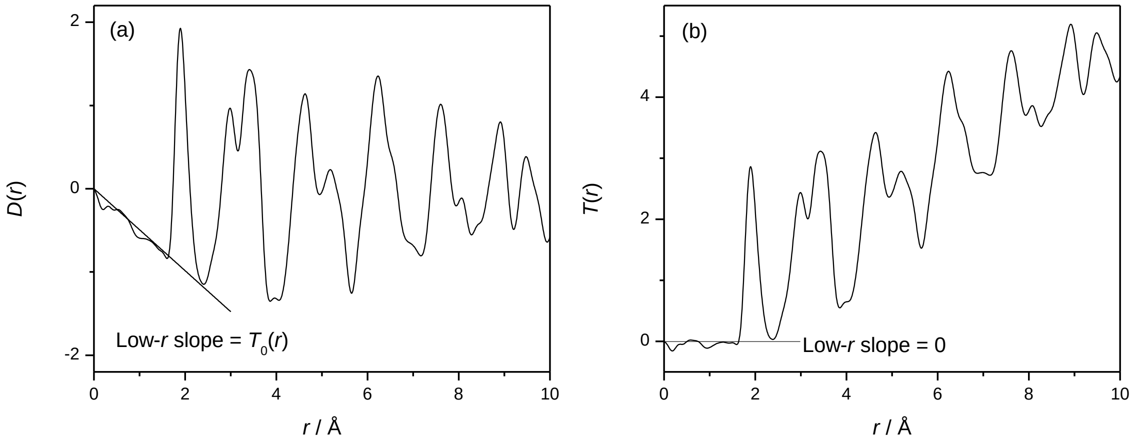

Figure 2.14 A comparison between (a) $D(r)$ and (b) $T(r)$, emphasising their relationship. $T(r)$ is obtained by adding a function with constant slope, $T_0(r)$, to $D(r)$.

The PDF ($D(r)$) has the advantage that it can be obtained without detailed knowledge of sample density, and that it does not weight the low-*r* peaks more strongly than the higher-*r* peaks. It can be extremely useful to use the slope of the $D(r)$ to check that the normalisation has been successful by comparing it with the calculated $T_0(r)$ constant.

The function $M(Q)$ in Equation 2.21, above, is a modification function applied to the $i(Q)$ to account for the non-infinite range of the data. This function can take the form of an abrupt cutoff or step, whereby the data are simply terminated at a certain $Q_{\max}$ (*i.e.* for $Q > Q_{\max}$, $i(Q) = 0$). This has the result of introducing "termination ripples" to the result of a Fourier transform. To some extent these ripples, having a constant period based on the value of $Q_{\max}$, can be well accounted for when fitting the data. However, it is often necessary to improve the visual quality of the data using a modification function such as the Lorch function.[23]

$$
\begin{aligned}
&Q < Q_{max} \quad M^L(Q) = \frac{\sin(Q\Delta r)}{Q\Delta r} \\
&Q > Q_{max} \quad M^L(Q) = 0
\end{aligned}
\tag{2.23}
$$

The Lorch function gradually dampens the data so the intensity is 0 above Q_{max} without an abrupt termination. The effect of using the Lorch function *versus* the abrupt-termination (step) function can be seen in Figure 2.15.

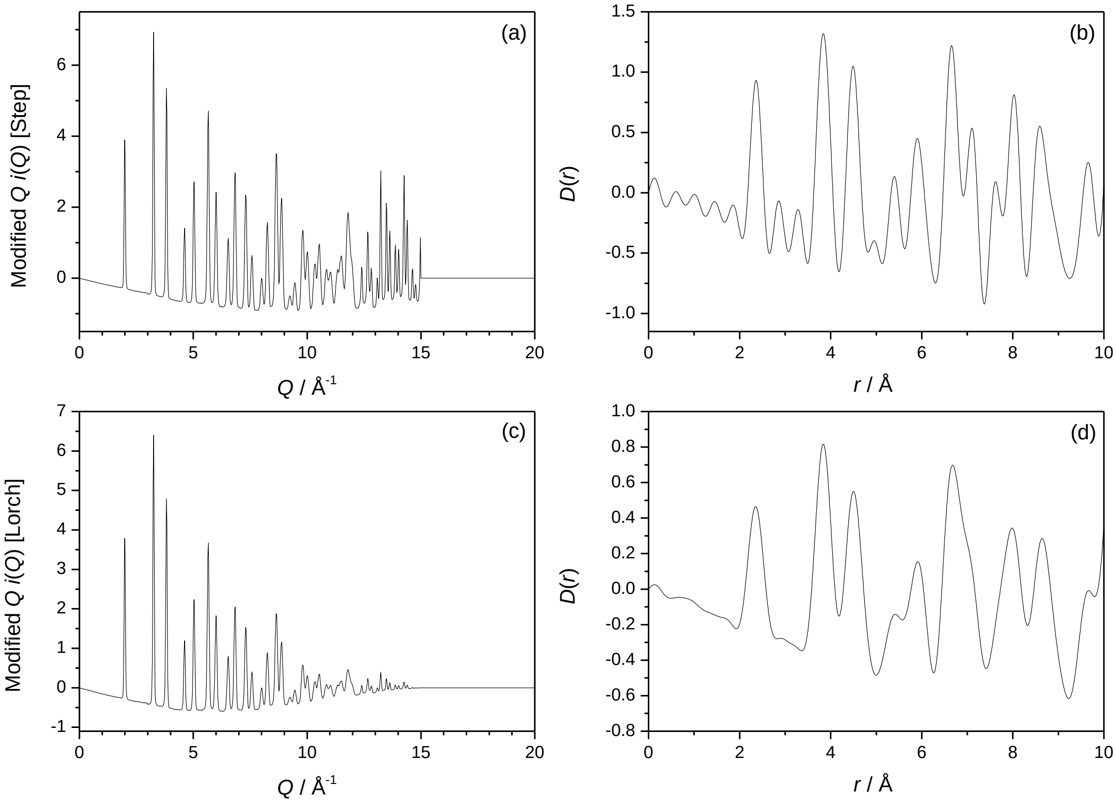

Figure 2.15 (a) The scattering data from crystalline Si after application of the step modification function at Q_{max} = 15 Å^{-1} and (b) the result of the Fourier transform. (c) The scattering data after application of the Lorch modification function at Q_{max} = 15 Å^{-1} and (d) the result of the Fourier transform. Note that the application of the Lorch function both greatly reduces the appearance of termination ripples in, and slightly broadens, the resultant *D*(*r*).

2.2.2.4. Properties of the correlation function D*(*r*)*

The effects of *Q*-space resolution on the *r*-space resolution of the correlation function are rather complex, and a detailed discussion can be found in the work by Qiu and coworkers.[24] However, there are several general points of significant importance.

The resolution of $D(r)$ is proportional to the Q-range of the $i(Q)$ data. For best results the data should be measured from as close to $Q = 0$ as possible and to a Q_{max} which is higher than the point at which oscillations have ceased to be visible in the data. It is also important to note that the application of the Lorch modification function also broadens the peaks in the $D(r)$. The effect is mitigated by using a higher Q_{max}.

The Q-space resolution of the instrument affects the damping of the PDF, particularly for longer distances, in that low-resolution diffraction data will more heavily damp the intensity of the peaks in the PDF than will high resolution data. Particle size, or more specifically, the size of ordered domains within the structure, also dampens the PDF, with the function tending to 0 at larger distances. Examples of this phenomenon will be presented in later chapters.

2.2.3. Pair Distribution Function analysis

Once obtained, information can be extracted from the PDF in several ways. Take, for example, the first peak. Its position is an indication of the shortest nearest neighbour distance in the material, say the M–O bond in a metal oxide, and its area can be used to determine the coordination number of the M atom. The peak can be fitted with a suitable function (or functions, if there are multiple pairs of atoms contributing to the peak) to extract this information. This is a particularly common method for the analysis of PDFs from glasses and other amorphous materials.

For crystalline or disordered crystalline materials, both of which have order over a much greater length scale, far more information can be extracted. It is relatively easy to take a model crystal structure and calculate its PDF, which can then be compared with the data. The model can be manually adjusted for things like thermal broadening until it matches well with the data. It is then possible to take this one stage further and apply an iterative procedure, analogous to that used in Rietveld refinement, to take a model and refine it until the difference between the model and the data is minimised. This method is known as PDF analysis and the software used in this thesis (again, analogous to programs like GSAS) is called PDFfit2/PDFgui.[25]

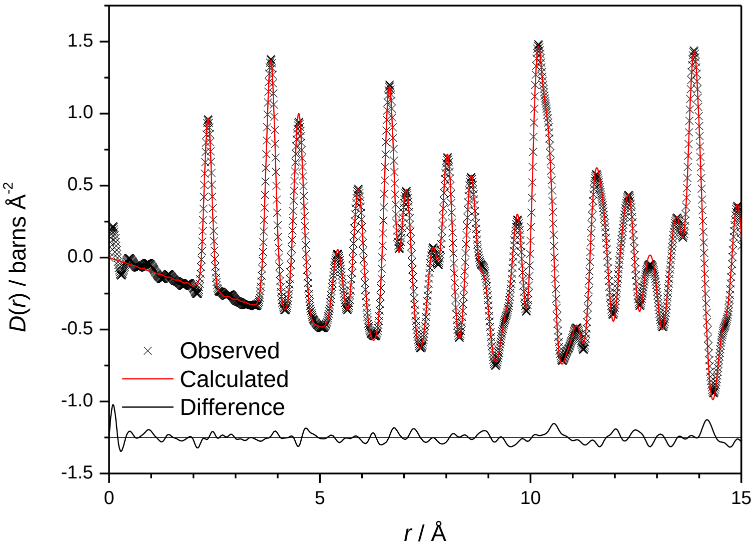

Figure 2.16 An example of PDF analysis using total neutron scattering data from a NBS (National Bureau of Standards) silicon standard sample.

Just as in Rietveld refinement, PDF analysis begins with a set of data and a model structure. There are various sets of refineable parameters relating to the model and the instrument used, as detailed in Table 2.2.

Table 2.2 The parameters available for refinement in PDFgui.

Parameter	Description
Scale factor	Although the PDF should be on an absolute scale, this is included to account for small errors in processing.
“Qbroad”	A term that describes the effect of instrument resolution on the widths of the peaks.
“Qdamp”	A term that describes the effect of instrument resolution on the damping of the PDF.
Unit cell dimensions	This can be for a single unit cell or a larger supercell if required.
Atomic positions	These are written out in full as per a material in space group P1, so that symmetry requirements can be relaxed if necessary.
Thermal displacement parameters	Either isotropic or anisotropic can be defined.
Correlated motion correction (delta1, delta2 or sratio)	A parameter which effectively sharpens the low-*r* peaks as they are less affected by thermal motion than the ones at higher *r*. There are several options because the effect may vary from sample to sample.
“spdiameter”	A term which convolutes the ideal calculated PDF with a spherical shape function to provide an estimate of particle size.

The terms “Qbroad” and “Qdamp” are instrument related and were obtained by refining a set of data from a NBS Silicon standard, the same as used for obtaining instrument parameters for Rietveld.

Although there are many similarities between the PDF analysis and Rietveld refinement techniques, there are also important differences, not least of which is the different length scales involved. In a highly crystalline material the Rietveld-obtained structural model should also fit the PDF, but if a material is disordered its local structure may be rather different from the average. PDF analysis allows these discrepancies to be identified and analysed.

2.2.4. Reverse Monte Carlo

Pair distribution function analysis is sometimes known as “small box” modelling, because it defines a relatively small group of atoms (the unit cell) and applies periodic boundary conditions. Over the course of the refinement, symmetry can be altered or broken but only within the length scales of the “box”. For some disordered materials a “large box” modelling procedure is better suited to providing insight into the structure of the material.

Reverse Monte Carlo (RMC) modelling (using, in this thesis, the program RMCProfile)[26] is a “large box” method which has been optimised for the analysis of disordered crystalline materials. As with standard Monte Carlo algorithms, the positions of a large number of atoms are adjusted, though the goal in a RMC refinement is not to minimise the energy but instead to improve the fit to a set of experimental data. Atom moves which improve the fit are accepted, and those which don’t are rejected (with the caveat that some “bad” moves are accepted based on a certain probability so as to reduce the risk of the fit getting stuck in a false minimum).

In RMCProfile, it is possible to include several datasets in the fitting procedure (Bragg diffraction, the neutron/X-ray $i(Q)$, the neutron/X-ray $D(r)$) which means that the result of the fit is consistent with both the local structure and the average structure. This means that local distortions can be modelled at the same time as maintaining an average symmetry, something which is very important for a disordered crystalline material.

Unlike PDF analysis which treats partial or mixed occupancy sites statistically, RMCProfile treats individual atoms and vacancies explicitly, defining for each a set of coordinates within the configuration box. This allows such things as vacancy ordering and the rearrangement of atoms surrounding a vacant site to be investigated.

RMCProfile can also incorporate chemical information, if known. Polyhedral restraints facilitate the modelling of materials like SiO_2 by maintaining the integrity of the tetrahedral units, and many other restraints on, for example, bond length, bond valence and stoichiometry, can also be defined.

The RMC work in this thesis was carried out in collaboration with Dr Matt Tucker.

2.2.5. X-ray total scattering

The theory of X-ray total scattering is very similar to that of neutron total scattering. However, a standard laboratory X-ray diffractometer with Cu Kα radiation is not an appropriate instrument for a total scattering experiment, because its maximum Q is very limited (for a maximum 2θ of 80°, Q_{max} = 5.2 Å^{-1} as per Equation 2.11). Higher energy X-rays are required to increase the Q range, which can be achieved by using a synchrotron X-ray source with a suitable high-energy beamline such as the dedicated beamline 11-ID-B at the Advanced Photon Source at Argonne National Laboratory, USA, which can easily achieve a useable Q_{max} of 25 – 30 Å^{-1}. A dedicated XPDF beamline is also under construction at the Diamond Light Source, UK. The use of laboratory diffractometers with silver or molybdenum X-ray sources is also possible, though the Q_{max} is still limited to 15 – 20 Å^{-1}.

A problem arises when attempting to put X-ray data on an absolute scale. Vanadium is an almost completely incoherent scatterer of neutrons and is therefore ideal for normalisation, but there is no equivalent material for X-rays. This requires somewhat different data processing techniques.

The sister program to Gudrun, GudrunX, was developed by Soper and Barney to analyse X-ray total scattering data.[27]

To normalise X-ray data, an iterative procedure is utilised, whereby an initial calibration factor is applied such that the data roughly overlay the calculated scattering intensity (based on sample composition and density) and then, once other corrections are applied (see below), the calibration factor is adjusted, and the process is repeated until good agreement between the data and the calculated intensity is achieved.

X-ray data must, similarly to neutron data, be corrected for scattering from the background and sample container, as well as for multiple scattering and attenuation. Additional corrections required for X-ray data include those for inelastic (Compton) scattering, Bremstrahlung intensity, and fluorescence. Full details of these corrections can be found in Soper *et al.*.[27]

It is also necessary to correct for the influence of the X-ray form factors on the higher-Q region of the data. This is known as "sharpening" and involves dividing the data by the product of the form factors calculated from the elements in the sample. This product can be determined in one of two ways: $\langle F\rangle^2$ or $\langle F^2\rangle$, and for this thesis, the former was used exclusively.

The ATLAS suite of programs was used to perform the Fourier transform on the X-ray $i(Q)$ obtained from GudrunX.

As mentioned earlier, because X-rays interact with the electron cloud and neutrons with the nucleus, the power of an atom to scatter X-rays is proportional to its atomic number, whereas the power of an atom to scatter neutrons shows no such trend. A light element such as oxygen is not very "visible" to X-rays, particularly in the presence of other heavier elements, but oxygen is a strong scatterer of neutrons: its "visibility" is roughly equal to that of many heavier elements. This means that X-ray and neutron (X and N)

PDFs have different relative peak weightings, with the XPDF being dominated by correlations involving the heavier elements and the NPDF being dominated by the correlations from whichever elements have the largest scattering lengths. The information provided by the two techniques is extremely complementary, and just like in Rietveld refinement, it is possible to do simultaneous PDF analysis on X-ray and neutron data.

2.2.5.1. Experimental details

X-ray total scattering data were collected using a Panalytical X'pert Pro diffractometer equipped with an Ag-anode X-ray tube using $K\alpha_{1/2}$ radiation (λ = 0.5609 Å), and with a Rh filter to remove the K_β radiation. The maximum scattering angle was approximately 156° giving a theoretical Q_{max} of 21.9 $Å^{-1}$, although in practice a value of around 16 $Å^{-1}$ was used. Samples were contained within 1 mm diameter silica glass capillaries. Datasets were also collected from the empty instrument and an empty capillary to act as backgrounds.

2.3. Hydrothermal and Solvothermal Synthesis

Solvothermal synthesis of inorganic solids involves the heating of suitable reagents in a solvent at temperatures at or above the boiling point of the solvent. Hydrothermal synthesis refers to the specific case where the solvent is water. The reactions are carried out in sealed vessels such that the reaction mixture is subject to an autogeneous pressure which is dependent on the solvent, temperature and percentage fill of the vessel.

The origins of laboratory hydrothermal synthesis, as would be recognised today, can be traced to Morey in 1914 who used what he called a "closed bomb" to synthesise sodium and potassium silicates.[28] A review article by Rabenau provides more information about the history of the hydrothermal technique.[29] As recognised by many researchers,[30-36] the initial synthetic applications of the technique were in the synthesis of open framework materials such as zeolites, but when it was extended to the synthesis of condensed inorganic materials its advantages relative to other synthetic techniques became undeniable.

Solvothermal synthesis displays numerous advantages when compared with traditional methods for the synthesis of ceramic materials, such as the so-called ceramic method, wherein solid reagents are mechanically ground together and heated to temperatures in the region of 1000 °C to promote the slow reaction between the grains of the reagents. It is often necessary to repeat a heating-cooling-regrinding cycle several times to obtain a homogeneous product. Because of the harsh conditions, it is not normally possible to control the size and morphology of the crystallites making up the products obtained. The conditions required for solvothermal synthesis are generally much milder. Size and shape control, much desired due to the increasing awareness of nanoscale materials and the size-dependence of certain properties, can be achieved by careful selection of reaction parameters such as temperature or pH, and there is tremendous scope for chemical ingenuity in the choice of reagents (for example, the selection of reagents for an *in situ* redox reaction). Of particular relevance to the work in this thesis is the fact that it is often possible using solvothermal methods to access metastable phases which would not be stable under ceramic conditions.

2.3.1. Experimental details

Solvothermal reactions were carried out in Teflon®-lined stainless-steel vessels with a volume of approximately 21 ml. Generally the volume of solvent was between 5 and 10 ml such that the vessel was not filled beyond 50%. Once sealed, the vessels were placed in pre-heated programmable fan ovens at the desired reaction temperature. Further details will be given as necessary in the chapters that follow.

2.4. Other Techniques

2.4.1. Electron microscopy

2.4.1.1. Scanning electron microscopy

Scanning electron microscopy (SEM) images were recorded using a Zeiss Supra 55-VP FEGSEM. Energy dispersive X-ray analysis (EDX) measurements, wherein the emission of X-rays characteristic to the elements present in samples under the bombardment of an electron beam is analysed, were carried out to provide an estimate of elemental composition and were made with an attached EDAX Genesis system. Samples were mounted on self-adhesive carbon tape before being sputter-coated with either gold or carbon prior to imaging to reduce charging. Some of the SEM images and EDX data presented herein (specifically those in Chapter 4, Section 4.2.1) were obtained by Craig Hiley.

2.4.1.2. Transmission electron microscopy

Transmission electron microscopy (TEM) images were collected by Dr Anna Carnerup using a JEOL 2010F instrument and by Dr Peter Dunne or Dr Reza Jalilikashtiban using a JEOL 2000FX instrument or a JEOL 2100 instrument. EDX measurements were made with an attached EDAX Genesis system. Samples were dropped onto lacy carbon coated copper grids from an acetone or water dispersion.

2.4.2. X-ray absorption near-edge spectroscopy

X-ray absorption near-edge spectroscopy (XANES) was used to determine the oxidation state of metals (such as Ce, Bi, Co and Fe) in mixed oxide samples. This was done by analysing the shape and position of the absorption edges relative to suitable standard samples. XANES was carried out on beamline B18 of the Diamond Light Source with the assistance of Dr Andy Dent and Dr Silvia Ramos. Samples were prepared by pressing pellets of 12 mm diameter and 1 – 2 mm thickness using polyethylene powder as a binder.

2.4.3. SQUID magnetometry

SQUID (superconducting quantum interference device) magnetometry measurements were carried out in collaboration with Dr Martin Lees and with the assistance of Robert Cook (both from Department of Physics, University of Warwick). The instrument used was a Quantum Designs MPMS-5S SQUID magnetometer. Samples were mounted into gel capsules, placed inside a non-magnetic straw and suspended within the instrument.

Experimental conditions were chosen based on individual sample requirements but generally, measurements were carried out at temperatures between 2 and 300 K, and magnetic fields between 0 and 5 Tesla.

2.4.4. Nuclear magnetic resonance

Solution ^{27}Al and ^{29}Si NMR was carried out on a Bruker AV III 600 instrument by Dr Ivan Prŏkes.

2.4.5. Infrared spectroscopy

Infrared spectroscopy of powder samples was carried out using a PerkinElmer Spectrum100 FT-IR instrument.

2.4.6. Thermogravimetric analysis

Thermogravimetric analysis was carried out by Dr Peter Dunne or Luke Daniels using a Mettler Toledo TGA/DSC 1 instrument. Measurements were carried out over a temperature range of 30 – 1000 °C using a heating rate of 10 °C/minute and under a flow of air at 50 ml/minute.

2.4.7. Pycnometry

Density of powder samples was measured using a Micromeritics Accupyc gas-displacement pycnometer with helium as the inert gas. Samples were purged under a constant flow of helium for 15 – 30 minutes, and the subsequent measurements were repeated until 5 consecutive volume readings were in agreement within ±0.0005 cm^{-3}.

2.5. References

1. Clearfield, A.; Reibenspies, J.; Bhuvanesh, N., *Principles and Applications of Powder Diffraction*. John Wiley & Sons, Ltd: 2008.
2. Hammond, C., In *The Basics of Crystallography and Diffraction*, Oxford University Press: Oxford, UK, 1997; pp 145.
3. Shirley, R. *The CRYSFIRE System for Automatic Powder Indexing* 1999.
4. Laugier, J.; Bochu, B. *LMGP - Suite of Programs for the interpretation of X-ray Experiments*, ENSP/Laboratoire des Matériaux et du Génie Physique: France.
5. Henry, N. F. M.; Lonsdale, K., *International Tables for X-Ray Crystallography*. 3rd ed.; Kynoch Press: Birmingham, UK, 1969; Vol. 1.
6. Squires, G. L., *Introduction to the Theory of Thermal Neutron Scattering*. Dover Publications, Inc.: Mineola, N.Y., 1996.
7. Billinge, S. J. L.; Egami, T., *Underneath the Bragg Peaks: Structural Analysis of Complex Materials*. Pergamon: Oxford, UK, 2003; Vol. 7.
8. Mitchell, D. P.; Powers, P. N., *Phys. Rev.* **1936,** *50*, 486.
9. Halban, H.; Preiswerk, P., *C. R. Hebd. Seances Acad. Sci.* **1936,** *203*, 73.
10. Shull, C. G., *Reviews of Modern Physics* **1995,** *67*, 753.
11. Hannon, A. C., *Nucl. Instrum. Methods Phys. Res., Sect. A* **2005,** *551*, 88.
12. Young, R. A., *The Rietveld Method*. Oxford University Press: 1993.
13. Rietveld, H., *J. Appl. Crystallogr.* **1969,** *2*, 65.
14. Larson, A. C.; Dreele, R. B. V., *Los Alamos National Laboratory Report LAUR 86-748.* **1994**.
15. Toby, B. H., *J. Appl. Crystallogr.* **2001,** *34*, 210.
16. Ikeda, S.; Carpenter, J. M., *Nucl. Instrum. Methods Phys. Res., Sect. A* **1985,** *239*, 536.
17. Lebail, A.; Duroy, H.; Fourquet, J. L., *Mater. Res. Bull.* **1988,** *23*, 447.
18. Hannon, A. C.; Howells, W. S.; Soper, A. K., *Inst. Phys. Conf. Ser.* **1990,** *107*, 193.
19. Placzek, G., *Phys. Rev.* **1952,** *86*, 377.
20. Yarnell, J. L.; Katz, M. J.; Wenzel, R. G.; Koenig, S. H., *Phys. Rev. A* **1973,** *7*, 2130.
21. Soper, A. K. *Rutherford Appleton Laboratory Technical Report RAL-TR-2011-013*, 2011.
22. Yang, H. X.; Walton, R. I.; Antonijevic, S.; Wimperis, S.; Hannon, A. C., *J. Phys. Chem. B* **2004,** *108*, 8208.
23. Lorch, E., *J. Phys. C.: Solid State Phys.* **1969,** *2*, 229.
24. Qiu, X.; Bozin, E. S.; Juhas, P.; Proffen, T.; Billinge, S. J. L., *J. Appl. Crystallogr.* **2004,** *37*, 110.
25. Farrow, C. L.; et al., *J. Phys.: Condens. Matter* **2007,** *19*, 335219.
26. Tucker, M. G.; Keen, D. A.; Dove, M. T.; Goodwin, A. L.; Hui, Q., *J. Phys.: Condens. Matter* **2007,** *19*, 335218.
27. Soper, A. K.; Barney, E. R., *J. Appl. Crystallogr.* **2011,** *44*, 714.
28. Morey, G. W., *J. Am. Chem. Soc.* **1914,** *36*, 215.
29. Rabenau, A., *Angew. Chem. Int. Ed.* **1985,** *24*, 1026.
30. Walton, R. I., *Chem. Soc. Rev.* **2002,** *31*, 230.

31. Byrappa, K.; Yoshimura, M., *Handbook of hydrothermal technology a technology for crystal growth and materials processing*. Noyes Publications: Norwich, N.Y., 2001.
32. Feng, S.; Xu, R., *Acc. Chem. Res.* **2000,** *34*, 239.
33. Somiya, S.; Roy, R., *Bull. Mater. Sci.* **2000,** *23*, 453.
34. Demazeau, G., *J. Mater. Chem.* **1999,** *9*, 15.
35. Clearfield, A., *Prog. Cryst. Growth Charact. Mater.* **1991,** *21*, 1.
36. Qinhua, X.; Aizhen, Y., *Prog. Cryst. Growth Charact. Mater.* **1991,** *21*, 29.

Chapter 3: The Polymorphism of Gallium Oxide

3. The Polymorphism of Gallium Oxide

3.1. Introduction

3.1.1. Background

Gallium sesquioxide, Ga_2O_3, is a binary solid with many applications whose polymorphism remains poorly defined despite several reported structural studies using diffraction, spectroscopic and theoretical methods.[1-5] It is well established that the thermodynamically stable form is the β modification, whose structure has been resolved from single crystal X-ray diffraction.[6-8] This monoclinic phase contains equal proportions of tetrahedrally and octahedrally coordinated gallium and an analogue is found in aluminium oxide chemistry in θ-Al_2O_3, a metastable form observed during heat treatment of boehmite (AlOOH) or bayerite ($Al(OH)_3$) prior to the formation of α-Al_2O_3.[9] The only other structurally characterised polymorph of gallium oxide is the α form, which contains solely octahedral gallium,[10] and is an analogue of the hexagonal α-Al_2O_3 (corundum) as first reported by Zachariasen.[11-12] The α-Ga_2O_3 polymorph is metastable, in contrast to the alumina analogue, and converts to β-Ga_2O_3 upon heating at atmospheric pressure at $\geq$600 °C.[1] The β-Ga_2O_3 polymorph converts irreversibly to α-Ga_2O_3 upon application of pressure due to the smaller molar volume of the latter.[13-14] For other reported polymorphs of Ga_2O_3 there is limited structural information, although it is widely believed that three further forms exist under ambient conditions: γ-Ga_2O_3, assumed to be structurally related to the defect spinels such as γ-Al_2O_3, η-Al_2O_3 and other M_2O_3 oxides;[15-21] δ-Ga_2O_3, possibly an analogue of bixbyite (C-type rare-earth structure) as found for In_2O_3;[22] and ε-Ga_2O_3, supposedly analogous to ε-Fe_2O_3 and κ-Al_2O_3 (see Figure 3.1).[23-27]

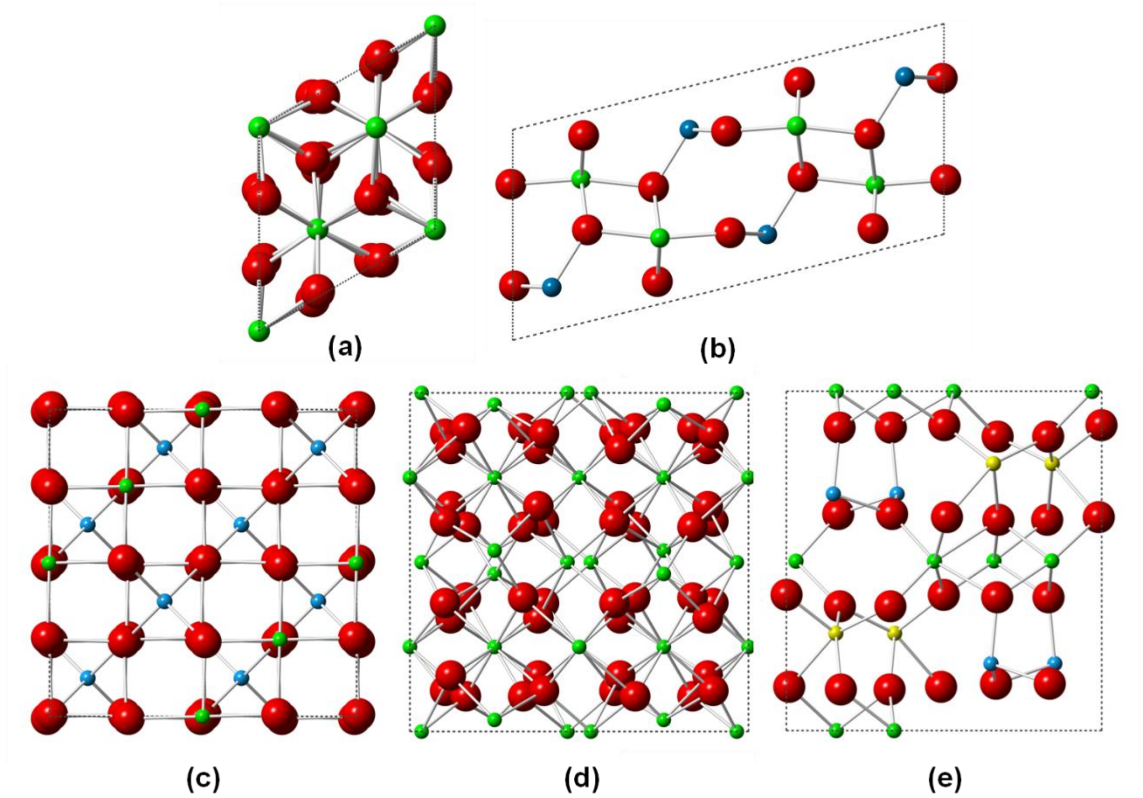

Figure 3.1 (a) The structure of α-Ga_2O_3, (b) The structure of β-Ga_2O_3, (c) The structure of γ-Al_2O_3, (d) The bixbyite structure (In_2O_3) and (e) The structure of κ-Al_2O_3. Green spheres are octahedral cation sites, blue spheres are tetrahedral sites and yellow spheres are pseudo-pentahedral sites.

For none of these three phases has a full crystallographic model been reported. This situation may be contrasted with the case of Al_2O_3 for which more than 12 structural forms have been identified, many of them with refined structures deduced from diffraction measurements and their interconversion as a function of temperature and pressure widely investigated.[9, 28-31]

The β-Ga_2O_3 polymorph is a wide band gap semiconductor (~ 4.7 eV)[32] that has been studied for potential applications in electronics, optics and catalysis. The conductivity of β-Ga_2O_3 is strongly linked to its defect structure, and can be tuned by the application of reducing or oxidising atmospheres during crystal growth.[33-35] β-Ga_2O_3 grown under reducing conditions is a promising transparent conducting oxide, particularly when its conductivity is further enhanced with suitable dopants.[35] Various Ga_2O_3 nanostructures have other, more specific applications. For example, an increase in conductivity under UV irradiation (λ = 254 nm), has led to the use of β-Ga_2O_3 nanowires as solar-blind photodetectors.[36] Optical-quality β-Ga_2O_3 nanowires have been used as waveguides for the light from a He-Ne laser,[37] and electroluminescence induced by transition metal doping has led to the application of β-Ga_2O_3 thin films in display devices.[38] Ga_2O_3 has attracted much interest as a new material for high-temperature-stable semiconducting gas sensors for both oxygen and reducing gases. The conductivity of β-Ga_2O_3 thin films has been found to be inversely proportional to the oxygen partial pressure in the temperature range 900 – 1000 °C.[39-41] At temperatures around 600 °C the oxygen sensitivity diminishes significantly and the films can instead be used to detect gases such as H_2 and CO.[42] The H_2 specificity of Ga_2O_3 based detectors can be improved with the addition of SiO_2 or by constructing Shottky diode devices with Pt and SiC.[43-44] Additionally, β-Ga_2O_3 nanoplates were successfully employed in an electrochemical CO sensor.[45]

In terms of catalysis, the polymorphism of Ga_2O_3 is important. In reactions such as the dehydrogenation of propane and the conversion of methanol to dimethyl ether, the behaviour of the polymorphs differed with structure and surface chemistry.[46-47] In the catalytic tests, the β and γ polymorphs performed best and β-Ga_2O_3 was found to have the highest intrinsic activity. β-Ga_2O_3 has also found applications as a catalyst support for Pd/Pt in the steam reforming of methanol;[48] as a stability-enhancing additive to ZrO_2 catalysts for the isomerisation of n-butane;[49] and as part of a γ-Ga_2O_3-Al_2O_3 composite catalyst for the reduction of NO_x to N_2.[50] Ga_2O_3 is also a promising photocatalyst. Three polymorphs (α, β and γ) have been shown to outperform TiO_2 when used for the decomposition of volatile aromatic compounds,[51-52] and β- and γ-Ga_2O_3 have also been applied to the photocatalytic splitting of H_2O and the photoreduction of CO_2.[53-54]

In addition to the physical properties of the various gallium oxide polymorphs, there are also examples of using β- and γ-Ga_2O_3 as precursors to other functional materials such as GaN and the various oxynitrides.[55-57] A poorly crystalline form of gallium oxide, produced by the thermal decomposition of gallium nitrate, has been widely used as a reactive source of gallium in the hydrothermal crystallisation of microporous gallium phosphate materials.[58-66]

Most of the assumptions regarding the methods of preparation, structures, stabilities and, indeed, existence of γ-, δ- and ε-Ga_2O_3 stem from a 1952 article by Roy *et al.*, who used a variety of solution methods to prepare and interconvert the various forms of Ga_2O_3.[1] Phase indentification was on the basis of powder X-ray diffraction with only tabulated peak positions and relative intensities presented; and yet for some of these materials these data remain the reference X-ray diffraction pattern, for example, for ε-Ga_2O_3 and δ-Ga_2O_3 (JCPDS card numbers 06-0509 and 06-0529).[67] The subsequent literature on gallium oxides has often assumed the conclusions of Roy *et al.*, and indeed their reaction scheme for the interconversion of gallium oxide polymorphs is reproduced in textbooks of inorganic chemistry.[68-69]

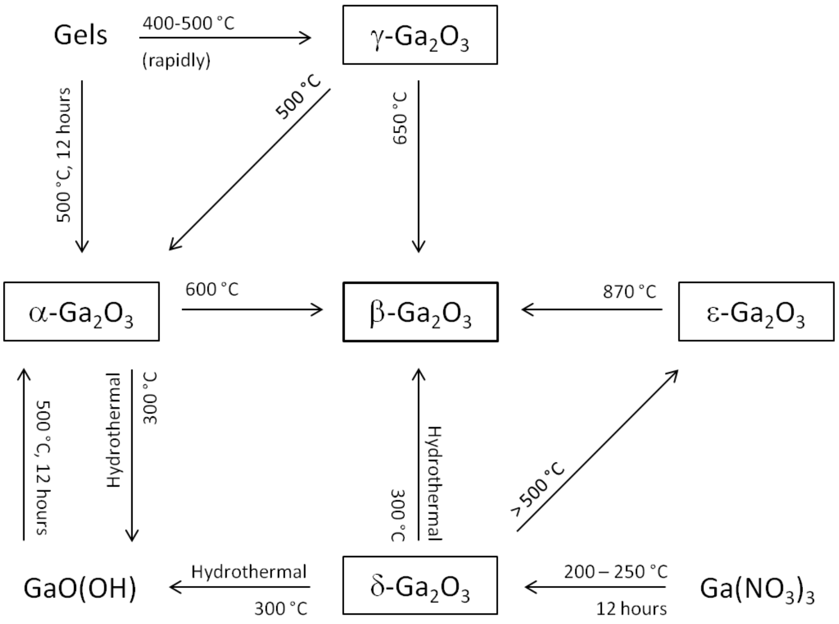

Gels
400-500 °C
(rapidly)
γ-Ga2O3
500 °C, 12 hours
500 °C
650 °C
α-Ga2O3
600 °C
β-Ga2O3
870 °C
ε-Ga2O3
500 °C, 12 hours
Hydrothermal
300 °C
Hydrothermal
300 °C
>500 °C
GaO(OH)
Hydrothermal
300 °C
δ-Ga2O3
200 – 250 °C
12 hours
Ga(NO3)3

Figure 3.2 A flow-chart of the interconversions of the polymorphs of Ga_2O_3 as described by Roy *et al.*[1]

A closer inspection of the literature, however, shows that the structural characterisation of these polymorphs has been hampered by their often poorly crystalline nature. Only for γ-Ga_2O_3 has a crystal structure been proposed, and this was simply a refinement of lattice parameters with atomic coordinates fixed at values taken from the known structure of the defect spinel γ-Al_2O_3.[70] It is worth comparing the situation with that of Fe_2O_3, another polymorphic system which may act as a structural model for Ga_2O_3, where only in the past few years have structures and interconversions of hitherto uncharacterised polymorphs been fully described.[25-26, 71-73]

3.1.2. Scope of this chapter

This chapter is concerned with a comprehensive study of the synthesis of, and interconversion between, the various polymorphs of Ga_2O_3, as well as the determination of the structures of the hitherto uncharacterised γ, δ and ε polymorphs which display various degrees of structural disorder.

Synthetic routes to the various polymorphs of Ga_2O_3 are presented, as are the syntheses of several new Ga-containing materials discovered in the course of the investigation.

The technique of total scattering is used in order to gain insight into the structures across a range of length scales from short-range atomic order to long-range crystallographic order. The use of total neutron scattering promotes roughly equal weighting of the Ga and O contributions (coherent scattering lengths for Ga = 7.288 fm and O = 5.803 fm) whereas total X-ray scattering effectively highlights the Ga contributions due to the difference in atomic number (Ga = 31 and O = 8). The two techniques are therefore highly complementary for this particular group of materials.

In this chapter the polymorphism of Ga_2O_3 is discussed with particular focus on challenging common assumptions and discussion of the many new insights gained from this detailed study.

3.2.Experimental

3.2.1. *Synthesis*

3.2.1.1. Alpha- and beta-Ga_2O_3

A reference sample of α-Ga_2O_3 was synthesised in two stages, using a procedure similar to that used by Lavalley *et al.*[47] and Hou *et al.*.[52] Gallium nitrate hydrate (3.0 g, Aldrich, 99.9% metals basis) was dissolved in distilled water (50 ml), and concentrated aqueous ammonia, diluted 50% v/v with distilled water, was added until no further precipitation was observed. The solution was left to stand overnight, then a fine white precipitate was collected by vacuum filtration, washed with water and acetone and dried at 70 °C overnight. The product was identified by powder XRD as gallium oxyhydroxide,

$GaOOH$.[1] The $GaOOH$ was heated at 500 °C for 4 hours at which point powder XRD showed a single phase of α-Ga_2O_3.[10]

A reference sample of β-Ga_2O_3 was obtained by heating gallium nitrate hydrate at 220 °C in air for 18 hours, followed by re-grinding and heating the product at 800 °C in air for 22 hours. The final product was identified by powder XRD as a single phase of β-Ga_2O_3.[6]

3.2.1.2. Gamma-Ga_2O_3

Samples of γ-Ga_2O_3 were synthesised by two methods.

The first was the solvothermal oxidation of metallic gallium, based on the method of Kim *et al.*,[74] but optimised to give the most crystalline products at lower temperatures. All reactions between 12 and 72 hours in length and in either 2-aminoethanol (MEA) or diethanolamine (DEA) were found to produce γ-Ga_2O_3, as confirmed by laboratory powder XRD (see Section 3.3.2.1). Two samples, one highly crystalline and one nanocrystalline, were chosen for neutron scattering studies and were prepared as follows. Sample one: 0.3 g of Ga (Aldrich 99.99%) and 5 ml of 2-aminoethanol (Aldrich ≥ 99.0%) were placed in a Teflon-lined stainless steel autoclave which was sealed and transferred to a pre-heated fan oven at 240 °C for 72 hours. The solid product was dispersed into 10 ml of hot methanol, recovered by suction filtration, washed with further methanol and dried at 70 °C overnight. Sample two: 0.3 g of Ga (Aldrich 99.99%) and approximately 5 ml of diethanolamine (Aldrich ≥ 98.5%) were placed in a Teflon-lined stainless steel autoclave which was sealed and transferred to a pre-heated fan oven at 240 °C for 11 hours. The reaction mixture was diluted with 15 ml of methanol, filtered to remove unreacted gallium and the white solid product was isolated and washed *via* centrifugation, before being dried at 70 °C overnight.

The second method used to prepare γ-Ga_2O_3 was that of Arean *et al.*.[75] Gallium nitrate hydrate (3 g, Aldrich 99.9% metals basis) was dissolved in ethanol (50 ml). Concentrated aqueous ammonia, diluted 50% v/v with ethanol, was added to the gallium nitrate solution to achieve a pH of 9.0. The resulting precipitate was immediately filtered, washed with ethanol and dried at 70 °C for 12 hours before being calcined at 500 °C for 1 hour.

3.2.1.3. A novel gallium oxyhydroxide

Similar solvothermal reactions to those used for the preparation of γ-Ga_2O_3, but performed for longer periods of time, resulted in the formation of a novel crystalline phase, $Ga_5O_7(OH)$, and optimal conditions for the preparation of this phase were found to be the use of 0.1 g Ga in a 1:7 water:diethanolamine mixture and a reaction time of 6 days at 240 °C.

3.2.1.4. Gallium nitrate nonahydrate

The as-purchased gallium nitrate hydrate (Aldrich, 99.9% metals basis) was examined by powder XRD and found to contain a secondary phase in addition to the expected $Ga(NO_3)_3.9H_2O$ whose structure was recently determined by Hendsbee *et al.*.[76] Several batches were purchased for testing and were always found to be the same.

An attempt to prepare phase pure $Ga(NO_3)_3.9H_2O$ using the method mentioned by Roy *et al.*[1] was made. Metallic gallium (0.21 g, Aldrich 99.99%) was added to distilled water (15 ml) and concentrated nitric acid (25 ml) and allowed to dissolve. The solution was heated to boiling until the volume had reduced by approximately 75% and was then rediluted with distilled water. The heating and re-dilution procedure was repeated thrice more and then the solution was left to slowly evaporate. On standing for several weeks, large (1 – 3 mm), colourless, rhomboidal crystals were observed. These were examined using single crystal X-ray diffraction and were found to be isostructural with gallium "nanoclusters" of formula $[Ga_{13}(\mu_3\text{-}OH)_6(\mu_2\text{-}OH)_{18}(H_2O)_{24}](NO_3)_{15}$ as described by Rather *et al.*.[77] Examination of powder XRD revealed that the nanoclusters were the secondary phase found in commercial gallium nitrate hydrate.

An *in situ* powder XRD examination of the thermal decomposition of commercial gallium nitrate hydrate confirmed the existence of these two phases by their different decomposition behaviours (Figure 3.3).

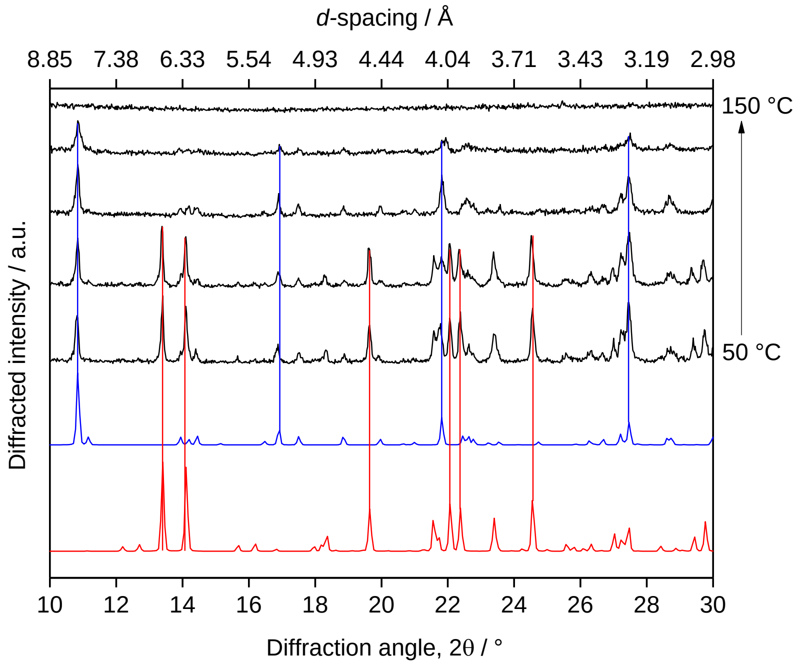

Figure 3.3 In black: thermodiffraction of the decomposition of commercial gallium nitrate hydrate. The red trace is the simulated pattern for $Ga(NO_3)_3.9H_2O$ and the blue trace is the simulated pattern for the $[Ga_{13}(\mu_3\text{-}OH)_6(\mu_2\text{-}OH)_{18}(H_2O)_{24}](NO_3)_{15}$ "nanoclusters".

A phase pure sample of $Ga(NO_3)_3.9H_2O$ was obtained *via* recrystallisation. Gallium nitrate hydrate (18 g, Aldrich, 99.9% metals basis) was dissolved in distilled water (50 ml) followed by addition of 1 ml concentrated HNO_3. The volume of the solution was reduced to approximately 3 ml on a rotary evaporator. The addition of water and HNO_3 and subsequent evaporation was repeated twice and then crystallisation was induced *via* agitation with a glass rod. For materials studied using neutron diffraction this proved to be a convenient method for preparing samples free of protons (thus reducing the problem of strong incoherent scattering from H in the measured data), by use of D_2O (Aldrich, 99.9 atom % D) in place of H_2O and inducing crystallisation within a nitrogen-filled glove-bag (Aldrich "AtmosBag").

3.2.1.5. Delta- and epsilon-Ga_2O_3

Heating $Ga(NO_3)_3.9H_2O$ (or $Ga(NO_3)_3.9D_2O$) at 220 °C for 12 hours in air produced a poorly crystalline material which is herein designated "δ-Ga_2O_3" as it would match the proposed phase of Roy *et al.*[1] (see Figure 3.2). Prolonged heating at 400 °C produced a more crystalline phase which is herein designated ε-Ga_2O_3, in line with literature precedent.[1]

The synthesis of ε-Ga_2O_3 *via* the decomposition of nanostructured GaOOH formed in a microwave reaction in the presence of urea as a templating agent was recently reported by Ge *et al.*.[78] Attempts to replicate this synthesis under standard hydrothermal conditions were unsuccessful.

3.3. Results and Discussion

3.3.1. Alpha- and beta-Ga_2O_3

The structures of α- and β-Ga_2O_3 have both been reported from single crystal x-ray diffraction and these two polymorphs were treated as reference samples in this work. The neutron $i(Q)$ of β-Ga_2O_3 is compared with an $i(Q)$ simulated from the published structure in Figure 3.4. The simulated $i(Q)$ was modified for small particle size (100 Å diameter) using a Mason factor, a technique which is discussed further in Section 3.3.4.2.

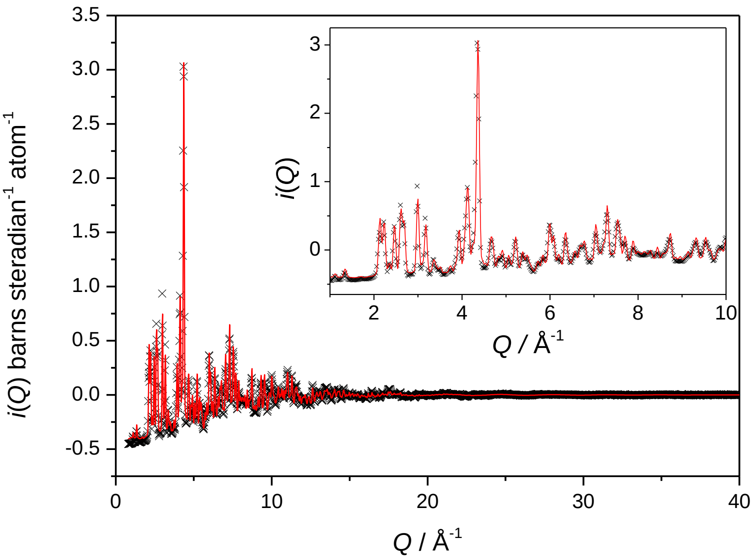

Figure 3.4 The measured *i*(*Q*) for β-Ga_2O_3 compared with a simulated *i*(*Q*) for particles of diameter 100 Å. The structure of β-Ga_2O_3 was taken from Ahman *et al.*.[8]

The results of PDF analysis for β-Ga_2O_3 are shown in Figure 3.5 and Table 3.1. An excellent fit to the PDF is obtained using the published crystal structure, indicating that the local structure is well described by the average structure. A wRp value of 9.67% is obtained, which is indicative of an excellent PDF fit.

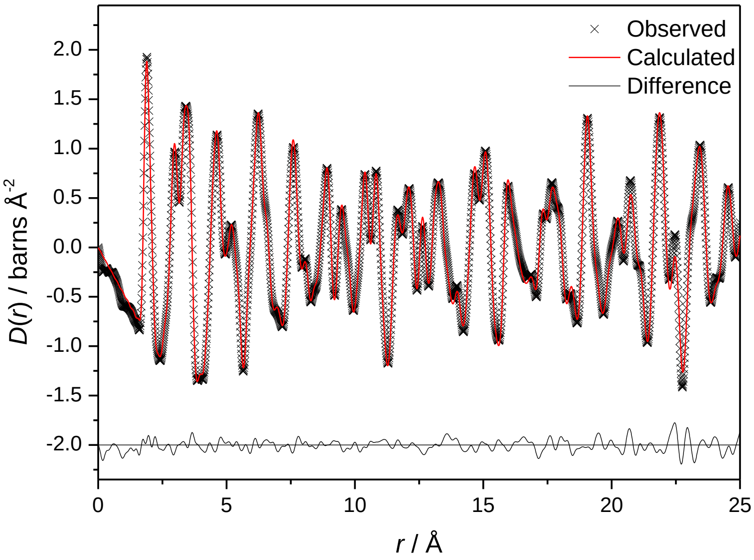

Figure 3.5 The results of PDF analysis for β-Ga_2O_3, wRp = 9.67%.

Table 3.1 Refined parameters from PDF analysis of β-Ga_2O_3 (Q_{max} = 30 Å^{-1}). Space group *C*2/*m*. Refined (and initial) cell parameters: *a* = 12.22530(6) Å (12.214 Å), *b* = 3.03636(1) Å (3.0371 Å), *c* = 5.80645(3) Å (5.7981 Å) and *β* = 103.7540(8)° (103.83°).

		Initial			**Refined**		
Atom	**Site**	**x**	**y**	**z**	**x**	**y**	**z**
Ga1	4i	0.0905	0	0.7946	0.090141(8)	0	0.79541(2)
Ga2	4i	0.1587	0.5	0.3140	0.158459(8)	0.5	0.31417(1)
O1	4i	0.1645	0	0.1098	0.16623(1)	0	0.11044(2)
O2	4i	0.1733	0	0.5632	0.173216(9)	0	0.56313(2)
O3	4i	-0.0041	0.5	0.2566	0.99559(1)	0.5	0.25620(2)

The comparison of the *i*(*Q*) of α-Ga_2O_3 to the simulated *i*(*Q*) for particles of 80 Å diameter is shown in Figure 3.6. The Bragg reflections agree extremely well but there are broad features in the low-*Q* region which are not accounted for. This is likely to be a result of the synthesis from an amorphous hydroxide gel.

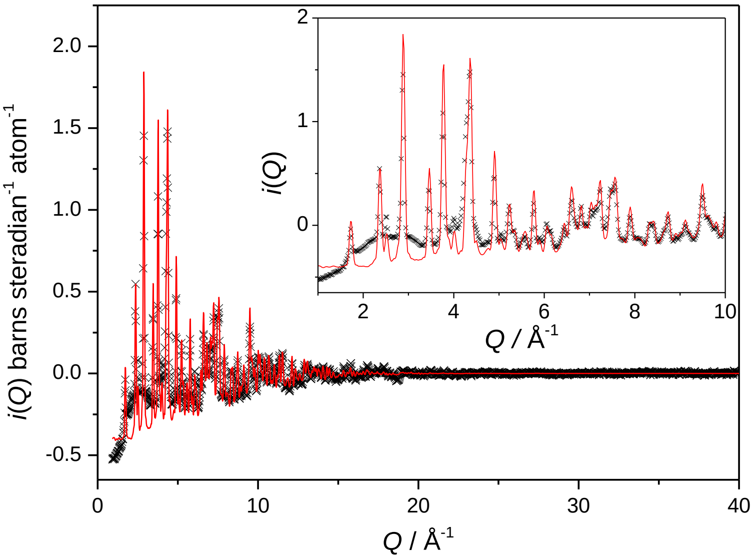

Figure 3.6 The measured *i*(*Q*) for α-Ga_2O_3 compared with a simulated *i*(*Q*) for particles of diameter 80 Å. The structure of α-Ga_2O_3 was taken from Marezio *et al.*[10]

The area of the first peak in the PDF, corresponding to the Ga–O bond distance(s), is directly related to the coordination number (C. N.) of the Ga atom, by the formula:

$$C.N. = \frac{\text{area} \times \text{position}}{\text{neutron coefficient}} \tag{3.1}$$

Therefore, information about the coordination environment of the Ga can be obtained by fitting the first PDF peak. In Figure 3.7 are the results of peak fitting for α- and β-Ga_2O_3. Due to the obviously asymmetrical nature of the peaks in the fitting, it was necessary to include two (α) and three (β) individual peaks which correspond well to the expected different bond lengths in the crystal structures for these phases. Summaries of these results are shown in Table 3.2 and Table 3.3. For β-Ga_2O_3 the expected average coordination number of 5 is obtained, however for α-Ga_2O_3 the value of 5.56 is slightly lower than the expected 6. The shorter of the two octahedral bond lengths also refines to a lower-than expected value. The peak fitting results for α-Ga_2O_3 imply that the material contains a small amount of tetrahedral gallium. This was also observed by

Zheng *et al.*[46] and Lavalley *et al.*,[47] and has been attributed either to the presence of a secondary impurity phase, or to surface reconstruction leading to small quantities of tetrahedrally coordinated Ga.

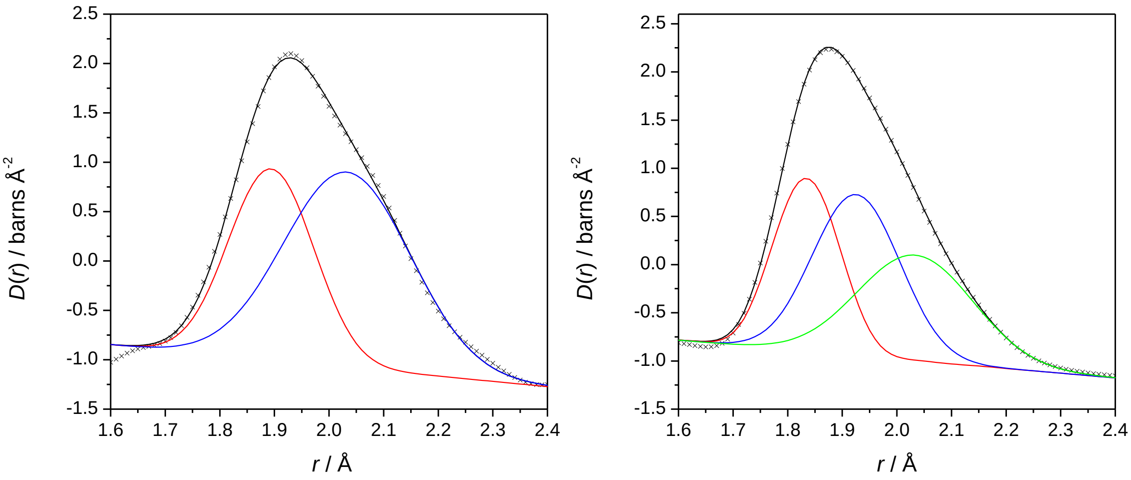

Figure 3.7 The results of fitting the first peak in the PDFs for (left) α- and (right) β-Ga_2O_3.

Table 3.2 The results of fitting the first peak of the PDF for α-Ga_2O_3. According to the crystal structure,[10] the average coordination number of Ga in α-Ga_2O_3 is 6.0.

	Fit parameters			**Crystal structure**
	Position / Å	**Area**	**C.N.**	**Position / Å**
Peak 1	1.89(1)	0.369	2.07	1.921
Peak 2	2.033(8)	0.582	3.49	2.077
C.N. (sum)			**5.56**	

Table 3.3 The results of fitting the first peak of the PDF for β-Ga_2O_3. According to the crystal structure,[8] the average coordination number of Ga in β-Ga_2O_3 is 5.0.

	Fit parameters			**Crystal structure**
	Position / Å	**Area**	**C.N.**	**Position / Å**
Peak 1	1.835(5)	0.271	1.47	1.832
Peak 2	1.93(2)	0.332	1.89	1.936
Peak 3	2.03(3)	0.290	1.74	2.074
C.N. (sum)			**5.1**	

3.3.2. Gamma-Ga_2O_3

3.3.2.1. General characterisation

The choice of aminoalcohol solvent and reaction time in the solvothermal preparation of γ-Ga_2O_3 affected the particle size as observed by powder X-ray diffraction (Figure 3.8). For samples made using DEA as the solvent, the particle size appeared to be unaffected by reaction time. Samples made using MEA were generally more crystalline, and longer reaction times further increased the particle size. The particle size of γ-Ga_2O_3 produced by the precipitation method was much smaller than all of the solvothermal samples.

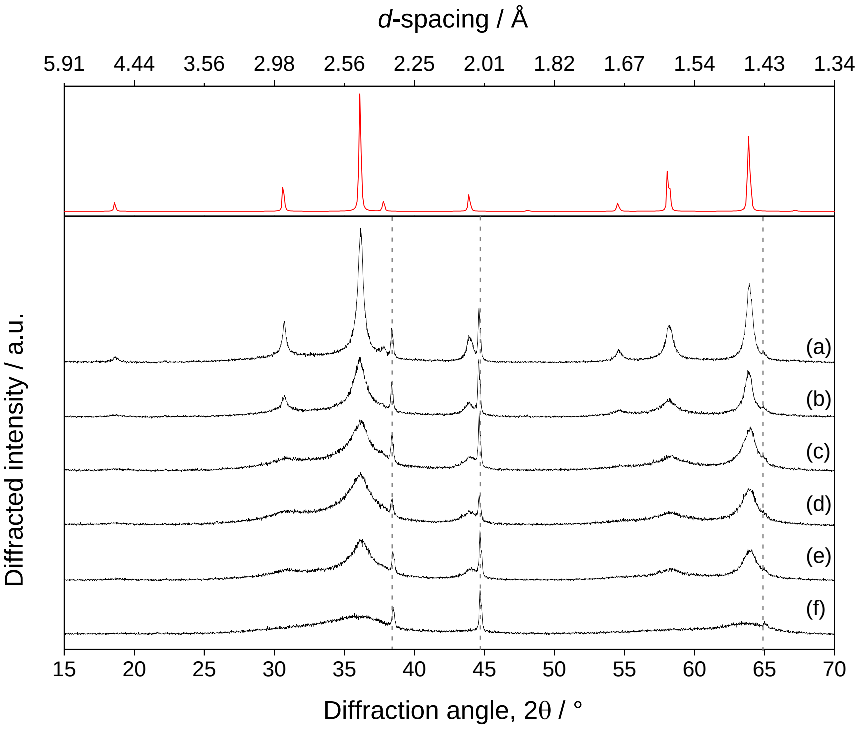

Figure 3.8 Plot showing XRD patterns for various samples of γ-Ga_2O_3: (a) MEA, 72 hrs (b) MEA, 18 hrs (c) DEA, 30 hrs (d) DEA, 18 hrs (e) DEA, 11 hrs (f) precipitation from aqueous solution. The sharp peaks marked with vertical dotted lines are from the Al sample holder, and the upper panel shows the simulated XRD pattern for the structure determined in Section 3.3.2.2.

Table 3.4 Estimated particle diameters using the Scherrer equation for various samples of γ-Ga_2O_3.

Solvent	**Temperature**	**Time**	***Dp* / nm**
MEA	240 °C	72 hours	29.5
MEA	240 °C	18 hours	16.4
DEA	240 °C	30 hours	14.6
DEA	240 °C	18 hours	13.0
DEA	240 °C	11 hours	13.7
Precipitation method	N/A	N/A	5.0

Samples of γ-Ga_2O_3 were heated *in situ* on the powder X-ray diffractometer to examine the phase transformation sequence reported by Roy *et al.*: γ-$Ga_2O_3 \rightarrow \alpha$-$Ga_2O_3 \rightarrow \beta$-$Ga_2O_3$.[1] No evidence for the formation of α-Ga_2O_3 was found and in fact the transformation to beta occurred cleanly at around 550 – 650 °C (Figure 3.9). Interestingly, the transformation temperature was affected by particle size, and the particle size of the final β product appeared to have an inverse relationship to the particle size of the γ-Ga_2O_3 sample used, implying that the smaller particles have greater reactivity.

It can be seen from SEM and TEM that the γ-Ga_2O_3 prepared by the precipitation-method consists of roughly spherical particles of less than 10 nm in diameter. In contrast, the solvothermal γ-Ga_2O_3 consists of thin platelets of approximate length 50 nm and thickness 5 nm which agglomerate into roughly spherical clusters, similar to those observed by Kim *et al.*[74] (see Figure 3.10).

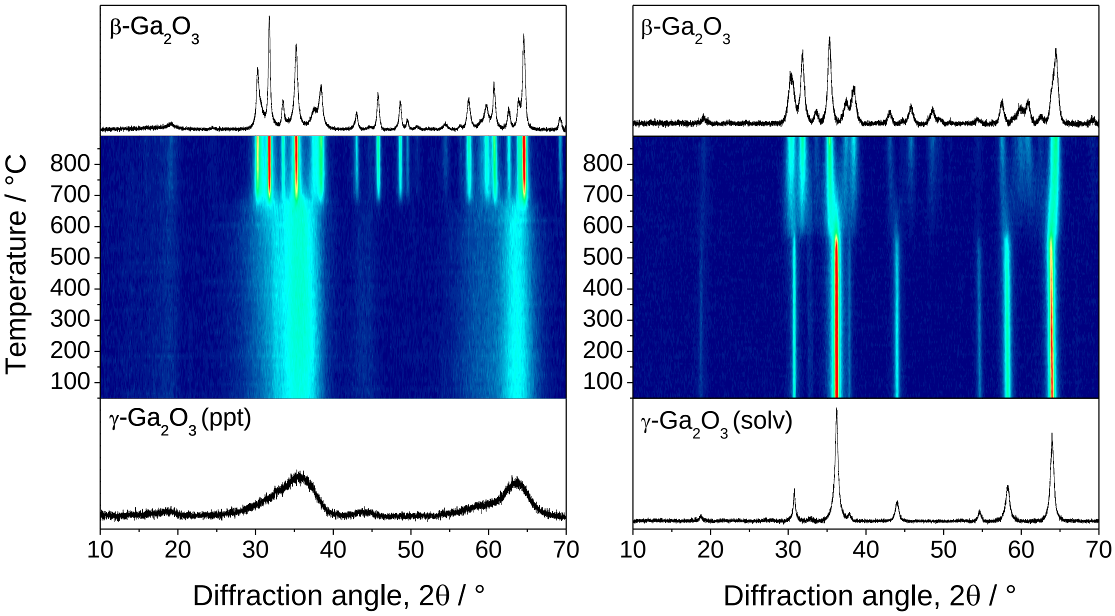

Figure 3.9 Contour plots of the *in situ* heating of γ-Ga_2O_3 where the Z axis is intensity and the first and last scans are highlighted. Left: heating of poorly crystalline γ-Ga_2O_3 produced *via* precipitation from aqueous solution. Right: heating of crystalline γ-Ga_2O_3 from solvothermal reaction.

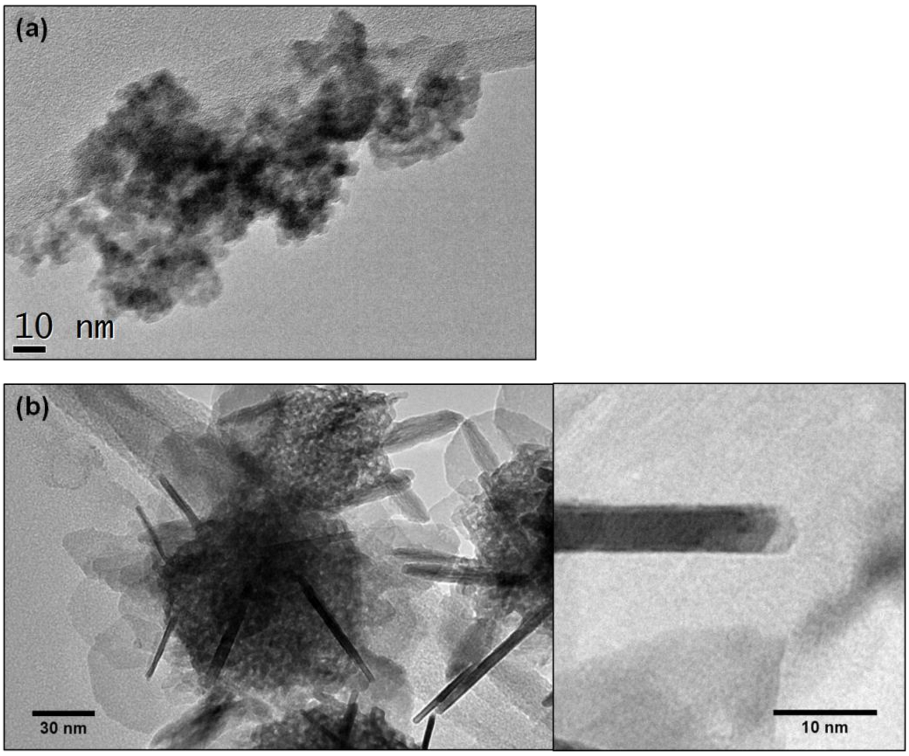

Figure 3.10 (a) TEM image of precipitation-method γ-Ga_2O_3. (b) TEM images of crystalline solvothermal γ-Ga_2O_3.

TGA/DSC plots can be seen in Figure 3.11. For precipitation-method γ-Ga_2O_3, a continuous mass loss is observed starting at 30 °C up to a maximum of 8.8% at 800 °C, which is likely due to the presence of a large amount of surface water and more strongly associated hydroxyl groups. For solvothermal-method γ-Ga_2O_3 there are two main regions of mass loss: an initial loss of 0.8% between 50 and 150 °C is observed, corresponding to the loss of surface water, and a further mass loss of ~ 4% between 300 and 500 °C, presumably due to strongly bound hydroxyl groups or surface-associated organic species arising from the preparation method.

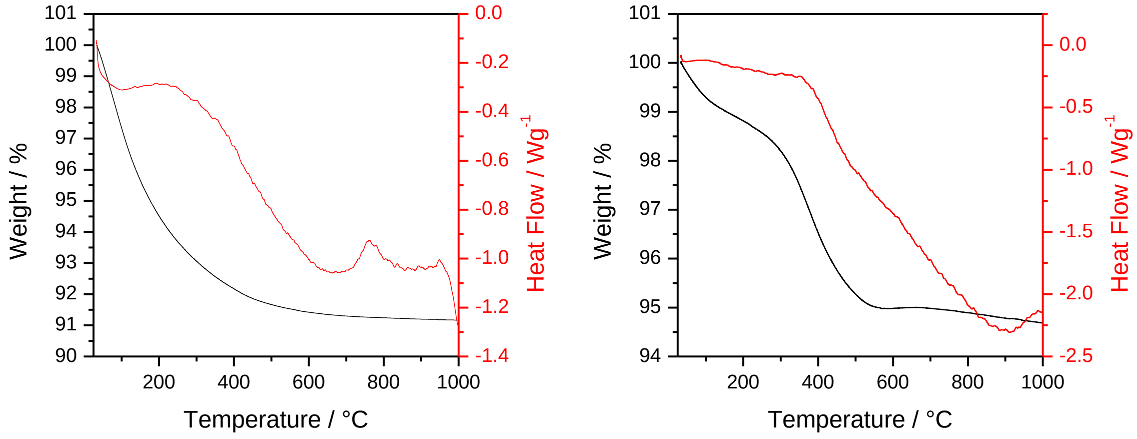

Figure 3.11 TGA/DSC results for γ-Ga_2O_3. Left: disordered γ-Ga_2O_3 from precipitation method. Right: crystalline solvothermal γ-Ga_2O_3.

3.3.2.2. Rietveld refinement

The first stage in the analysis of the neutron diffraction data collected from the highly crystalline γ-Ga_2O_3, produced by the solvothermal oxidation of gallium metal in ethanolamine, was Rietveld refinement. The existing structural model for γ-Ga_2O_3 was not chosen as a starting model since not all of the structural parameters were refined in that work due to the poorly crystalline nature of the sample.[70] Instead, the structure of the analogous γ-Al_2O_3 phase, as obtained from single crystal XRD,[15] was chosen. This model consisted of four partially occupied Ga sites, the two ideal spinel sites: 8a (tetrahedral) and 16d (octahedral), and two non-spinel sites: 16c (octahedral) and 48f (tetrahedral). In addition to the profile and instrumental parameters, there were a total of 9 refineable structural parameters: the unit cell parameter, *a*, the fractional coordinates *x* (= *y* = *z*) for the O atom, the *x*-coordinate for the 48f Ga atom, two U_{iso} values (one for all Ga atoms and one for the O atom) and the four Ga site occupancies.

In GSAS, constraints can be applied to the shifts of refineable parameters to prevent the refinement from giving unphysical results. Each parameter can only appear in one constraint equation, and so, because of the four partially occupied sites in the model for γ-Ga_2O_3, in order to constrain the stoichiometry to Ga_2O_3, it was necessary to add duplicate or “dummy” atoms. The 8a site was split into 3, and the occupancies defined such that:

$$\mathrm{Occ}\left(Ga_{[8a]}\right) = \mathrm{Occ}\left(Ga_{[8a(i)]}\right) + \mathrm{Occ}\left(Ga_{[8a(ii)]}\right) + \mathrm{Occ}\left(Ga_{[8a(iii)]}\right) \quad \textbf{(3.2)}$$

Then the shifts applied to the occupancies were constrained such that:

$$\begin{aligned} 2\Delta\left[\mathrm{Occ}\left(Ga_{[8a(i)]}\right)\right] &= -\Delta\left[\mathrm{Occ}\left(Ga_{[16d]}\right)\right] \\ 2\Delta\left[\mathrm{Occ}\left(Ga_{[8a(ii)]}\right)\right] &= -\Delta\left[\mathrm{Occ}\left(Ga_{[16c]}\right)\right] \\ 6\Delta\left[\mathrm{Occ}\left(Ga_{[8a(iii)]}\right)\right] &= -\Delta\left[\mathrm{Occ}\left(Ga_{[48f]}\right)\right] \end{aligned} \quad \textbf{(3.3)}$$

This allowed the occupancies to refine freely, without biasing the ratio of gallium atoms in octahedral and tetrahedral sites and without deviating from the correct stoichiometry. The results of the refinement are shown in Figure 3.12 and Table 3.5.

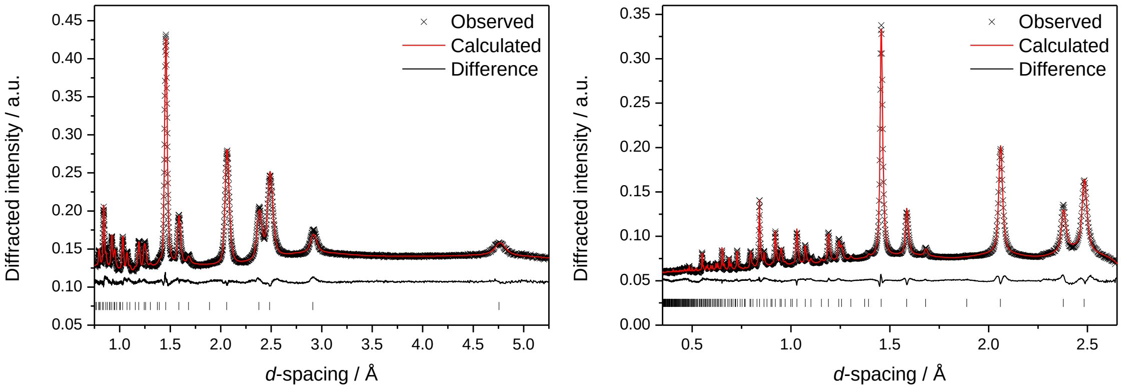

Figure 3.12 Result of Rietveld refinement for solvothermal γ-Ga_2O_3. Left: data from GEM bank 3 (mean scattering angle 34.9°). Right: data from GEM bank 5 (mean scattering angle 91.3°).

Table 3.5 Table 1: Crystal parameters for γ-Ga_2O_3, space group *Fd$\bar{3}$m*, *a* = 8.23760(9) Å. Rp = 1.23%, wRp = 1.36%. Measured density = 5.7607 gcm^{-3}, calculated density = 5.9376 gcm^{-3}.

Atom	Wyckoff site	x	y	z	U_{iso} / Å^2	Occupancy
Ga1	8a	0.125	0.125	0.125	0.0129(2)	0.741(8)
Ga2	16d	0.5	0.5	0.5	0.0129(2)	0.741(3)
Ga3	48f	0.368(2)	0.125	0.125	0.0129(2)	0.066(1)
Ga4	16c	0	0	0	0.0129(2)	0.024(1)
O	32e	0.2552(1)	0.2552(1)	0.2552(1)	0.0135(1)	1

In the constrained fit, the ratio of octahedral to tetrahedral Ga sites is 1.35:1 and the ratio of spinel to non-spinel sites is 5:1. The occupancy constraints were then lifted, at which point the stoichiometry refined to $Ga_{1.98}O_3$ and the octahedral:tetrahedral and the spinel:non-spinel ratios were unchanged. Thus, the plausibility of the four-site model was confirmed.

As additional confirmation, a two-site model where only the spinel sites were occupied was considered. Even the “best fit” in this case was rather poor (see Figure 3.13) and therefore it is clear that the partial occupancy of the two non-spinel sites is required to fit these data.

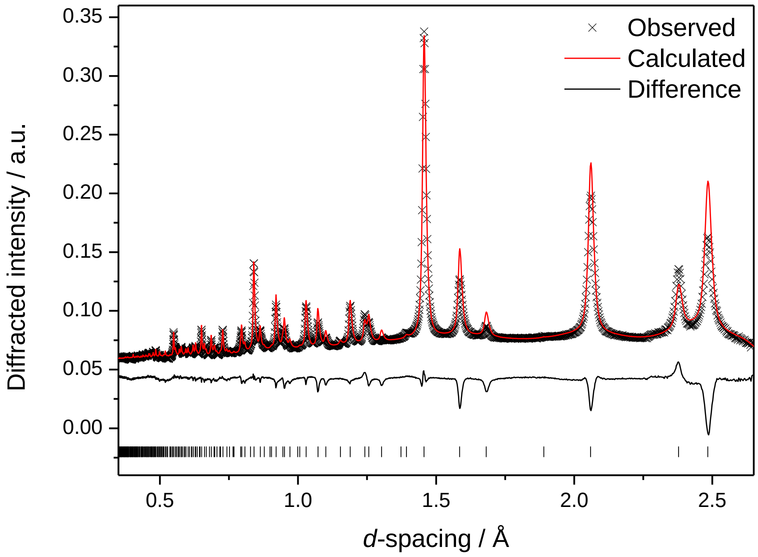

Figure 3.13 Result of an attempted Rietveld refinement for γ-Ga_2O_3 on GEM bank 5 data using a model with only the ideal spinel sites occupied.

3.3.2.3. Pair distribution function analysis

Rietveld refinement of the neutron diffraction data revealed a rather complex average structure for γ-Ga_2O_3 with multiple partially occupied sites and a significant degree of particle size broadening (Scherrer analysis yields an estimated particle size of 38 nm). Thus, the local structure was examined using PDF analysis.

The fit of the Rietveld structure to the neutron PDF of γ-Ga_2O_3 is very good, particularly at $r > 4.0$ Å (Figure 3.14), and could not be significantly improved by further refinement within the parameters of the cubic spinel model. However, the fit is rather poor in the low-*r* region ($r < 4.0$ Å) which implies that the local structure is not well accounted for by the average structural model (Figure 3.15(a)).

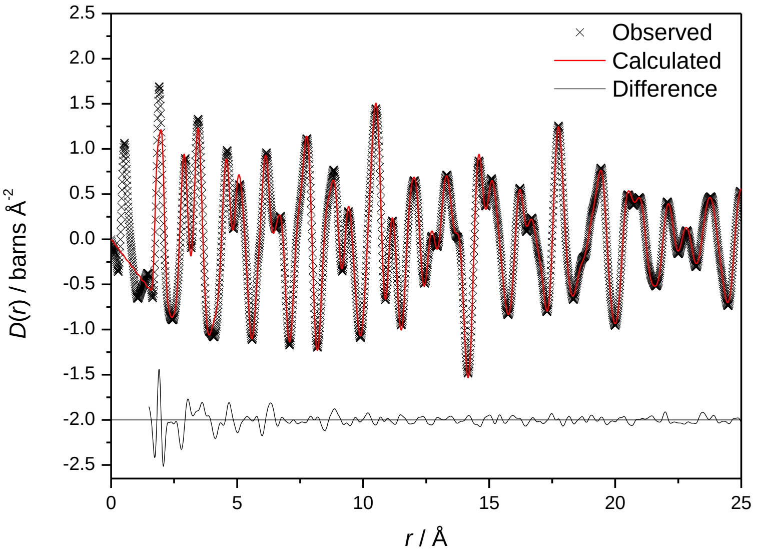

Figure 3.14 The fit of the Rietveld refined structure to the neutron PDF for γ-Ga_2O_3.

Close examination of the discrepancies in the short-range correlations reveal that they arise mainly from the Ga–O bond lengths, *i.e.* the local coordination environment of the Ga atoms, and from the Ga– –Ga nearest-neighbour distances.

The two fully characterised polymorphs of Ga_2O_3 (α and β) contain significantly distorted GaO_6 octahedra, with three shorter and three longer Ga–O bonds (approximate bond lengths are 1.92 and 2.08 Å). The cubic spinel structure contains regular GaO_6 octahedra with 6 equal bond lengths, and it is therefore likely that the local structure of γ-Ga_2O_3 is distorted from this to retain the apparently preferred coordination geometry as seen in α- and β-Ga_2O_3.

To account for this distortion, the low-*r* region of the PDF was fit using a model based on the space group $F\bar{4}3m$, a maximal subgroup of $Fd\bar{3}m$. In this model, the Ga atoms on the octahedral 16d sites are able to move away from the ideal spinel position, and the 48f oxygen site is split into two 24g sites which can move independently of each other. Refinement using this model leads to an excellent fit to the low-*r* region of the PDF, as shown in Figure 3.15(b), and the geometry of the refined octahedral gallium site closely resembles those found in the α and β polymorphs (Table 3.6 and Figure 3.16).

Table 3.6 Atomic parameters for $F\bar{4}3m$ model of γ-Ga_2O_3. Italics designate unrefined parameters.

			Initial			**Refined**		
Atom	**$Fd\bar{3}m$**	**$F\bar{4}3m$**	**x**	**y**	**z**	**x**	**y**	**z**
Ga1	8a	4a	*0*	*0*	*0*	*0*	*0*	*0*
		4d	*3/4*	*3/4*	*3/4*	*3/4*	*3/4*	*3/4*
Ga2	16d	16e	0.375	= *x*	= *x*	0.371153(4)	= *x*	= *x*
Ga3	48f	24f	0.2432	*0*	*0*	0.2320(6)	*0*	*0*
		24g	0.9932	*1/4*	*1/4*	0.978(1)	*1/4*	*1/4*
Ga4	16c	16e	*0.875*	*0.875*	*0.875*	*0.875*	*0.875*	*0.875*
O	32e	16e	0.1303	= *x*	= *x*	0.135673(9)	= *x*	= *x*
		16e	0.6198	= *x*	= *x*	0.622396(6)	= *x*	= *x*

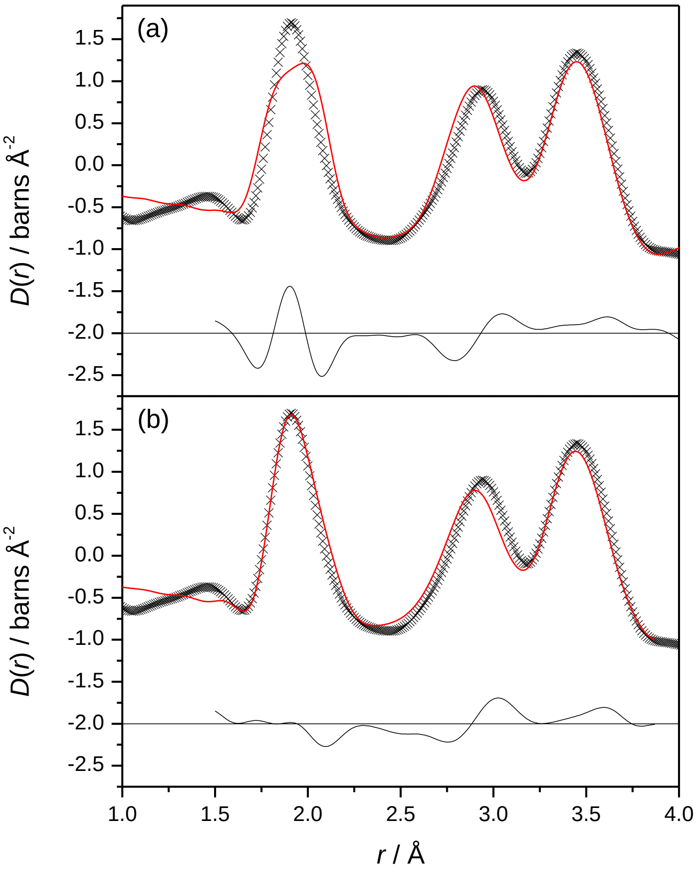

Figure 3.15 (a) The low-*r* region of the PDF fit to the cubic spinel model (from Rietveld refinement) and (b) the fit using the non-centrosymmetric $F\bar{4}3m$ model.

The remaining discrepancies in the fit (at $r \sim 2.5 - 3.2$ Å) can be attributed to a non-statistical distribution of gallium atoms over the partially occupied sites. Occupancy of the non-spinel sites must occur at the expense of the occupancy of neighbouring sites because otherwise unphysically short (< 2.4 Å) Ga–Ga distances are introduced. However, the Bragg diffraction contains no evidence of an ordered superstructure.

Occupancy of different spinel and non-spinel sites changes the nearest-neighbour Ga–Ga correlations in the PDF. When only the spinel sites (8a and 16d) are occupied, two well-defined peaks at 2.9 and 3.45 Å are visible. The occupancy of non-spinel sites alters the broadness and the relative intensity of the peaks in this region (Figure 3.17).

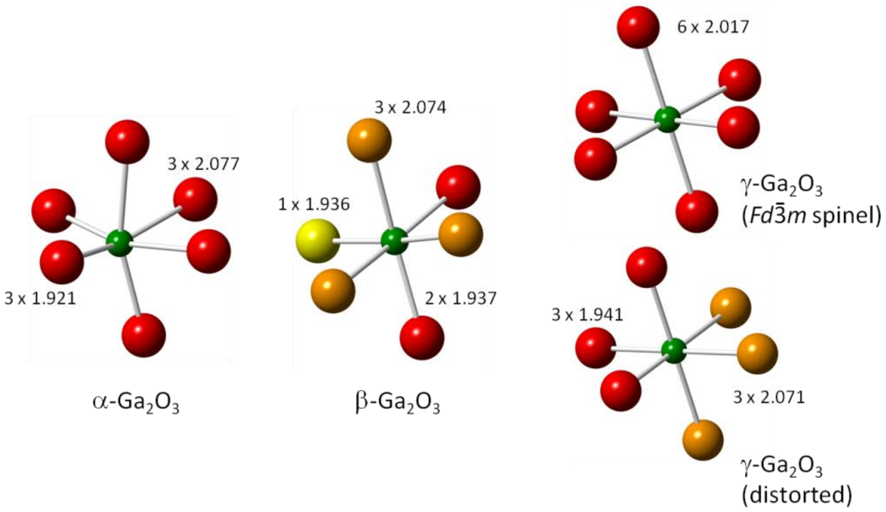
6 x 2.017
3 x 2.074
3 x 2.077
1 x 1.936
γ-Ga_2O_3
($Fd\bar{3}m$ spinel)
3 x 1.921
2 x 1.937
3 x 1.941
3 x 2.071
α-Ga_2O_3
β-Ga_2O_3
γ-Ga_2O_3
(distorted)

Figure 3.16 Comparison of the octahedral coordination of gallium in various Ga_2O_3 structures.

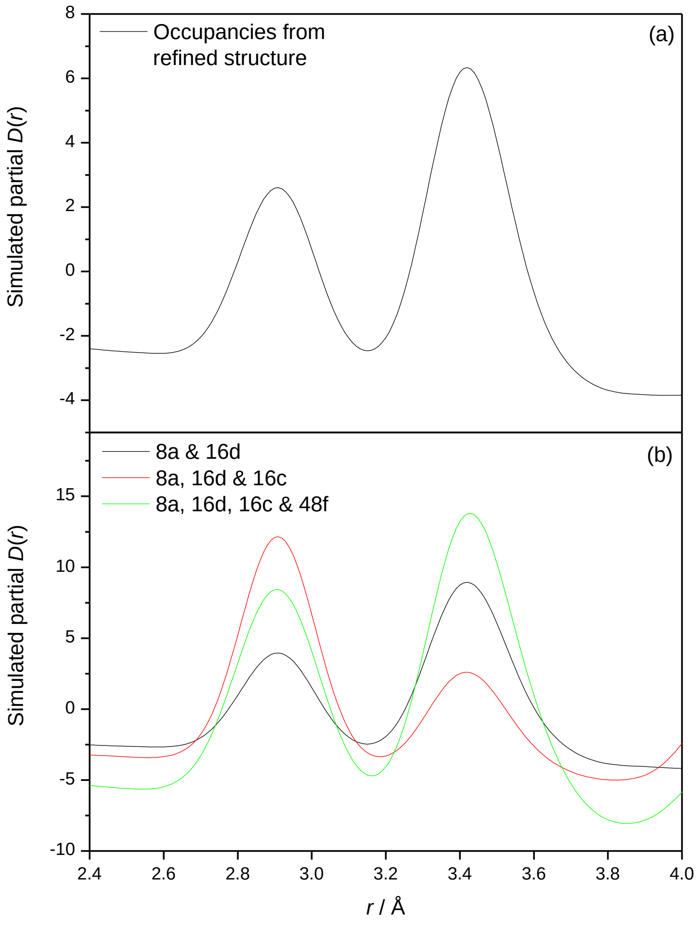

Figure 3.17 (a) The simulated Ga–Ga partial $D(r)$ for the refined γ-Ga_2O_3 structure; (b) The Ga–Ga partial $D(r)$s for models with various cation sites fully occupied.

3.3.2.4. RMCProfile

In an attempt to further understand the structural distortion and the effect of non-statistical partial site occupancy on the gallium-gallium correlations in γ-Ga_2O_3, reverse Monte Carlo (RMC) modelling was undertaken.

A 5 × 5 × 5 supercell of the crystal structure obtained from Rietveld refinement was created, and then, with each crystallographically distinct Ga site being treated separately, the correct proportions of "occupied" and "vacant" sites were created at random. As mentioned earlier, this randomised distribution of atoms produces some unphysically short Ga– –Ga correlations, and so to remove this the RMCProfile software was used to swap pairs of atoms and vacancies to reduce the numbers which violated a “minimum distance” constraint. Unfortunately, a point of stagnation, where no further swaps could be made, was always reached prior to all the unphysical correlations being removed.

A 2 × 2 × 2 supercell of the crystal structure was then used to manually arrange the correct numbers of atoms and vacancies until a configuration with no violations of the minimum acceptable distance between gallium atoms was reached. From this, a 6 × 6 × 6 supercell was created for RMCProfile. Before the data were introduced into the refinement, an atom-swapping procedure was used to re-randomise the configuration and reduce bias in the fitting. Fitting was then carried out simultaneously to both the *i*(*Q*) and the *T*(*r*) and the resulting fits (after a run-time of 48 hours, at which point no further improvement was observed) can be seen in Figure 3.18 and Figure 3.19.

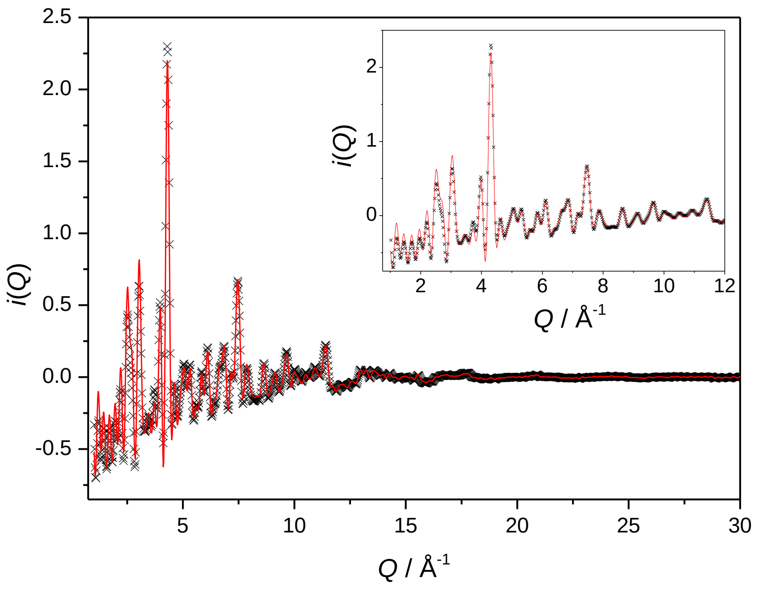

Figure 3.18 Result of RMC refinement of γ-Ga_2O_3: the final fit to the *i*(*Q*).

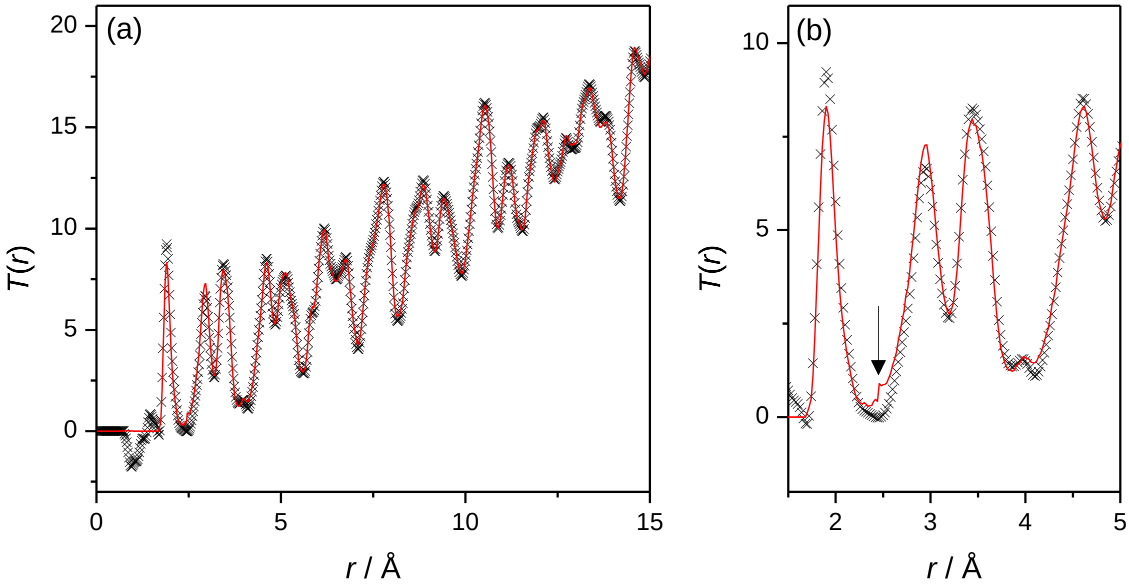

Figure 3.19 Result of RMC refinement of γ-Ga_2O_3: the final fit to the *T*(*r*) over (a) the full data range and (b) close up of the low-*r* region.

It can be seen that the fit to the peak positions in the real-space data is much better than that from PDF analysis. There is a small, unphysical feature in the fitted function at ~2.5 Å which results from the "minimum distance" for the O– –O correlations being slightly too high and will not have an adverse effect on the quality of the structural model produced.

Preliminary analysis of the refined configuration of atoms was carried out by collapsing the 6 × 6 × 6 supercell back onto the original unit cell, in order to determine the relationship of the atom and vacancy positions with the crystal structure. Figure 3.20 shows a representation of the various Ga sites in the crystallographic model and Figure 3.21 shows the results from RMCProfile.

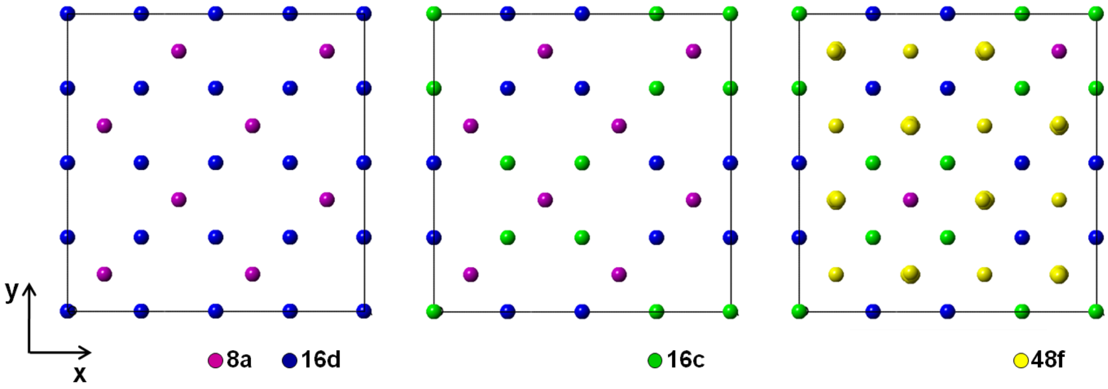

Figure 3.20 The arrangement of Ga atoms in the cubic $Fd\overline{3}m$ spinel model of γ-Ga_2O_3. Colours denote different Ga sites. Note that in these projections, the 16c and 48f sites obscure some of the 8a and 16d sites.

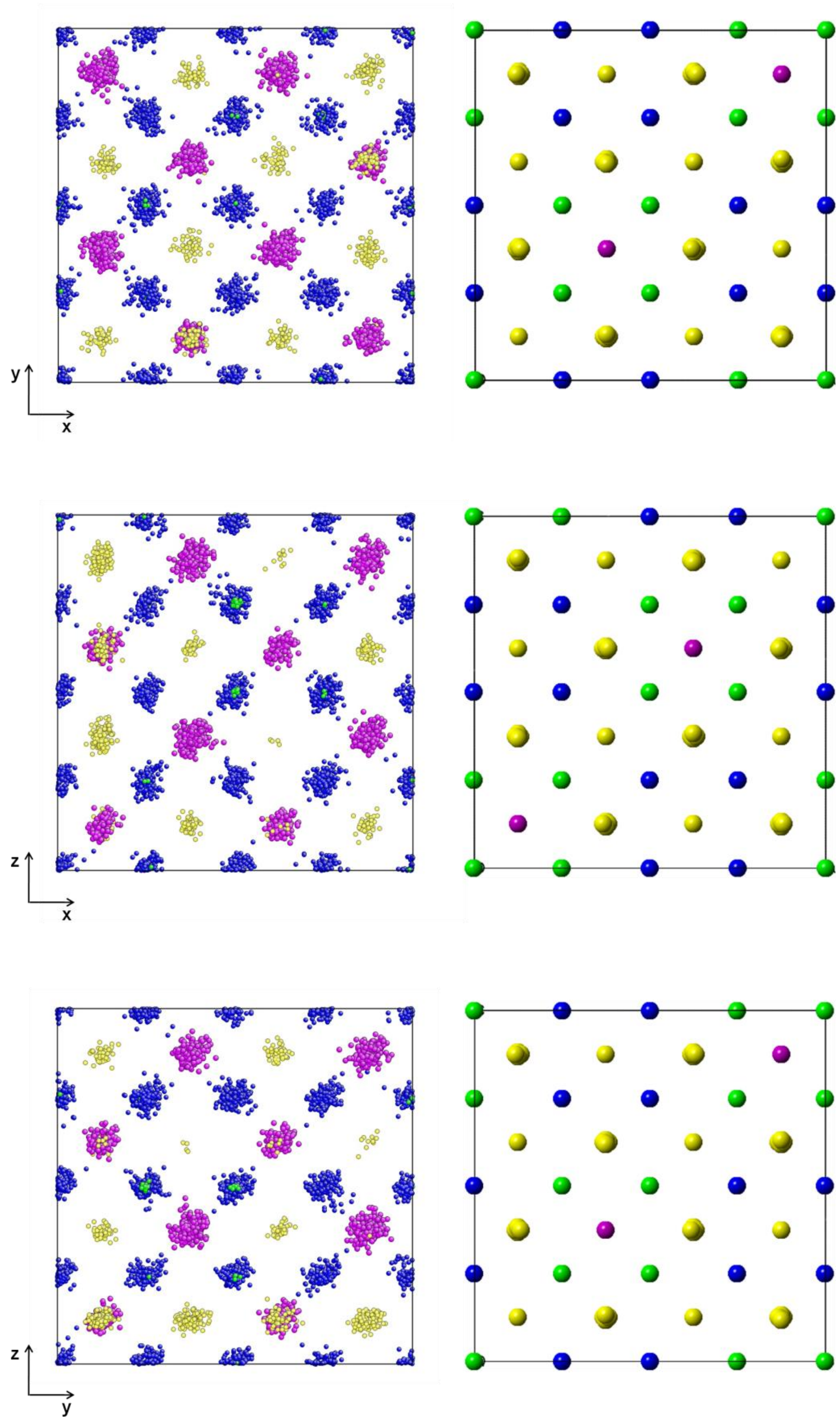

Figure 3.21 The results of RMC modelling for γ-Ga_2O_3. Collapsed RMC unit cells are shown on the left with the crystallographic model on the right for comparison. Colour conventions are as in Figure 3.20.

Sites on which only a few spheres are visible in the RMC configuration should be thought of as vacancies, and those with many spheres as occupied sites. Generally speaking, the occupied sites deviate very little from their crystallographic location, although interestingly the atoms on the spinel sites (8a and 16d) show a tendency to migrate towards each other. The 48f site "clouds" are far more compact. No vacancy ordering is apparent, although the fact that some sites are visibly (almost) vacant in the collapsed structure implies that these sites are preferentially vacant in most or all of the cells that make up the supercell.

The refined Ga–O partial functions are shown in Figure 3.22(a), and the partial functions from the starting configuration are shown in Figure 3.22(b). It can be seen that the O–Ga_{16d} partial $D(r)$ has refined from a single sharp peak at 2.0 Å to a rather asymmetric peak extending to much shorter r: as would be expected if the octahedra were distorted to produce a range of Ga–O bond lengths. This is independent confirmation of the validity of modelling the local structure with the non-centrosymmetric $F\bar{4}3m$ model (Section 3.3.2.3). Interestingly, while the Ga–O correlations arising from the tetrahedral sites (8a and 48f) remain fairly symmetrical, the bond lengths surrounding the 48f site have refined upwards, closer to those around the 8a site.

The results from RMC modelling are consistent with the conclusion that the defect spinel model with site occupancies as derived from Rietveld refinement can adequately describe the structure of the material at a range of length scales, provided that some means to relax the symmetry of the octahedral sites is provided.

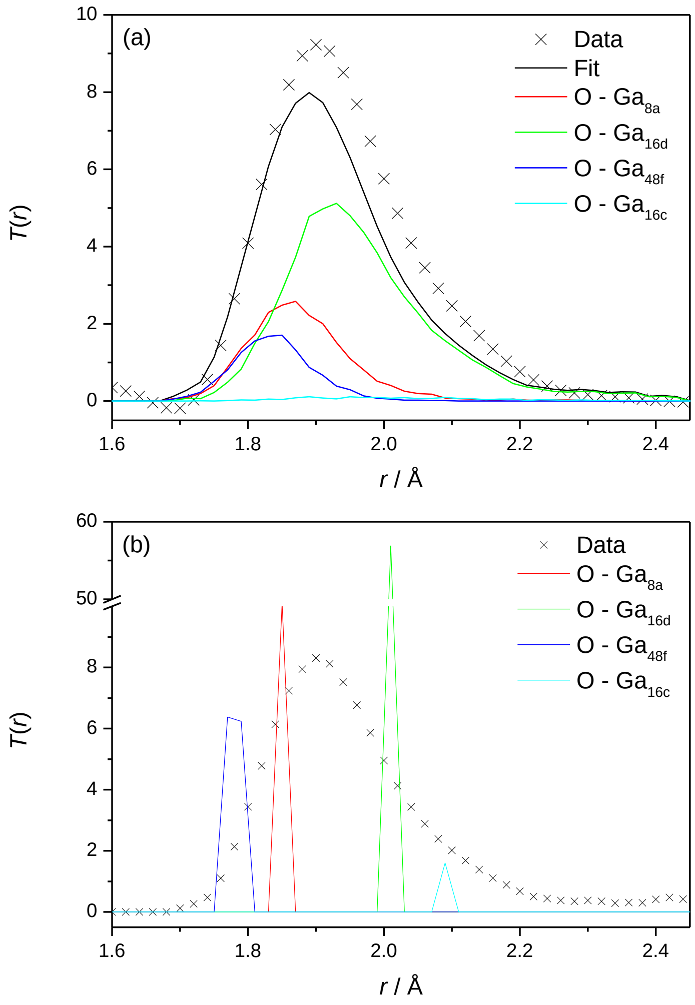

Figure 3.22 (a) Refined Ga–O partial correlation functions from RMC for γ-Ga_2O_3 and (b) the Ga–O partial functions from the starting configuration.

3.3.2.5. The structure of nanocrystalline γ-Ga_2O_3 from a short solvothermal reaction

A sample of γ-Ga_2O_3 prepared from the solvothermal reaction of gallium metal in DEA for 11 hours and with a approximate particle size of 13.7 nm determined by Scherrer analysis, was also examined using total neutron scattering.

The previously obtained structural model for the most crystalline γ-Ga_2O_3 was used as the starting model for Rietveld refinement and the results are shown in Figure 3.23 and Table 3.7.

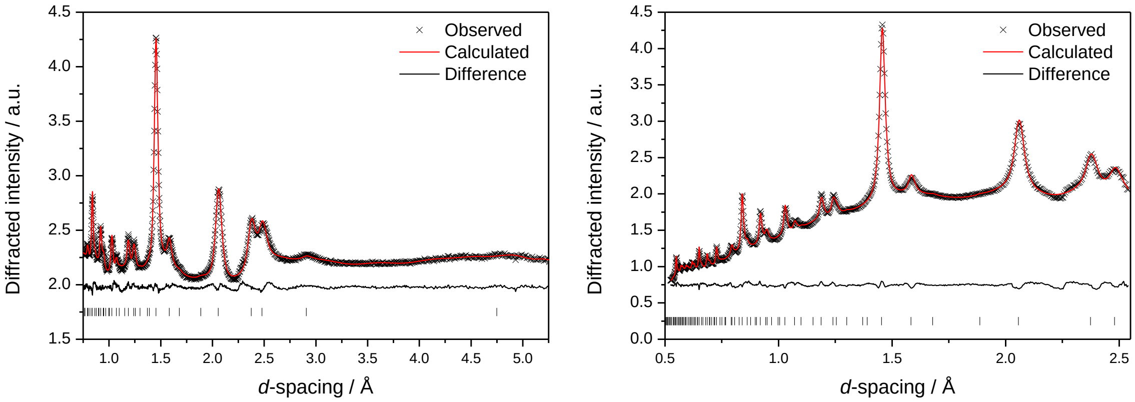

Figure 3.23 Result of Rietveld refinement for nanocrystalline solvothermal γ-Ga_2O_3. Left: data from GEM bank 3 (mean scattering angle 34.9°). Right: data from GEM bank 5 (mean scattering angle 91.3°).

Table 3.7 Crystal parameters from nanocrystalline, solvothermal γ-Ga_2O_3. Space group $Fd\bar{3}m$, a = 8.2240(2) Å. Rp = 0.66%, wRp = 0.92%.

Atom	**Wyckoff site**	**x**	**y**	**z**	**U_{iso} / $Å^2$**	**Occupancy**
Ga1	8a	0.125	0.125	0.125	0.0129(2)	0.54(2)
Ga2	16d	0.5	0.5	0.5	0.0129(2)	0.610(7)
Ga3	48f	0.348(1)	0.125	0.125	0.0129(2)	0.118(3)
Ga4	16c	0	0	0	0.0129(2)	0.100(6)
O	32e	0.251(3)	0.251(3)	0.251(3)	0.0135(1)	1

Rietveld refinement reveals that the ratio of octahedral: tetrahedral sites is 1.14:1 (1.35:1 in crystalline γ-Ga_2O_3) and the ratio of spinel:non-spinel sites is 1.94:1 (5:1 in crystalline γ-Ga_2O_3). Therefore, as well as having a slightly smaller lattice parameter, the average structure of nanocrystalline solvothermal γ-Ga_2O_3 has a different cation distribution, with a slightly higher proportion of Ga atoms on tetrahedral sites and, in general, more cations on non-spinel sites than its more crystalline counterpart. Also, the oxygen sublattice (defined by the O *x* coordinate) is closer to “perfect” close packing in the nanocrystalline sample. These differences emphasise the inherent flexibility and variability of the spinel structure.

The neutron PDF of nanocrystalline solvothermal γ-Ga_2O_3 reveals a feature at 1.49 Å (Figure 3.24) which is likely to arise from significant amounts of residual organic species on the surface of the particles, specifically C–C and C–N bonds (which in the crystalline form of the solvent, DEA, are 1.51 Å and 1.47 Å respectively). Both carbon and nitrogen are relatively strong scatterers of neutrons (coherent scattering lengths for C = 6.646 fm and N = 9.36 fm).

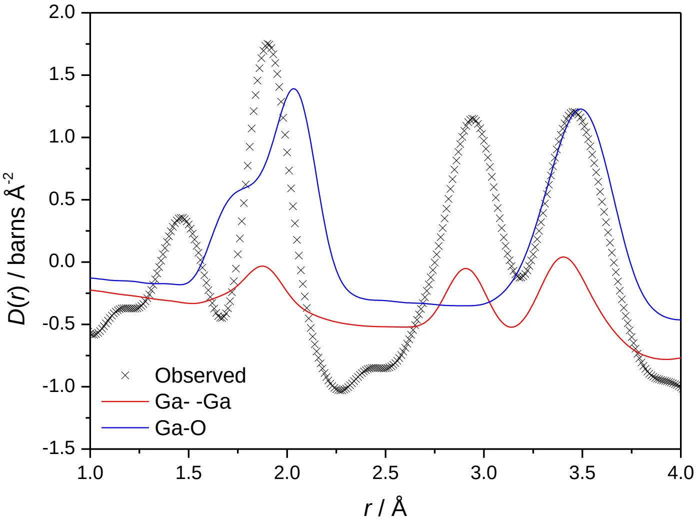

Figure 3.24 The measured PDF of nanocrystalline solvothermal γ-Ga_2O_3 with calculated Ga–O and Ga– –Ga partial functions. Also shown is the feature at 1.5 Å due to C–N and C–C bonds in the residual surface-associated organic species.

The presence of organic groups is also seen in the FT-IR spectrum of this material (Figure 3.25(b)) with peaks at ~1060 cm^{-1} due to C–O stretching and 1470 cm^{-1} due to C–H bending. These features agree well with those in the FT-IR spectrum of liquid DEA. The same features to a smaller extent are also present in the crystalline solvothermal sample, however in that case, the amount of organic residue was clearly below the detection limit of the neutron scattering experiment.

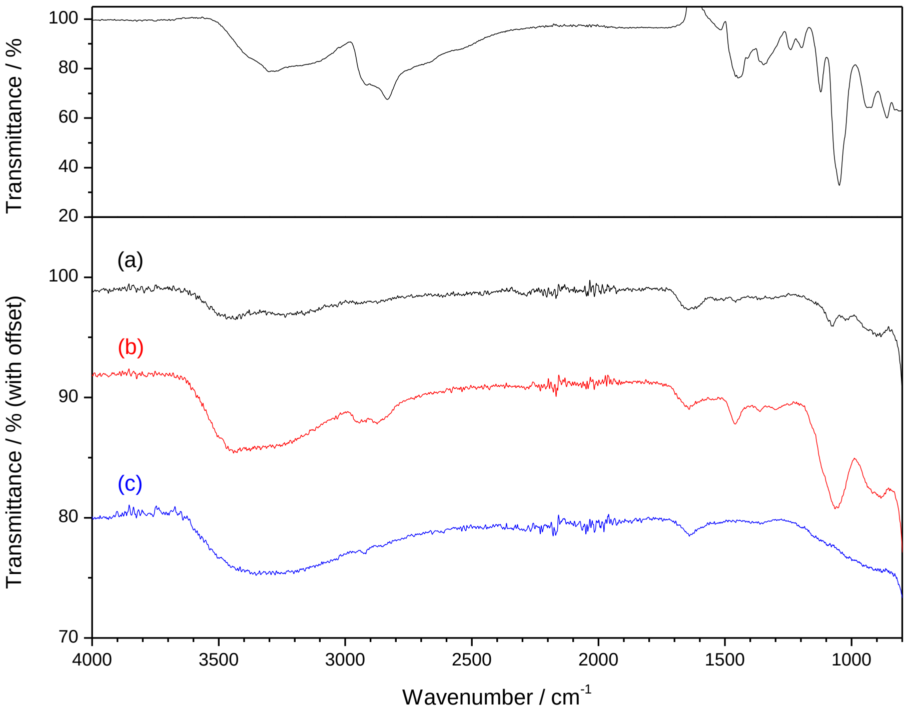

Figure 3.25 The FT-IR spectrum of liquid DEA (upper panel) compared with the spectra of (a) crystalline solvothermal γ-Ga_2O_3, (b) nanocrystalline solvothermal γ-Ga_2O_3 and (c) disordered precipitation method γ-Ga_2O_3.

The presence of a significant quantity of organic residue is supported by TGA which reveals a mass loss of ~10% coupled with an exothermic feature in the DSC trace at ~ 350 – 400 °C, (Figure 3.26)

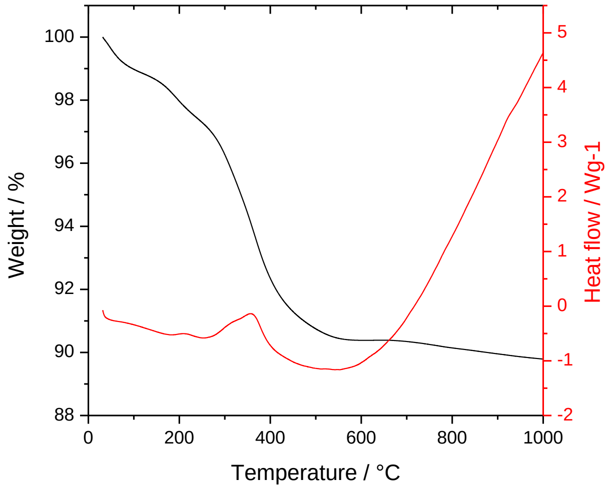

Figure 3.26 TGA/DSC result for nanocrystalline solvothermal γ-Ga_2O_3.

PDF analysis was attempted using the Rietveld model as a starting point. Due to the fairly large proportion of cations on non-spinel sites, the statistical model has a significant (though non-physical) Ga–Ga correlation at ~1.8 Å (Figure 3.24) and so to avoid bias, the first peak of the PDF was excluded from the fit. The result is shown in Figure 3.27.

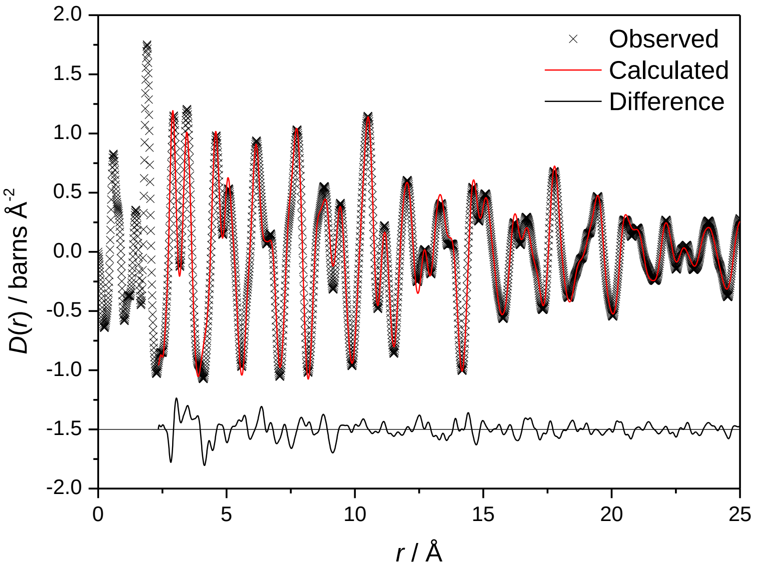

Figure 3.27 The result of PDF analysis using the Rietveld-derived structural model for nanocrystalline solvothermal γ-Ga_2O_3.

The contributions to the PDF of the surface-associated organic species are of course neglected in this fit, which would explain some of the discrepancies in the low-*r* region.

3.3.2.6. *The structure of γ-Ga_2O_3 made by the precipitation method*

As described in Section 3.3.2.1, γ-Ga_2O_3 prepared by the precipitation method exhibited smaller particle size and a larger proportion of surface water/hydroxyl groups than the solvothermal γ-Ga_2O_3.

Figure 3.28 shows the X-ray *i*(*Q*)s (measured using Ag radiation) for crystalline solvothermal γ-Ga_2O_3 and disordered precipitation-method γ-Ga_2O_3. Significant peak broadening is observed in the disordered sample, but otherwise the functions show good agreement, implying that they have the same average structure. Figure 3.29 shows the neutron *i*(*Q*)s for the same samples, and some differences in peak intensities in the region 1.0 – 2.5 Å^{-1} are observed. The (111), (220) and (311) (Q = 1.32, 2.16 and 2.53 Å^{-1} respectively) peaks are not visible in the disordered sample, and the (222) peak appears anomalously broadened and slightly shifted towards higher Q (see right hand panel of Figure 3.29). These changes in peak intensities suggest that the cation distribution in precipitation method γ-Ga_2O_3 is different to that in either the crystalline or nanocrystalline γ-Ga_2O_3. It is also possible that this sample contains structural hydrogen which creates a superstructure that is only visible in the neutron data; and/or that a hydrogen-containing impurity phase, with a strong diffraction peak at Q = 2.67 Å^{-1}, is present in addition to the γ-Ga_2O_3 phase.

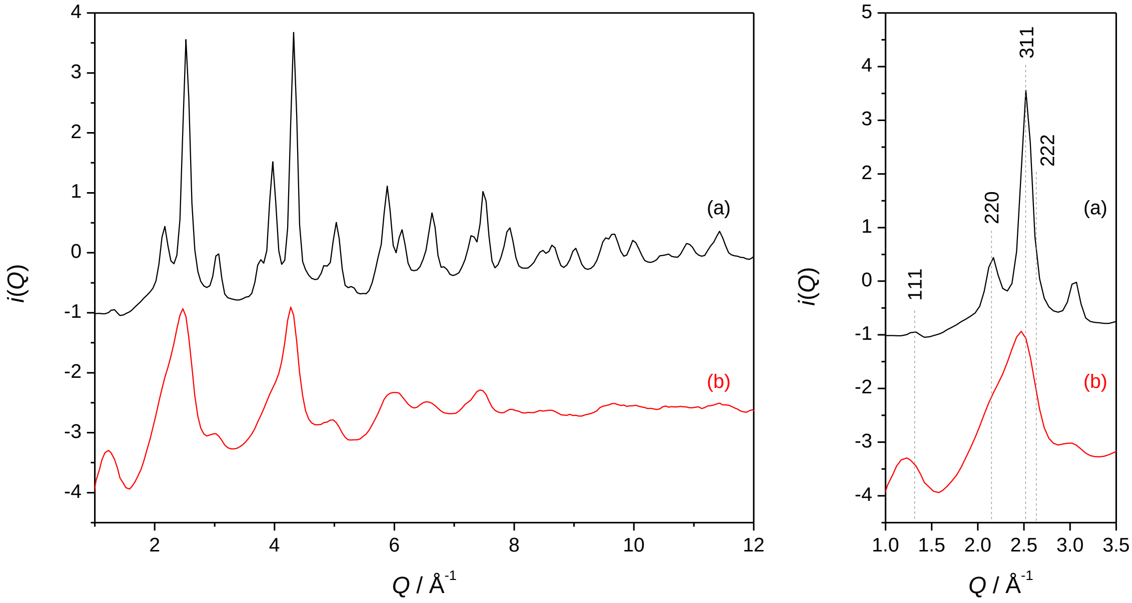

Figure 3.28 X-ray *i*(*Q*)s for (a) solvothermal γ-Ga_2O_3 and (b) disordered γ-Ga_2O_3 from the precipitation method. Left panel is full data range, right is close-up of low-*Q* region.

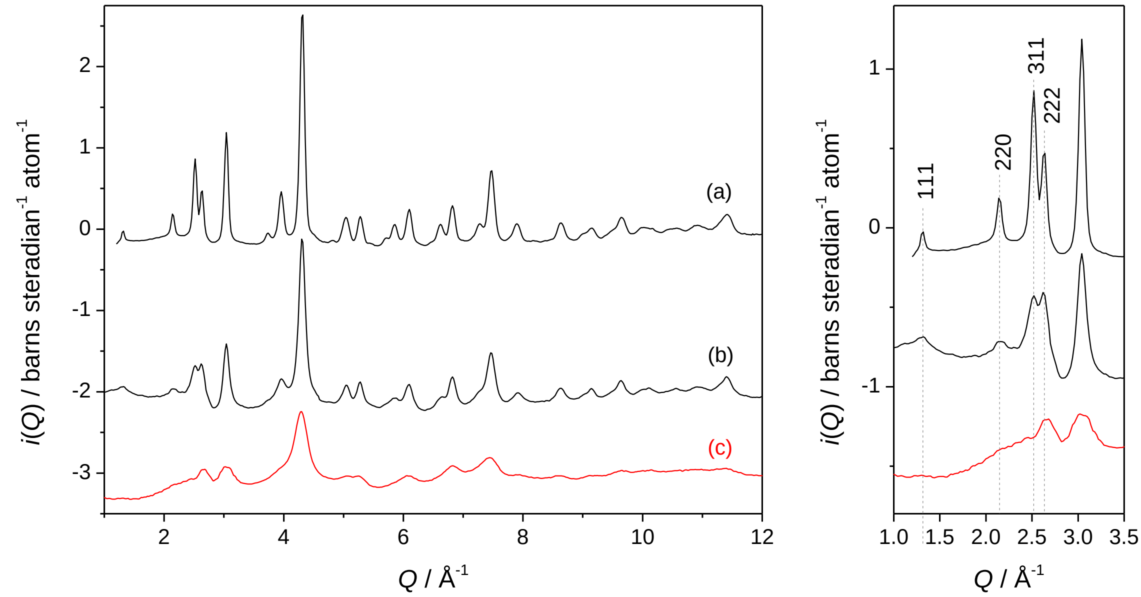

Figure 3.29 Neutron *i*(*Q*)s for (a) solvothermal γ-Ga_2O_3, (b) solvothermal γ-Ga_2O_3 with a smaller particle size from a shorter reaction and (c) disordered γ-Ga_2O_3 from the precipitation method. Left panel is full data range, right is close-up of low-*Q* region.

The Bragg peak intensities of the neutron diffraction pattern can be well matched using a modified spinel structure with an octahedral:tetrahedral ratio of 0.82:1 and a spinel:non spinel ratio of 0.51:1 which indicates that the trend seen going from crystalline to nanocrystalline solvothermal γ-Ga_2O_3 (*i.e.* an increase in the amount of tetrahedral gallium and increased occupancy of non-spinel sites) may well continue as the particle size further decreases (see Table 3.8 and Figure 3.30).

Table 3.8 The modified spinel model used to describe disordered γ-Ga_2O_3 made by the precipitation method.

Atom	$Fd\bar{3}m$ site	x	y	z	Occupancy
Ga1	8a	1/8	1/8	1/8	0.3
Ga2	8b	3/8	3/8	3/8	0.3
Ga3	16d	1/2	1/2	1/2	0.3
Ga4	16c	0	0	0	0.3
Ga5	48f	0.3679	1/8	1/8	0.1445
O	32e	0.2552	0.2552	0.2552	1

The neutron PDF from this model reproduces the measured PDF well if combined with a small amount (10% by mass) of a boehmite-like gallium oxyhydroxide phase which has solely octahedral Ga sites (Figure 3.30). Although the commonly reported GaOOH phase has the diaspore structure, a boehmite-like structure is plausible, particularly through analogy with the Al_2O_3 system where boehmite is a precursor to γ-Al_2O_3. In fact, a detailed PDF study revealed that remnants of the layered boehmite structure were present in γ-Al_2O_3, causing the local structure to deviate from the average spinel.[79] The presence of this impurity could account for the high water content of the material and the discrepancies between X-ray and neutron data. The strongest neutron diffraction peak from the proposed impurity phase occurs at ~ 2.7 $Å^{-1}$ and is therefore a possible explanation for the anomalously broad (222) spinel peak.

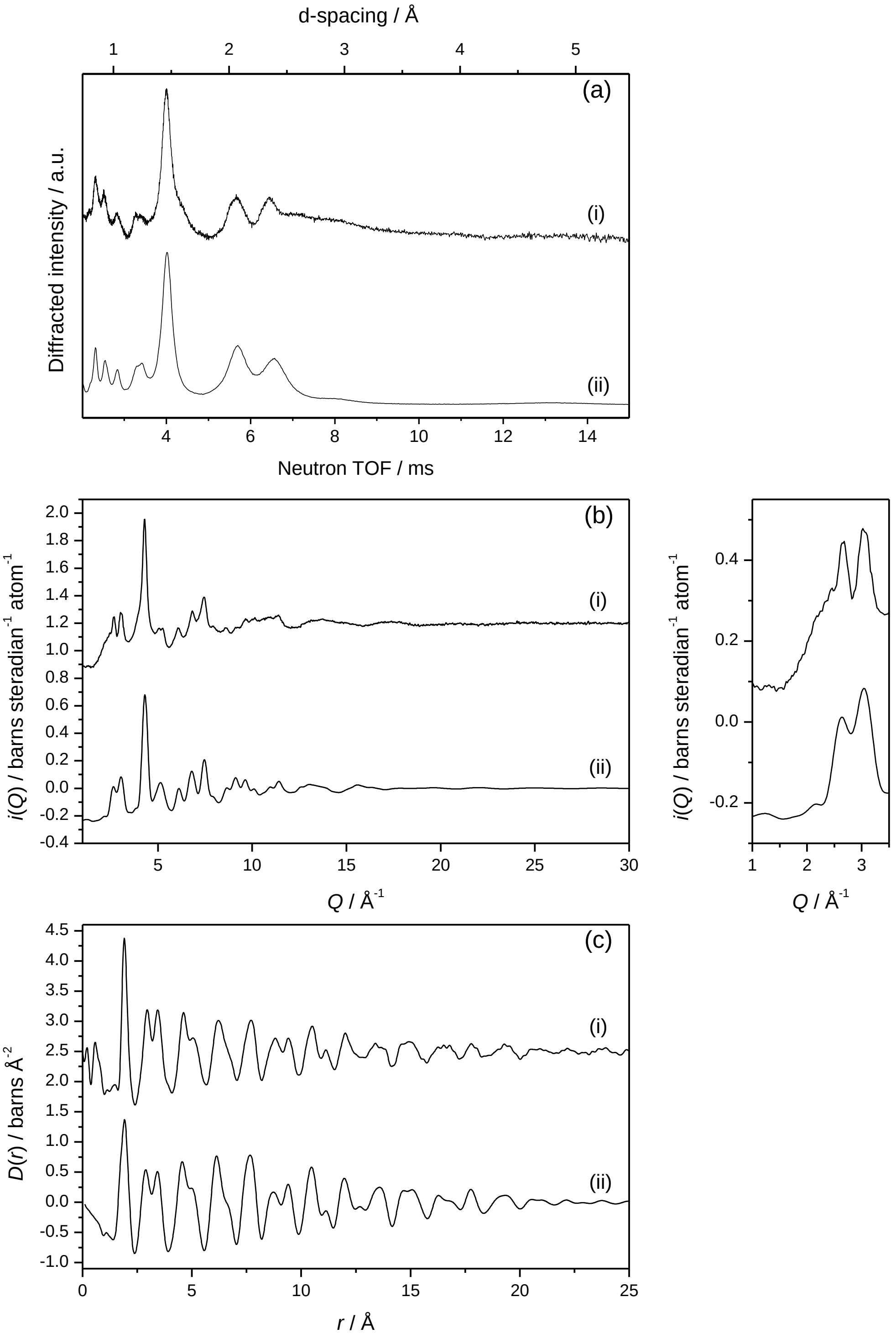

Figure 3.30 (a) A comparison of neutron diffraction data (GEM bank 3) from disordered γ-Ga_2O_3 (i) with the simulated and broadened pattern from the modified spinel model (ii). (b) A comparison of the neutron *i*(*Q*) from disordered γ-Ga_2O_3 (i) with the *i*(*Q*) simulated for the modified spinel model, adjusted for small particle size (diameter 20 Å) using a Mason factor (ii). (c) A comparison of the measured neutron PDF from disordered γ-Ga_2O_3 (i) with the simulated PDF from a mixture of the modified spinel model (90%) and a boehmite-like GaOOH phase (10%) (ii).

3.3.3. *Epsilon-Ga_2O_3*

3.3.3.1. General characterisation

Thermal decomposition of $Ga(NO_3)_3.9H_2O$ at 220 °C in air produces a poorly crystalline material, designated δ-Ga_2O_3, which will be discussed subsequently in Section 3.3.4. Prolonged heating of this material at 400 °C (14 days) produces a more crystalline phase which is herein designated ε-Ga_2O_3 according to Roy's original scheme,[1] (see Section 3.2.1.5). This material undergoes phase transformation to β-Ga_2O_3 at temperatures in excess of 600 °C, however as can be seen from the contour plot in Figure 3.31, a transient intermediate phase is also present at temperatures between 600 – 850 °C (peaks from this phase are marked with arrows). This intermediate phase is discussed further in Section 3.3.6.

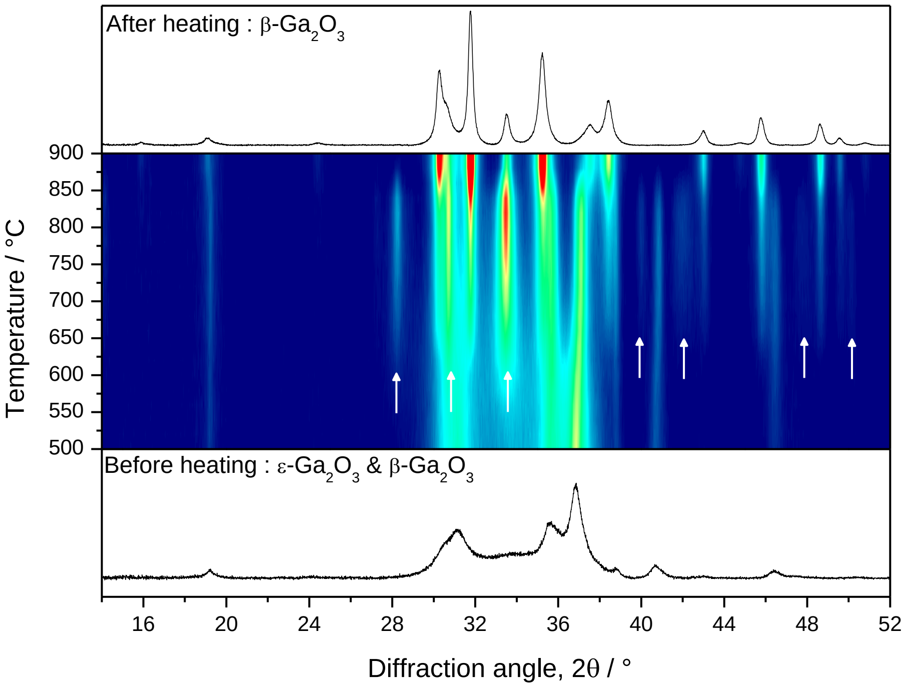

Figure 3.31 Thermodiffraction of ε-Ga_2O_3. An intermediate phase is formed during the heating process which can be seen *via* peaks at 28, 39, 42. 48 and 50° appearing and then disappearing, and the intensity of the peaks at ~31 and 34° increasing and then decreasing between 625 – 850 °C.

TEM imaging of ε-Ga_2O_3 reveals that the material consists of aggregated oblong-shaped particles (Figure 3.32).

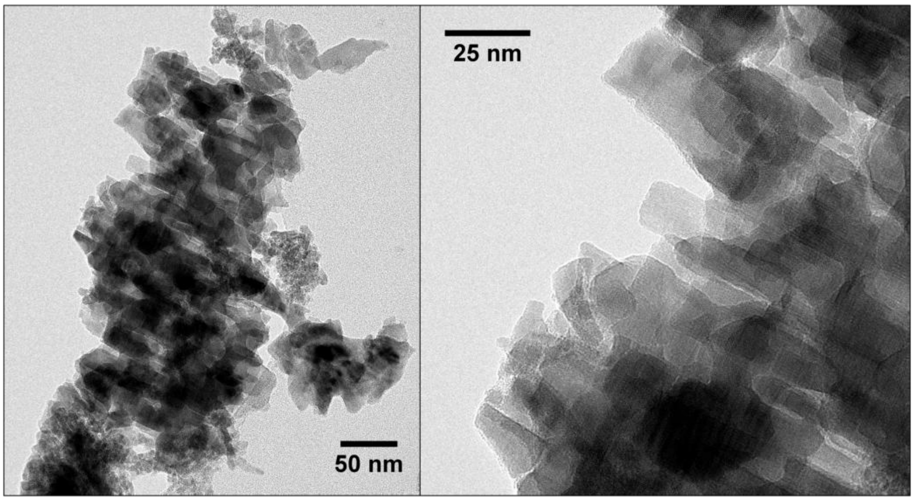

Figure 3.32 TEM images of ε-Ga_2O_3.

3.3.3.2. *Rietveld refinement*

The first report of ε-Ga_2O_3 by Roy *et al.*[1] did not suggest a space group or indeed any structural parameters for this polymorph, although apparent isomorphism with κ-Al_2O_3 was later suggested by the same authors.[2] The structure of ε-Ga_2O_3 was recently simulated using density functional theory (DFT) in the space group $Pna2_1$ (the same as for κ-Al_2O_3 and ε-Fe_2O_3) by Yoshioka,[5] but no other structural characterisation has been reported. Therefore, the structure of orthorhombic ε-Fe_2O_3 was chosen as the initial starting model for structural analysis of ε-Ga_2O_3.

Figure 3.33 shows the powder XRD pattern for ε-Ga_2O_3. The simulated pattern from the initial structural model has only superficial similarity.

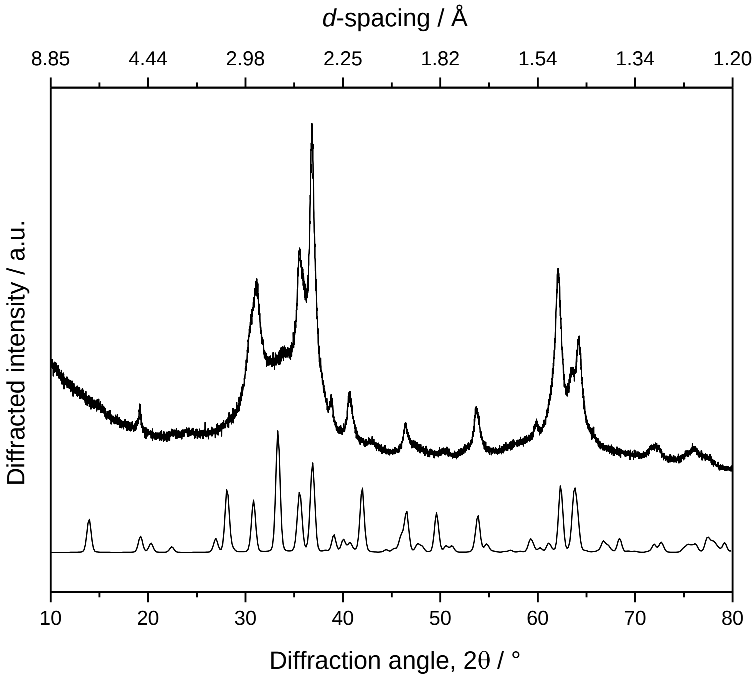

Figure 3.33 The measured XRD pattern for ε-Ga_2O_3 with the simulated pattern from the orthorhombic κ-Al_2O_3/ε-Fe_2O_3 model.

Figure 3.34 shows the results of a Le Bail profile refinement of neutron diffraction data, used to determine potential unit cell dimensions and to evaluate the suitability of the chosen space group. There are significant discrepancies in the region 2.3 – 3 Å suggesting that this spacegroup is not appropriate and confirming that the structural model is not correct.

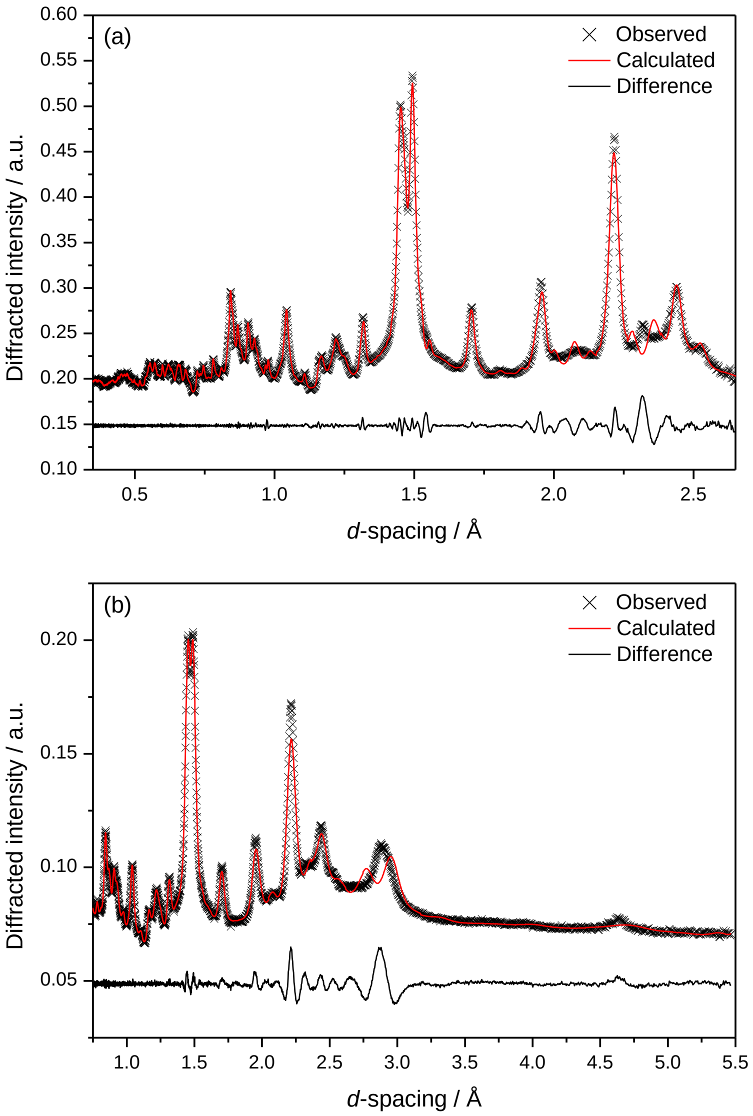

Figure 3.34 The results of a Le Bail profile refinement for ε-Ga_2O_3 using space group *Pna*2_1 and with *a* = 5.1306(4) Å, *b* = 8.6812(4) Å and *c* = 9.4006(7) Å. Plots shown are from two different GEM banks, (a) bank 5 (average scattering angle 91.3 °) and (b) bank 3 (average scattering angle 34.9 °).

A search of the literature for a structural model that better fits the observed pattern revealed that in 1998 Tronc *et al.* published a study of ε-Fe_2O_3 that identified a disordered variation of the polymorph, with hexagonal symmetry, but based on a close-packed array of oxide ions with partial filling of 2 tetrahedral and 2 octahedral sites.[24]

The structure generated from the coordinates presented in the paper by Tronc *et al.* is shown in Figure 3.35. One Ga atom appears to be overlapping an oxygen and a neighbouring Ga, which is clearly the result of a typographical error and can be easily corrected by swapping the *x* and *y* coordinates of the Ga 4 site shown in dark green in Figure 3.35.

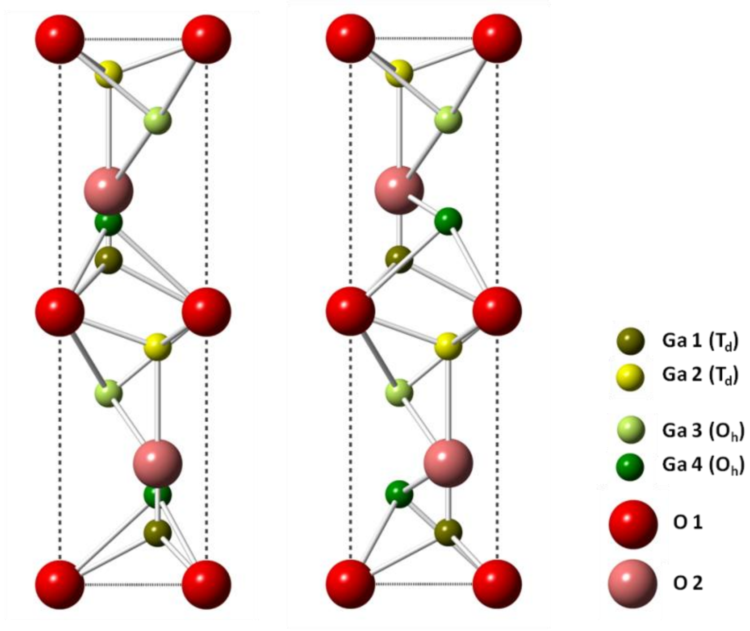

Figure 3.35 The structure of hexagonal ε-Fe_2O_3 as stated by Tronc *et al.*[24] (Left) and the structure after correcting the *x* and *y* coordinates of the Ga atom overlapping the O. (Right).

Once the structure is corrected, hexagonal ε-Fe_2O_3 is an excellent candidate structural model for ε-Ga_2O_3, if the reasonable assumption that β-Ga_2O_3 (which is always produced by prolonged heating) is also present, is made (Figure 3.36). The coincidence of the Bragg peak positions from a “hexagonal ε” plus β mixture with those from the orthorhombic epsilon phase illustrates the ease with which the data can be misinterpreted (and indeed have been in the literature), although the absence of a large peak at $2\theta \approx 28°$ and the low intensity of the peak at $2\theta \approx 33°$ represent the obvious discrepancies.

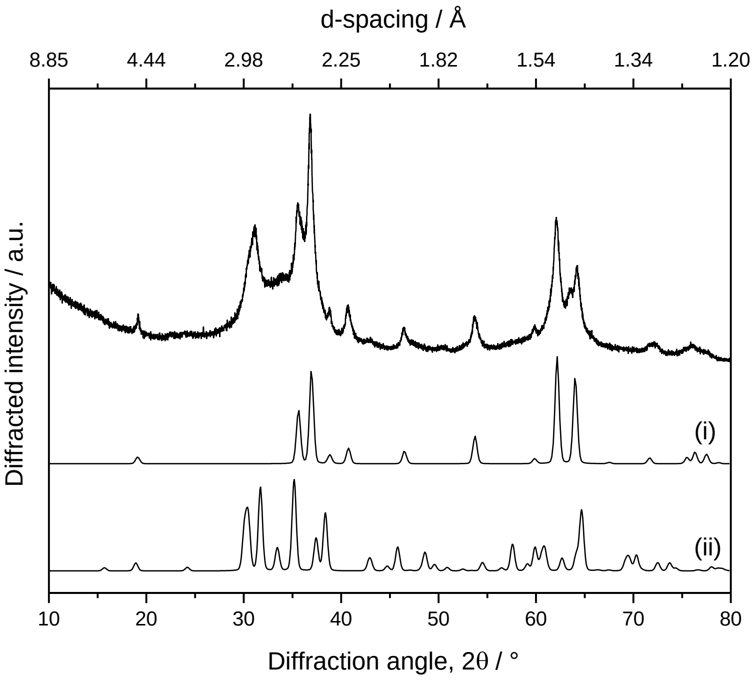

Figure 3.36 The measured XRD pattern for ε-Ga_2O_3 with the simulated pattern from (i) the hexagonal ε-Fe_2O_3 model and (ii) β-Ga_2O_3.

The result of Rietveld refinement of the neutron data using this two-phase structural model is shown in Figure 3.37 and Table 3.9. It should be noted that the occupancy of the second tetrahedral metal site refined to zero in the initial stages of the refinement and the site was thus removed from the model.

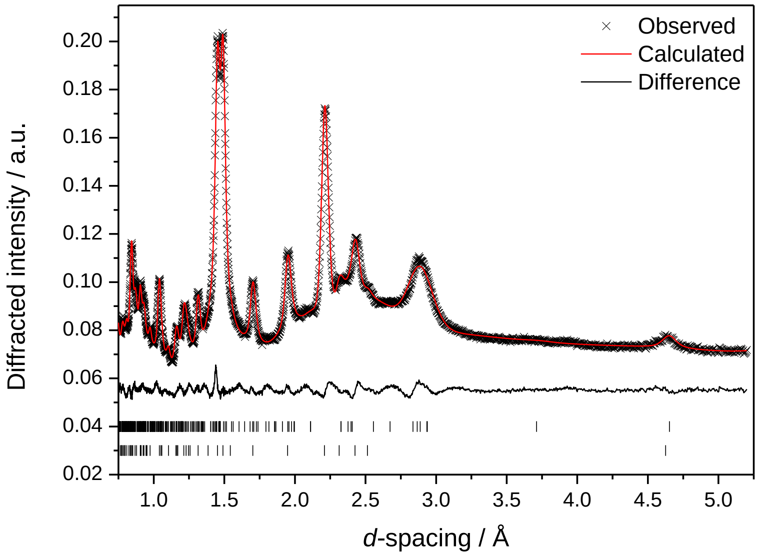

Figure 3.37 The result of Rietveld refinement for ε-Ga_2O_3 using two phases (hexagonal "ε-Fe_2O_3" model and β-Ga_2O_3). Phase fractions are ε = 54.43(5)% , β = 45.57(6)%. The data are from GEM bank 3 (mean scattering angle 34.9°).

Table 3.9 Refined crystal parameters for ε-Ga_2O_3 from Rietveld refinement. Space group *P*6_3*mc*. *a* = 2.9036(2) Å, *c* = 9.2554(9) Å, wRp = 1.48%.

Atom	**Wyckoff Site**	**x**	**y**	**z**	**U_{iso} / $Å^2$**	**Occupancy**
Ga1	2b	1/3	2/3	0.5598(6)	0.0044(2)	0.423(3)
Ga3	2b	2/3	1/3	0.6538(5)	0.0044(2)	0.399(2)
Ga4	2b	1/3	2/3	0.3705(4)	0.0044(2)	0.511(3)
O1	2a	0	0	-0.0016(6)	0.0091(2)	1
O2	2b	1/3	2/3	0.7556(6)	0.0091(2)	1

The calculated density of the appropriate fractions of the ε and β structures is 6.0622 gcm^{-3} which is in reasonable agreement with the measured density of 5.4770 gcm^{-3}.

3.3.3.3. PDF analysis

The results of PDF analysis using the Rietveld structure as a starting point are shown in Figure 3.38 and Table 3.10. Some refinement of the ε-Ga_2O_3 structure was necessary to obtain a good fit, and the PDF-refined structure exhibits more distorted octahedral environments and a less distorted tetrahedral environment than the Rietveld structure (see Table 3.11).

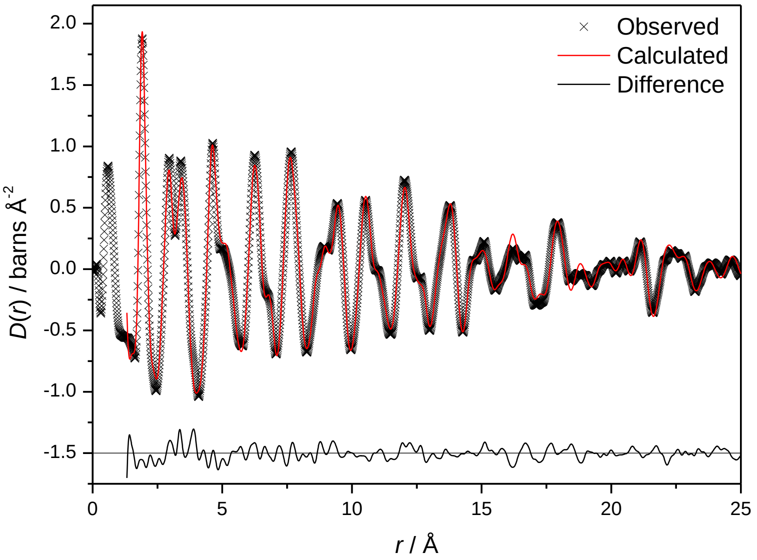

Figure 3.38 The result of PDF refinement of ε-Ga_2O_3 using the Rietveld model as a starting point. Phase fractions are ε = 57.05(5)%, β = 42.95(5)%.

Table 3.10 Refined crystal parameters for ε-Ga_2O_3 from PDF analysis. Space group *$P6_3mc$*. *a* = 2.90726(5) Å, *c* = 9.2559(3) Å, wRp = 12.7%

Atom	**Wyckoff Site**	**x**	**y**	**z**	**U_{iso} / Å^2**	**S.O.F**
Ga1	2b	1/3	2/3	0.5622(2)	0.01382(3)	0.3701(7)
Ga3	2b	2/3	1/3	0.65568(9)	0.01382(3)	0.322(2)
Ga4	2b	1/3	2/3	0.36433(5)	0.01382(3)	0.641(2)
O1	2a	0	0	0.99915(7)	0.01433(3)	1
O2	2b	1/3	2/3	0.75599(8)	0.01433(3)	1

Table 3.11 Comparison of Ga–O bond lengths in the Rietveld and PDF models for ε-Ga_2O_3.

	Rietveld model / Å	**PDF model / Å**
Ga1	3 × 1.769	3 × 1.774
	1 × 1.812	3 × 1.793
Ga2	3 × 1.922	3 × 1.916
	3 × 2.208	3 × 2.215
Ga3	3 × 1.984	3 × 1.953
	3 × 2.052	3 × 2.089

It will be noted that the fit is very good in the low-*r* region, which suggests that the local structure is well represented by the average structure. The hexagonal ε-Ga_2O_3 structural model has two octahedral sites which are significantly distorted similarly to those in α- and β-Ga_2O_3, which means that a further local distortion as observed in γ-Ga_2O_3 is not necessary.

Similarly to γ-Ga_2O_3, there are multiple partially occupied Ga sites in ε-Ga_2O_3, and due to their proximity (distance Ga1–Ga2 = 1.89 Å, Ga1–Ga3 = 1.75 Å and Ga2–Ga3 = 2.01 Å), non-statistical occupancy must be observed, again, similarly to γ-Ga_2O_3. However, since all of the sites have less than 50% occupancy, the distribution is likely to be far less complex than that in γ-Ga_2O_3 and no further modelling has been carried out.

3.3.4. *Delta-Ga_2O_3*

3.3.4.1. General characterisation

As mentioned in the preceding section, the product of thermal decomposition of $Ga(NO_3)_3.9H_2O$ at 220 °C in air is a poorly crystalline material, which herein is designated “δ-Ga_2O_3”. This material transforms readily and cleanly to β-Ga_2O_3 on heating, as seen in the *in situ* powder XRD shown in Figure 3.39. There is no evidence that any intermediate phase is formed during heating.

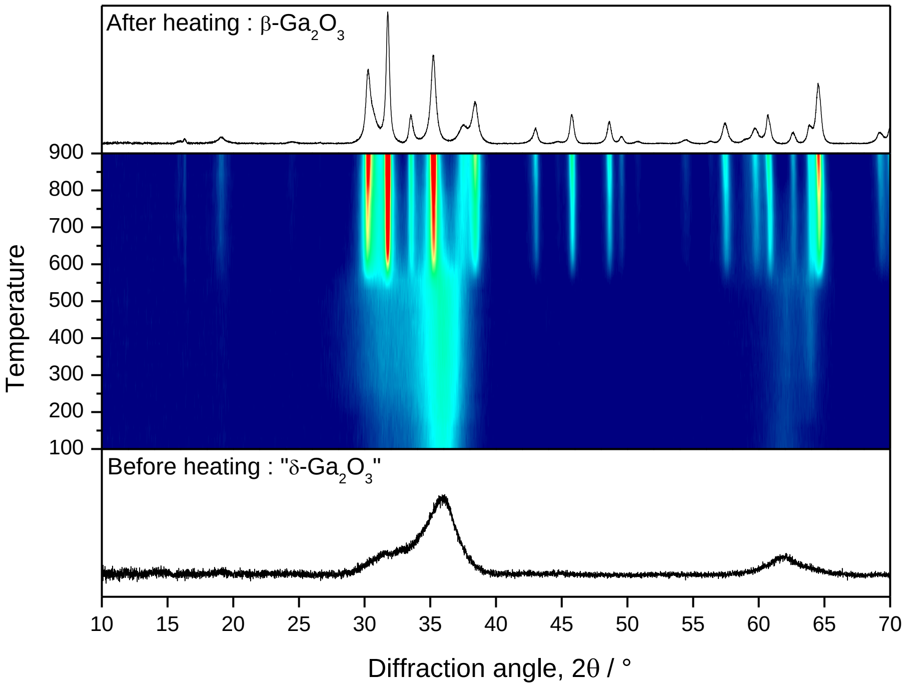

Figure 3.39 Thermodiffraction of “δ-Ga_2O_3”. It can be seen that the peaks due to β-Ga_2O_3 appear cleanly at around 550 °C.

TEM imaging of “δ-Ga_2O_3” reveals agglomerated crystalline nanoparticles (30 - 50 nm) surrounded by an apparently amorphous layer of much lower density (Figure 3.40).

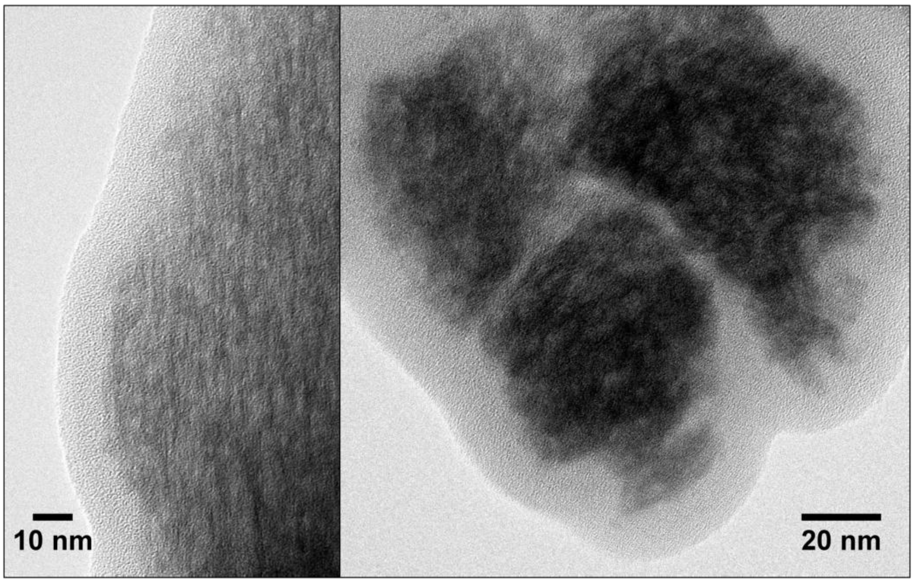

Figure 3.40 TEM images of "δ-Ga_2O_3"

3.3.4.2. In situ neutron diffraction

For the poorly crystalline material referred to as "δ-Ga_2O_3", the initial product of thermal decomposition of $Ga(NO_3)_3.9H_2O$, Roy proposed the bixbyite structure. Often referred to as the "C-type rare earth" structure, it is body centred cubic and has the space group $Ia\overline{3}$. It is a known structure for various M_2O_3 oxides, such as In_2O_3 and Mn_2O_3, and contains solely octahedral metal sites. Figure 3.41(a) shows a comparison of the XRD of "δ-Ga_2O_3" with a simulated pattern for bixbyite Ga_2O_3, and it is clear that the structural assignment is not correct. In fact, the original indexing of "δ-Ga_2O_3" was incorrect with a peak assigned to *hkl* indices (511), forbidden in an *I*-centred lattice.

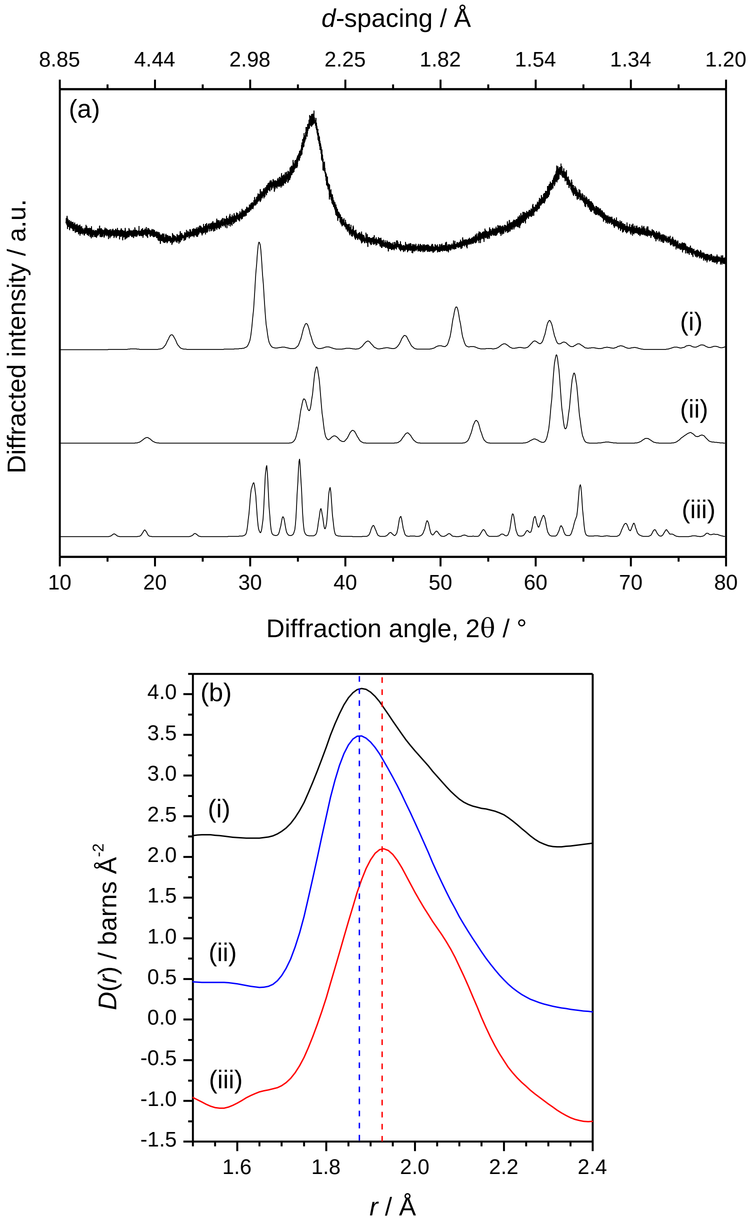

Figure 3.41 (a) The powder XRD pattern of "δ-Ga_2O_3" with the simulated patterns for (i) bixbyite model based on the structure of Mn_2O_3 with Mn replaced by Ga and the lattice parameter adjusted to give the closest match, (ii) hexagonal ε-Ga_2O_3 model and (iii) β-Ga_2O_3. (b) The first peaks from the neutron PDFs of (i) "δ-Ga_2O_3", (ii) β-Ga_2O_3 and (iii) α-Ga_2O_3 after Fourier transformation with a Q_{max} = 50 Å^{-1}. The dotted lines show the different positions of the peak maxima, at ~1.92 Å for α-Ga_2O_3 and ~1.87 Å for δ- and β-Ga_2O_3.

Figure 3.41(b) shows the first peaks of the PDFs from α-, β- and "δ"-Ga_2O_3. The bixbyite structure, like α-Ga_2O_3, contains solely octahedral metal sites, however, the

Ga–O bonding in “delta” is more like that in β-Ga_2O_3, which suggests that a model with a mixture of tetrahedral and octahedral sites is required.

It should also be noted from Figure 3.41(a) that the broad peaks of “δ-Ga_2O_3” match well with those from the hexagonal ε-Ga_2O_3. That “δ-Ga_2O_3” could be a nanocrystalline modification of ε-Ga_2O_3, rather than a distinct polymorph, was identified as a clear possibility and this was examined using *in situ* neutron total scattering. A sample of “δ-Ga_2O_3” produced from $Ga(NO_3)_3.9D_2O$ was heated in stages first to 400 °C and then to 700 °C while data were collected repeatedly in runs of approximately 90 minutes each. Upon examination, datasets with no visible differences were combined to provide composite datasets of higher statistical quality for Fourier transformation to produce the PDFs.

The PDF measured for the sample at room temperature clearly exhibits peaks at r = 1.0 and 1.2 Å which can be assigned to O–D and N=O bonds (Figure 3.42) thus providing evidence that the decomposition of the gallium nitrate was not complete. The amorphous layer visible in the TEM images (Figure 3.40) is presumably the location of the residual nitrate and hydrate material. The PDF for the sample measured at 400 °C is unchanged other than the disappearance of these peaks, and hence was considered the “ideal” sample of “δ-Ga_2O_3” for further analysis. The heating data show a gradual evolution from “δ-Ga_2O_3” to β-Ga_2O_3 with no evidence for a distinct intermediate phase.

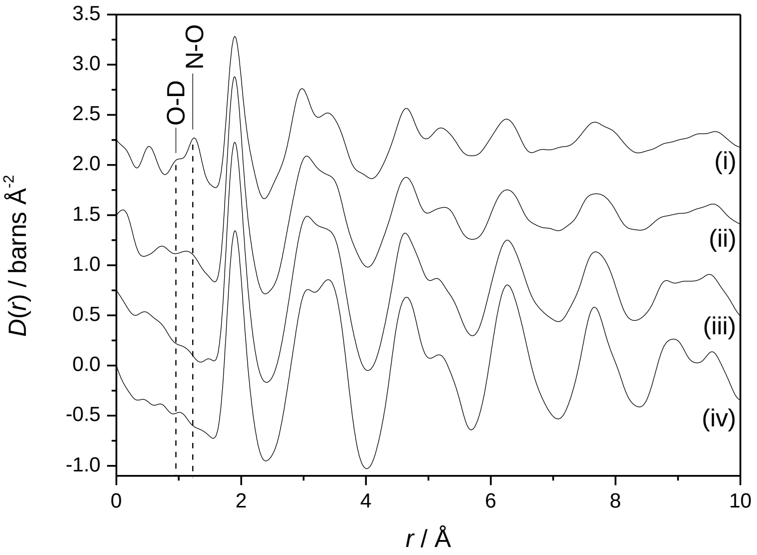

Figure 3.42 The PDFs measured during heating of “δ-Ga_2O_3” at (i) room temperature, (ii) 400 °C, (iii) 600 °C and (iv) 700 °C.

Due to the extremely small particle size of the samples, as evidenced by TEM as well as by the broadness of the Bragg peaks, Rietveld refinement was not possible. Instead, the data were modelled *via* comparison with simulated $i(Q)$ functions which were derived from simulated radial distribution functions that were altered for the effects of small particle size using a Mason factor, assuming a simple spherical particle.

The Mason factor,[80] is a correction factor which is applied when calculating a radial distribution function from a finite sized packing of hard spheres, to account for the fact that some of the spheres (*i.e.* those nearer the edge of the packing) have incomplete shells of neighbours.

The results of modelling the data obtained from the *in situ* neutron diffraction of “δ-Ga_2O_3” are shown in Figure 3.43. Modelling the data at all temperatures required simulated $i(Q)$ from a two-phase mixture of hexagonal ε-Ga_2O_3 and β-Ga_2O_3, however the proportion of β-Ga_2O_3 increased at higher temperatures. The data at 700 °C were recreated well with a mixture of 80% β-Ga_2O_3 and 20% ε-Ga_2O_3, both with a particle size of 60 Å (6 nm) and the data at 600 °C required a mixture of 75% β-Ga_2O_3 (25 Å) and 25% ε-Ga_2O_3 (50 Å). The data collected at 400 °C, the first temperature at which the sample did not obviously contain the residual nitrate and hydrate, required a mixture of 60% β-Ga_2O_3 (22 Å) and 40% ε-Ga_2O_3 (30 Å). Note that the particle sizes of both constituent phases appear to increase with temperature, which is physically reasonable.

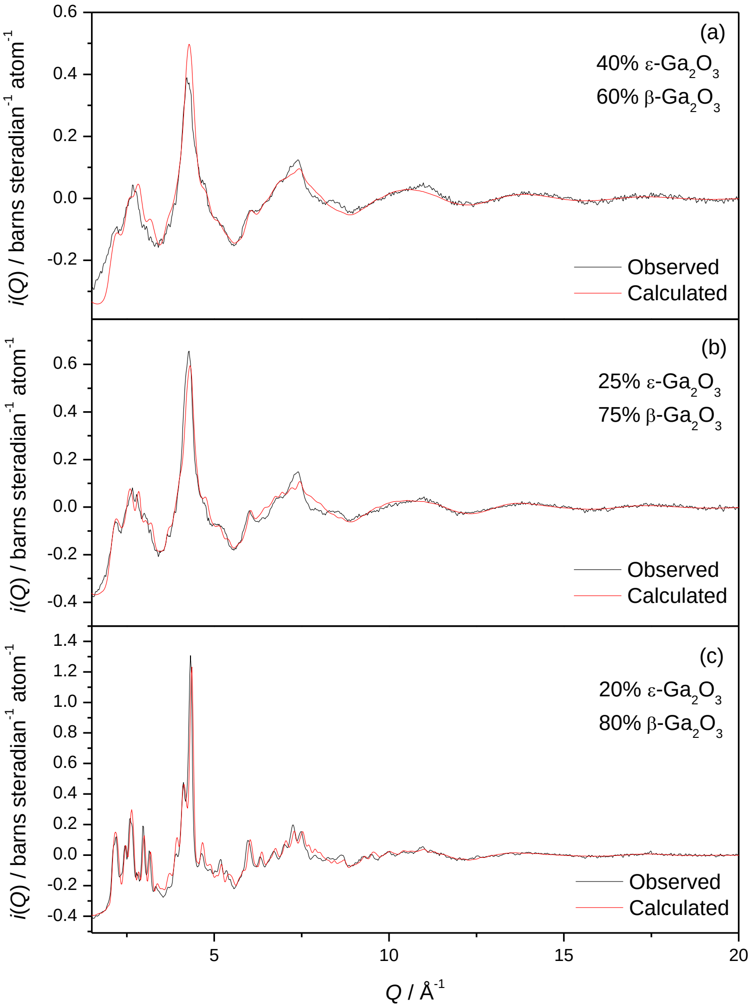

Figure 3.43 The fitting of the neutron total scattering data measured during heating of "δ-Ga_2O_3" at (a) 400 °C, (b) 600 °C and (c) 700 °C using *i*(*Q*) simulated from a two-phase mixture of ε-Ga_2O_3 and β-Ga_2O_3 and modified for the effects of small particle size using a Mason factor.

It should be noted that the modelling procedure does not account for the thermal expansion of the component phases and thus a slight discrepancy in peak position is observed between the observed and calculated $i(Q)$. The results of the fitting procedure imply that the presence of β-Ga_2O_3 is unavoidable during the thermal decomposition of $Ga(NO_3)_3.9D_2O$. The total neutron scattering data support the conclusion that δ-Ga_2O_3 is a nanocrystalline modification of ε-Ga_2O_3.

3.3.5. A novel gallium oxyhydroxide

3.3.5.1. General characterisation

The solvothermal oxidation of gallium metal in DEA, when allowed to continue for longer than the 72 hours found to be optimal for the production of crystalline γ-Ga_2O_3, produced a novel, highly crystalline material whose powder XRD pattern resembled that of a hydrated aluminium oxide, $Al_2O_3.1/5H_2O$, known as tohdite and also sometimes referred to by its mineral name, akdalaite.[81-84]

TGA of Ga-tohdite (Figure 3.44) revealed a mass loss of 2.5%, which is consistent with the formula $Ga_2O_3.1/5H_2O$ (expected mass loss on conversion to Ga_2O_3 = ~1.9%), however this formula is misleading, as the structure contains a terminal –OH moeity rather than H_2O (see below). As such, the alternative formula $Ga_5O_7(OH)$ is proposed to avoid confusion and more accurately represent Ga-tohdite as an oxyhydroxide, rather than a hydrate.

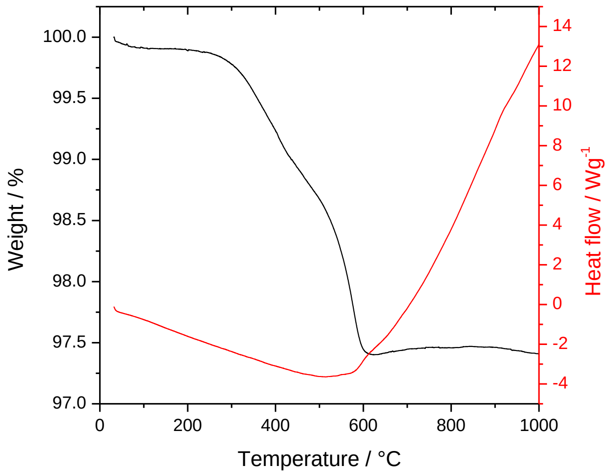

Figure 3.44 TGA/DSC trace of Ga-tohdite.

FT-IR spectroscopy, as shown in Figure 3.45, revealed a peak at 3300 cm^{-1} consistent with an OH stretching mode and a peak at 770 cm^{-1} which can be assigned to a Ga–O–H bending mode.[85] This spectrum is quite distinct from that of γ-Ga_2O_3 (Figure 3.25) which exhibits a broad band in the region 3500 – 3000 cm^{-1} due to the presence of water or hydroxyl groups on the surface.

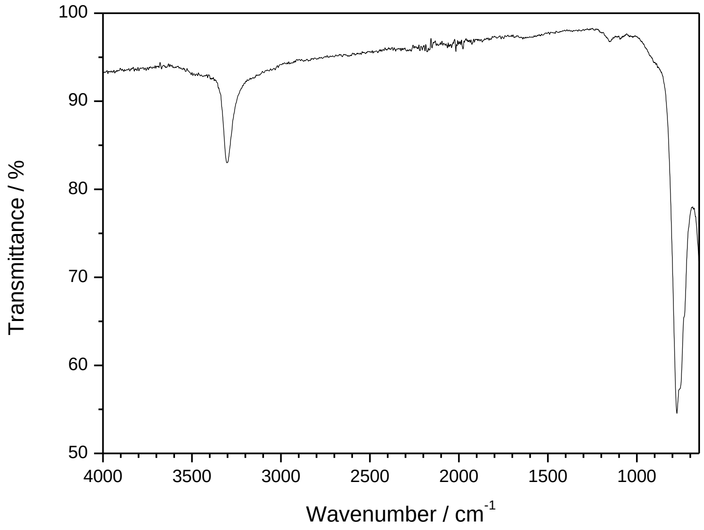

Figure 3.45 FT-IR spectrum of Ga-tohdite.

SEM and TEM microscopy revealed that $Ga_5O_7(OH)$ forms thin, roughly hexagonal, micron-sized plates. Dark field imaging reveals that the plates do not appear to be isolated single crystals, and the unusual patterns of the bright areas in the image (see Figure 3.46 (d)) could be evidence for significant strain in the particles.

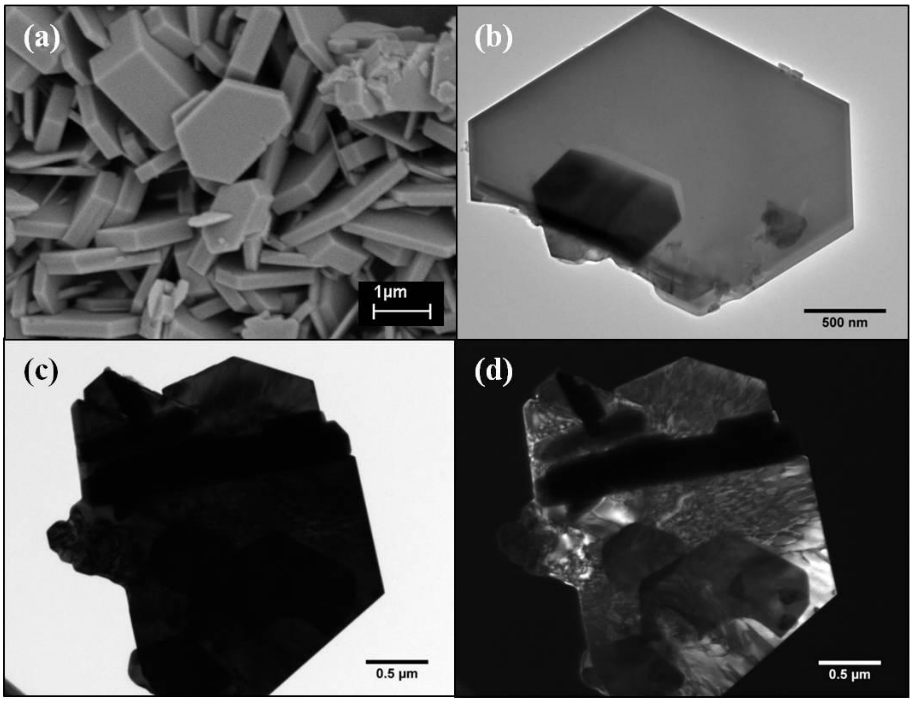

Figure 3.46 SEM (a) and TEM (b)-(d) microscopy of Ga-tohdite. (c) and (d) are bright and dark-field images of the same particle.

3.3.5.2. Neutron diffraction

Powder neutron diffraction data for Ga-tohdite were used for Rietveld refinement. The structure of Al-tohdite (refined from powder X-ray diffraction data) was used as a starting model.[83] Some small impurity peaks were identified as belonging to γ-Ga_2O_3, which was therefore included as a secondary phase. After the refinement had converged, an attempt was made to locate the hydrogen atoms using a Fourier difference map. The results are shown in Figure 3.47 and Table 3.12. The hydrogen atom is located off-centre in a vacant octahedral site closely associated with one of the surrounding oxygen atoms and with an O–H bond length of approximately 1.06 Å. This is in good agreement with the location of the H atom in the aluminium analogue proposed by Digne *et al.* during a theoretical examination of its structure.[86]

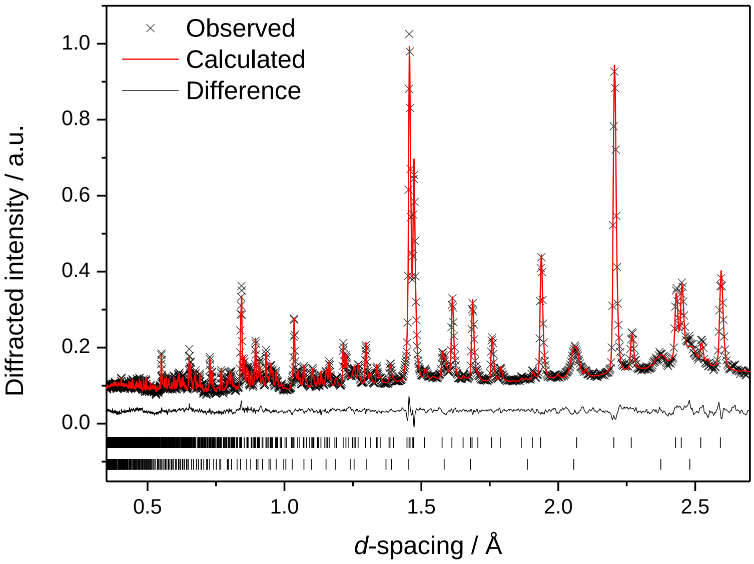

Figure 3.47 Results of Rietveld refinement of Ga-tohdite, $Ga_5O_7(OH)$, using neutron diffraction data from GEM bank 5 (average scattering angle 91.3°). Tick marks are allowed reflections for (upper): $Ga_5O_7(OH)$ and (lower): γ-Ga_2O_3.

Table 3.12 Crystal parameters for Ga-tohdite, $Ga_5O_7(OH)$. Space group $P6_3mc$, a = 5.82107(8) Å, c = 9.0662(2) Å. Rp = 2.87%, wRp = 3.48%.

Atom	Wyckoff site	x	y	z	U_{iso} / Å^2	Occupancy
Ga1	6c	0.1654(2)	0.3309(5)	0.3633(3)	0.0055(3)	1
Ga2	2b	2/3	1/3	0.1598(5)	0.0052(3)	1
Ga3	2b	1/3	2/3	0.0439(4)	0.0052(3)	1
O1	2a	0	0	-0.0173(5)	0.0051(2)	1
O2	6c	0.5133(2)	0.0265(4)	0.0004(4)	0.0051(2)	1
O3	6c	0.8334(7)	0.6668(13)	0.2594(4)	0.0051(2)	1
O4	2b	1/3	2/3	0.2503(5)	0.0051(2)	1
H	2a	0	0	0.100(2)	0.045(3)	1

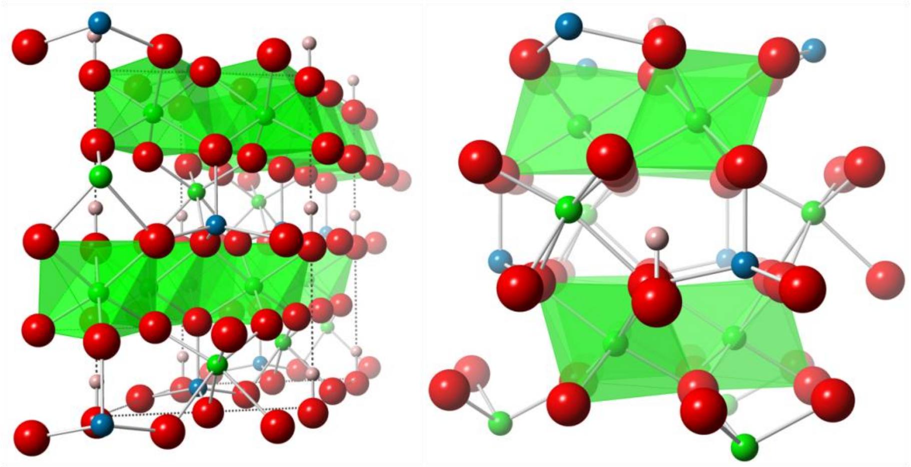

Figure 3.48 The structure of Ga-tohdite as determined from Rietveld refinement of powder neutron diffraction data. Green spheres are octahedral sites, blue are tetrahedral. The left-hand panel shows the layered structure as it extends in the *ab* plane. The right hand panel shows the environment of each hydrogen atom in the structure.

3.3.5.3. High resolution powder XRD

Owing to the very crystalline nature of the $Ga_5O_7(OH)$ material, high-resolution X-ray diffraction data were obtained from Diamond beamline I11 for further examination of the structure (λ = 0.825993 Å, sample mounted in 0.5 mm diameter capillary).

The structure obtained from Rietveld refinement of neutron diffraction data was used as the starting model for refinement of the X-ray data, and the initial fit is shown in Figure 3.49. It should be noted that it was not possible to use the same batch of the material for the X-ray measurement as for the neutron measurement, but the sample studied was prepared under identical conditions.

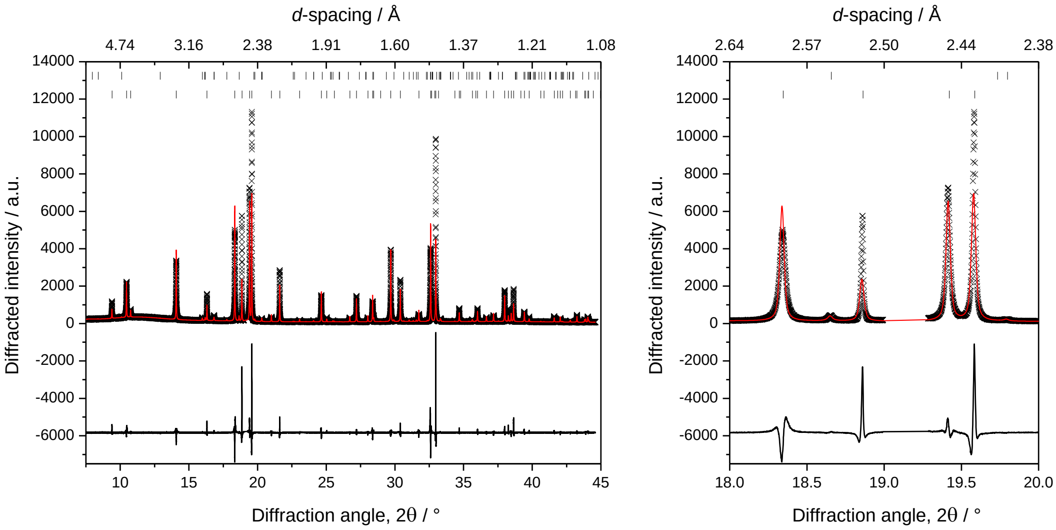

Figure 3.49 Initial Rietveld fit of high resolution XRD data for Ga-tohdite, using the structure detemined from neutron diffraction. Lower tickmarks are for Ga-tohdite, upper for β-Ga_2O_3. Rp = 11.0% wRp = 16.41%.

Both β- and γ-Ga_2O_3 are minor impurity phases in the sample used to collect the X-ray data, however only the strongest peak from γ-Ga_2O_3 was visible and was very broad, so the region of that peak (19.0 -19.3°) was simply excluded from the fit.

A few weak low-angle peaks exhibit some asymmetry due to axial divergence and this can be reasonably well accounted for by using GSAS X-ray profile function 4 which incorporates the Finger, Cox and Jephcoat model of axial divergence.[87]

The high resolution of these data reveals significant anisotropic broadening. For example, the 103 peak at 18.35° is nearly twice the width of the 200 peak at 18.86° despite the two being separated by only 0.51°. In GSAS, X-ray profile function 4 incorporates Stephens' phenomenological model of microstrain broadening,[88] in which peaks belonging to different *hkl* classes are broadened by different amounts. The different classes are defined depending on the symmetry of the model structure. To determine whether this type of broadening was applicable in the case of Ga-tohdite, the individual peaks were fit separately with pseudo-Voigt functions to determine their full-width-at-half-maximum (FWHM). Figure 3.50 shows that the FWHM of the peaks in the XRD pattern of Ga-tohdite show no apparent trend respective to *d*-spacing. There does, however, appear to be a linear relationship between FWHM and the "*l*" part of the *hkl* Miller indices, and indeed, the *hk*0 peaks are the least broad while the 00*l* peaks are the most broad.

These observations imply one (or both) of two things: that the crystallites exhibit anisotropic size broadening due to their plate-like nature; or that there is disorder along the long axis of the hexagonal structure, perhaps due to stacking faults. The structure is made up of layers of edge-sharing GaO_6 octahedra perpendicular to this axis, with the H atoms, the tetrahedral and second octahedral sites situated between these layers, so stacking faults could be considered likely.

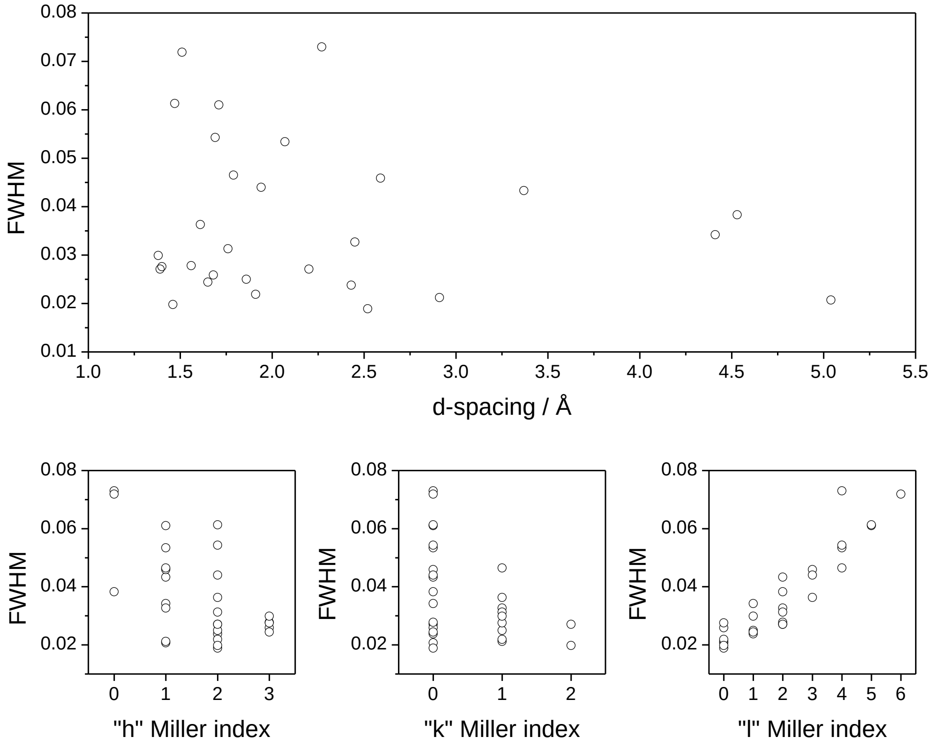

Figure 3.50 Plot of FWHM *vs* *d*-spacing for the peaks of Ga-tohdite (upper) and plots of FWHM *vs* Miller index (lower).

It can be seen from Figure 3.51 that the peak widths are very well accounted for by GSAS' X-ray profile function 4. Nevertheless, the relatively high Rp and wRp values for the fit indicate that there are still deficiencies in the model. Further refinement of atom positions and thermal parameters did not improve the fit. It can be seen from the difference between observed and calculated patterns that some of the peaks exhibit a slight shift from their expected positions. The shifts occur in different directions depending on the reflection class and this could be due to strain. No further modelling of this phenomenon has been attempted.

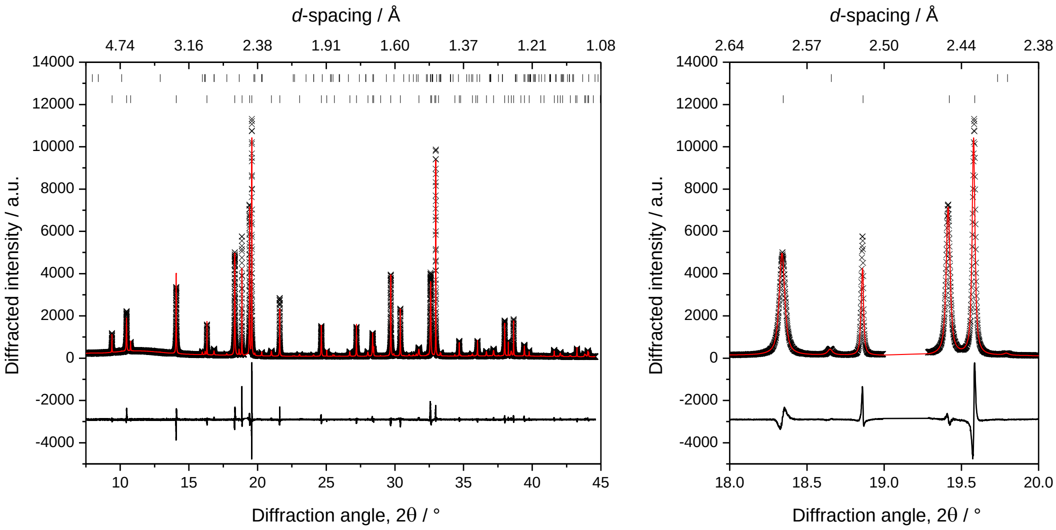

Figure 3.51 Rietveld fit of high resolution XRD data for Ga-tohdite, using the structure detemined from neutron diffraction and implementing Stephens' model of anisotropic broadening. Lower tickmarks are for Ga-tohdite, upper for β-Ga_2O_3. Rp = 7.52% , wRp = 10.23%.

3.3.6. *Kappa-Ga_2O_3*

It was reported by Okumiya *et al.*[89] that on dehydration, Al-tohdite forms orthorhombic κ-Al_2O_3 (the initial model for the structure of ε-Ga_2O_3, see Section 3.3.3.2) prior to the thermodynamically stable α-Al_2O_3. Thus, *in situ* X-ray diffraction was used to examine the behaviour of Ga-tohdite and the results are shown in Figure 3.52. It can be seen that Ga-tohdite undergoes phase transformation to β-Ga_2O_3 at around 550 °C, however a second phase is also present at temperatures between 600 and 800 °C. The diffraction peaks unique to this intermediate phase match those expected for the orthorhombic κ-Al_2O_3/ε-Fe_2O_3 model discussed and rejected for the product of thermal decomposition of gallium nitrate in Section 3.3.3.2 (also see Figure 3.33). In analogy with Al_2O_3 and to avoid confusion with the aforementioned ε-Ga_2O_3, this orthorhombic phase should be referred to as κ-Ga_2O_3.

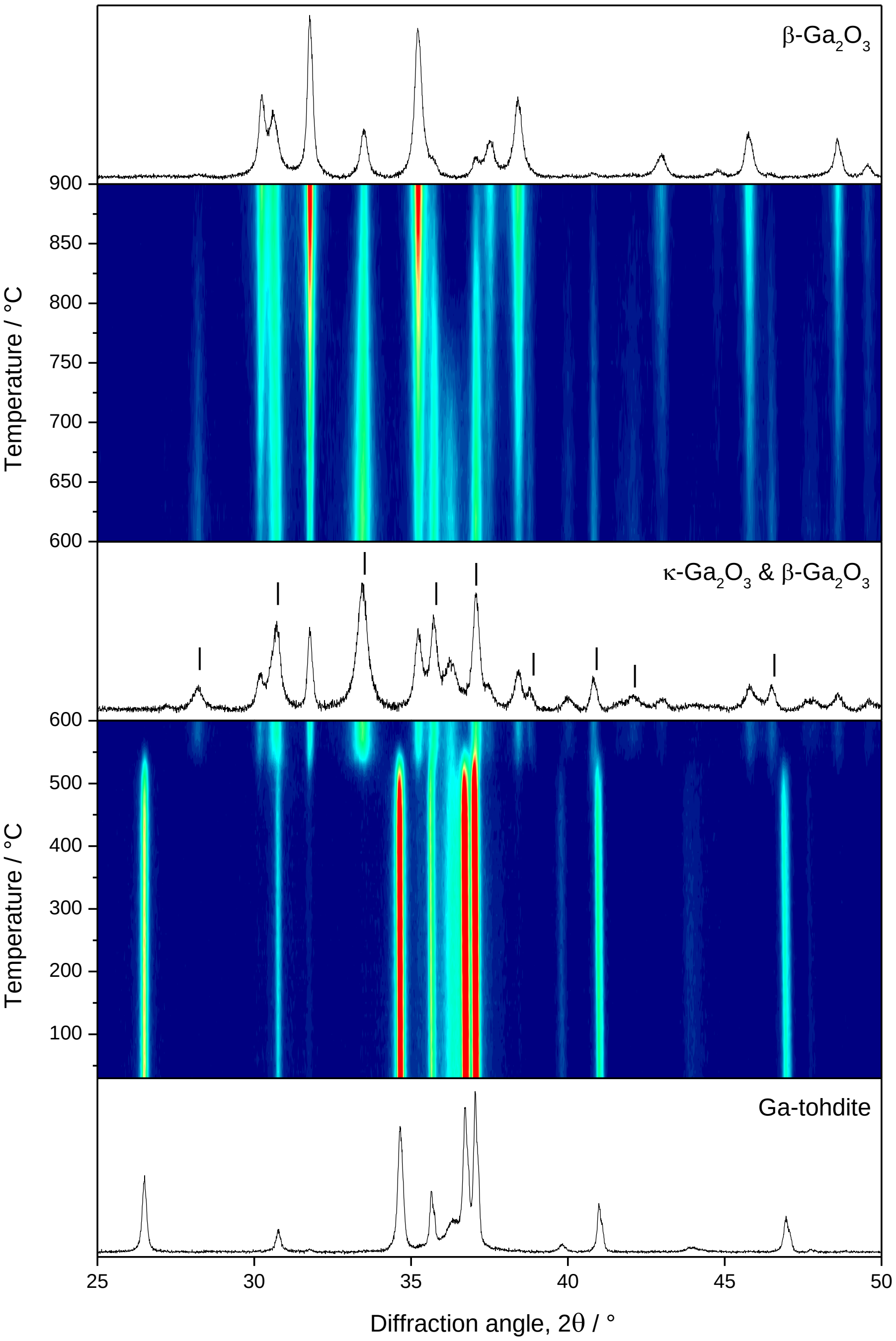

Figure 3.52 Contour plot of in situ heating XRD on Ga-tohdite, with intensity on the Z axis and the first, last and an illustrative intermediate scan highlighted. Tick-marks in the centre panel are peaks from κ-Ga$_2$O$_3$.

Isolation of this phase was not possible, as Ga-tohdite and γ-Ga$_2$O$_3$ were present simultaneously at lower temperatures and β-Ga$_2$O$_3$ was always present at higher temperatures, however, the X-ray diffraction pattern of the sample with the greatest proportion of the κ-Ga_2O_3 phase was used for a Le Bail profile fit, the result of which can be seen in Figure 3.53. The unit cell parameters of κ-Ga_2O_3, in orthorhombic space group $Pna2_1$, are a = 5.0557(1) Å, b = 8.68842(9) Å and c = 9.27585(6) Å.

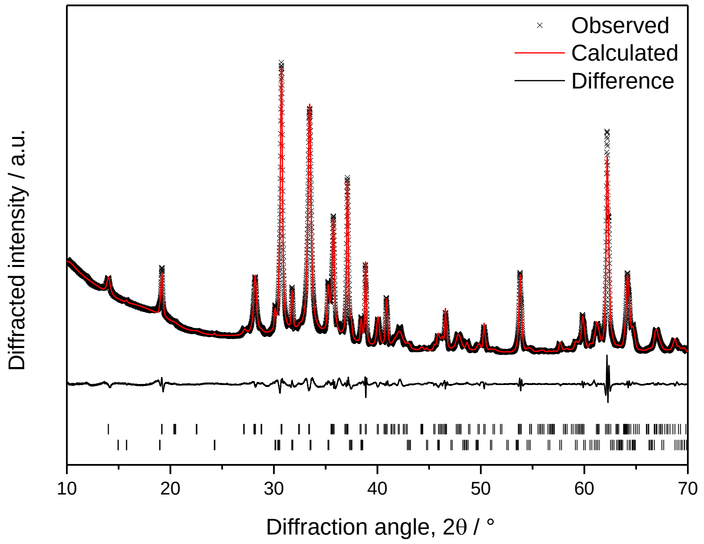

Figure 3.53 A Le Bail profile refinement of XRD data for a mixture of κ-Ga_2O_3 (upper tickmarks) and β-Ga_2O_3 (lower tickmarks).

3.4. Conclusions

The synthesis and interconversion of the polymorphs of Ga_2O_3 have been examined in detail, and the findings are illustrated in Figure 3.54. This scheme should be compared with the scheme originally proposed by Roy *et al.*[1] and shown in Figure 3.2.

A solvothermal synthesis route to crystalline γ-Ga_2O_3 has been optimised and the structure of this polymorph has been determined as a defect spinel with four partially occupied Ga sites and a degree of local distortion to account for the apparent preference of Ga for distorted octahedral coordination environments. The cation arrangement in γ-Ga_2O_3 is altered by the particle size of the sample and by the method of its synthesis.

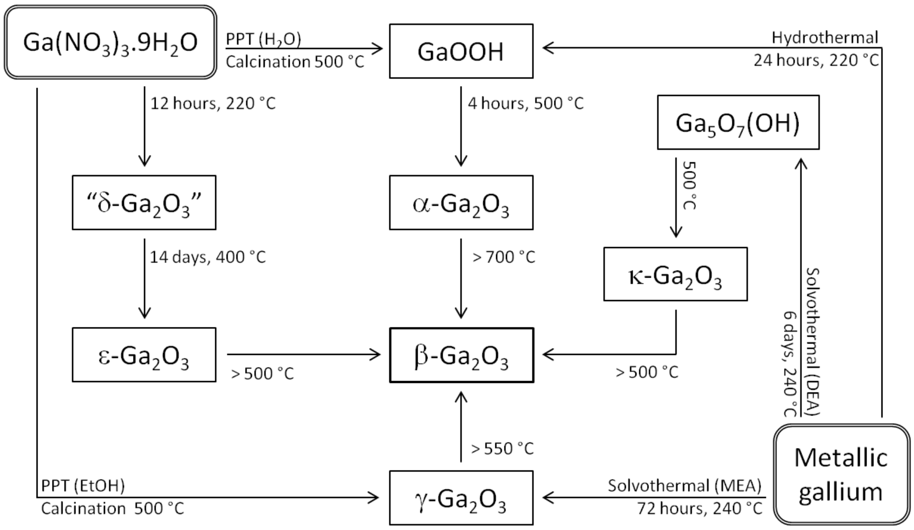
Ga(NO3)3.9H2O
PPT (H2O)
Calcination 500 °C
GaOOH
Hydrothermal
24 hours, 220 °C
12 hours, 220 °C
4 hours, 500 °C
Ga5O7(OH)
500 °C
"δ-Ga2O3"
α-Ga2O3
14 days, 400 °C
> 700 °C
κ-Ga2O3
Solvothermal (DEA)
6 days, 240 °C
ε-Ga2O3
> 500 °C
β-Ga2O3
> 500 °C
> 550 °C
PPT (EtOH)
Calcination 500 °C
γ-Ga2O3
Solvothermal (MEA)
72 hours, 240 °C
Metallic gallium

Figure 3.54 Summary of the synthesis and interconversion of polymorphs of Ga_2O_3 and related phases. Note that "δ-Ga_2O_3" is a nanocrystalline form of ε-Ga_2O_3.

The structure of ε-Ga_2O_3 has been determined as analogous to a disordered form of ε-Fe_2O_3 with a hexagonal structure.[24] The *d*-spacings reported for ε-Ga_2O_3 by Roy *et al.*[1] (and assumed by others) and attributed to the orthorhombic ε-Fe_2O_3/κ-Al_2O_3 structure are better accounted for by a mixture of hexagonal ε-Ga_2O_3 and β-Ga_2O_3.

The existence of bixbyite-structured δ-Ga_2O_3 has been disproven: in fact, "δ-Ga_2O_3" is a nanocrystalline modification of ε-Ga_2O_3.

The use of total neutron scattering techniques was vital to determining the structures of these disordered materials as their average crystal structures do not fully describe them. For example: total scattering revealed the local distortion in γ-Ga_2O_3 and examination of PDFs measured during heating "δ-Ga_2O_3" revealed that the nitrate precursor was not fully removed and that the phase transition to β-Ga_2O_3 occurred gradually and with no intermediate phase.

A novel gallium oxyhydroxide with formula $Ga_5O_7(OH)$ has been synthesised *via* solvothermal reaction. Its structure is analogous to the “hydrated alumina” tohdite and the mineral akdalaite. When investigating the thermal decomposition of Ga-tohdite an intermediate phase was observed prior to the formation of β-Ga_2O_3 and was identified as κ-Ga_2O_3, having the orthorhombic ε-Fe_2O_3/κ-Al_2O_3 structure.

The structural relationships between the polymorphs of Ga_2O_3, Al_2O_3 and Fe_2O_3 are summarised in Table 3.13 and idealised representations of the structures of the Ga_2O_3 polymorphs are shown in Figure 3.55.

Table 3.13 The polymorphs of Ga_2O_3 and the related Al_2O_3 and Fe_2O_3 phases.

Ga_2O_3			**Al_2O_3**		**Fe_2O_3**	
Phase	**S.G.**	**Unit cell / Å**	**Phase**	**Unit cell**	**Phase**	**Unit cell**
α[10]	$R\bar{3}c$	$a = 4.9825$ $c = 13.433$	α[90]	$a = 4.7586$ $c = 12.9897$	α[73]	$a = 5.036$ $c = 13.749$
β[8]	$C2/m$	$a = 12.214$ $b = 3.0371$ $c = 5.7981$ $\beta = 103.83$	θ[17]	$a = 11.854$ $b = 2.904$ $c = 5.622$ $\beta = 103.83$	-	
γ*	$Fd\bar{3}m$	$a = 8.23760(9)$	γ[17] η[17]	$a = 7.911$ $a = 7.914$	**γ (S.G. $P4_132$)**[73]	$a = 8.351$
ε*	$P6_3mc$	$a = 2.9036(2)$ $c = 9.2554(9)$	-		**ε (disordered)**[24]	$a = 2.92$ $c = 9.44$
κ*	$Pna2_1$	$a = 5.0557(1)$ $b = 8.68842(9)$ $c = 9.27585(6)$	κ[27]	$a = 4.8437$ $b = 8.3300$ $c = 8.9547$	ε[24]	$a = 5.095$ $b = 8.789$ $c = 9.437$

*This work.

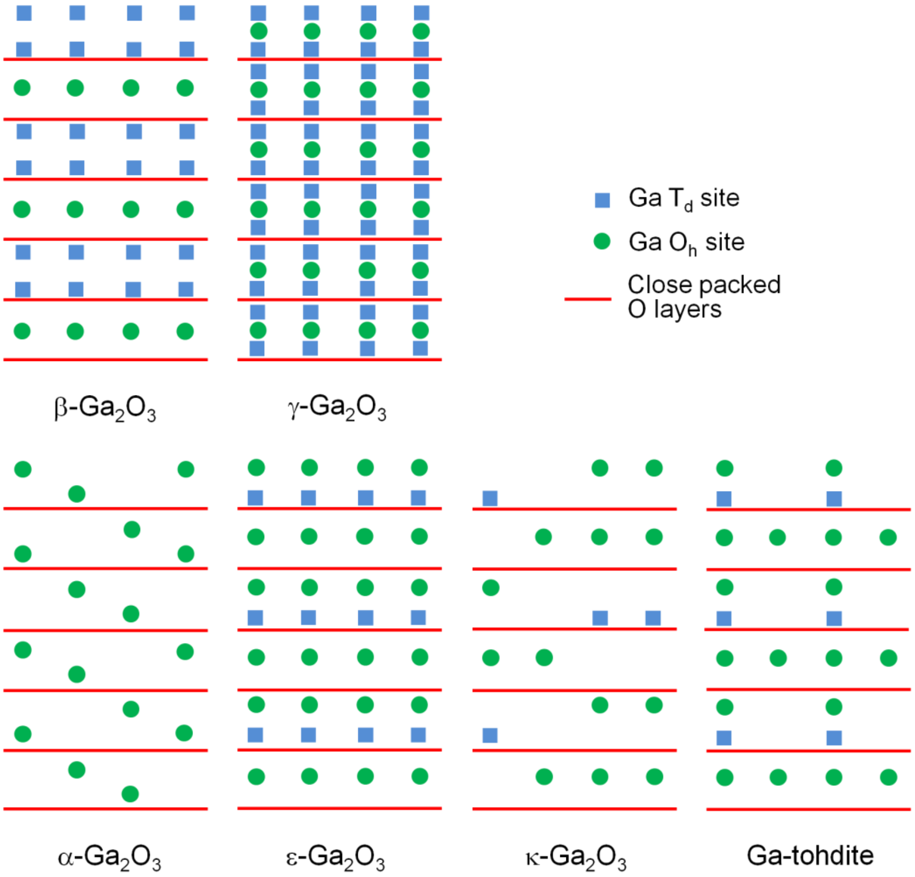
Ga T$_d$ site
Ga O$_h$ site
Close packed O layers
β-Ga$_2$O$_3$
γ-Ga$_2$O$_3$
α-Ga$_2$O$_3$
ε-Ga$_2$O$_3$
κ-Ga$_2$O$_3$
Ga-tohdite

Figure 3.55 Idealised cartoon representations of the structures of the polymorphs of Ga_2O_3. Upper row: the polymorphs based on a face centred cubic oxygen lattice and lower row: the polymorphs based on a hexagonal close packed oxygen lattice. Note that in reality the oxide layers may be distorted from planarity, and that not all Ga sites are fully occupied.

3.5. References

1. Roy, R.; Hill, V. G.; Osborn, E. F., *J. Am. Chem. Soc.* **1952,** *74*, 719.
2. Roy, R.; Hill, V. G.; Osborn, E. F., *Ind. Eng. Chem.* **1953,** *45*, 819.
3. Sato, T.; Nakamura, T., *Thermochim. Acta* **1982,** *53*, 281.
4. O'Dell, L. A.; Savin, S. L. P.; Chadwick, A. V.; Smith, M. E., *Appl. Magn. Reson.* **2007,** *32*, 527.
5. Yoshioka, S.; Hayashi, H.; Kuwabara, A.; Oba, F.; Matsunaga, K.; Tanaka, I., *J. Phys.: Condens. Matter* **2007,** *19*, 346211.
6. Geller, S., *J. Chem. Phys.* **1960,** *33*, 676.
7. Geller, S., *J. Solid State Chem.* **1977,** *20*, 209.
8. Ahman, J.; Svensson, G.; Albertsson, J., *Acta Crystallogr., Sect. C: Cryst. Struct. Commun.* **1996,** *52*, 1336.
9. Levin, I.; Brandon, D., *J. Am. Ceram. Soc.* **1998,** *81*, 1995.
10. Marezio, M.; Remeika, J. P., *J. Chem. Phys.* **1967,** *46*, 1862.
11. Zachariasen, W. H., *Nor. Vidensk. Akad.-Oslo Arbok.* **1928,** *41*, 1.
12. Zachariasen, W. H., *British Chemical Abstracts* **1929**, 1131.
13. Machon, D.; McMillan, P. F.; Xu, B.; Dong, J., *Phys. Rev. B* **2006,** *73*.
14. Ma, Y. M.; Chen, H. Y.; Yang, K. F.; Li, M.; Cui, Q. L.; Liu, J.; Zou, G. T., *Chin. Phys. Lett.* **2008,** *25*, 1603.
15. Smrcok, L.; Langer, V.; Krestan, J., *Acta Crystallogr. C* **2006,** *62*, i83.
16. Gutiérrez, G.; Taga, A.; Johansson, B., *Phys. Rev. B* **2001,** *65*, 012101.
17. Zhou, R. S.; Snyder, R. L., *Acta Crystallogr. B* **1991,** *47*, 617.
18. Shirasuka, K.; Yanagida, H.; Yamaguchi, G., *J. Ceram. Assoc. Jpn.* **1976,** *84*, 610.
19. Jørgensen, J.-E.; Mosegaard, L.; Thomsen, L. E.; Jensen, T. R.; Hanson, J. C., *J. Solid State Chem.* **2007,** *180*, 180.
20. Haneda, K.; Morrish, A. H., *Solid State Commun.* **1977,** *22*, 779.
21. Chaudron, M. G., *C. R. Hebd. Seances Acad. Sci.* **1957,** *244*, 617.
22. Marezio, M., *Acta Crystallogr.* **1966,** *20*, 723.
23. Dezsi, I.; Coey, J. M. D., *Phys. Status Solidi A* **1973,** *15*, 681.
24. Tronc, E.; Chaneac, C.; Jolivet, J. P., *J. Solid State Chem.* **1998,** *139*, 93.
25. Sakurai, S.; Jin, J.; Hashimoto, K.; Ohkoshi, S.-i., *J. Phys. Soc. Jpn.* **2005**, *74*, 1946.
26. Kelm, K.; Mader, W., *Z. Anorg. Allg. Chem.* **2005,** *631*, 2383.
27. Ollivier, B.; Retoux, R.; Lacorre, P.; Massiot, D.; Ferey, G., *J. Mater. Chem.* **1997,** *7*, 1049.
28. Frary, F. C., *Ind. Eng. Chem.* **1946,** *38*, 129.
29. Stumpf, H. C.; Russell, A. S.; Newsome, J. W.; Tucker, C. M., *Ind. Eng. Chem.* **1950,** *42*, 1398.
30. Wefers, K.; Misra, C. *Oxides and Hydroxides of Aluminum*; 19; ALCOA Laboratories: Pittsburgh, PA, 1987; p 20.
31. Santos, P. S.; Santos, H. S.; Toledo, S. P., *Materials Research* **2000,** *3*, 104.
32. Tippins, H. H., *Phys. Rev.* **1965,** *140*, A316.
33. Lorenz, M. R.; Woods, J. F.; Gambino, R. J., *J. Phys. Chem. Solids* **1967,** *28*, 403.
34. Harwig, T.; Wubs, G. J.; Dirksen, G. J., *Solid State Commun.* **1976,** *18*, 1223.

35. Ueda, N.; Hosono, H.; Waseda, R.; Kawazoe, H., *Appl. Phys. Lett.* **1997,** *70,* 3561.
36. Feng, P.; Zhang, J. Y.; Li, Q. H.; Wang, T. H., *Appl. Phys. Lett.* **2006,** *88.*
37. Wang, F.; Han, Z. H.; Tong, L. M., *Physica E* **2005,** *30,* 150.
38. Miyata, T.; Nakatani, T.; Minami, T., *J. Lumin.* **2000,** *87–89*, 1183.
39. Sasaki, T.; Hijikata, K., *Proc. Inst. Nat. Sci., Nihon Univ.* **1974,** *9,* 29.
40. Cojocaru, L. N., *Rev. Roum. Phys.* **1973,** *18,* 409.
41. Fleischer, M.; Meixner, H., *Sens. Actuators, B* **1991,** *4,* 437.
42. Fleischer, M.; Meixner, H., *Sens. Actuators, B* **1992,** *6,* 257.
43. Weh, T.; Frank, J.; Fleischer, M.; Meixner, H., *Sens. Actuators, B* **2001,** *78,* 202.
44. Trinchi, A.; Wlodarski, W.; Li, Y. X., *Sens. Actuators, B* **2004,** *100,* 94.
45. Yan, S. C.; Wan, L. J.; Li, Z. S.; Zhou, Y.; Zou, Z. G., *Chem. Commun.* **2010,** *46*, 6388.
46. Zheng, B.; Hua, W.; Yue, Y.; Gao, Z., *J. Catal.* **2005,** *232*, 143.
47. Lavalley, J. C.; Daturi, M.; Montouillout, V.; Clet, G.; Arean, C. O.; Delgado, M. R.; Sahibed-dine, A., *Phys. Chem. Chem. Phys.* **2003,** *5*, 1301.
48. Iwasa, N.; Mayanagi, T.; Ogawa, N.; Sakata, K.; Takezawa, N., *Catal. Lett.* **1998,** *54*, 119.
49. Moreno, J. A.; Poncelet, G., *J. Catal.* **2001,** *203*, 453.
50. Haneda, M.; Kintaichi, Y.; Mizushima, T.; Kakuta, N.; Hamada, H., *Appl. Catal., B* **2001,** *31*, 81.
51. Hou, Y. D.; Wang, X. C.; Wu, L.; Ding, Z. X.; Fu, X. Z., *Environ. Sci. Technol.* **2006,** *40*, 5799.
52. Hou, Y. D.; Wu, L.; Wang, X. C.; Ding, Z. X.; Li, Z. H.; Fu, X. Z., *J. Catal.* **2007,** *250*, 12.
53. Sakata, Y.; Matsuda, Y.; Yanagida, T.; Hirata, K.; Imamura, H.; Teramura, K., *Catal. Lett.* **2008,** *125*, 22.
54. Teramura, K.; Tsuneoka, H.; Shishido, T.; Tanaka, T., *Chem. Phys. Lett.* **2008,** *467*, 191.
55. Kerlau, M.; Merdrignac-Conanec, O.; Reichel, P.; Barsan, N.; Weimar, U., *Sens. Actuators, B* **2006,** *115*, 4.
56. Buha, J.; Djerdj, I.; Antonietti, M.; Niederberger, M., *Chem. Mater.* **2007,** *19*, 3499.
57. Cailleaux, X.; de Lucas, M. D. M.; Merdrignac-Conanec, O.; Tessier, F.; Nagasaka, K.; Kikkawa, S., *J. Phys. D: Appl. Phys.* **2009,** *42*.
58. Srdanov, V. I.; Blake, N. P.; Markgraber, D.; Metiu, H.; Stucky, G. D., In *Advanced Zeolite Science and Applications*, Jansen, J. C.; Stöcker, M.; Karge, H. G.; Weitkamp, J., Eds. Elsevier Science: Amsterdam, 1994; p 102.
59. Mertens, M. M.; Schottdarie, C.; Reinert, P.; Guth, J. L., *Microporous Mater.* **1995,** *5*, 91.
60. Reinert, P.; SchottDarie, C.; Patarin, J., *Microporous Mater.* **1997,** *9*, 107.
61. Beitone, L.; Guillou, N.; Millange, F.; Loiseau, T.; Ferey, G., *Solid State Sciences* **2002,** *4*, 1061.
62. Bonhomme, F.; Thoma, S. G.; Nenoff, T. M., *Microporous Mesoporous Mater.* **2002,** *53*, 87.
63. Antonijevic, S.; Ashbrook, S. E.; Walton, R. I.; Wimperis, S., *J. Mater. Chem.* **2002,** *12*, 1469.

64. Yang, Y. L.; Mu, Z. C.; Xu, Y.; Chen, C.; Wang, W.; Yi, Z.; Ye, L.; Liu, Y. L.; Pang, W. Q., *J. Solid State Chem.* **2004,** *177*, 2183.
65. Berbenni, V.; Milanese, C.; Bruni, G.; Marini, A., *J. Therm. Anal. Calorim.* **2005,** *82*, 401.
66. Amri, M.; Walton, R. I., *Chem. Mater.* **2009,** *21*, 3380.
67. Powder Diffraction File, International Centre for Diffraction Data, Newtown Square, PA.
68. Bailar, J. C.; Emeleus, H. J.; Nyholm, R.; Trotman-Dickenson, A. F., *Comprehensive Inorganic Chemistry*. Pergamon Press, Ltd.: Oxford, 1973; Vol. 1.
69. Greenwood, N. N.; Earnshaw, A., *Chemistry of the Elements*. 2nd ed.; Butterworth-Heinemann: Oxford, 1997.
70. Zinkevich, M.; Morales, F. M.; Nitsche, H.; Ahrens, M.; Ruhle, M.; Aldinger, F., *Z. Metallk.* **2004,** *95*, 756.
71. Zboril, R.; Mashlan, M.; Petridis, D., *Chem. Mater.* **2002,** *14*, 969.
72. Sakurai, S.; Namai, A.; Hashimoto, K.; Ohkoshi, S.-i., *J. Am. Chem. Soc.* **2009**.
73. Machala, L.; Tuček, J. i.; Zbořil, R., *Chem. Mater.* **2011,** *23*, 3255.
74. Kim, S.-W.; Iwamoto, S.; Inoue, M., *Ceram. Int.* **2009,** *35*, 1603.
75. Arean, C. O.; Bellan, A. L.; Mentruit, M. P.; Delgado, M. R.; Palomino, G. T., *Microporous Mesoporous Mater.* **2000,** *40*, 35.
76. Hendsbee, A. D.; Pye, C. C.; Masuda, J. D., *Acta Crystallogr. E* **2009,** *65*, i65.
77. Rather, E.; Gatlin, J. T.; Nixon, P. G.; Tsukamoto, T.; Kravtsov, V.; Johnson, D. W., *J. Am. Chem. Soc.* **2005,** *127*, 3242.
78. Ge, S. X.; Zhang, L. Z.; Jia, H. M.; Zheng, Z., *J. Mater. Res.* **2009,** *24*, 2268.
79. Paglia, G.; Bozin, E. S.; Billinge, S. J. L., *Chem. Mater.* **2006,** *18*, 3242.
80. Mason, G., *Nature* **1968,** *217*, 733.
81. Torkar, K.; Krischner, H., *Monatsh. Chem.* **1960,** *91*, 658.
82. Yamaguchi, G.; Yanagida, H.; Ono, S., *Bull. Chem. Soc. Jpn.* **1964,** *37*, 752.
83. Yamaguchi, G.; Okumiya, M.; Ono, S., *Bull. Chem. Soc. Jpn.* **1969,** *42*, 2247.
84. Hwang, S. L.; Shen, P. Y.; Chu, H. T.; Yui, T. F., *Int. Geol. Rev.* **2006,** *48*, 754.
85. Demichelis, R.; Noel, Y.; Zicovich-Wilson, C. M.; Roetti, C.; Valenzano, L.; Dovesi, R., In *Ab Initio Simulation of Crystalline Solids: History and Prospects - Contributions in Honor of Cesare Pisani*, Dovesi, R. O. R. R. C., Ed. 2008; Vol. 117, pp 12013.
86. Digne, M.; Sautet, P.; Raybaud, P.; Toulhoat, H.; Artacho, E., *J. Phys. Chem. B* **2002,** *106*, 5155.
87. Finger, L. W.; Cox, D. E.; Jephcoat, A. P., *J. Appl. Crystallogr.* **1994,** *27*, 892.
88. Stephens, P. W., *J. Appl. Crystallogr.* **1999,** *32*, 281.
89. Okumiya, M.; Yamaguchi, G.; Yamada, O.; Ono, S., *Bull. Chem. Soc. Jpn.* **1971,** *44*, 418.
90. Thompson, P.; Cox, D. E.; Hastings, J. B., *J. Appl. Crystallogr.* **1987,** *20*, 79.

Chapter 4: Gallium-containing Mixed Metal Oxides with the Spinel Structure

4. Gallium-containing Mixed Metal Oxides with the Spinel Structure

4.1. Introduction

4.1.1. Background

Mixed metal oxides, that is, metal oxides which contain more than one type of metal, are incredibly important functional materials. Often the addition of dopant metal (or metals) to an oxide structure results in dramatic changes in properties, due to differences in size between parent and dopant metal, or differences in their electronic or magnetic properties. As an example, consider Bi_2O_3, whose high temperature fluorite-like “delta” polymorph exhibits extremely high oxide-ion conductivity and can be stabilised at room temperature by the addition of dopants.[1] Also, as discussed in Chapter 3 of this thesis, β-Ga_2O_3 is a promising transparent conducting oxide but has only a relatively low conductivity based on intrinsic defects. Suitable dopants, such as tin, drastically improve its conductivity.[2]

Mixed metal oxides with the spinel structure have been enthusiastically targeted for many years. Grimes, in 1975,[3] wrote of the versatility of the structure and of the many potential applications provided by it. The spinel structure (named for the mineral $MgAl_2O_4$) consists of an almost cubic close packed oxygen array with cations in the tetrahedral and octahedral interstitial sites (Table 4.1 and Figure 4.1) Spinel oxides usually crystallise in the cubic space group $Fd\bar{3}m$. The mineral spinel is an example of a II:III spinel $[Mg^{II}(Al^{III})_2O_4]$ but there are also many examples of II:IV [*e.g.* $(Mg^{II})_2Ge^{IV}O_4$] and I:V [*e.g.* $(Na^{I})_2Mo^{V}O_4$] spinels. The spinel structure is not limited to oxides, either, with various AB_2X_4 chalcogenides (particularly chromites, where B = Cr and X = S, Se) extensively studied due to their magnetic properties.[4-5]

Table 4.1 The ideal crystal parameters of the spinel structure, in space group $Fd\bar{3}m$ and with both origin choices. In this thesis, origin choice 2 is used exclusively.

Site	Wyckoff position	Coordinates (origin choice 1)			Coordinates (origin choice 2)		
		x	**y**	**z**	**x**	**y**	**z**
A	8a	0	0	0	0.125	0.125	0.125
B	16d	0.625	0.625	0.625	0.5	0.5	0.5
O	32e	0.375 (= x)*	x	x	0.25 (= x)*	x	x

* The value of x given here would give perfect cubic close packing of the oxygen atoms, but the value in real spinels often deviates from this.

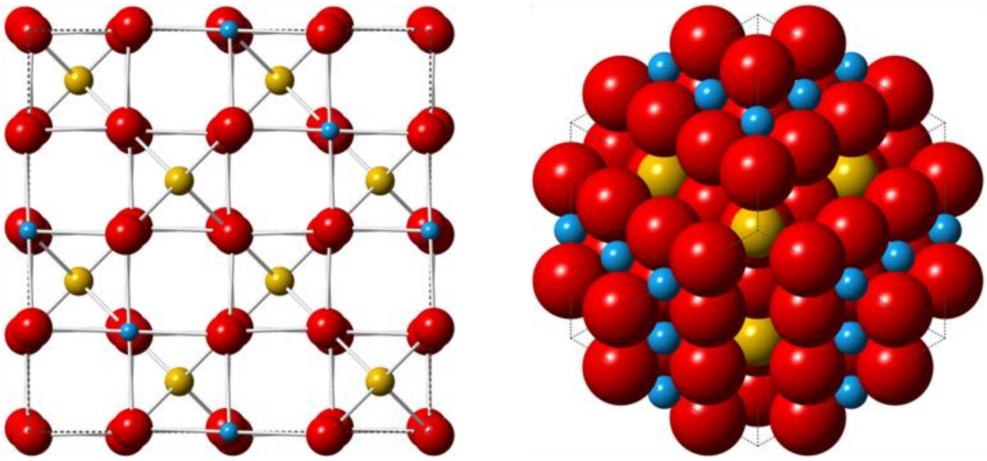

Figure 4.1 The spinel structure. Left: the unit cell of the spinel structure with cations in tetrahedral sites in yellow and cations in octahedral sites in blue. Right: the spinel structure viewed along the [111] direction showing the positions of cations in the interstices of the cubic close packed oxygen lattice.

Amongst the II:III spinel oxides, there is a great deal of flexibility in the cation arrangement. A normal spinel is defined as having the divalent cation on the tetrahedral 8a site, and the trivalent cation (of which there are twice as many) on the octahedral 16d site. An inverse spinel has half of the trivalent cations on the tetrahedral 8a site, and the other half on the octahedral 16d site, along with the divalent cations. An inversion parameter, x, is sometimes defined to quantify the number of trivalent cations on the A site, as in the following:

$$^{IV}(A_{1-x}B_x) \quad ^{VI}[A_xB_{2-x}]\,O_4 \tag{4.1}$$

Where $x = 0$ denotes a completely normal spinel and $x = 1$ denotes a completely inverse spinel. Many spinels are partially inverted, and it is often possible to alter the cation distribution by changing synthesis conditions or temperature. In the case of spinels containing transition metals the cation distribution and degree of inversion can often be rationalised through crystal field stabilisation energy (CFSE).

Although so far only stoichiometric spinels (with 24 cations to 32 oxygens in the unit cell) have been discussed, there are also many examples of of so-called defect spinels such as cation deficient γ-Ga_2O_3 or γ-Fe_2O_3 (21.333 cations to 32 oxygens, can be written as $\square_{0.33}M_{2.67}O_4$ where $\square$ denotes a vacancy) or cation rich $Ni_{2.62}Ti_{0.69}O_4$ in which some of the cations occupy the octahedral 16c site (at coordinates 0, 0, 0 if using origin choice 2) in addition to the 8a and 16d sites.[6]

Spinel oxides are incredibly flexible in terms of the numbers and types of cations that can be incorporated. This in turn leads to many interesting properties.[3] If any of the cations involved in the structure are magnetic, the exchange interaction between different sites (*i.e.* tetrahedral A and octahedral B sites) is much stronger than that between sites of the same type. This often leads to the spins on A–B pairings being antiparallel, while A–A and B–B pairings are arranged parallel. Thus, depending on the cation distribution the magnetic properties of a spinel can alter dramatically. The spinel structure can be thought of as two sublattices made up of A cations and B cations, respectively, and the magnetic moment on these two sublattices is rarely equal. This means that ferrimagnetic behaviour is very common in spinel structured oxides. The competing magnetic interactions coupled with the geometry of the spinel structure mean that spin glass behaviour is also commonly observed in spinel oxides. The electrical conductivity of spinels can often be increased by the inclusion of mixed-valence cations, for example the presence of Fe^{2+} and Fe^{3+} in ferrites.

It was the combination of ferromagnetism and electrical conductivity that led to initial industrial interest in spinels, particularly the ferrites, for applications in electronics and magnetic data storage.[3] This continues to this day with new interests in transparent conducting oxides,[7] lithium-containing spinels for battery materials,[8] and many potential applications in catalysis,[9-10] and photocatalysis.[11]

Navrotsky *et al.*[12] investigated the formation of a large number of simple ternary spinels, including manganites, ferrites, aluminates and gallates. Of these, ferrites and gallates have received particular interest. The gallates reported by Navrotsky were of the form AGa_2O_4 where A = Mg, Co, Ni, Cu, Zn or Cd. These materials have subsequently been investigated for a variety of interesting properties and potential applications.

$MgGa_2O_4$ is a potential phosphor material which exhibits blue luminescence after vacuum annealing,[13] green and red luminescence after doping with Mn^{2+},[14] and near IR emission after Ni^{2+} doping. [15]

$ZnGa_2O_4$ is a UV transparent conductor.[16] Unlike most of the other gallates its synthesis *via* soft chemical routes has been investigated extensively, *via* methods including hydrothermal synthesis,[17-18] and direct precipitation.[19] It was found to be an excellent candidate for a phosphor material as it was highly stable and unreactive towards the filaments.[20] $ZnGa_2O_4$ nanowires exhibited blue luminescence from native defects, and green and red emissions coule be obtained using Mn^{2+} and Cr^{3+} as dopants.[21] $ZnGa_2O_4$ has also been investigated as a photocatalyst for the degradation of benzene.[22]

$Mn_xGa_{3-x}O_4$ nanowires have also been reported and the material with stoichiometric composition ($x = 1$) exhibited photoluminescence.[23] A range of stable compositions with $0.33 < x < 0.56$ were reported to form the spinel structure *via* a diaspore (an oxyhydroxide *e.g.* GaOOH) like precursor by Sanford *et al.*.[24]

$CdGa_2O_4$ is promising transparent conducting oxide,[25] and was also found to exhibit high sensitivity and selectivity for gas phase sensing of ethanol.[26] $CuGa_2O_4$ was also evaluated as a potential gas sensor and found to have sensitivity towards hydrogen, liquid petroleum gas (LPG) and ammonia.[27] Additionally, $CuGa_2O_4$ has been used as a photocatalyst for the production of ‘solar hydrogen’ from H_2S, and it was found that co-doping with Fe and RuO_2 co-catalysts vastly increased its activity.[28]

$NiGa_2O_4$ was investigated as a potential catalyst for NO reduction with propene and with Mn_2O_3 as a co-catalyst,[29] and as a photocatalyst for water splitting to H_2 with RuO_2 as a co-catalyst.[30] $NiGa_2O_4$ was determined to be a perfectly inverse spinel by Greenwald *et al.*,[31] and Pajaczkowska *et al.*[32] observed possible spin-glass like behaviour below 5.8 K. In contrast, thin films of $NiGa_2O_4$ were found to be non stoichiometric (gallium rich) and with Ni^{2+} distributed on both sites.[33]

$CoGa_2O_4$ also has been reported to display spin-glass like behaviour at low temperature due to competing magnetic interactions caused by a distribution of Co atoms across both sites (inversion parameter = 0.6).[34]

A series of iron gallates with formula $Fe_xGa_{2-x}O_4$ ($x = 1 - 2.1$) was reported by Oles *et al.*[35] who determined their structures from neutron diffraction as inverse spinels. Ghose reported that Ga^{3+} exhibited no apparent preference for the octahedral or tetrahedral site in the presence of Fe^{2+} in $FeGa_2O_4$, and that the material exhibited no long range magnetic order.[36] This could be altered in $Fe_{1+x}Ga_{2-x}O_4$ by the addition of Fe^{3+} under which condition the Fe^{2+} exhibited a strong preference for the octahedral site.[36]

In addition to the binary and ternary spinels, there are quaternary spinels (*i.e.* those with a third type of cation) often in the form of solid solutions between two ternary end-members. Examples of quaternary gallium-containing spinels include $CoFe_{2-x}Ga_xO_4$,[37] a solid solution where $0 \leq x \leq 2$ and whose members exhibit spin-glass behaviour; and $Zn(Ga,Fe)O_4$,[19] a solid solution with the added complexity of mixed valence iron.

Based on the enormous variety of structure and properties displayed by the few materials discussed in this section, it is abundantly clear that in the spinel systems there is a great deal of complexity. New synthetic routes to mixed metal spinels may allow access to novel compositions and new soft chemical routes could have the added advantage of a degree of control over crystal form.

4.1.2. Scope of this chapter

In this chapter, a synthetic approach applicable to several gallium containing spinels is described based on the synthesis of γ-Ga_2O_3 (defect spinel) as discussed in Chapter 3. The synthesis of $M_xGa_{y-x}O_{4-\delta}$ with M = Zn, Ni, Co and Fe is presented.

An investigation into the structure and magnetic properties of the materials with M = Co and M = Fe is presented. Total neutron scattering is used for the structural studies to provide the necessary contrast between the various cations (b_{coh} = 7.288 fm (Ga), 2.49 fm (Co) and 9.45 fm (Fe)) and XANES spectroscopy provides complementary information about the transition metal cations. The use of SQUID magnetometry to investigate the magnetic properties of these materials is also presented.

4.2. Results and Discussion

4.2.1. Synthetic approach

As discussed in Chapter 3, Section 3.2.1.2, spinel structured γ-Ga_2O_3 can be prepared *via* the solvothermal oxidation of gallium metal in an aminoalcohol solvent. The adaptation of this technique to the synthesis of mixed oxides was investigated using metal salts which were soluble in the aminoalcohol solvent. In a typical synthesis, 0.1 g (1.4 mM) of metallic gallium (Aldrich 99.99%) and an appropriate amount of a metal salt (0.7, 1.4 or 2.8 mM) were added to 5 ml of 2-aminoethanol (Aldrich ≥99.0%) or diethanolamine (Aldrich ≥ 98.5%) in a Teflon® autoclave liner and heated in a water bath at ~70 °C for 10-15 minutes. The reaction mixtures were then sealed in a stainless steel autoclave and heated in a fan oven at 240 °C for 3 – 6 days. In this manner, mixed spinels of composition $M_xGa_{3-x}O_4$ with M = Zn, Ni and Co were synthesised (see Figure 4.2 and Table 4.2).

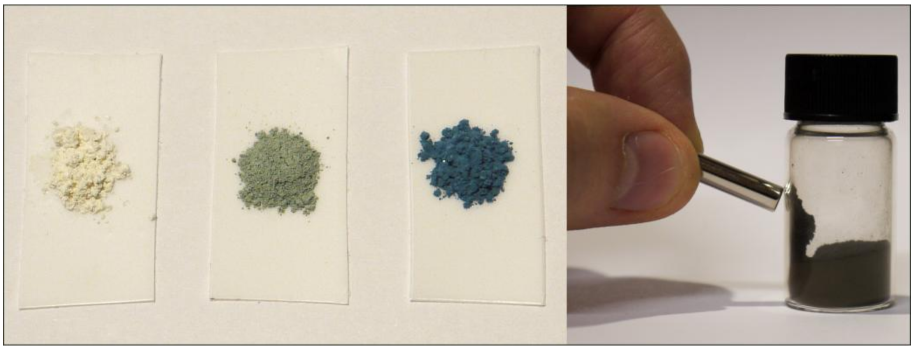

Figure 4.2 The as-synthesised spinel powders, L-R: M = Zn, Ni, Co and Fe. Note that for M = Fe, the sample is attracted to a magnet at room temperature.

Table 4.2 Synthesis conditions and lattice parameters for solvothermally produced mixed spinels.

Spinel	M^{2+} salt used	Synthesis conditions	Lattice parameter, a / Å
$\mathbf{ZnGa_2O_4}$	$ZnCl_2$	DEA, 6 days	8.3382(2)
$\mathbf{NiGa_2O_4}$	$Ni(NO_3)_2.6H_2O$	50:50 DEA + H_2O, 6 days	8.2714(4)
$\mathbf{Co_xGa_{3-x}O_{4-\delta}}$	$Co(NO_3)_2.6H_2O$	50:50 DEA + H_2O, 6 days	8.31288(9)*
$\mathbf{Fe_xGa_{3-x}O_{4-\delta}}$	$FeCl_2.4H_2O$	DEA, sonicator, 6 days	8.3127(5)*

* See Sections 4.2.2.2 and 4.2.3.2.

An iron gallate spinel was also synthesised in the manner described above, however it was found by TEM to be inhomogeneous with both iron-rich and gallium-rich crystallites observed by EDX. Due to its potential for interesting magnetic properties, its synthesis was optimised as part of an undergraduate research project by David Burnett.[38] An apparently single phase $Fe_xGa_{y-x}O_{4-\delta}$ spinel was only produced when the initial reaction mixture was warmed and an ultrasonic probe was used to disperse the molten gallium. It was also found that the choice of iron source and aminoalcohol solvent greatly affected the outcome of the reaction, with iron(II) chloride and diethanolamine producing the most homogeneous product. Unlike the other reactions where a Ga:M ratio of 2:1 was optimal, an apparently homogeneous Ga:Fe product was only obtained when the ratio was 1:1.

A reference sample of orthorhombic ε-$GaFeO_3$ was also prepared by David Burnett *via* the ceramic method: β-Ga_2O_3 and α-Fe_2O_3 were ground together and heated at 1400 °C in air for 12 hours.

During the synthesis of the cobalt gallate spinel it was observed that an impurity phase was always present as a grey powder, which was apparently amorphous by X-ray diffraction. This powder, presumably a highly disordered form of metallic cobalt, was attracted to a strong permanent magnet. To remove it, the product was suspended in methanol and poured slowly through a funnel surrounded by magnets such that the impurity phase remained on the magnets and the spinel passed through. This procedure was repeated multiple times to ensure complete removal of the impurity.

SEM images of the M = Zn and Ni spinels are shown in Figure 4.3 and Figure 4.4. It can be seen that the morphologies are rather different, with the Ga-Zn spinel forming smooth, spherical particles of roughly 200 nm in diameter, and the Ga-Ni consisting of much smaller particles arranged in tubular shapes and apparently agglomerated into larger spheres of several micrometers diameter.

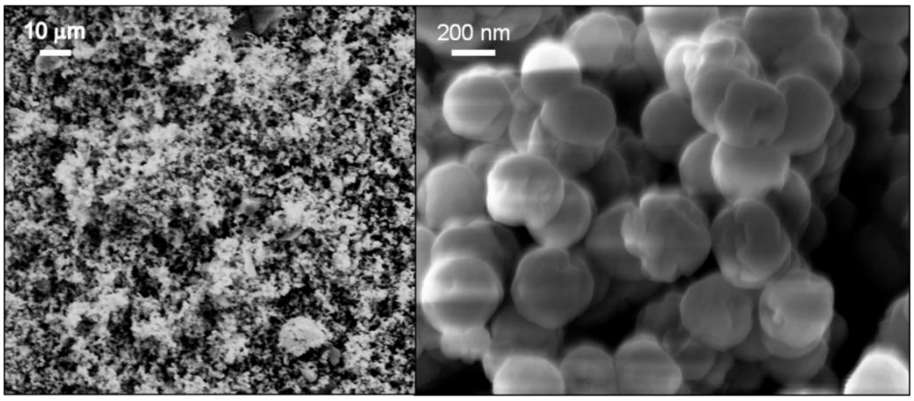

Figure 4.3 SEM images of the gallium-zinc spinel.

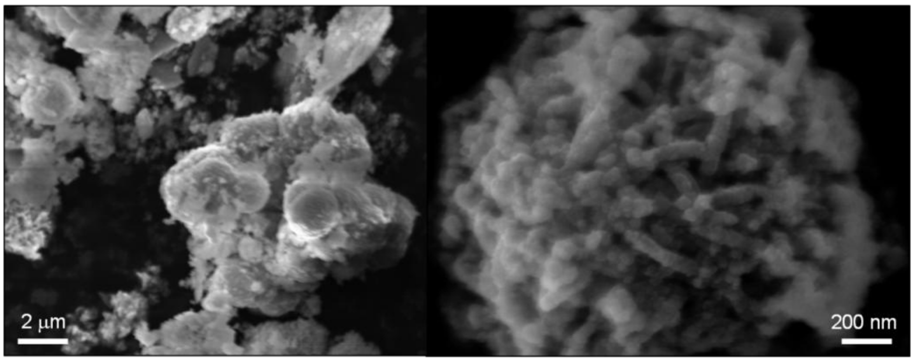

Figure 4.4 SEM images of the gallium-nickel spinel.

For both the Ga-Zn and Ga-Ni spinels, EDX analysis revealed an M:Ga ratio of 1:2.2, which is in good agreement with the expected composition of MGa_2O_4.

The cubic lattice parameters of the M = Zn and Ni spinels were determined from high-resolution laboratory X-ray diffraction patterns (λ = 1.5406 Å), using the Le Bail profile refinement technique (Figure 4.5 and Table 4.2). For $ZnGa_2O_4$ the lattice parameter of *a* = 8.3382(2) Å is in good agreement with the value of 8.3349 Å reported by Hirano *et al.*[17] for hydrothermally produced nanoparticles. The lattice parameter of $NiGa_2O_4$, *a* = 8.2714(4) Å, is in good agreement with that of Arean *et al.*,[39] 8.261 Å.

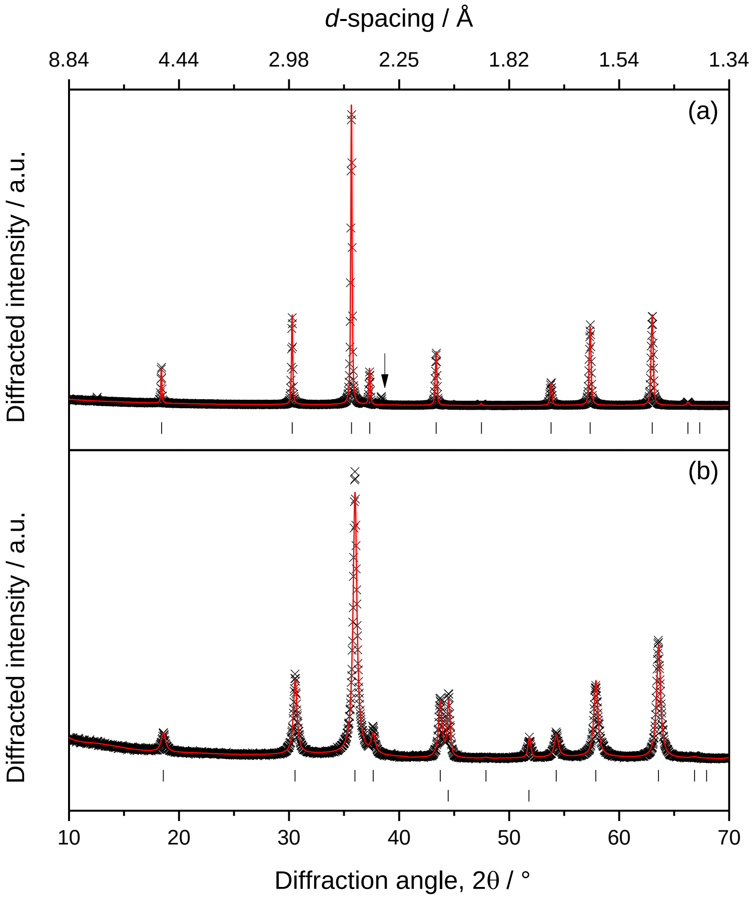

Figure 4.5 Le Bail fits to X-ray diffraction patterns of the MGa_2O_4 spinels where (a) M = Zn (Rp = 7.68%, wRp = 11.1%) and (b) M = Ni (Rp = 6.58%, wRp = 8.7%). Note: a small peak due to metallic Zn is labelled with an arrow in (a) and peaks due to metallic Ni were included in the fit and shown by the lower set of tick marks in (b).

A full Rietveld refinement was not attempted due to the constituent metals having rather similar atomic numbers, and thus being difficult to distinguish meaningfully by X-ray diffraction. The presence of metallic Zn, Ni (and presumably Co) as impurities is unexpected and implies that a simultaneous oxidation-reduction process is occurring under solvothermal conditions, with the metallic Ga being oxidised and a portion of the M^{2+} salts being reduced. The structure and properties of the M = Co and M = Fe spinels were investigated in detail and are discussed in the remainder of this chapter.

4.2.2. Cobalt gallium oxide

4.2.2.1. General characterisation

SEM and TEM microscopy and EDX spectroscopy were used to characterise the Co-Ga spinel material. As shown in Figure 4.6, the material consists of small (~25 nm), relatively uniform crystallites of roughly spherical morphology, and the individual particles are clearly highly crystalline. The EDX results from several crystallites revealed an average Co:Ga ratio of 1:1.83, and considering the expected errors in EDX compositions, as a starting point for further analysis, the spinel was assumed to be stoichiometric $CoGa_2O_4$.

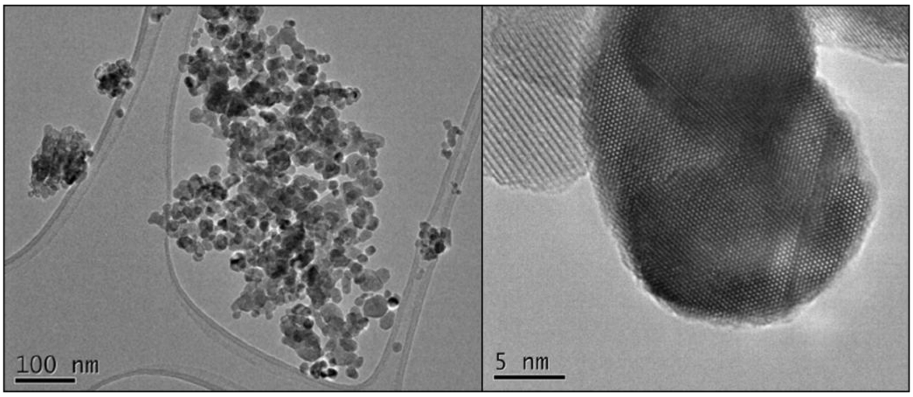

Figure 4.6 Representative TEM images of the Co-Ga spinel.

The initial assumption of a stoichiometric spinel was supported by the Co K-edge XANES spectrum which is consistent with the majority of the Co in the +2 oxidation state, see for example Hall *et al.*[40] (Figure 4.7). The intensity of the pre-edge feature in the Co XANES spectrum can be related to the amount of Co in non-centrosymmetric (*e.g.* tetrahedral) coordination environments, because it arises from an electronic transition (1s → 3d) that is forbidden when the absorbing cation possesses a centre of inversion symmetry. The XANES spectra therefore indicates that there is very little tetrahedrally coordinated Co in the mixed spinel material.

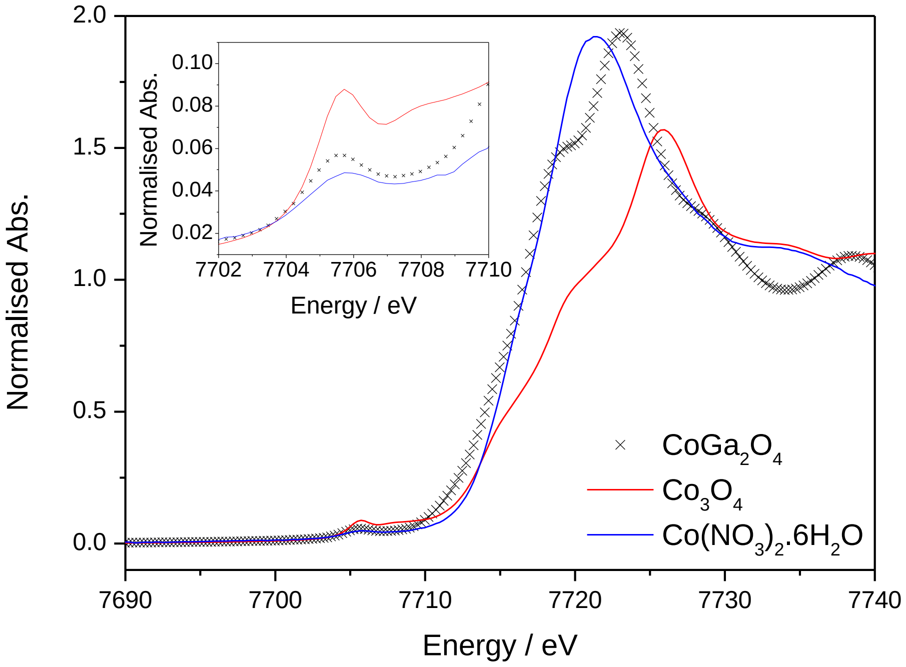

Figure 4.7 XANES at the Co K-edge of $CoGa_2O_4$ with relevant Co(II) and Co(II/III) standards.

Thermogravimetric analysis (Figure 4.8) carried out in air reveals two small mass losses of ~0.5% at 100 °C, which is probably due to surface water, and ~1.5% at about 300 °C ascribed to loss of surface-associated organic species.

The thermal stability of solvothermal $CoGa_2O_4$ was assessed using *in situ* X-ray diffraction. The maximum temperature reached was 900 °C, and the spinel structure was stable throughout the heating experiment. Comparison of the patterns at 50 and 900 °C exhibit a positive thermal expansion, however, the contour plot (Figure 4.9) reveals that in the temperature range 250 – 450 °C the material apparently exhibits negative thermal expansion, with the diffraction peaks shifting to higher 2θ values.

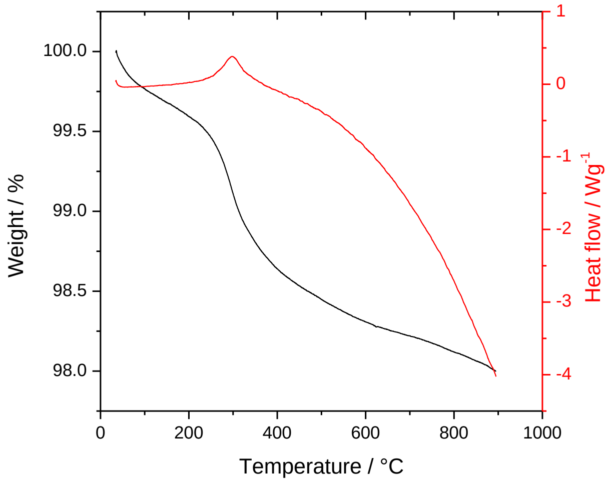

Figure 4.8 TGA trace of $CoGa_2O_4$.

The existence of a correlation between the degree of cation disorder in the spinel structure (characterised by the degree of inversion), the position of the oxygen-site, and the overall lattice parameter, has been the subject of several theoretical studies, though it has been observed experimentally only rarely.[41-42] In $MgAl_2O_4$ the trend is for the lattice parameter to decrease with an increasing degree of inversion, although the available data only go to $x = 0.4$.[42] In $NiAl_2O_4$ the same trend was observed.[43] Indeed a comparison of two published structures of $CoGa_2O_4$ reveals that Christensen *et al.*[44] reported a lattice parameter of 8.3229 Å and a degree of inversion, $x = 1$, and Nakatsuka *et al.*[45] reported a lattice parameter of 8.3281 Å when $x = 0.575$. If the cation distribution of the solvothermal cobalt gallate were to change as a function of temperature, it is possible that the lattice parameter could initially contract on heating if the temperature increase also caused the inversion parameter to increase.

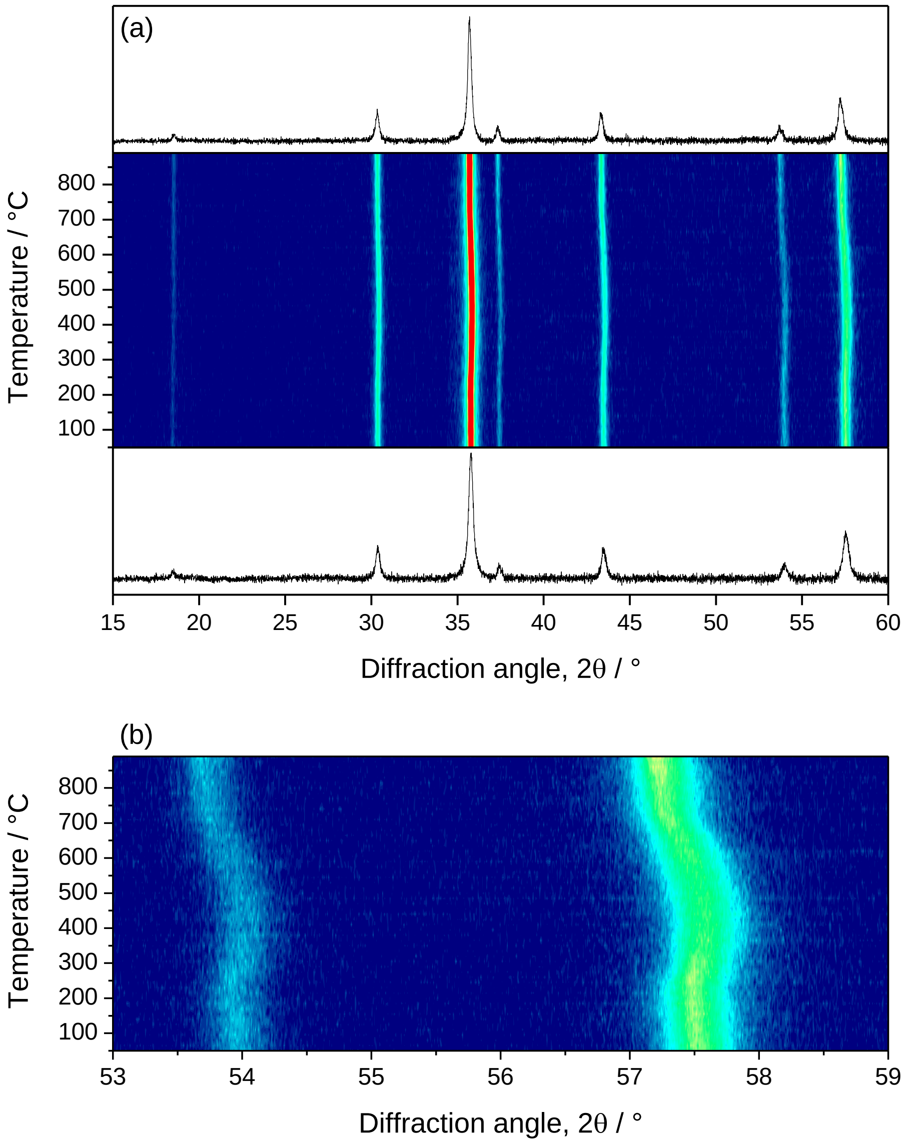

Figure 4.9 (a) Thermodiffraction of $CoGa_2O_4$. (b) Close-up of region showing non-typical thermal expansion behaviour.

4.2.2.2. Total neutron scattering

Neutron diffraction was used for the structural analysis of the cobalt gallate spinel because the atomic numbers of cobalt and gallium differ by only 4, and hence X-ray diffraction is rather insensitive to their distribution across the different sites.

4.2.2.2.1. *Model 1*

Rietveld refinement of neutron diffraction data was first carried out using a stoichiometric $CoGa_2O_4$ model as determined by Nakatsuka *et al.*[45] for a single crystal sample. The inversion parameter of the starting model was 0.575, *i.e.* a partially inverse spinel. The results of Rietveld refinement of the solvothermal $CoGa_2O_4$ are shown in Figure 4.10 and Table 4.3. A constraint was initially applied to the occupancies of the cation sites to maintain 100% occupancy on both sites. When this constraint was lifted the occupancies refined to unphysically large values and the wRp reduced only slightly, from 2.38% to 2.37%, therefore this was not considered a significant result.

Table 4.3 Crystal parameters for $Co_{1.106(8)}Ga_{1.893(8)}O_{3.95}$, using the stoichiometric model. Space group $Fd\bar{3}m$, a = 8.31393(8) Å. Rp = 1.49%, wRp = 2.38%. Measured density = 5.437 g cm^{-3}, calculated density = 6.019 g cm^{-3}.

Wyckoff site	Atom	x	y	z	U_{iso} / Å^2	Occupancy
8a	Ga	0.125	0.125	0.125	0.0069(2)	0.796(4)
	Co	0.125	0.125	0.125	0.0069(2)	0.204(4)
16d	Ga	0.5	0.5	0.5	0.0077(2)	0.549(3)
	Co	0.5	0.5	0.5	0.0077(2)	0.451(3)
32e	O	0.25628(6)	0.25628(6)	0.25628(6)	0.0065(2)	0.987*

* Note that the occupancy of the O site was not refined.

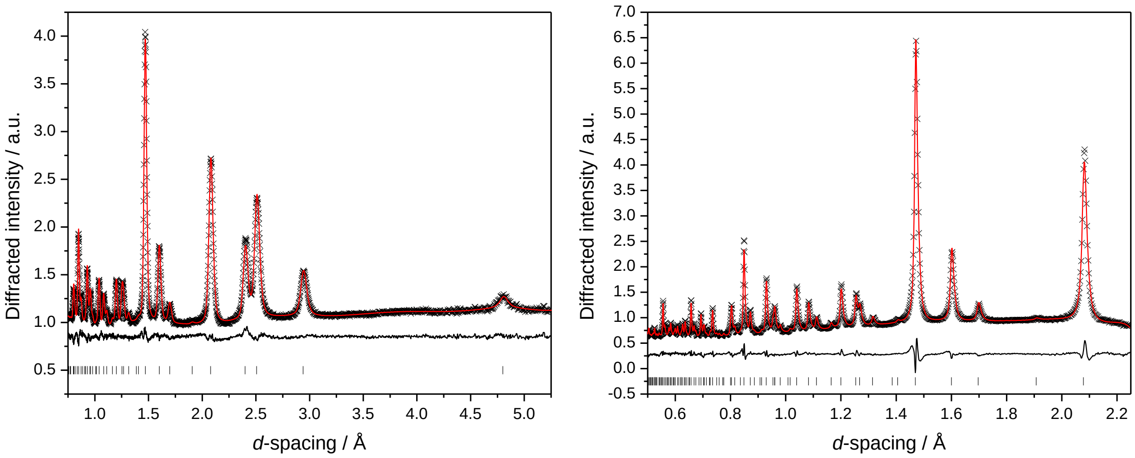

Figure 4.10 Result of Rietveld refinement for solvothermal $Co_{1.1}Ga_{1.9}O_{3.95}$ using the stoichiometric $CoGa_2O_4$ as a starting model. Left: data from GEM bank 3 (mean scattering angle 34.9°). Right: data from GEM bank 5 (mean scattering angle 91.3°).

It can be seen from these results that solvothermal cobalt gallate in this model is largely inverse ($x = 0.796$) and that it appears to be slightly Co rich, hence a small number of oxygen vacancies must be introduced to maintain the charge balance. However, considering that the refined structure contains 8.84 Co atoms per unit cell, rather than the 8.0 in $CoGa_2O_4$, this model should probably be considered to be stoichiometric to within error.

A Fourier difference map was calculated to determine whether any cations were situated on non-spinel sites, as was found to be the case for γ-Ga_2O_3, but none were identified in this case. It was also found that arbitrarily placing small amounts of either Ga or Co on the non-spinel sites did not improve the fit.

4.2.2.2.2. Model 2

A second refinement was carried out starting from the structure of γ-Ga_2O_3 as determined in Chapter 3 of this thesis, introducing Co^{2+} on only the octahedral sites (to be consistent with the XANES result). In this case, the occupancies of the non-spinel sites refined to zero and the end result was a defect spinel with approximate composition $Co_{0.76}Ga_{1.50}O_3$. The fit was reasonable (see Figure 4.11 and Table 4.4), however, the calculated density of this material is 4.841 g cm^{-3} – a value that is in disagreement with the measured density. Therefore, this structural model was disregarded.

Table 4.4 Crystal parameters for $Co_{0.756(4)}Ga_{1.495(4)}O_3$, using the model based on γ-Ga_2O_3. Space group $Fd\bar{3}m$, a = 8.3133(1) Å. Rp = 1.92%, wRp = 2.87%. Measured density = 5.437 g cm^{-3} , calculated density = 4.841 g cm^{-3}.

Wyckoff site	Atom	x	y	z	U_{iso} / $Å^2$	Occupancy
8a	Ga	0.125	0.125	0.125	0.0051(1)	0.713(2)
16d	Ga	0.5	0.5	0.5	0.0051(1)	0.439(2)
	Co	0.5	0.5	0.5	0.0051(1)	0.402(2)
32e	O	0.25625(5)	0.25625(5)	0.25625(5)	0.0073(1)	0.798*

* Note that the occupancy of the O site was not refined.

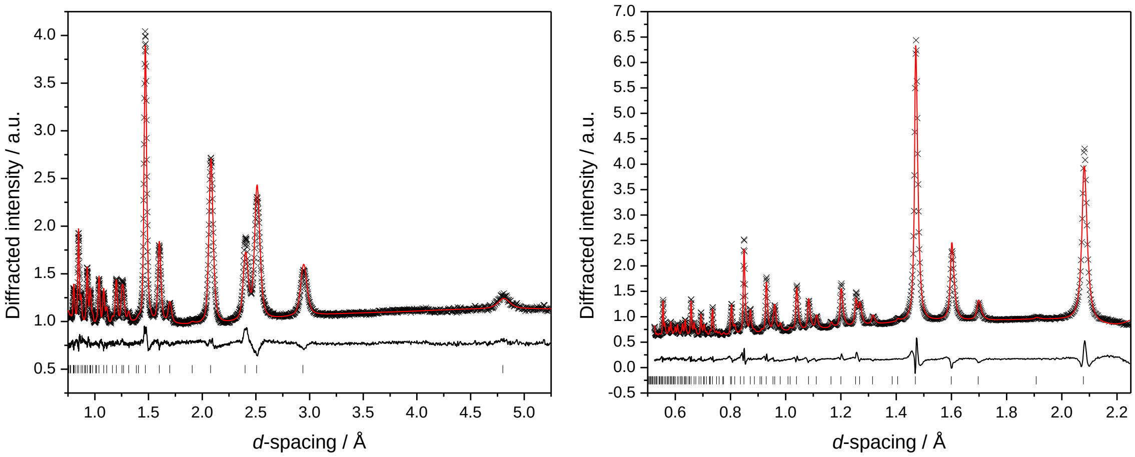

Figure 4.11 Result of Rietveld refinement for solvothermal cobalt gallate using γ-Ga_2O_3 as a starting model. Left: data from GEM bank 3 (mean scattering angle 34.9°). Right: data from GEM bank 5 (mean scattering angle 91.3°).

4.2.2.2.3. Model 3

Comparing the measured density of the cobalt gallate spinel with that calculated for the (nearly) stoichiometric model, it can clearly be seen that the density of the model is too large. Although some error might be expected in the pycnometer reading due to the presence of surface water, or simply the incomplete purging of the chamber, a discrepancy of this size suggests a different structural model is required. Therefore, a third refinement was carried out, this time using a defect spinel (21 ⅓ cations per unit cell, rather than 24 in the stoichiometric model) as the starting point. The (cationic) composition of this defect spinel and the ratio of octahedral:tetrahedral Ga and Co was the same as the stoichiometric model. The results are shown in Table 4.5 and Figure 4.12. The refined model has the composition $CoGa_{1.56}O_{3.34}$, which is extremely oxygen deficient (13.85% of the oxygen sites vacant). Although spinels with oxygen deficiency have been reported, including natural spinel $MgAl_2O_4$,[46] the maximum oxygen deficiency reported seems to be around 7% for a $LiMn_2O_{4-\delta}$ spinel.[47] Additionally, the calculated density of the "defect" model is lower than the measured density, and it is difficult to imagine a scenario in which experimental error could lead to a measured density greater than the crystallographic one. Therefore, another model, with a more reasonable composition and density, was sought.

Table 4.5 Crystal parameters for $Co_{1.000(7)}Ga_{1.562}O_{3.34}$, using the defect model. Space group $Fd\bar{3}m$, a = 8.31288(9) Å. Rp = 1.73%, wRp = 2.57%. Measured density = 5.437 g cm^{-3}, calculated density = 5.291 g cm^{-3}.

Wyckoff site	**Atom**	**x**	**y**	**z**	**U_{iso} / Å^2**	**Occupancy**
8a	Ga	0.125	0.125	0.125	0.0060(1)	0.684(4)
	Co	0.125	0.125	0.125	0.0060(1)	0.197(4)
16d	Ga	0.5	0.5	0.5	0.0060(1)	0.463(3)
	Co	0.5	0.5	0.5	0.0060(1)	0.417(3)
32e	O	0.25622(6)	0.25622(6)	0.25622(6)	0.0065(1)	0.8615*

*Note that the occupancy of the O site was not refined.

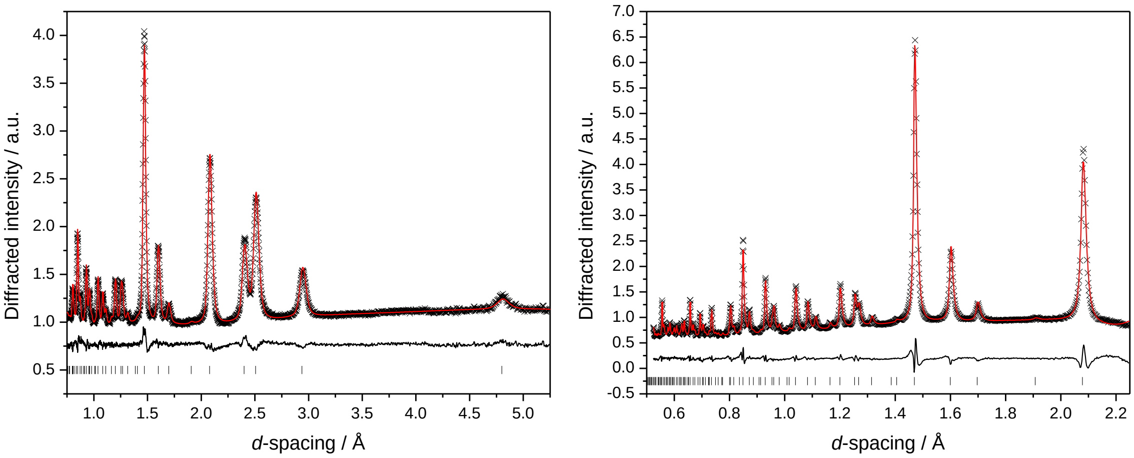

Figure 4.12 Result of Rietveld refinement for solvothermal $CoGa_{1.56}O_{3.34}$ starting from the defect spinel model. Left: data from GEM bank 3 (mean scattering angle 34.9°). Right: data from GEM bank 5 (mean scattering angle 91.3°).

4.2.2.2.4. Model 4

To obtain a model for the cobalt gallium spinel without excessive oxygen deficiency, it was necessary to include a proportion of Co^{3+} rather than basing the model solely on Co^{2+}. This is chemically reasonable, as the spinel Co_3O_4 also exhibits mixed valency. The starting point for this refinement was a model with composition $(Co^{2+}_{0.75}Co^{3+}_{0.125})Ga_{1.875}O_{3.75}$, which to balance charges requires that 6.25 % of the oxygen sites are vacant. The results are presented in Table 4.6 and Figure 4.13

Table 4.6 Crystal parameters for $Co_{0.973(8)}Ga_{1.767(8)}O_{3.752(8)}$, using the partially defect, mixed valence model. Space group *Fd$\bar{3}$m*, *a* = 8.31282(9) Å. Rp = 1.71%, wRp = 2.54%. Measured density = 5.437 g cm^{-3}, calculated density = 5.563 g cm^{-3}.

Wyckoff site	Atom	x	y	z	U_{iso} / Å^2	Occupancy
8a	Ga	0.125	0.125	0.125	0.0058(1)	0.745(4)
	Co	0.125	0.125	0.125	0.0058(1)	0.175(4)
16d	Ga	0.5	0.5	0.5	0.0058(1)	0.511(3)
	Co	0.5	0.5	0.5	0.0058(1)	0.399(3)
32e	O	0.25641(6)	0.25641(6)	0.25641(6)	0.0064(1)	0.938(2)

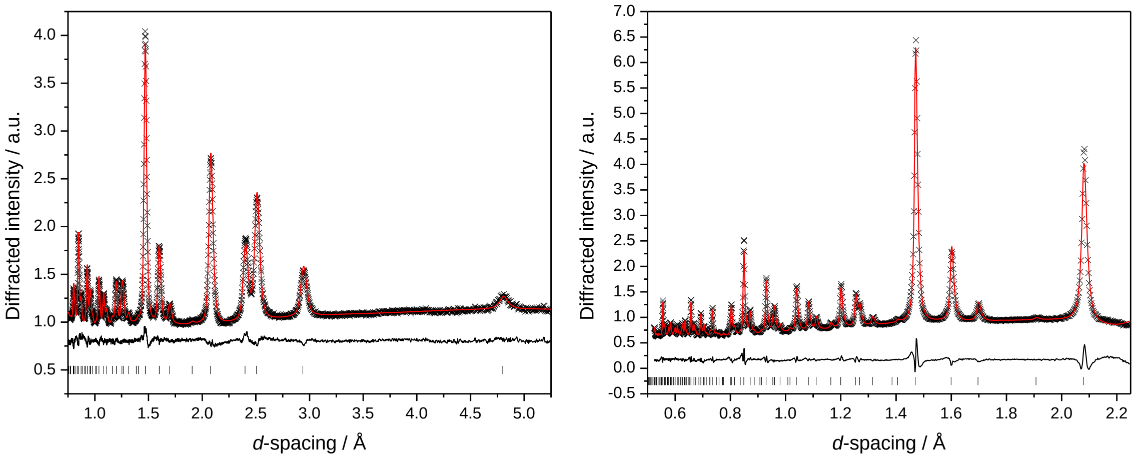

Figure 4.13 Result of Rietveld refinement for solvothermal CoGaO using the partially defect, mixed valence model. Left: data from GEM bank 3 (mean scattering angle 34.9°). Right: data from GEM bank 5 (mean scattering angle 91.3°).

The refined composition is $Co_{0.973(8)}Ga_{1.767(8)}O_{3.752(8)}$, and charge balance requires approximately 20% of the Co to be Co^{3+}. The assignment of the +2 oxidation state from Co K-edge XANES was by qualitative comparison with standard samples only and is therefore uncertain enough that the presence of some Co^{3+} is entirely plausible. No attempt was made to determine the distribution of Co^{2+}/Co^{3+} across the spinel sites, although Co_3O_4 is a normal spinel with the Co^{3+} occupying the octahedral sites, due to the high crystal-field stabilisation energy for this low-spin d^6 ion in octahedral coordination, so it is possible that the Co^{3+} in the cobalt gallate spinel would also show a preference for octahedral coordination.

4.2.2.2.5. PDF analysis

All of the models discussed above are extremely similar in terms of composition and cation distribution (Table 4.7 and Table 4.8), however, only model 4 is consistent with all experimental observations and this will therefore be used for PDF analysis.

Table 4.7 Comparison of Co:Ga ratios for the various spinel models for the cobalt gallate spinel.

	Model 1	Model 2	Model 3	Model 4
Ga	1.73	1.97	1.78	1.82
Co	1	1	1	1

Table 4.8 Comparison of cation distribution in the two spinel models for the cobalt gallate spinel. Numbers given are % cations on each site.

	Model 1		Model 2		Model 3		Model 4	
	O_h	T_d	O_h	T_d	O_h	T_d	O_h	T_d
Ga	58	42	55	45	60	40	58	42
Co	82	18	100	0	79	21	82	18

The low-*r* region of the pair distribution function (PDF) of the cobalt gallate spinel is shown in Figure 4.14. The $T_0(r)$ constant as determined by fitting the low-*r* region up to and including the first peak, is 0.3388. This value is in good agreement with that calculated for Model 4, which is 0.3676.

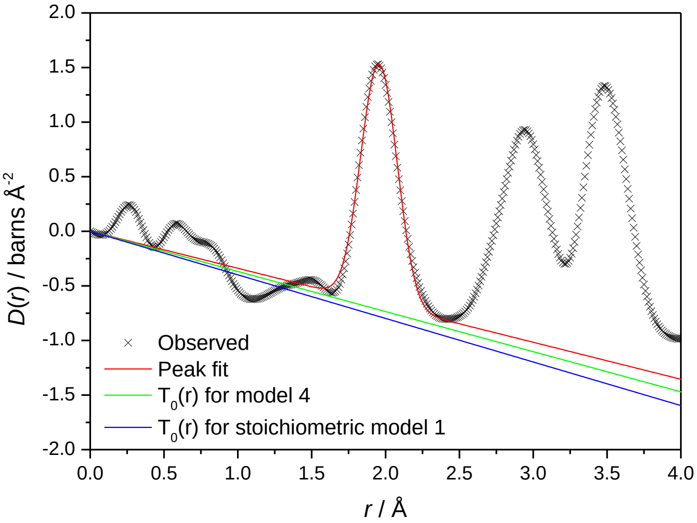

Figure 4.14 The measured PDF of the cobalt gallate spinel with the result of peak fitting (red), and the calculated $T_0(r)$ slopes for model 4 (green) and stoichiometric model 1 (blue).

The initial fit of spinel model 4 to the PDF, obtained by refining only the thermal broadening and correlated motion parameters, was very good (Figure 4.15). No further improvement to the fit could be made within the parameters of the cubic ($Fd\bar{3}m$) structure.

On close examination of the low-*r* region of the fit, it is clear that the first peak is not described adequately by this model. This was also found to be the case for γ-Ga_2O_3 (Section 3.3.2.3), and was attributed to a local distortion of the GaO_6 octahedra, and a model in space group $F\bar{4}3m$ with 3 long and 3 short octahedral Ga–O bonds was able to account for it. This type of octahedral distortion appears to be common for gallium oxides as it is also found in the α and β polymorphs. In $CoGa_2O_4$, however, 40% of the octahedral sites are occupied by Co^{2+}, which, with a d^7 electronic configuration, would perhaps be likely to show a Jahn-Teller distortion with 4 longer (or shorter) and 2 shorter (or longer) bonds. This means that modelling the low-*r* region of the PDF with a 3 + 3 type octahedral distortion as for γ-Ga_2O_3 would be inappropriate. It is also important to note that the neutron scattering lengths of Ga and Co are rather different (Ga = 7.288 fm and Co = 2.49 fm) and so the contributions of Ga will dominate the neutron PDF, which suggests that any attempt to model the local distortion of this structure with regard to cobalt would not be meaningful.

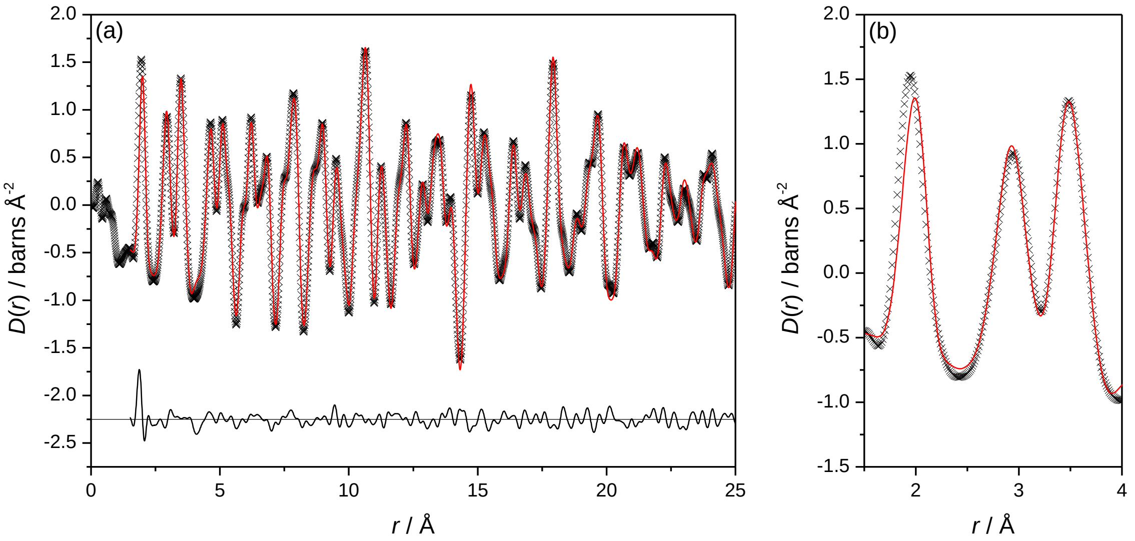

Figure 4.15 (a) The result of PDF analysis of $CoGa_2O_4$ using the Rietveld model 4 as a starting point. wRp = 13.3% (b) Close-up view of the low-*r* region of the fit, emphasising the discrepancy in the position and shape of the first peak.

The $CoGa_2O_4$ spinel produced by solvothermal oxidation of gallium metal has an average structure which can be described by a non-defect, largely inverse spinel in space group $Fd\bar{3}m$. Its local structure is distorted from cubic symmetry, as evidenced by PDF analysis. Due to the complexity of the material with mixed cation occupancy on both octahedral and tetrahedral sites, no further modelling has been carried out.

4.2.2.3. Magnetic behaviour

The magnetisation of the solvothermal $CoGa_{1.78}O_{3.67}$ was studied by SQUID magnetometry. The zero-field cooled (ZFC) and field cooled (FC) magnetisation (*M*) *vs* temperature (*T*) curves are shown in Figure 4.16 and the *M vs* applied field (*H*) hysteresis loops are shown in Figure 4.17. The sample is clearly paramagnetic at temperatures above 18 K, as evidenced by the reduction in *i* with temperature and the lack of hysteresis loop in the *M vs H* data at high temperature.

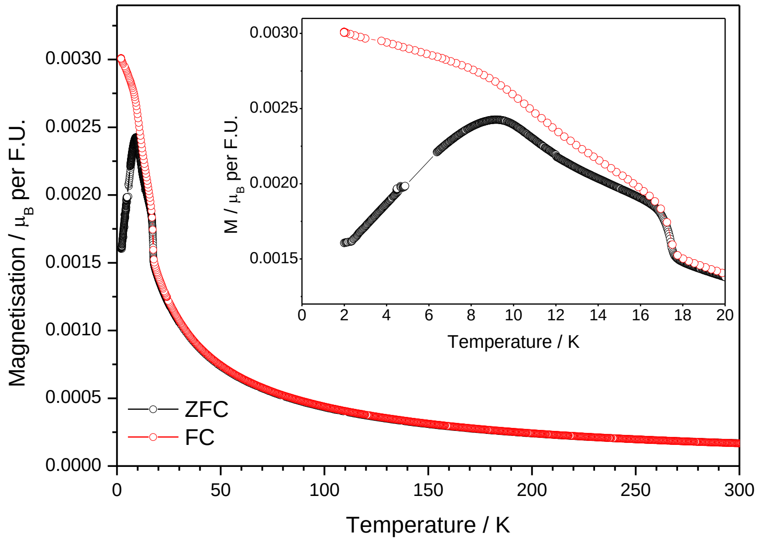

Figure 4.16 Magnetisation *vs* temperature for solvothermal cobalt gallate, with inset showing an enlargement of the low temperature region.

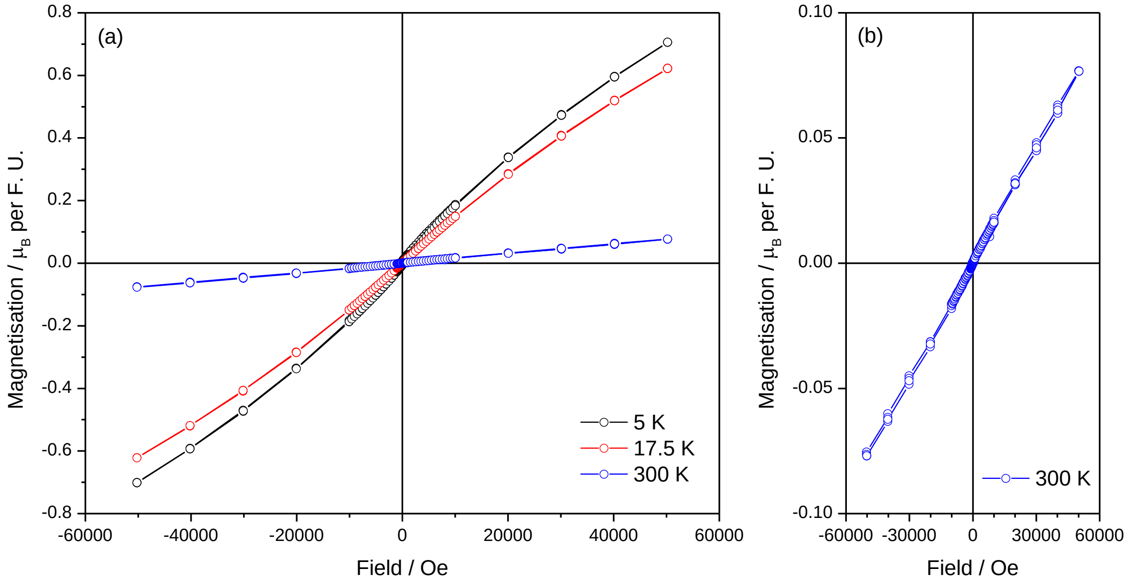

Figure 4.17 (a) Magnetisation *vs* applied field curves for the cobalt gallate spinel at three different temperatures and (b) view of the 300 K data showing its linearity.

Magnetic ordering is present at temperatures below 18 K, as evidenced by the slightly “s-shaped” *M vs H* hysteresis loops which are characteristic of a ferrimagnetic material - one in which there are two antiferromagnetically aligned magnetic sublattices whose moments are unequal, thus a net moment is present in a certain direction. The magnetic behaviour of a $CoGa_2O_4$ spinel, produced by the ceramic method and with a reported inversion parameter, $x = 0.29$, was examined by Fiorani *et al.*.[48] who determined that the material was antiferromagnetic with a Néel temperature, $T_N = 10$ K. The ZFC data for the solvothermal cobalt gallate indeed reaches a maximum at 10 K, however then it displays different behaviour in the region 10 – 18 K. As T_N is often reported as the temperature at which the ZFC and FC curves diverge, it would be more accurate to quote the value of 18 K for this material. Close inspection of the low-field region of the *M* vs *H* loops at 5 K and 17.5 K reveals that the loop is "closed" at 17.5 K, while it is open at 5 K, (Figure 4.18) indicating that the sample exhibits greater remanence (the magnetisation which remains in the material when an external field is removed) and coercivity (the reverse applied field necessary to remove the magnetisation, *i.e.* the resistance of the material to becoming demagnetised) at the lower temperature. The hysteresis loops also indicate that the material does not become magnetically saturated with an applied field of 50000 Oe.

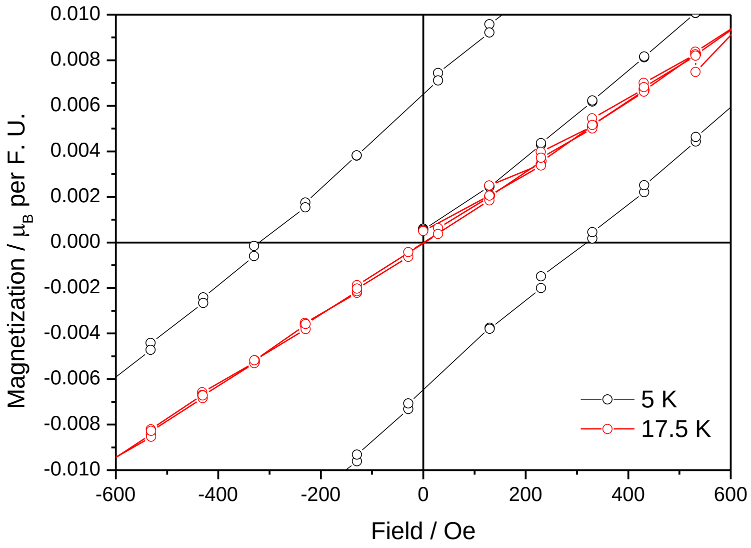

Figure 4.18 Close up of the low-field region of the *M* vs *H* curves for the cobalt gallate spinel at 5 K and 17.5 K

4.2.3. Iron gallium oxide

4.2.3.1. General characterisation

As for the Co-Ga spinel, TEM imaging and EDX were used to characterise the Fe-Ga spinel. It was found to be nanocrystalline, consisting of oblong particles with a fairly wide size distribution, between 20 and 200 nm (Figure 4.19). EDX results indicated that the average Fe:Ga ratio was close to 1:1, however some areas of the sample were noticeably Fe rich (see Table 4.9 and Figure 4.19).

Table 4.9 EDX results for gallium iron spinel from the regions labelled in Figure 4.19.

Region	Fe / wt %	Ga / wt %	Region	Fe / wt %	Ga / wt %
1	83	17	**7**	34	66
2	43	57	**8**	43	57
3	39	61	**9**	35	65
4	41	59	**10**	44	56
5	40	60	**11**	37	63
6	84	16	**12**	26	74

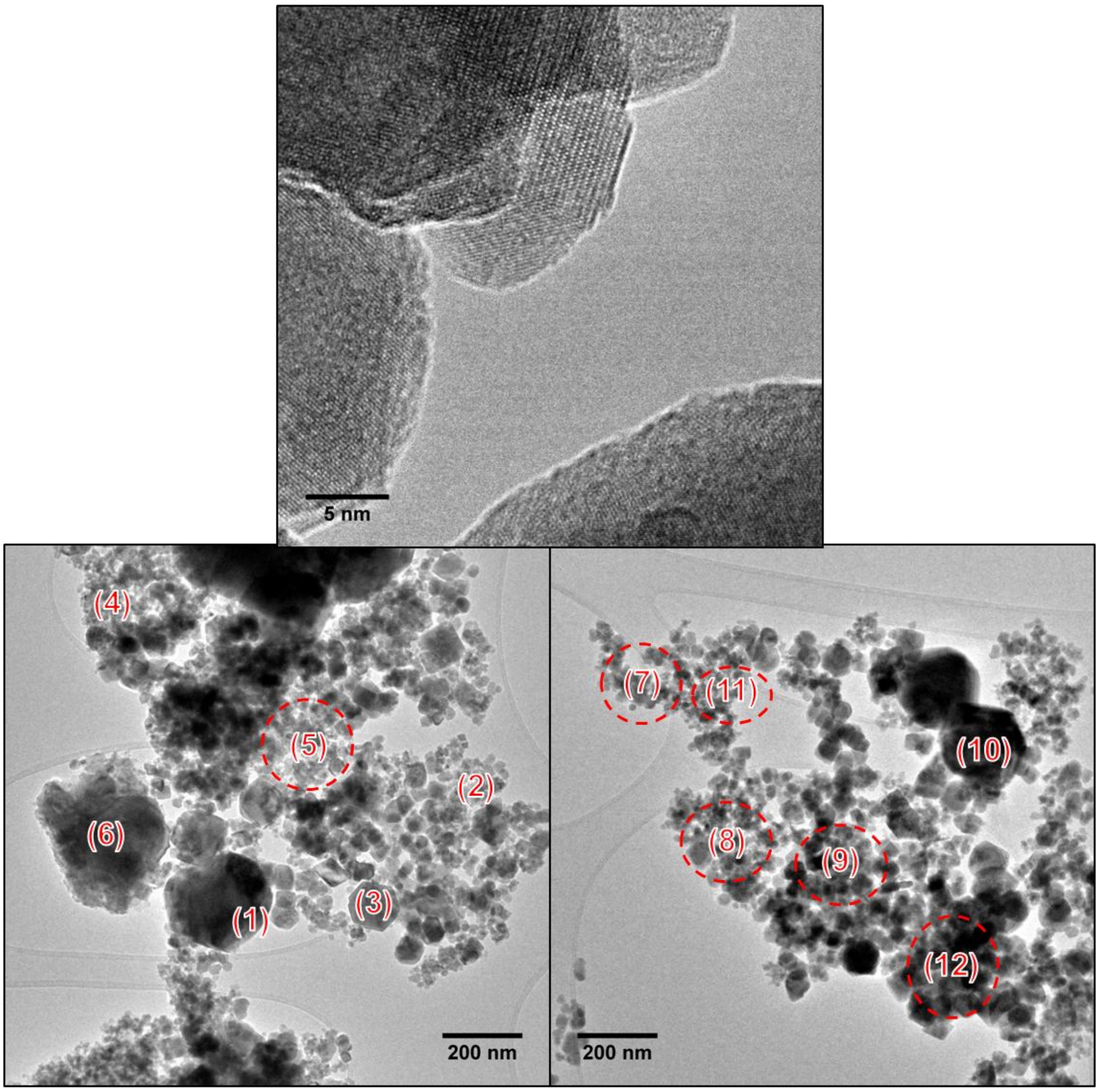

Figure 4.19 TEM images of the iron gallium spinel. The numbers in the lower panels correspond to regions used for EDX analysis in Table 4.9.

Fe K-edge XANES was carried out to elucidate the oxidation state of iron in the spinel, which was found to be apparently purely Fe^{2+} (Figure 4.20). The oxidation state of ε-$GaFeO_3$ produced by the ceramic method was clearly Fe^{3+} as for the standard Fe_2O_3. The pre-edge feature is far smaller in the iron gallate spinel than in the reference materials, indicating a lower proportion of Fe in non-centrosymmetric environments. Hence, the Fe^{2+} in the iron gallium spinel is likely to be largely in octahedral coordination.

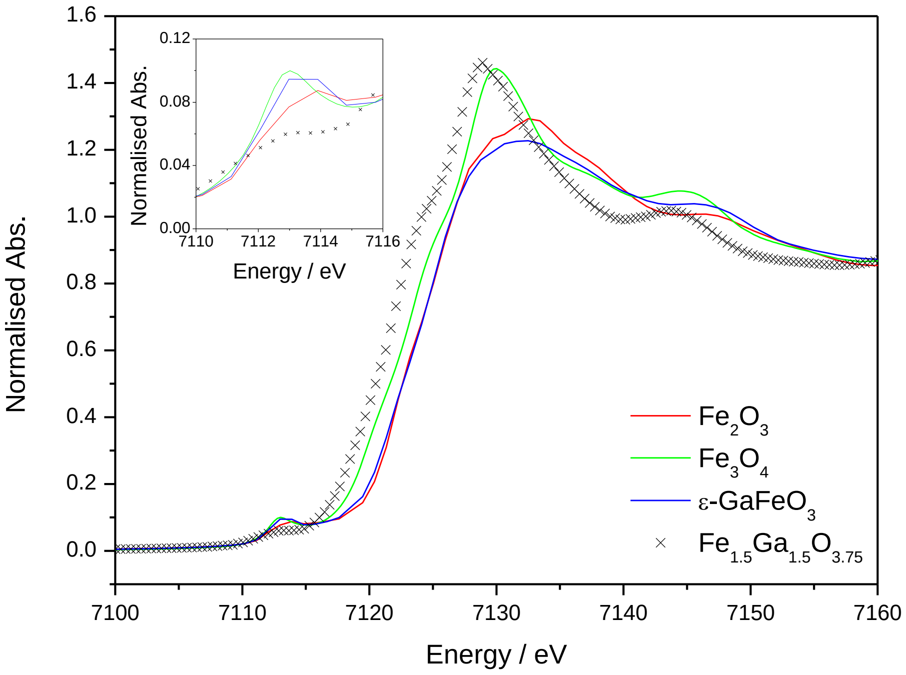

Figure 4.20 Fe K-edge XANES of the iron gallium spinel and relevant standard materials.

The thermal behaviour of the iron gallium spinel was investigated with *in situ* X-ray diffraction and TGA. No change in the XRD pattern of the material was observed up to a temperature of 450 °C, at which point there was a sudden change in peak positions to lower angle (indicating a sudden increase in lattice parameter) and an increase in crystallinity (Figure 4.21). Further *ex situ* heating to a temperature of ~1400 °C was required to bring about the phase change to orthorhombic ε-$GaFeO_3$.[38]

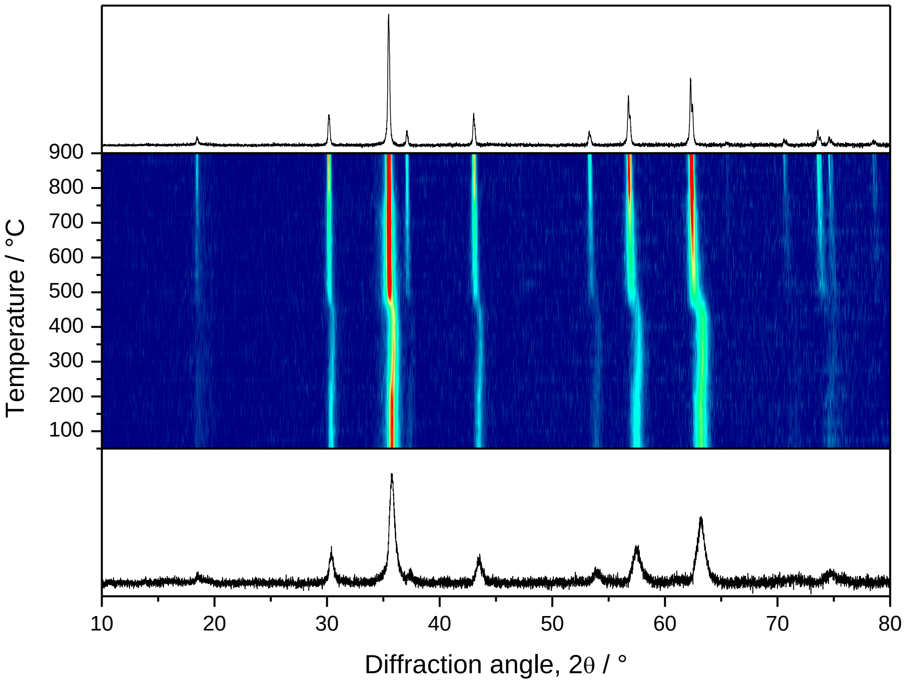

Figure 4.21 Thermodiffraction of the iron gallium spinel.

Thermogravimetric analysis in air, Figure 4.22(a), revealed an initial mass loss of 1.5%, attributed to the loss of water and surface-associated residual organic groups. Starting at approximately 450 °C a mass increase is observed which can be attributed to the uptake of oxygen for the oxidation of the Fe^{2+}. This oxidation could be responsible for the changes observed in the X-ray diffraction pattern at this temperature. In contrast, TGA in $N_{2,}$ Figure 4.22(b), reveals an initial mass loss of 1% at around 200 °C and a subsequent mass loss of 3% by the time the maximum temperature was reached.

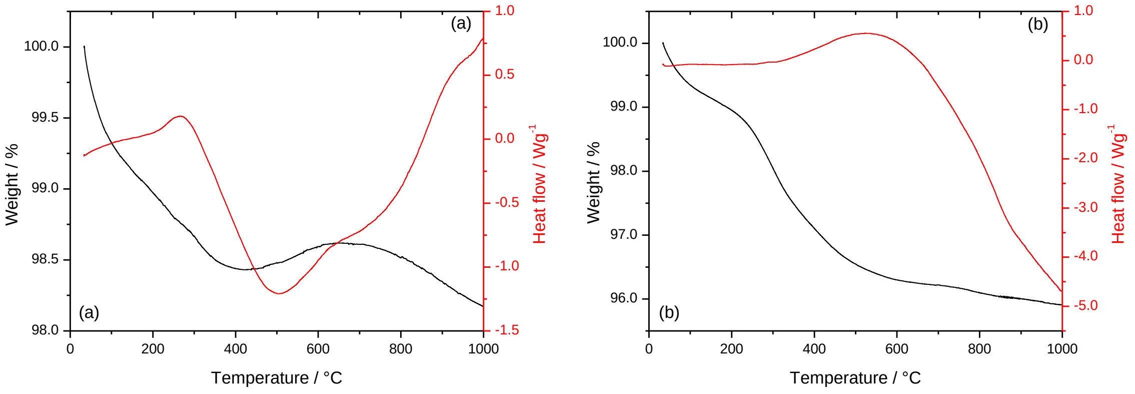

Figure 4.22 TGA traces of the iron gallium spinel, (a) measured in air and (b) measured in N_2

The as-synthesised iron gallium spinel was attracted to a strong magnet at room temperature (see Figure 4.2), indicating the presence of some kind of magnetic ordering, and a net magnetic moment, in the material.

The XRD pattern of ε-$GaFeO_3$ made by the ceramic method is shown in Figure 4.23. All the observed peaks are consistent with the orthorhombic phase.

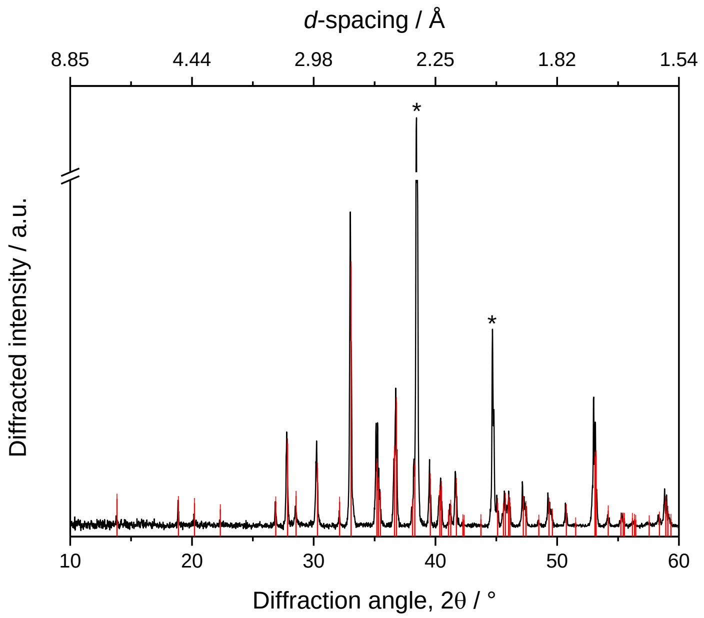

Figure 4.23 The X-ray diffraction pattern of ε-$GaFeO_3$ prepared by the ceramic method with vertical bars denoting the expected peak positions and intensities. Peaks marked with a * are from the aluminium sample holder.

4.2.3.2. *Total neutron scattering*

The result of a Le Bail profile fit to the neutron diffraction data for the iron gallium spinel is shown in Figure 4.24. A Le Bail fit was used to obtain well-fitting profile parameters for the broadened peaks from this nanocrystalline sample, prior to attempting a full refinement. It can be seen that the goodness of fit is rather poor, particularly for a profile fit which is not biased by the model structure, which implies that the chosen space group ($Fd\bar{3}m$) is probably not appropriate for this sample. Figure 4.25 shows a close-up view of the fit revealing a noticeable offset in several of the peaks and some broad features in the background which may be evidence of superstructure of some kind.

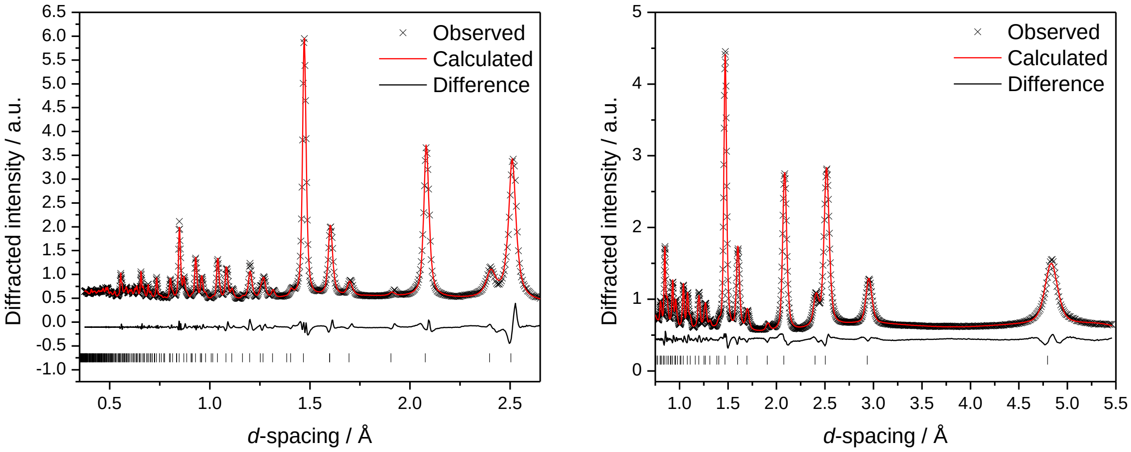

Figure 4.24 The result of a Le Bail fit to the neutron diffraction data for the iron gallium spinel using space group $Fd\bar{3}m$. Left: GEM bank 5, Right: GEM bank 3. The cubic lattice parameter, *a* = 8.3043(6) Å, Rp = 2.75%, wRp = 3.36%.

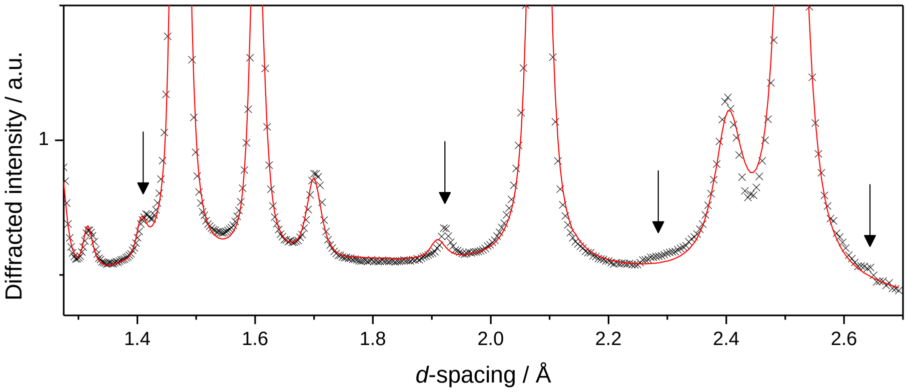

Figure 4.25 Close-up view of a region of the Le Bail fit for the iron gallium spinel in space group $Fd\bar{3}m$, with arrows identifying the subtle but significant discrepancies in the fit.

The high-resolution powder XRD pattern from a Panalytical Pro X'pert diffractometer (λ = 1.54056 Å) of this sample is shown in Figure 4.26. Although the background level was unexpectedly high (probably due to fluorescence which is a common problem for iron-containing materials when using Cu K_α radiation) it is clear that the material is not a single phase, and that one phase is far more highly crystalline than the other. It appears that both phases can be assigned the $Fd\bar{3}m$ spinel structure but with slightly different lattice parameters and based on the relative peak intensities it is reasonable to assume that the less crystalline material is the majority phase.

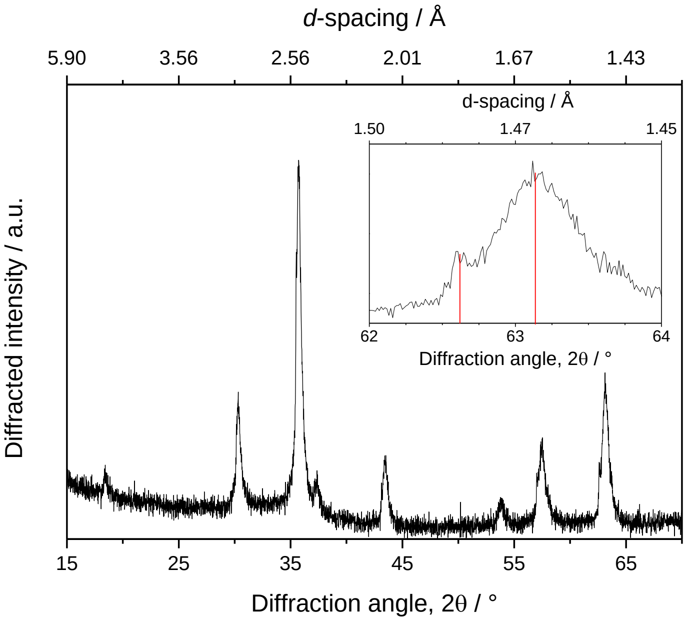

Figure 4.26 The powder XRD pattern of the gallium iron spinel.

Figure 4.27 shows the result of a two-phase Le Bail fit to the neutron diffraction pattern where both phases were cubic spinels and had starting cell parameters based on the positions of the peaks in the powder XRD pattern (a_1 = 8.383 Å and a_2 = 8.323 Å)

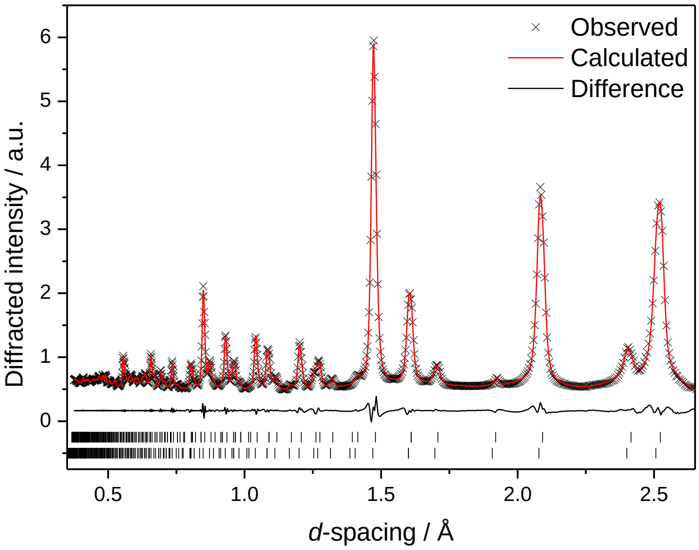

Figure 4.27 The result of a Le Bail fit to the neutron diffraction data for the iron gallium sample using two spinels in space group $Fd\bar{3}m$. Left: GEM bank 5, Right: GEM bank 3. The cubic lattice parameters are, a_1 = 8.3668(9) Å and a_2 = 8.3127(5) Å, Rp = 1.74%, wRp = 2.24%.

The identity of the two phases is now in question. Whilst a pure iron oxide is perhaps the most obvious choice for one of them, the larger lattice parameter (a_1 = 8.3668(9) Å) does not agree with that of Fe_3O_4 (a = 8.3941 Å)[49] and Fe_2O_3 (a = 8.3474 Å)[50] is unlikely due to the overwhelming majority of the iron present being in the +2 oxidation state, according to the XANES result (Figure 4.20). The EDX results (Figure 4.19) tend to suggest that both phases are mixed metal oxides, one with approximately 60% gallium and the other with approximately 20%.

As shown in Figure 4.2, the solvothermal iron-gallium spinel apparently exhibits room temperature magnetic order. Since neutrons have a spin of ½ and the associated magnetic moment, they are able to interact with magnetic moments caused by the electron clouds surrounding atoms. In a magnetically ordered material this can give rise to Bragg peaks from which the symmetry of the magnetic structure can be deduced. Since magnetic neutron scattering arises from an electronic and not nuclear interaction it is subject to a form factor, and thus the intensity of magnetic peaks reduces rather rapidly at higher scattering angle.

This effect can be seen in Figure 4.28 where the calculated neutron diffraction patterns of magnetite Fe_3O_4 (which, of course, also adopts the spinel structure) with and without magnetic contributions on the Fe sites are compared. The magnetic contributions are rather small at $d < 1.5$ Å. In some cases (notably the 111, 222, 331 and 531 peaks) the magnetic scattering intensity is greater than the nuclear scattering intensity.

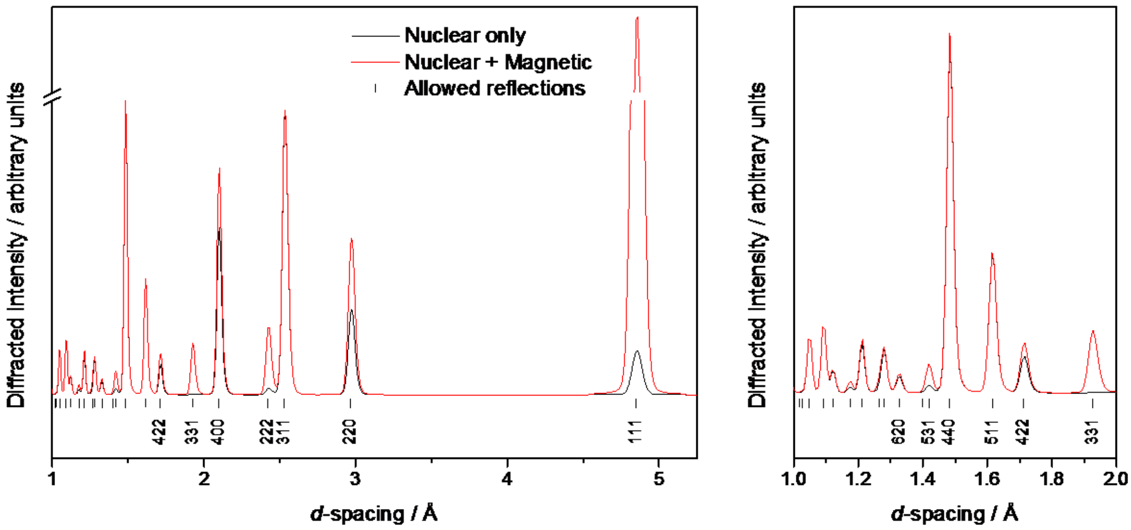

Figure 4.28 The calculated neutron diffraction patterns for magnetite Fe_3O_4 both with and without magnetic contribution. Panel on the right is a closer view of the region $1 \leq d \leq 2$ Å.

Since the atomic arrangement in the iron gallium spinel(s) is likely to be quite similar to that of magnetite, at least in terms of which sites are occupied by magnetic cations, some insight into their structures can be gained from the above discussion. The major contribution to the intensities of the 331 and 531 peaks in the iron gallium sample must come from the spinel with the larger unit cell (as otherwise they are simply not in the correct position). Therefore, since these peaks have a strong magnetic component, it follows that the spinel with the larger unit cell is the more strongly magnetic. This is in accordance with the assumption that the phase with the larger unit cell is the iron-rich spinel. In order to complete a full structural refinement of the iron-gallium spinel sample, the magnitude and orientation of the magnetic moments on the iron atoms *in both phases* would need to be accounted for. The magnetic scattering is likely to contribute intensity to the higher *d*-spacing peaks. Because of the lack of a robust model for their atomic structure(s), further analysis of the magnetic structure of these materials cannot be attempted.

The neutron PDF of the iron-gallium spinel was fitted using two spinel phases with the lattice parameters and proportions from the Le Bail fit to the neutron diffraction data (Table 4.10). Model 1 (minority phase) was taken from Oles *et al.*[35] and Model 2 is a nearly stoichiometric spinel which is consistent with the XANES result (that the majority of the sample has iron in the +2 oxidation state and in octahedral coordination) and the composition from EDX (60% Ga, 40% Fe). It was not possible to refine these models.

Table 4.10 The site occupancies of two spinel models proposed for the iron gallium sample

Site	Element	Model 1 $Ga_{0.9}Fe_{2.1}O_4$ $a_1 = 8.3668$ Å		Model 2 $Ga_{1.8}Fe_{1.2}O_{3.9}$ $a_2 = 8.3127$ Å	
8a	Ga	0.58		1	
	Fe	0.42		0	
16d	Ga	0.16		0.4	
	Fe	0.84		0.6	
32e	O	1.0	$x = 0.255$	0.975	$x = 0.2546$

The fit is shown in Figure 4.29, and is quite satisfactory (wRp = 18.7%). There is evidence for local structural distortion as has also been the case for γ-Ga_2O_3 and the cobalt gallate spinel.

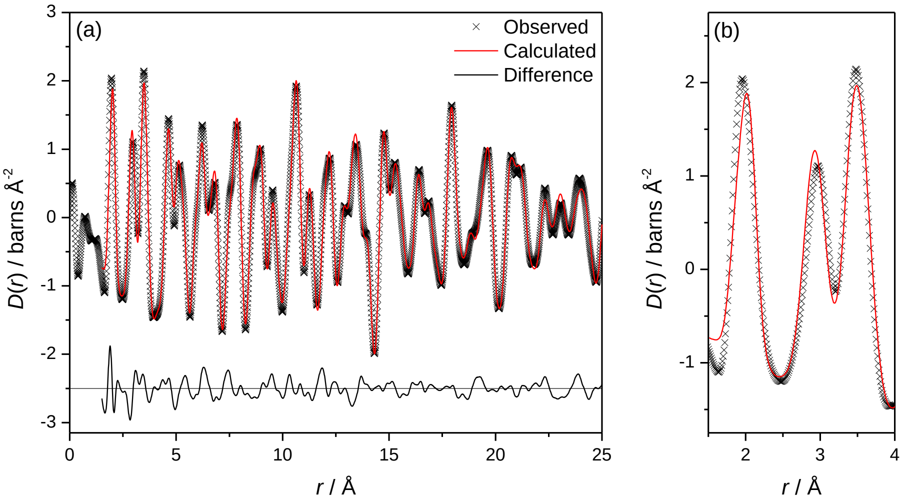

Figure 4.29 (a) The result of PDF analysis for the iron gallium spinel and (b) a close-up view of the low-*r* region showing discrepancies in the fit to the first two peaks.

It is important to note that there is a magnetic contribution to the PDF, which is non-trivial to define because of the magnetic form factor affecting the scattered intensity. However, magnetic correlation peaks tend to be rather broad and the PDF is therefore usually dominated by nuclear scattering.

4.2.3.3. Magnetic behaviour

The *M vs T* and *M vs H* curves for ε-$GaFeO_3$ are shown in Figure 4.30. The material is ferrimagnetic due to the presence of Fe on multiple sites within the structure,[51-53] with its Curie temperature apparently dependent on the synthesis method. For this sample of ε-$GaFeO_3$, the Curie temperature, defined as a maximum in $|dM/dT|$, is 300 K. The *M vs H* hysteresis reveals the expected behaviour for a ferrimagnetic material, with a saturation magnetisation of around 0.8 μ_B per formula unit. These properties are in excellent agreement with those quoted for an equivalent ceramic-method produced sample by Mohamed *et al.*[52] The shape of the hysteresis loop is known as "wasp waisted" as it is much less open in the middle section than in the upper and lower sections, and this behaviour is usually observed in systems with multiple magnetic components, as is the case when a material is made up of a mixture of grain sizes.[54]

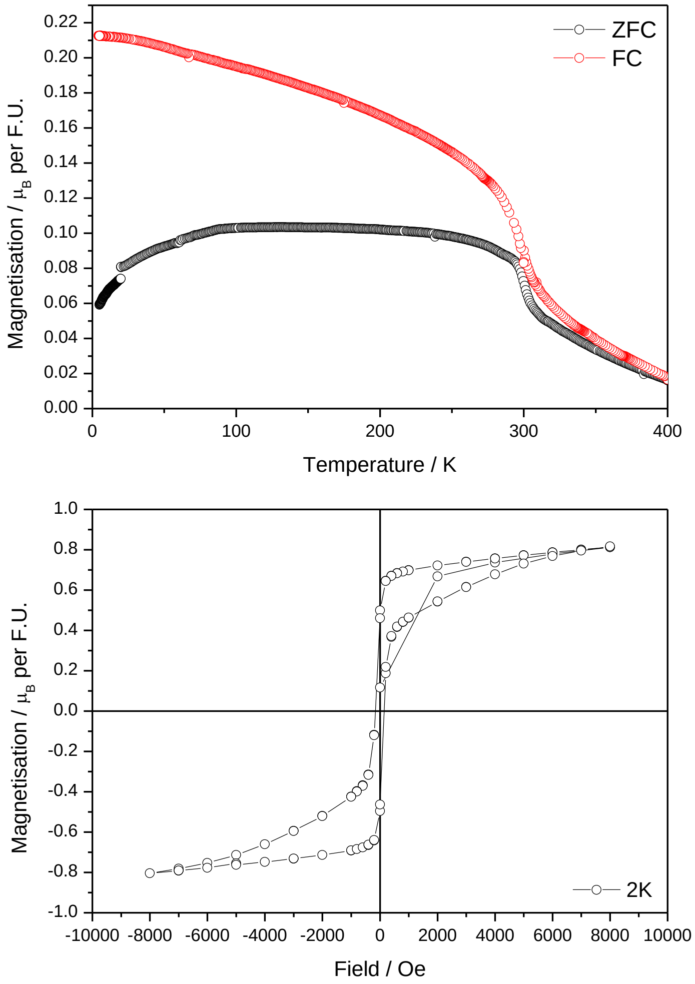

Figure 4.30 Upper: the FC and ZFC *M vs T* curves for ε-$FeGaO_3$. Lower: *M* vs *H* hysteresis loop measured at 2K.

It is impossible to accurately determine the magnetic properties of the solvothermal iron-gallium spinel sample since it appears to consist of two different materials, both spinels and both with the potential to have a distribution of cations across the A and B sites. Previous reports of $FeGa_2O_4$, for example, found that the Fe^{2+} ions were distributed fairly equally across both cation sites, leading to a weak ferrimagnetism at low temperatures.[55-56] A study of Ga-doped Fe_3O_4 found that low-level (up to 20%)

doping increased the net magnetic moment of the material because the Ga substituted preferentially onto the tetrahedral site, thus lessening the "cancelling out" effect of the distribution of Fe over the two sites.[57]

The *M vs T* curves (Figure 4.31) are consistent with ferrimagnetism at lower temperatures, and although the ZFC magnetisation begins to decrease at temperatures above 125 K, the behaviour is not paramagnetic and long-range magnetic order apparently persists to temperatures in excess of 300 K.

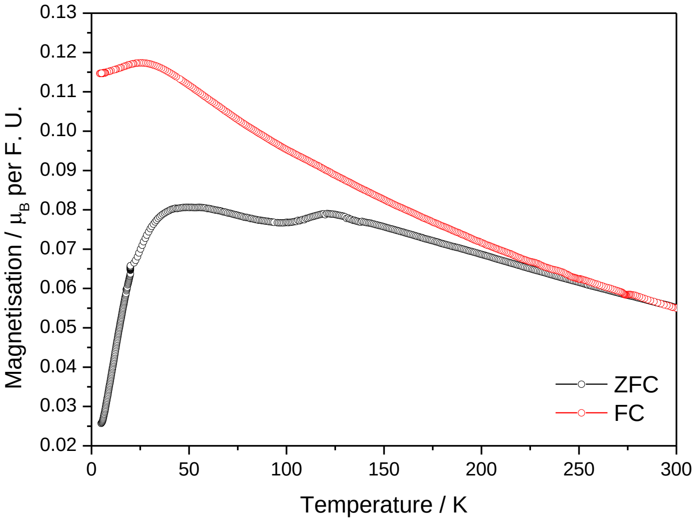

Figure 4.31 *M vs T* curves for the solvothermal iron gallium spinel.

The *M vs H* hysteresis loops are shown in Figure 4.32. It will be noted that the hysteresis loop at 300 K is closed (Figure 4.32), which may simply be a result of being close to the ordering temperature, as was seen in the hysteresis loop of the cobalt-gallium spinel at 17.5 K (Figure 4.18). Alternatively, this behaviour, when observed in nanometric samples is often associated with superparamagnetism. This occurs when individual nanoparticles consisting of a single magnetic domain interact with other particles, with their moments aligning under an applied magnetic field as with a paramagnetic material. The interactions are much stronger than those in a "normal" paramagnet, leading to the shape of the hysteresis curve and the obvious attraction of the bulk sample to a strong magnet. Further measurements would be required to determine whether this sample exhibits superparamagnetism.

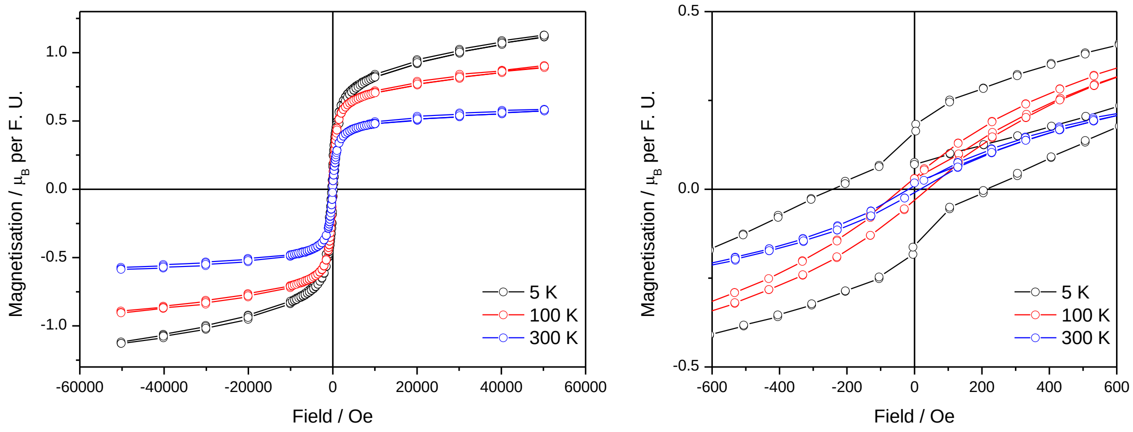

Figure 4.32 Left: M *vs* H loops for the solvothermal iron gallium spinel measured at 5, 100 and 300 K, and Right: close-up view of the low-field region of the hysteresis loops.

4.3. Conclusions

The solvothermal synthesis of several gallium-containing mixed metal oxides with the spinel structure has been achieved. The materials have the general formula $M_xGa_{3-x}O_{4-y}$ where M = Zn, Ni, Co and Fe. This simple synthetic method offers great potential for the synthesis of other mixed oxides, including solid solutions between the already-made spinels and other complex ternary/quaternary oxides.

The cobalt gallium spinel produced by solvothermal oxidation of gallium metal has an average structure which can be described by a slightly oxygen-deficient spinel in space group $Fd\bar{3}m$ with formula $Co_{0.973(8)}Ga_{1.767(8)}O_{3.752(8)}$. To achieve charge balance, approximately 20% of the Co content must be Co^{3+}. The local structure is distorted from cubic symmetry, as evidenced by PDF analysis, however due to the complexity of the material with mixed cation occupancy on both octahedral and tetrahedral sites, no further modelling has been carried out. The cobalt gallium spinel exhibits ferrimagnetic behaviour at low temperatures with the transition to paramagnetism occurring at ~ 18K.

The iron gallium spinel was found to contain a small amount of an iron-rich impurity phase which, combined with the magnetic ordering of the material at room temperature, prevented detailed structure refinements (Rietveld or PDF). Nevertheless the experimental observations are consistent with the majority phase being a cubic spinel of composition $Ga_{1.8}Fe_{1.2}O_{3.9}$ where all the iron is in the +2 oxidation state. The magnetic behaviour of the iron gallium spinel is consistent with ferri or ferromagnetic ordering at temperatures below 125 K, and although the zero-field-cooled magnetisation decreases above this temperature there is no obvious transition to paramagnetic behaviour, indicating that long range order persists at temperatures in excess of 300 K.

4.4. References

1. Punn, R.; Feteira, A. M.; Sinclair, D. C.; Greaves, C., *J. Am. Chem. Soc.* **2006,** *128*, 15386.
2. Ueda, N.; Hosono, H.; Waseda, R.; Kawazoe, H., *Appl. Phys. Lett.* **1997,** *70*, 3561.
3. Grimes, N. W., *Physics in Technology* **1975,** *6*, 22.
4. Wojtowicz, P., *Magnetics, IEEE Transactions on* **1969,** *5*, 840.
5. Tretyakov, Y. D.; Gordeev, I. V.; Kesler, Y. A., *J. Solid State Chem.* **1977,** *20*, 345.
6. Lager, G. A.; Armbruster, T.; Ross, F. K.; Rotella, F. J.; Jorgensen, J. D., *J. Appl. Crystallogr.* **1981,** *14*, 261.
7. Kawazoe, H.; Ueda, K., *J. Am. Ceram. Soc.* **1999,** *82*, 3330.
8. Chen, Y. C.; Xie, K.; Pan, Y.; Zheng, C. M., *J. Power Sources* **2011,** *196*, 6493.
9. Cheng, F. Y.; Shen, J. A.; Peng, B.; Pan, Y. D.; Tao, Z. L.; Chen, J., *Nature Chemistry* **2011,** *3*, 79.
10. Wachs, I. E.; Routray, K., *Acs Catalysis* **2012,** *2*, 1235.
11. Conrad, F.; Bauer, M.; Sheptyakov, D.; Weyeneth, S.; Jaeger, D.; Hametner, K.; Car, P. E.; Patscheider, J.; Gunther, D.; Patzke, G. R., *Rsc Advances* **2012,** *2*, 3076.
12. Navrotsky, A.; Kleppa, O. J., *J. Inorg. Nucl. Chem.* **1968,** *30*, 479.
13. Liu, Z. S.; Hu, P.; Jing, X. P.; Wang, L. X., *J. Electrochem. Soc.* **2009,** *156*, H43.
14. Costa, G. K. B.; Pedro, S. S.; Carvalho, I. C. S.; Sosman, L. P., *Opt. Mater.* **2009,** *31*, 1620.
15. Suzuki, T.; Murugan, G. S.; Ohishi, Y., *J. Lumin.* **2005,** *113*, 265.
16. Omata, T.; Ueda, N.; Ueda, K.; Kawazoe, H., *Appl. Phys. Lett.* **1994,** *64*, 1077.
17. Hirano, M.; Imai, M.; Inagaki, M., *J. Am. Ceram. Soc.* **2000,** *83*, 977.
18. Hirano, M.; Sakaida, N., *J. Am. Ceram. Soc.* **2002,** *85*, 1145.
19. Hirano, M.; Okumura, S.; Hasegawa, Y.; Inagaki, M., *J. Solid State Chem.* **2002,** *168*, 5.
20. Itoh, S.; Toki, H.; Sato, Y.; Morimoto, K.; Kishino, T., *J. Electrochem. Soc.* **1991,** *138*, 1509.
21. Yu, Z.; Chen, H.; Li, Z. W.; Yang, Z. M.; Song, H. B.; Gao, Y. L.; Zhang, Y. S.; Jin, Y.; Jiao, Z. F.; Gong, M.; Zhu, J. G.; Sun, X. S., *Mater. Lett.* **2009,** *63*, 37.
22. Chen, X.; Xue, H.; Li, Z. H.; Wu, L.; Wang, X. X.; Fu, X. Z., *J. Phys. Chem. C* **2008,** *112*, 20393.
23. Lee, J. Y.; Kim, D. S.; Na, C. W.; Park, J., *J. Phys. Chem. C* **2007,** *111*, 12207.
24. Sanford, S.; Kazmierczak, A. L.; Edwards, D. D., *Solid State Sciences* **2007,** *9*, 914.
25. Omata, T.; Ueda, N.; Hikuma, N.; Ueda, K.; Mizoguchi, H.; Hashimoto, T.; Kawazoe, H., *Appl. Phys. Lett.* **1993,** *62*, 499.
26. Chu, X. F.; Zheng, C. M., *Mater. Chem. Phys.* **2004,** *88*, 110.
27. Biswas, S. K.; Sarkar, A.; Pathak, A.; Pramanik, P., *Talanta* **2010,** *81*, 1607.
28. Gurunathan, K.; Baeg, J. O.; Lee, S. M.; Subramanian, E.; Moon, S. J.; Kong, K. J., *Int. J. Hydrogen Energy* **2008,** *33*, 2646.
29. Chen, L. Y.; Horiuchi, T.; Mori, T., *Appl. Catal., A* **2001,** *209*, 97.

30. Xue, H.; Li, Z. H.; Ding, Z. X.; Wu, L.; Wang, X. X.; Fu, X. Z., *Cryst. Growth. Des.* **2008,** *8*, 4511.
31. Greenwald, S.; Pickart, S. J.; Grannis, F. H., *The Journal of Chemical Physics* **1954,** *22*, 1597.
32. Pajaczkowska, A.; Demelo, O.; Leccabue, F.; Pelosi, C.; Fiorani, D.; Testa, A. M.; Paparazzo, E., *J. Cryst. Growth* **1990,** *104*, 498.
33. Shi, J. M.; Yu, W. T.; Bergmann, I.; Bremers, H.; Sepelak, V.; Mader, W.; Becker, K. D., *J. Alloys Compd.* **2010,** *504*, S432.
34. Soubeyroux, J. L.; Fiorani, D.; Agostinelli, E., *J. Magn. Magn. Mater.* **1986,** *54-7*, 83.
35. Oles, A., *Acta Phys. Pol.* **1966,** *30*, 125.
36. Ghose, J., *J. Solid State Chem.* **1989,** *79*, 189.
37. Bhattacharya, U.; Darshane, V. S., *J. Mater. Chem.* **1993,** *3*, 299.
38. Burnett, D., MChem dissertation, Warwick, 2012.
39. Areán, C. O.; Trobajo-Fernandez, M. C., *physica status solidi (a)* **1985,** *92*, 443.
40. Hall, M. D.; Underwood, C. K.; Failes, T. W.; Foran, G. J.; Hambley, T. W., *Aust. J. Chem.* **2007,** *60*, 180.
41. O'Neill, H. S. C.; Navrotsky, A., *Am. Mineral.* **1983,** *68*, 181.
42. Ball, J. A.; Pirzada, M.; Grimes, R. W.; Zacate, M. O.; Price, D. W.; Uberuaga, B. P., *J. Phys.: Condens. Matter* **2005,** *17*, 7621.
43. Roelofsen, J. N.; Peterson, R. C.; Raudsepp, M., *Am. Mineral.* **1992,** *77*, 522.
44. Christensen, A. N.; Norby, P.; Hanson, J. C., *Powder Diffr.* **1995,** *10*, 185.
45. Nakatsuka, A.; Ikeda, Y.; Nakayama, N.; Mizota, T., *Acta Crystallogr., Sect. E: Struct. Rep. Online* **2006,** *62*, I109.
46. Fregola, R. A.; Bosi, F.; Skogby, H., *Periodico di Mineralogia* **2011,** *80*, 27.
47. Kanno, R.; Yonemura, M.; Kohigashi, T.; Kawamoto, Y.; Tabuchi, M.; Kamiyama, T., *J. Power Sources* **2001,** *97-98*, 423.
48. Fiorani, D.; Viticoli, S., *Solid State Commun.* **1978,** *25*, 155.
49. Fleet, M., *Acta Crystallogr. B* **1981,** *37*, 917.
50. Shmakov, A. N.; Kryukova, G. N.; Tsybulya, S. V.; Chuvilin, A. L.; Solovyeva, L. P., *J. Appl. Crystallogr.* **1995,** *28*, 141.
51. Arima, T.; Higashiyama, D.; Kaneko, Y.; He, J. P.; Goto, T.; Miyasaka, S.; Kimura, T.; Oikawa, K.; Kamiyama, T.; Kumai, R.; Tokura, Y., *Phys. Rev. B* **2004,** *70*, 064426.
52. Mohamed, M. B.; Senyshyn, A.; Ehrenberg, H.; Fuess, H., *J. Alloys Compd.* **2010,** *492*, L20.
53. Mukhopadhyay, K.; Sutradhar, S.; Modak, S.; Roy, S. K.; Chakrabarti, P. K., *The Journal of Physical Chemistry C* **2012,** *116*, 4948.
54. Roberts, A. P.; Cui, Y.; Verosub, K. L., *Journal of Geophysical Research* **1995,** *100*, 17909.
55. Ghose, J.; Hallam, G. C.; Read, D. A., *J. Phys. C.: Solid State Phys.* **1977,** *10*, 1051.
56. Leccabue, F.; Panizzieri, R.; Watts, B. E.; Fiorani, D.; Agostinelli, E.; Testa, A.; Paparazzo, E., *J. Cryst. Growth* **1991,** *112*, 644.
57. Pool, V. L.; Klem, M. T.; Chorney, C. L.; Arenholz, E. A.; Idzerda, Y. U., *J. Appl. Phys.* **2011,** *109*.

Chapter 5: The Structures of Fluorite-like Cerium Bismuth Oxides and a Cerium Titanate Pyrochlore

5. The Structures of Fluorite-like Cerium Bismuth Oxides and a Cerium Titanate Pyrochlore

5.1. Introduction

5.1.1. Background

Cerium dioxide or ceria, CeO_2, is an industrially important material which exhibits high solid-state oxide ion mobility and a reversible reduction/oxidation cycle between Ce^{4+} and Ce^{3+} at relatively low temperatures.[1-2] These properties have led to the application of CeO_2 in many types of catalysis, including automotive three-way catalysis (for the removal of noxious gases from vehicle exhaust),[3] the water-gas-shift reaction (for the conversion of carbon monoxide and water to carbon dioxide and hydrogen),[4-5] and hydrocarbon reforming (for the production of hydrogen from hydrocarbons such as methane).[6] In these applications, CeO_2 is often used in conjunction with other oxides or as a support for catalytically active metals, usually to act as a buffer against changes in oxygen concentration.

The fluorite structure adopted by CeO_2 consists of a cerium centre surrounded by a cubic arrangement of oxygen atoms which are in turn tetrahedrally coordinated to four cerium atoms (Figure 5.1 and Table 5.1). The openness of the structure contributes to the ease with which oxide ions migrate within it. A wide range of dopant metals can be used to enhance the redox properties and oxide-ion conductivity of $CeO_{2.}$ Dopants like Y^{3+}, Gd^{3+}, Sm^{3+}, Ca^{2+} and Sr^{2+} introduce oxygen vacancies and potentially improve oxide ion migration,[7-9] and transition metal cations such as Ti^{4+} and Fe^{2+} may contribute their own, additional, redox activity.[10-11]

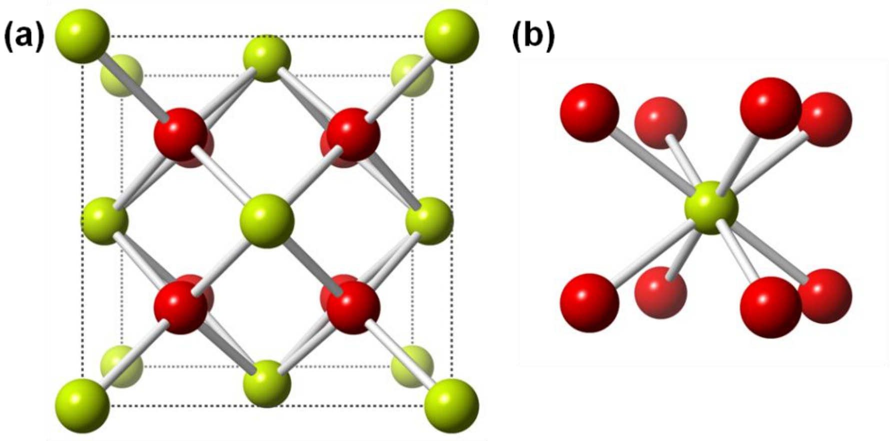

Figure 5.1 The structure of CeO_2.[12] (a) the unit cell of CeO_2, space group $Fm\bar{3}m$ (b) the cubic, 8-coordinate arrangment of oxygen atoms around each cerium atom. Yellow spheres are Ce atoms and red spheres are O atoms.

Table 5.1 The crystallographic description of the CeO_2 fluorite structure in space group $Fm\bar{3}m$.

Atom	**Site**	***x***	***y***	***z***
Ce	4a	0	0	0
O	8c	0.25	0.25	0.25

There are of course a range of cerium containing materials which do not adopt the fluorite structure, and these may also exhibit superior catalytic behaviour. Some recent examples include Ce(IV) pyrochlore oxides of general formula $(Na_xCe_{1-x})_2Ti_2O_7$ and $(Na_xCe_{1-x})_2(Sn_yTi_{1-y})_2O_7$,[13-14] and a series of pyrochlore related cerium zirconates of general formula $Ce_2Zr_2O_{7+\delta}$.[15]

5.1.2. *Scope of this chapter*

This chapter is concerned with the elucidation of the structure of two types of Ce(IV) containing materials using total neutron scattering. Both are expected to exhibit disorder in a range of “flavours” including small particle size, local symmetry distortions and mixed site occupancy, which may be responsible for their favourable properties in the type of applications mentioned above.

The first of these materials is a series of nanocrystalline, fluorite-like, bismuth doped cerium oxides of general formula $Ce_{1-x}Bi_xO_{2-y}$. Oxides of similar composition to those discussed herein have been made by several researchers, including Dikmen *et al.*[16] who used a hydrothermal method beginning with the ambient temperature precipitation of a gel from a $Ce(NO_3)_3.6H_2O/Bi(NO_3)_3.6H_2O$ mixed solution, and Li *et al.*[17] who used similar reagents but did not pre-precipitate the gel. The apparent solubility limit of Bi in CeO_2 differed significantly from $x = 0.2$ in the former referenced work to $x = 0.5$ in the latter, presumably due to differences in synthesis method. Bismuth doping of CeO_2 is of particular interest because Bi^{3+} has a lone pair of $6s^2$ valence electrons which leads to a preference for an asymmetric coordination environment, something which it is not possible to satisfy in the fluorite structure without some distortion. Despite this, there have been no reported structural investigations of these materials beyond the determination of lattice parameters. As it has previously been observed that Bi substitution can enhance the ionic conductivity of CeO_2,[16] and it is possible that localised distortion of the fluorite lattice could be responsible for this phenomenon, a full structural characterisation of these materials was carried out.

The second material is the aforementioned sodium cerium titanate pyrochlore for which the proposed formula on its initial report was $(Na_{0.33}Ce_{0.67})_2Ti_2O_7$ and whose structure was not examined in detail in earlier published work.[13] The material was found to adopt a pyrochlore-type structure and XANES measurements revealed the presence of Ce(IV) and Ti(IV). Further motivation for this detailed structural investigation came from several observed inconsistencies, including a discrepancy between the measured density of the sample (4.912 g cm^{-3}) and that calculated for the pyrochlore model (5.288 g cm^{-3}), and the fact that successful synthesis of the phase pure material always required an excess of Ti to be used, relative to the amount in the assumed formula.[14] It is also important that the material is inherently disordered with three different metals sharing two crystallographically unique sites. Neutron diffraction offers the ability to differentiate between the constituent elements due to significant differences in their coherent scattering lengths (Na = 3.63 fm, Ce = 4.84 fm, Ti = –3.438 fm and O = 5.803 fm)[18] and it was therefore desirable to employ this technique to obtain a complete structural description.

In the following pages, the structures of these materials will be discussed in detail with reference to both their average/long-range and their local/short-range order, with particular focus on the differences between the two length scales.

5.2. Results and Discussion

5.2.1. *Cerium bismuth oxide*

5.2.1.1. Synthesis

Three bismuth doped cerium oxides with general formula $Ce_{1-x}Bi_xO_{2-1/2x}$ (x = 0.25 – 0.6) were synthesised hydrothermally from $CeCl_3.7H_2O$ and $NaBiO_3.nH_2O$ by Dr Kripasindhu Sardar.[19] The general procedure used was as follows: $NaBiO_3.2H_2O$ (the value of n = 2 was determined by TGA) and $CeCl_3.7H_2O$ in the appropriate stoichiometric ratio (for intended cerium content of 75, 50 or 25%) were stirred in 4 ml of 4 M HNO_3 solution for 10 minutes. Then, 4 ml of 10 M NaOH was added dropwise and stirring continued for another 25 minutes, after which time the reaction mixtures were sealed in Teflon lined stainless-steel autoclaves and placed in a preheated fan oven at 240 °C for 96 hours. The solid products were collected by suction filtration and washed with hot water.

ICP analysis of these samples, carried out by MEDAC LTD., was used to determine their compositions. The Ce/Bi ratios were determined to be 76/24, 52/48 and 41/59 respectively, and the samples will therefore be subsequently referred to as Ce75, Ce50 and Ce40. These results imply that the solubility limit of Bi in CeO_2 for these samples is ~60% of metal content.

5.2.1.2. Total neutron scattering

Total neutron scattering data for three cerium bismuth oxides of differing Ce/Bi ratios were collected using the instrument GEM at ISIS. The data were processed and corrected using Gudrun and ATLAS as described in Chapter 2. The samples appeared dry and therefore did not require correcting for the incoherent scattering of hydrogen. The Fourier transform was carried out using the Lorch modification function and a Q_{max} of 27 Å^{-1}.

The results of Rietveld refinement of the cubic fluorite structure against neutron diffraction data for each of the cerium bismuth oxides are shown in Figure 5.2 and Table 5.2.

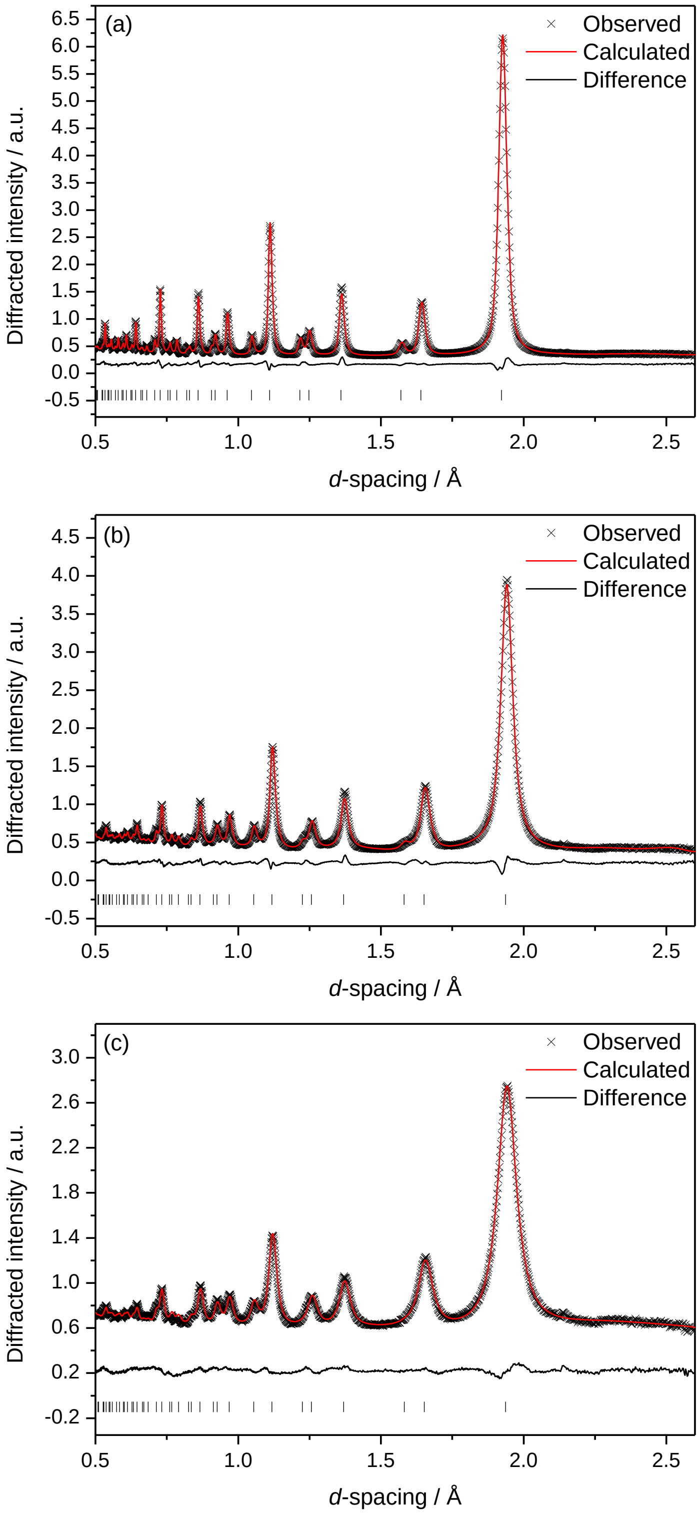

Figure 5.2 The results of Rietveld refinement against neutron diffraction data for (a) Ce75, (b) Ce50 and (c) Ce40. The ticks show allowed reflections for the refined fluorite structure.

Table 5.2 Refined structural parameters for Ce-Bi oxides from Rietveld refinement of neutron diffraction data.

Sample	**Ce75**	**Ce50**	**Ce40**
***a* /Å**	5.4380 (7)	5.4771 (1)	5.4786 (2)
Occ. Ce (4a)	0.773 (7)	0.65 (1)	0.206 (7)
Occ. Bi (4a)	0.227 (7)	0.35 (1)	0.794 (7)
Occ. O (8c)	0.943 (7)	0.913 (1)	0.802 (7)
U_{iso} (Ce, Bi) /Å^2	0.0071 (3)	0.0081 (5)	0.0116 (2)
U_{iso} (O) /Å^2	0.0099 (2)	0.0179 (6)	0.0194 (3)
wRp	3.28%	3.03%	2.26%
Rp	2.31%	2.33%	2.03%

In each case an excellent fit was obtained with the lattice parameter, a = 5.4380, 5.4771 and 5.4786 Å for Ce75, Ce50 and Ce40 respectively, implying that increasing bismuth content leads to an increase in lattice parameter, an observation which is in accord with their respective ionic radii (Ce^{4+} = 97 pm and Bi^{3+} = 103 pm). During the refinement, any attempt to refine the occupancy parameters independently led to instability which was not unexpected given the broadness of the peaks, and therefore it was necessary to apply a charge-balancing constraint to the refinement such that changes in the Ce/Bi ratio were automatically countered by the appropriate change in O content in line with the expected formula $Ce_{1-x}Bi_xO_{2-1/2x}$. This formula was supported by XANES spectroscopy which showed the presence of Bi^{3+} exclusively.

Despite the excellent fits shown above, the broad diffraction peaks are evidence of the nanocrystalline nature of the samples and cause a certain amount of ambiguity in the Rietveld refinements. It is possible that the samples, particularly those with higher bismuth content, actually consist of a mixture of CeO_2 and α-Bi_2O_3 (the thermodynamically stable polymorph of Bi_2O_3 which has a monoclinic structure)[20] rather than a single mixed-metal phase, and that using a two-phase model for the fitting could also produce a good result. Conversely, the differences between a single phase and a two-phase fit to the real-space data are likely to be much larger and therefore, PDF fitting will enable the possibility of a two-phase mixture to be properly examined.

The neutron *i*(*Q*) and *D*(*r*) functions from the cerium bismuth oxides are shown in Figure 5.3 and Figure 5.4. The *D*(*r*) have been plotted out to 100 Å in order to show the damping in the oscillations caused by the decreasing particle size.

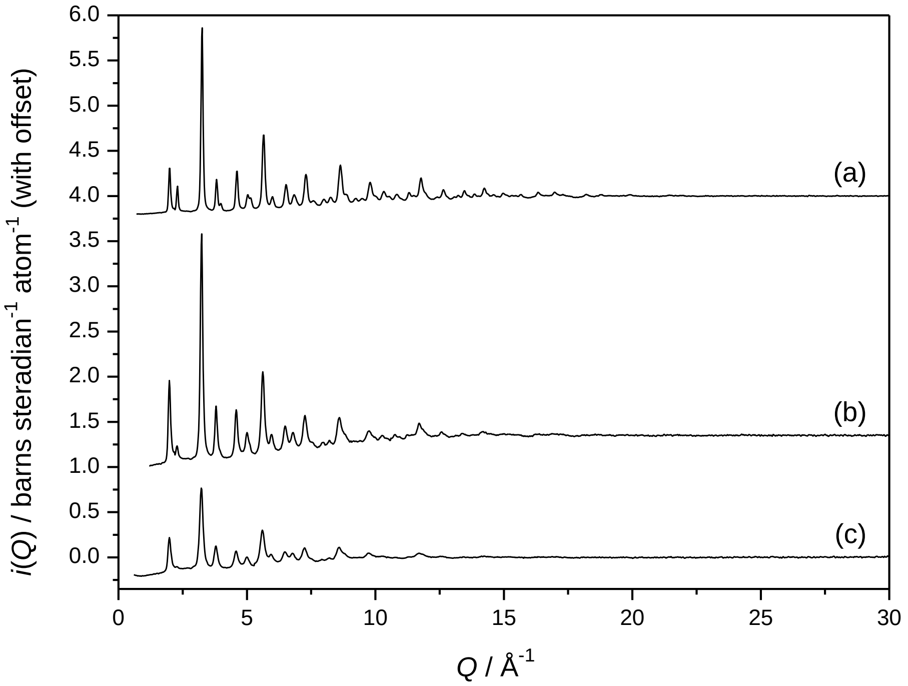

Figure 5.3 The *i*(*Q*) for (a) Ce75, (b) Ce50 and (c) Ce40.

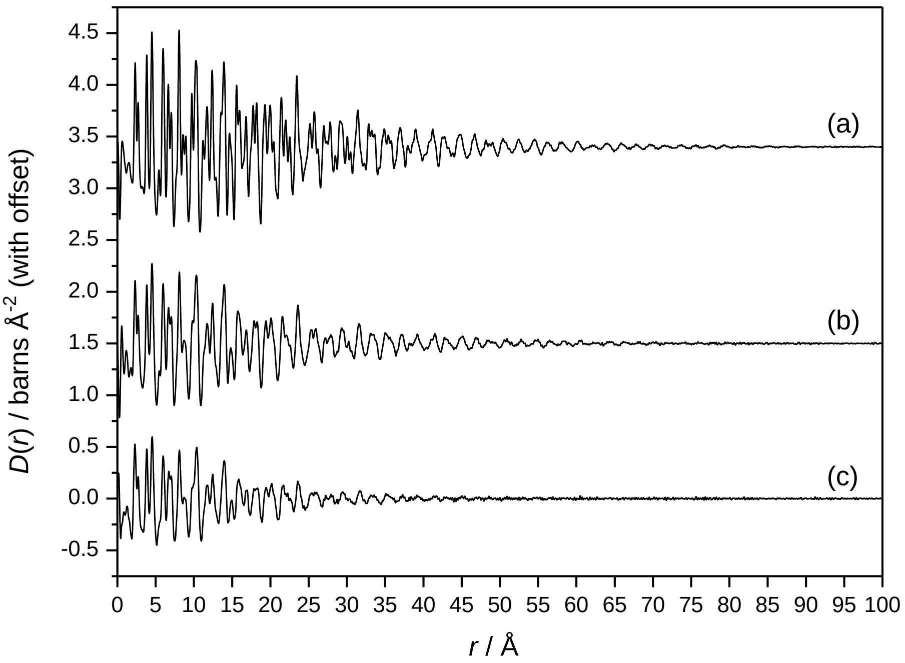

Figure 5.4 The *D*(*r*) for (a) Ce75, (b) Ce50 and (c) Ce40. The decrease in particle size with increasing Bi content is obvious from the damping of the *D*(*r*) at high-*r*.

The real space data were used for PDF analysis. For the fitting, a maximum *r* of 25 Å was chosen as small enough to not cause the iterative procedure to be too computationally demanding, yet still sufficiently high to allow a reasonably accurate refinement of lattice parameters. Two different models were tested: the first being the mixed phase CeO_2 + α-Bi_2O_3 model and the second being the single phase $Ce_{1-x}Bi_xO_{2-1/2x}$ model. The results of fitting with the mixed phase model are shown in Figure 5.5.

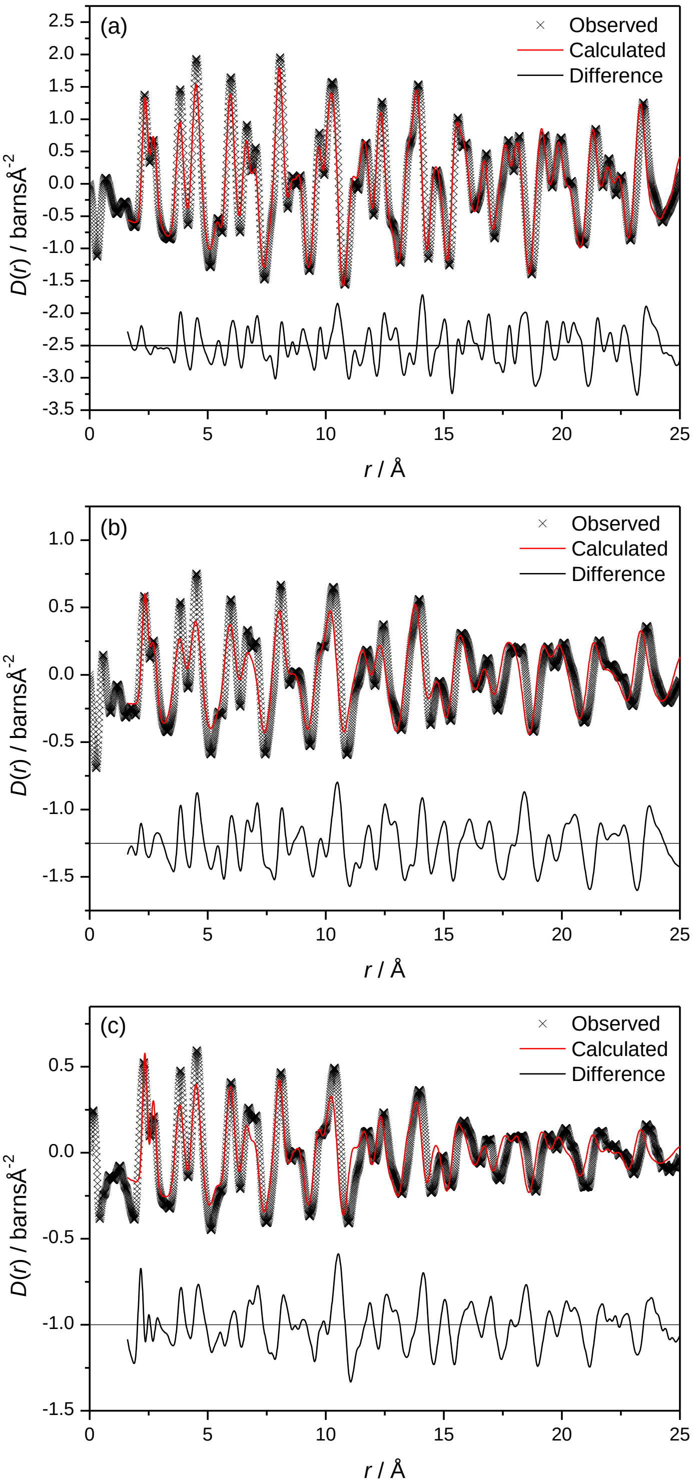

Figure 5.5 Plot showing the results of PDF analysis of (a) Ce75, (b) Ce50 and (c) Ce40, using the mixed phase CeO_2 + α-Bi_2O_3 model.

In these fits only the thermal displacement parameters, the phase fractions and the terms accounting for correlated motion were refined (see Chapter 2 for description of the PDF analysis process). As the model represented a discrete mixture of two phases the unit cell parameters were not allowed to vary. It is obvious that the mixed phase model is not correct as the “fits” are very poor.

The results of fitting with the single phase model are shown in Table 5.3 and Figure 5.6. It can be seen that excellent fits are obtained for all three samples. As in the Rietveld refinement, a charge balancing constraint was applied to reduce the number of independent parameters and improve stability, and as before, the refined compositions agree well with the ICP analysis. The PDF refinement was carried out entirely independently of the Rietveld fit in order to avoid bias in the results and, therefore, the generally good agreement between the two analysis methods both highlights their complementarity and provides support for the validity of the results.

Table 5.3 Refined structural parameters for Ce-Bi oxides from PDF analysis of neutron diffraction data.

Sample	**Ce75**	**Ce50**	**Ce40**
***a* /Å**	5.4390 (2)	5.4682 (4)	5.4801 (1)
Occ. Ce (4a)	0.800 (1)	0.457 (2)	0.334 (4)
Occ. Bi (4a)	0.200 (1)	0.543 (2)	0.666 (4)
Occ. O (8c)	0.950 (1)	0.864 (2)	0.834 (4)
U_{iso} Ce, Bi /Å^2	0.00885 (2)	0.01602 (5)	0.01448 (8)
U_{iso} O /Å^2	0.01298 (1)	0.01865 (4)	0.02007 (9)
wRp	16.9%	26.3%	26.5%
spdiameter /Å[a]	114	71	42

[a] This parameter provides an estimate of particle size by convoluting the ideal PDF with a spherical shape function to recreate the observed damping of the PDF oscillations.

The parameter “spdiameter” is unique to the PDF analysis method. It is an estimate of particle size obtained by simulating an “ideal” PDF (assuming a bulk sample whose PDF is broadened and dampened only by instrumental resolution effects) and convoluting it with a spherical shape function. The accuracy of this value is improved if the fitting range is reasonably close to the particle size, however a reasonable estimate should be obtained if the instrumental parameters are well defined. For example, an spdiameter of 71 Å was obtained for Ce50 from fitting up to 25 Å, which in simple terms means that no oscillations should be visible in the PDF above 71 Å, and this is in good agreement with the PDF plotted out to 100 Å shown in Figure 5.4, plot (b).

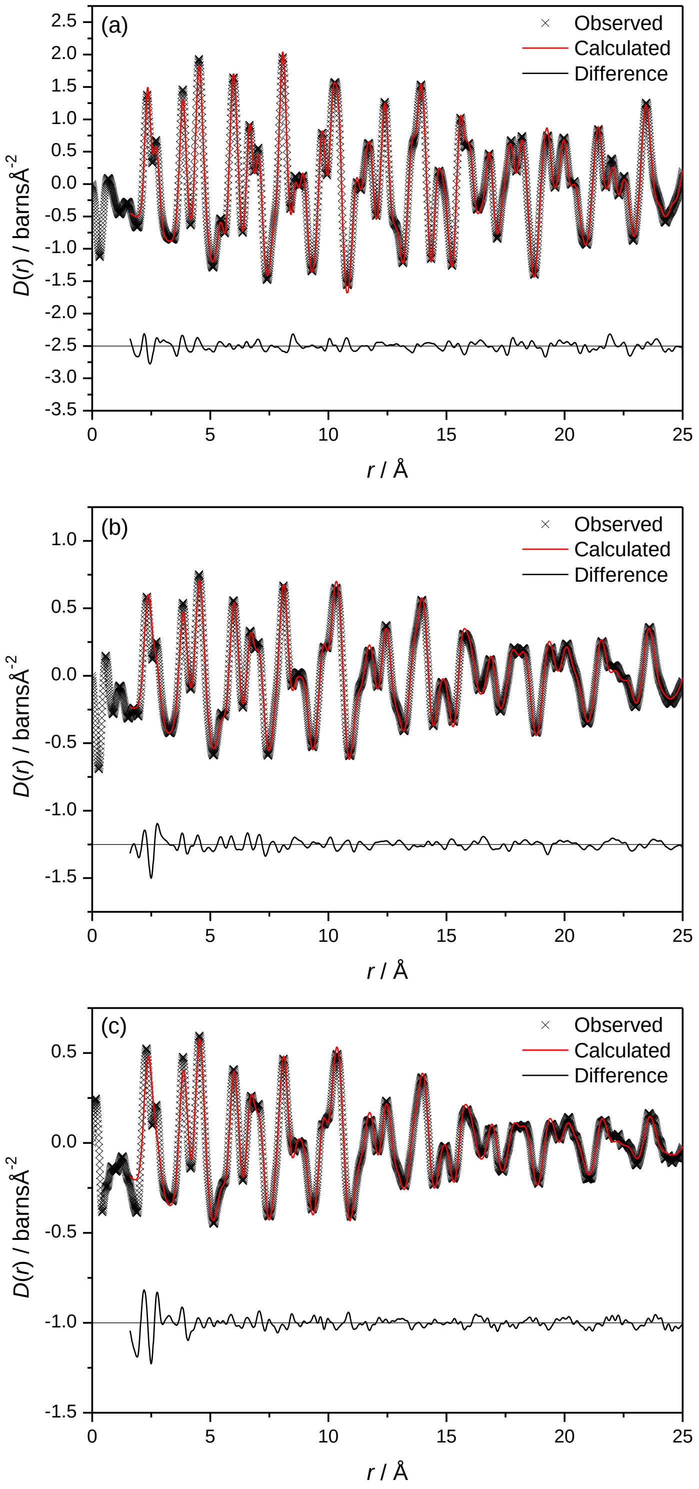

Figure 5.6 Plot showing the results of PDF analysis of (a) Ce75, (b) Ce50 and (c) Ce40, using the single phase model.

It will be noticed that there are some discrepancies between refined Ce/Bi ratios obtained from Rietveld and PDF methods and the results of ICP analysis (see Table 5.4). However, in all cases the expected trend is clearly observed and the effect of fixing the ratio to the values obtained from ICP caused very little change in the quality of the fits. The biggest discrepancy is in the Ce/Bi ratio from the Rietveld fit to Ce50 and Ce40. This is unsurprising as the peaks are rather broadened and significantly overlapped, such that the intensities cannot be determined with great accuracy.

Table 5.4 The composition of the cerium bismuth oxides, as determined by various methods.

Sample		Expected	ICP	XRF	PDF	Rietveld
Ce75	**Ce**	0.75	0.78	0.76	0.80	0.77
	Bi	0.25	0.22	0.24	0.20	0.23
Ce50	**Ce**	0.50	0.65	0.52	0.46	0.65
	Bi	0.50	0.35	0.48	0.54	0.35
Ce40	**Ce**	0.25	0.32	0.41	0.33	0.20
	Bi	0.75	0.68	0.59	0.67	0.80

The results from PDF analysis corroborate the results from Rietveld refinement and it can therefore be stated that the average structure of these materials is best described as a single, mixed oxide phase. However, when examined closely, the fit of this model to the low-*r* region of the PDFs is not adequate (see Figure 5.7) The peaks in the PDF in the region 2.0 – 3.0 Å can be attributed to the nearest neighbour M–O and O– –O correlations – *i.e.* the coordination environment around the Ce/Bi site.

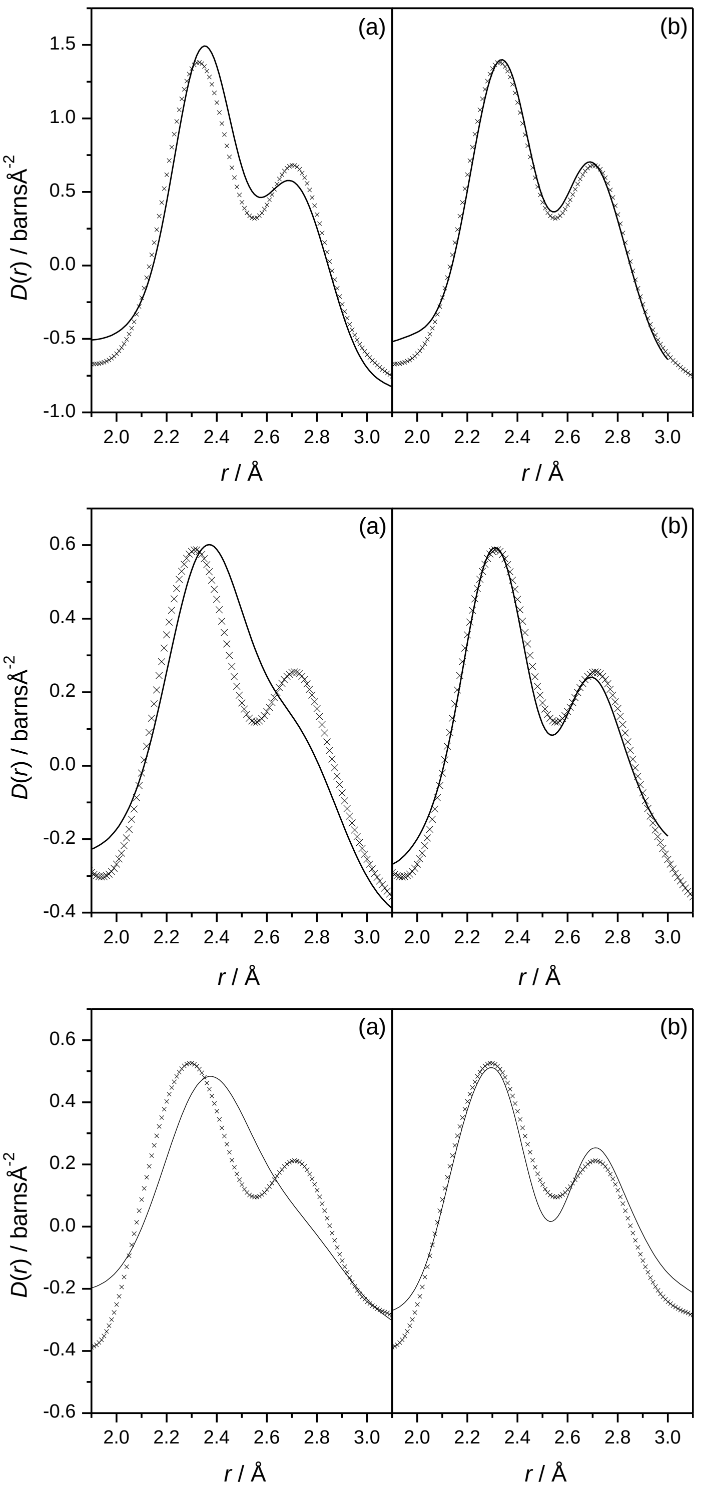

Figure 5.7 Comparison of the low-*r* region of the PDF fitting of (top to bottom) Ce75, Ce50, Ce40, for (a) the single phase model and (b) the distorted β-Bi_2O_3/CeO_2 model.

In the fluorite structure the cation environment is cubic - there are 8 equal M–O bonds and 12 equal O– –O correlations. This type of coordination is unlikely to satisfy the bonding requirements of Bi^{3+} which tends to prefer an asymmetric, often 5 coordinate, environment. There are several polymorphs of Bi_2O_3 whose structures support this assertion. The thermodynamically stable α-Bi_2O_3 phase has a monoclinic structure and has two non equivalent Bi sites, both of which have distorted 5-coordinate geometry, and the single Bi site in tetragonal β-Bi_2O_3 has a similar geometry (see Table 5.5). The high-temperature polymorph, δ-Bi_2O_3, has the same cubic fluorite structure as CeO_2 with a proportion of oxygen vacancies, however a recent study by Hull *et al.*[21] examined the structure of δ-Bi_2O_3 using neutron diffraction and RMC and found that although the average structure was consistent with the fluorite structure, the local structure closely resembled that of β-Bi_2O_3. The authors concluded that the distorted BiO_5 pentahedra were arranged in multiple different orientations across the lattice, thus maintaining the average, cubic, symmetry.

Table 5.5 The Bi–O bond lengths, in Å, found in α-Bi_2O_3,[12] β-Bi_2O_3, [21] and the distorted Bi environment in the $Ce_xBi_{1-x}O_2$ local structure.

	α-Bi_2O_3		**β-Bi_2O_3**	**$Ce_xBi_{1-x}O_2$**
	Bi1	**Bi2**	**Bi1**	**Bi1**
O1	2.63	2.56	2.09	2.17
O2	2.55	2.42	2.18	2.27
O3	2.13	2.13	2.74	2.89
O4	2.22	2.20	2.09	2.20
O5	2.21	2.28	2.53	2.63

A similar local distortion to that described above could be responsible for the discrepancies in the fit at low-*r* observed for the $Ce_{1-x}Bi_xO_{2-1/2x}$ samples. Therefore the low-*r* region of the data was fitted with a mixture of CeO_2 and β-Bi_2O_3 to account for the differences in coordination preference of the two metals. A similar method was used recently to model the local order in gadolinium doped CeO_2.[22] The resulting fits are shown in Figure 5.7 and the local Bi environment is detailed in Table 5.5 and Figure 5.8. This model fits the low-*r* data extremely well, and the refined Bi environment is consistent with those in α- and β-Bi_2O_3. It should be noted at this point that a two-phase fit over the full data range was attempted using CeO_2 and β-Bi_2O_3 and that the results were extremely similar to those using CeO_2 and α-Bi_2O_3. The fit to Ce50 is shown in Figure 5.9, for reference.

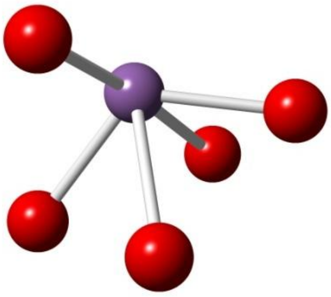

Figure 5.8 The local environment of the "β-Bi_2O_3 like" Bi from the low-*r* fit of the mixed-phase model for Ce75, Ce50 and Ce25.

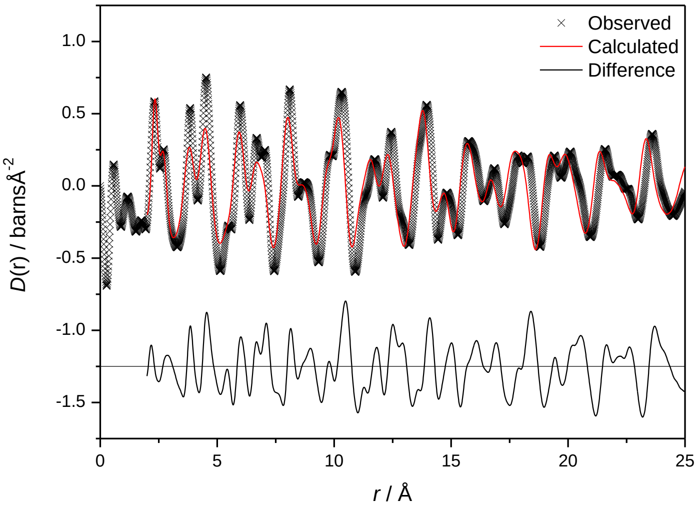

Figure 5.9 Plot showing the result of PDF analysis for Ce50 using the two phase CeO_2 + β-Bi_2O_3 model.

Fitting the low-*r* data with this two phase model is not intended to imply that the sample consists of two phases at this length scale. However, the Rietveld refinement and the higher-*r* PDF analysis both assume a statistical distribution of Ce and Bi; each atom on the metal site contributes to the scattering as a weighted average of the two. In terms of the local structure, however, each metal site is *either* a Ce *or* a Bi atom. Since it is likely that the two metals "prefer" different coordination environments, it is reasonable to model them separately at this length scale. A limitation of this model is that it does not provide any information about metal-metal arrangements (*i.e.* how many of a cerium atom's nearest metal neighbours are bismuth and *vice versa*). Although a Ce–Ce correlation would have a slightly different contribution to the PDF than a Ce–Bi correlation, since it would appear in the region of 4 Å (3.85 – 3.88 Å for undistorted CeO_2 structure) where there are also O– –O correlations, the changes in the PDF would be small.

A multi-length scale model, consisting of the average cubic fluorite structure and a distorted local environment similar to that found in β-Bi_2O_3, has been obtained which fits well with all the observations made for the cerium-bismuth samples.

5.2.2. *Sodium cerium titanate pyrochlore*

5.2.2.1. *Synthesis*

The hydrothermal synthesis of a sodium cerium titanate pyrochlore with assumed composition $(Na_{0.33}Ce_{0.67})_2Ti_2O_7$ was first reported by Wright *et al.*[13]. The synthesis was further developed by Dr Deena Modeshia, who provided the samples for the total neutron scattering studies described herein.[14] In the synthesis, $CeCl_3.7H_2O$, TiF_3 and $NaBrO_3$ (0.37, 0.26 and 0.375 g, respectively) were stirred in 4 ml of 10 M NaOH solution for 30 minutes, made up to 8 ml with water and placed in a Teflon lined stainless-steel autoclave, followed by heating at 240 °C for 5 hours. The product was collected by suction filtration and washed with hot water.

5.2.2.2. Total neutron scattering

*The data discussed in this section (5.2.2.2) were collected by Dr Deena Modeshia and the initial data reduction and correction was carried out by Dr Emma Barney. The analysis described herein was carried out on the i(*Q*) and* D*(*r*) functions provided to the author by those researchers.*

Total scattering data were provided for two samples. One had been annealed at 300 °C to remove surface water, and the other had been annealed at 700 °C to improve crystallinity. The two samples will therefore subsequently be referred to as P300 and P700. The neutron $i(Q)$ and $D(r)$ for both samples are shown in Figure 5.10. For the Fourier transforms, a $Q_{\max}$ of 20 $Å^{-1}$ was used due to the increased noise in the $i(Q)$s beyond this value (see inset of Figure 5.10). The Lorch modification function was also used. The first peak in the PDF is negative due to Ti having a negative neutron scattering length and the first peak being associated with the Ti–O bond. In fact, all Ti–containing correlations will contribute negative peaks to the PDF, except the Ti–Ti correlations, due to the fact that the neutron scattering coefficient for an atom pair is defined as $f_{ij} = c_i c_j b_i b_j$ (where c_i is the number concentration of atom i and b_i is its coherent scattering length) and therefore, when both b_i and b_j are negative, f_{ij} is positive.

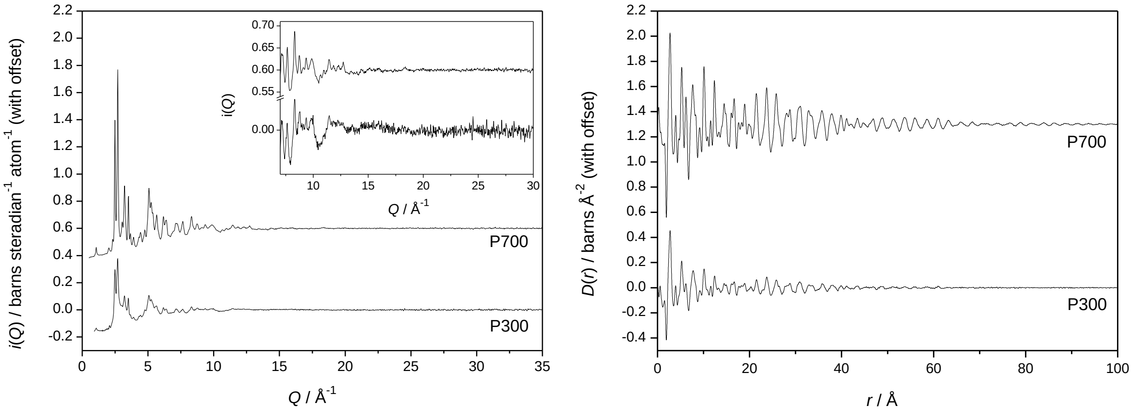

Figure 5.10 Left: *i*(*Q*) for the two pyrochlore samples, with inset showing expanded high-*Q* region. Right: *D*(*r*) for the two samples.

The starting structural model, a stoichiometric $A_2B_2O_7$ pyrochlore as suggested from X-ray diffraction data,[13] is described in Table 5.6. Of the two possible settings for the space group $Fd\bar{3}m$, the one chosen has the B (16c) site at the origin. The A (16d) site (8-coordinate, cubic) consists of ⅔ Ce^{4+} and ⅓ Na^{+}, while the B site (6-coordinate, octahedral) contains Ti^{4+} only. There are only 2 refineable structural parameters: the cubic lattice parameter and the 48f O site *x*-coordinate.

Table 5.6 The structural parameters for the starting pyrochlore model. Space group $Fd\bar{3}m$.

Atom	**Site name**	**Wyckoff site**	**Occupancy**	**x**	**y**	**z**
Na	A	16d	0.33	1/2	1/2	1/2
Ce	A	16d	0.67	1/2	1/2	1/2
Ti	B	16c	1	0	0	0
O	O1	48f	1	0.328	1/8	1/8
O	O2	8b	1	3/8	3/8	3/8

This model was used for the initial PDF analysis, with the scale factor, spdiameter and correlated motion corrections refined in addition to the model parameters. The results are shown in Figure 5.11 It can be seen that the general forms of the fitted PDFs are in good agreement with the data, although there are significant discrepancies in the intensities of some of the features, particularly in the low-*r* region. To attempt to find an explanation for the discrepancies, the various partial correlation functions were simulated to identify the correlations responsible for the poorly fitting features. The first two peaks are assigned to the B site Ti–O and A site M–O bonds as well as the nearest-neighbour O– –O non-bonded correlations, while the peaks in the region 3.5 - 5 Å are due to a combination of M– –O and 48f O– –O correlations (see Figure 5.12). This information implies that the model may be improved by a) considering the occupation of the metal sites more closely and b) examining possible alteration/disordering of the oxygen sublattice.

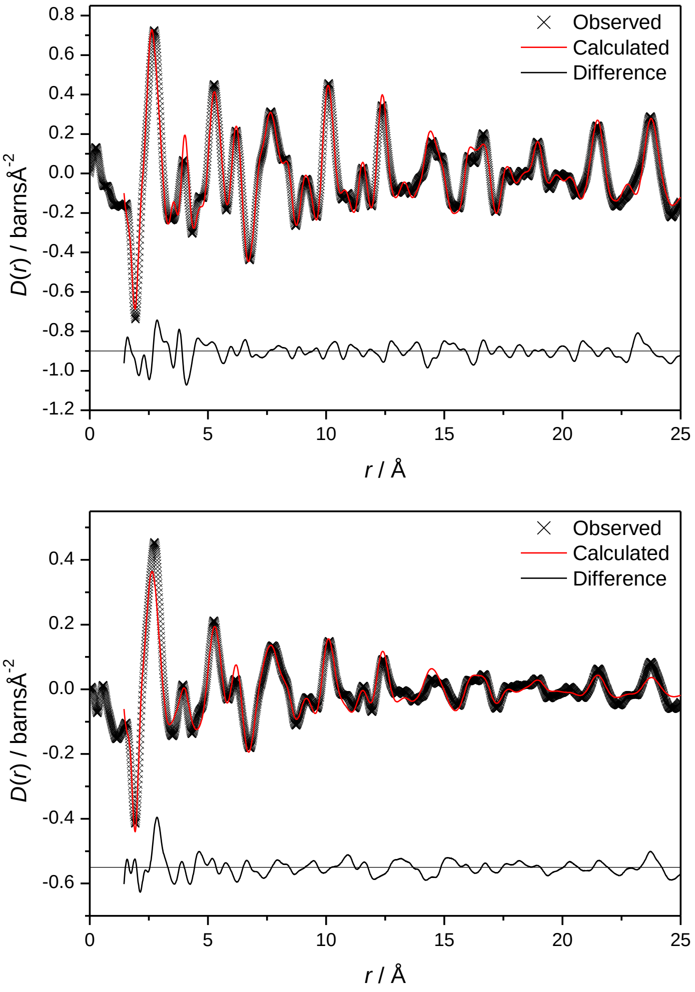

Figure 5.11 The results of PDF analysis using the simple pyrochlore model for (upper) P700 and (lower) P300.

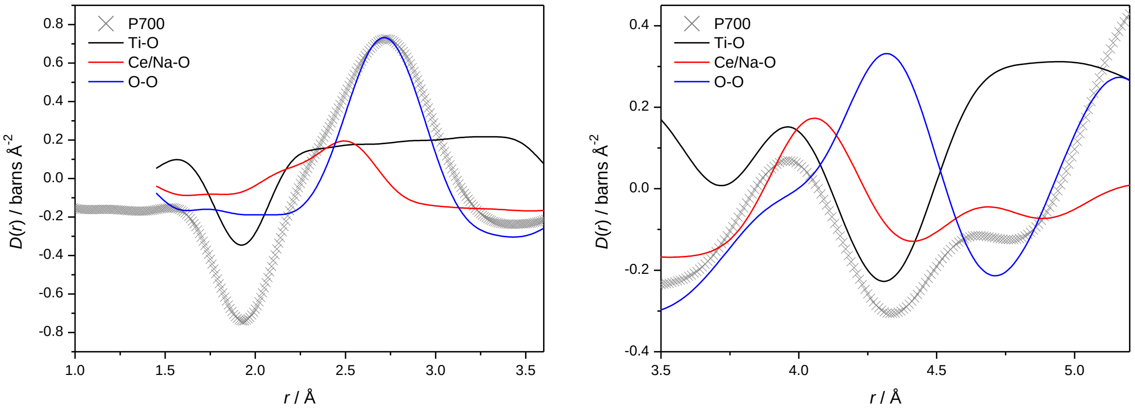

Figure 5.12 Simulated partial correlation functions from the simple pyrochlore model and their comparison with the measured *D(r)* for P700.

The simple pyrochlore model confines the Ti to the B site, but A site Ti has been observed for other pyrochlore materials,[23] and its presence could alter the intensity ratio of the first two peaks.

Furthermore, if the *i*(*Q*) of P700 is examined closely, several peaks not associated with the pyrochlore model are visible, and can be assigned to CeO_2. Additionally the strongest of these peaks is also visible in the *i*(*Q*) for P300. Obviously an impurity phase will also contribute to the PDF and must be added to the fitting.

The results of PDF analysis after the addition of A site Ti to the primary phase and CeO_2 as a secondary phase are shown in Figure 5.13 and Table 5.7. To further improve the fit, anistropic temperature factors were also added. These fits are modest improvements from the simple pyrochlore model, as evidenced by the reduction in wRp from 21.7% to 18.8% for P700 and 27.6% to 23.0% for P300. The occupancy of Ti on the A site consistently refined from 0 to values of 0.13 for P700 and 0.15 for P300, and the amount of CeO_2 refined to 6.7% for P700 and 2.0% for P300. The larger amount of CeO_2 in P700 is evidence that some phase separation had started to occur, although no Na or Ti containing phases were observed. The A site Ti is in addition to the fully occupied B site and therefore accounts for the excess Ti used in the synthesis and for the density discrepancy, as the calculated density for the modified pyrochlore/CeO_2 mixed phase model for P300 is 4.95 g cm^{-3}, much closer to the measured value of 4.912 g cm^{-3}. A comparison of the diffraction pattern of P700 with that simulated from the refined pyrochlore/CeO_2 mixture shows excellent agreement (see Figure 5.14). The profile parameters describing peak shape and width were obtained from a Le Bail fit of the diffraction pattern.

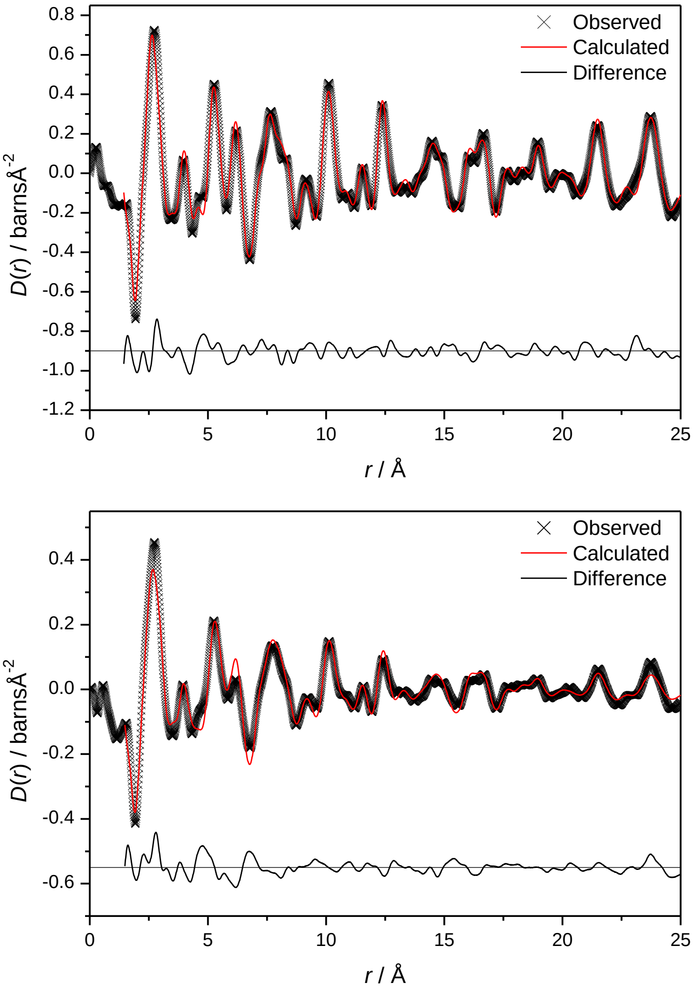

Figure 5.13 The results of PDF analysis using the modified pyrochlore model with A-site Ti and CeO_2 as a secondary phase for (upper) P700 and (lower) P300.

Table 5.7 The refined parameters from the modified pyrochlore + CeO_2 model.

	P700	**P300**
***a* / Å**	10.1162	10.1292
A site ADPs[a]	*U*11 = 0.0115(6) *U*12 = 0.0032(5)	*U*11 = 0.0247(4) *U*12 = -0.0029(4)
B site ADPs[a]	*U*11 = 0.0196(8) *U*12 = -0.0017(5)	*U*11 = 0.0343(6) *U*12 = -0.0080(4)
O1 site ADPs[b]	*U*11 = 0.0292(6) *U*22 = 0.0261(4) *U*23 = 0.0128(8)	*U*11 = 0.0366(4) *U*22 = 0.0373(3) *U*23 = 0.0239(4)
O2 site ADPs[c]	*U*11 = 0.0231(6)	*U*11 = 0.0174(3)
Ti occupancy (A site)	0.127(8)	0.149(2)
O1 *x*-coordinate	0.3253(1)	0.3279(6)
CeO_2 content (%)	6.7	2.0
wRp	18.8%	23.0%

[a] *U*11 = *U*22 = *U*33, *U*12 = *U*13 = *U*23; [b] *U*11, *U*22 = *U*33, *U*23; [c] *U*11 = *U*22 = *U*33

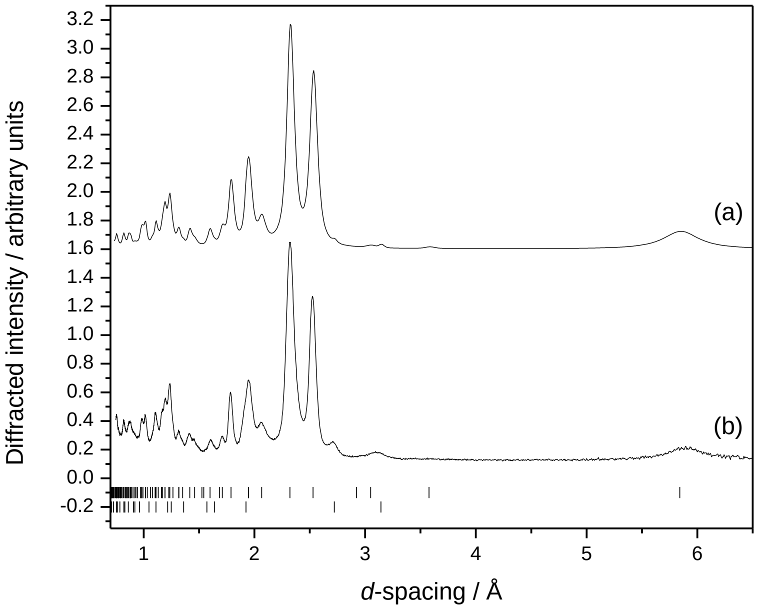

Figure 5.14 Comparison of (a) simulated diffraction pattern of the PDF analysis model, with (b) the measured diffraction pattern from P700. Tick marks are allowed reflections from the refined pyrochlore model (upper) and CeO_2 (lower).

From Figure 5.15 it can be clearly seen that the significant discrepancies between measured and fitted PDFs remain in the region 3.5 – 5 Å. As established earlier, these are due to A– –O and O– –O correlations. Disordering of the oxygen sublattice is a possible cause of the discrepancies.

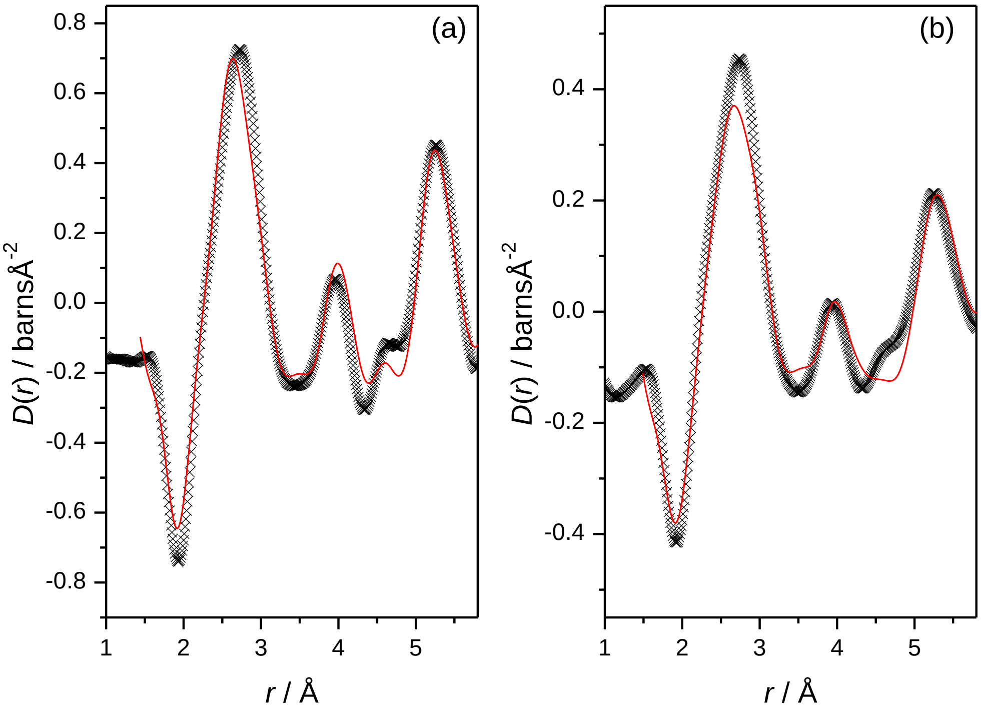

Figure 5.15 The low-*r* region of the results of PDF analysis using the modified pyrochlore model with A-site Ti and CeO_2 as a secondary phase for (a) P700 and (b) P300.

Heremans *et al.*[24] investigated a series of $Y_2(Zr_yTi_{1-y})_2O_7$ materials whose structure changed progressively, on increasing *y*, from an ordered pyrochlore to a defect fluorite structure. This disordering involved migration of some oxygen from the 48f site to the 8a site, followed by relaxation of the now under-occupied 48f site towards the ideal fluorite position and further migration of 8b oxygen to the 8a site. In the defect fluorite structure, all three sites are equivalent. Concurrent randomisation of cation occupancy between the A and B sites was also observed (see Figure 5.16).

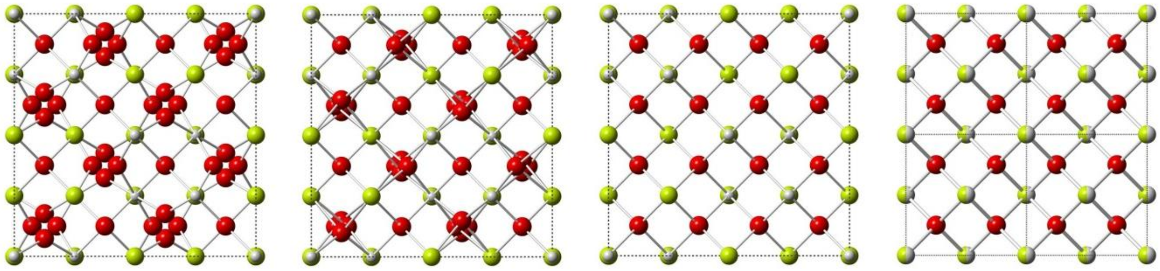

Figure 5.16 Evolution of pyrochlore structure (far left) to defect fluorite structure (far right) *via* relaxation of 48f oxygen towards the ideal fluorite position, occupation of the previously vacant 8a site and subsequent cation mixing. See text and Heremans *et al.*[24] for further explanation.

Although the defect fluorite structure is certainly not applicable to P300 and P700, because the first two peaks in the PDFs clearly show that there are two distinct cation environments, the migration of small amounts of oxygen from the 48f and 8b sites was tested as a possible cause of the observed discrepancies in the fitted PDFs. In both cases, the occupancy of the 8a site refined to a negative value and forcing oxygen onto this site noticeably worsened the fits. Disordering involving overall oxygen deficiency or excess was also examined, with the Ce/Na ratio adjusted to maintain charge balance, but this also failed to improve the fits, with the oxygen occupancies refusing to refine significantly away from the starting values.

Disordering involving symmetry lowering displacements of oxygen atoms away from their ideal pyrochlore positions has been observed occasionally, for materials such as oxygen deficient $Pb_2Ru_2O_{6.5}$,[25] oxygen rich $Ce_2Zr_2O_{7.5}$,[15] and stoichiometric Y-doped $Bi_2Sn_2O_7$.[26] These materials were all assigned the spacegroup $F\bar{4}3m$, which is a subgroup of $Fd\bar{3}m$ and allows the position of the "48f" oxygen to vary. Each of the oxygen sites from the $Fd\bar{3}m$ structure are split in two in the $F\bar{4}3m$ structure, and the two 24 multiplicity sites can move independently of one another.

Although there is no evidence for the lowering of symmetry in the Bragg diffraction of P700 or P300, oxygen displacement could still occur locally, similarly to the displacement of Bi atoms in the cerium bismuth oxides discussed earlier. This is particularly likely in view of the complexity of the A site, for example, the bonding requirements of Ti^{4+} are unlikely to be satisfied by a regular 8-coordinate cubic environment and local changes in the arrangement of oxygen atoms would be unsurprising. Therefore, the low-*r* region of the PDFs were fitted with a $F\bar{4}3m$ model, derived from the $Fd\bar{3}m$ model as described in Table 5.8.

Table 5.8 The conversion of the $Fd\bar{3}m$ pyrochlore model to $F\bar{4}3m$.

	$Fd\bar{3}m$				$F\bar{4}3m$			
	Site	**Coordinates**			**Site**	**Coordinates**		
A site (Na, Ce, Ti)	16d	1/2	1/2	1/2	16e	0.875	0.875	0.875
B site (Ti)	16c	0	0	0	16e	0.375	0.375	0.375
O1	48f	0.324	1/8	1/8	24f	0.301	0	0
					24g	0.051	1/4	1/4
O2	8b	3/8	3/8	3/8	4a	0	0	0
					4d	3/4	3/4	3/4

The results of the fits using the $F\bar{4}3m$ model are shown in Figure 5.17 and Table 5.9. The cut-off point for the fitting was chosen as 5.8 Å, because this is a point which lies between correlations.

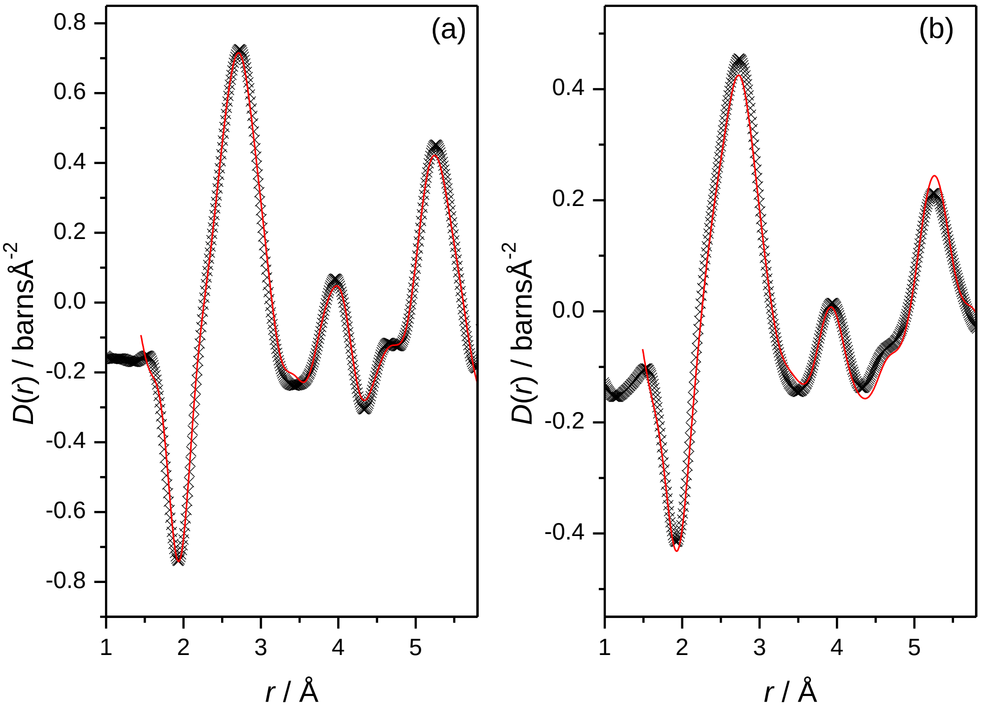

Figure 5.17 The results of fitting the low-*r* region of the PDFs with the $F\bar{4}3m$ model for (a) P700 and (b) P300.

Table 5.9 The refined parameters from the $F\bar{4}3m$ model fitting of the low-*r* (*r* < 5.8 Å) region of the PDFs.

	P700	**P300**
***a* / Å**	10.2050(6)	10.2042(7)
A site (16e)	$x = y = z = 0.86795(5)$	$x = y = z = 0.8646(1)$
B site (16e)	$x = y = z = 0.38292(5)$	$x = y = z = 0.3760(1)$
O1a (24f)	$x = 0.29696(8)$, $y = z = 0$	$x = 0.2911(1)$, $y = z = 0$
O1b (24g)	$x = 0.06180(5)$, $y = z = 1/4$	$x = 0.06013(6)$, $y = z = 1/4$
A site ADPs[a]	$U11 = 0.0838(4)$ $U12 = -0.0396(2)$	$U11 = 0.0326(7)$ $U12 = -0.0136(6)$
B site ADPs[a]	$U11 = 0.00408(8)$ $U12 = 0.0027(1)$	$U11 = 0.0088(4)$ $U12 = 0.0088(3)$
O1a site ADPs[b]	$U11 = 0.0114(1)$ $U22 = 0.0237(2)$ $U23 = -0.0109(2)$	$U11 = 0.0062(4)$ $U22 = 0.094(2)$ $U23 = -0.061(2)$
O1b site ADPs[b]	$U11 = 0.0139(2)$ $U22 = 0.0197(1)$ $U23 = 0.0082(2)$	$U11 = 0.0045(2)$ $U22 = 0.0172(3)$ $U23 = 0.0074(5)$
O2a site ADPs[c]	$U11 = 0.0063(1)$	$U11 = 0.0119(3)$
O2b site ADPs[c]	$U11 = 0.189(1)$	$U11 = 0.1$
wRp	5.5%	11.0%

[a] $U11 = U22 = U33$, $U12 = U13 = U23$; [b] $U11$, $U22 = U33$, $U23$; [c] $U11 = U22 = U33$

It can be seen that the $F\bar{4}3m$ model fits the low-r regions of the pyrochlore data extremely well. The geometry of the A site is rather heavily distorted with A–O bond lengths ranging from 2.2 to 2.6 Å, while the B site remains a fairly ordered octahedron (see Figure 5.18).

On average, the structure of the sodium cerium titanate pyrochlore is described by the ‘standard’ stoichiometric $Fd\bar{3}m$ pyrochlore model, with significant cation disorder on the A site due to the presence of Na (33%), Ce (52-54%) and Ti (13-15%) on this site. The local structure is distorted from the ideal pyrochlore structure, presumably due to the significantly different coordination environments preferred by the different A site metals, and this distortion can be modelled by lowering the symmetry to $F\bar{4}3m$ when fitting the low-r region of the PDF. This allows the A site to distort significantly from the regular cubic environment in the normal pyrochlore.

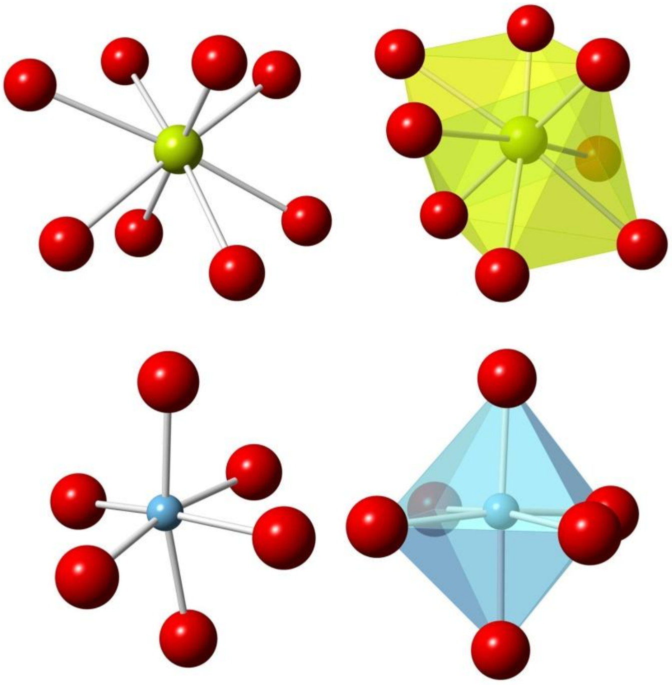

Figure 5.18 Upper: two views of the geometry of the A site in the $F\bar{4}3m$ pyrochlore model. Lower: two views of the geometry of the B site in the $F\bar{4}3m$ pyrochlore model. Red spheres are oxygen, yellow are cerium and blue are titanium.

The $F\bar{4}3m$ model is of course, still an approximation. The A site is still treated as a single cation which behaves as an average of the three constituent metals. In reality, each of the three metal environments is likely to be slightly different, and a truly realistic fitting or simulation regime would model them separately. This was not plausible with only one data set, however. The proportion of Ti on the A site is very small and its contributions would be almost impossible to separate reliably from those of the other A site metals. Therefore, no further modelling was attempted.

5.3. Conclusions

In this chapter, the elucidation of the structures of two types of cerium-containing materials has been described. The materials exhibit several forms of disorder, including small particle size, partial or mixed site occupancy, and symmetry distortions. In both cases a full structural description required that the average and local structure be considered separately, as analysis of the PDFs revealed shortcomings in the bulk structural models.

The average structure of a series of cerium bismuth oxides (general formula $Ce_{1-x}Bi_xO_{2-1/2x}$ where $x = 0.25 - 0.6$) can be described using the cubic fluorite structure, with increasing Bi content leading to increasing lattice parameter. The fluorite structure did not fit the low-*r* region of the PDFs satisfactorily because the local structure is disordered as a result of the preference of Bi^{3+} for an asymmetric coordination environment. This disorder can be modelled in the low-*r* region with a mixture of CeO_2 and β-Bi_2O_3, wherein the 5-coordinate Bi environment is heavily distorted. Since the average cubic symmetry was maintained, the distorted Bi site was concluded to exist in multiple orientations throughout the structure, as described for the cubic δ-Bi_2O_3 phase by Hull *et al.*[21]

The average structure of a sodium cerium titanate pyrochlore of composition $(Na_{0.33}Ce_{0.53}Ti_{0.14})_2Ti_2O_7$ was found to be consistent with a cubic pyrochlore structure with excess Ti on the A site. The complexity of the A site led to local distortions in the geometry of this site, which were modelled with a lower symmetry $F\bar{4}3m$ pyrochlore model. As with the cerium bismuth oxides, the distortions did not propagate into the bulk of the material in an ordered fashion, as no evidence for lower symmetry was found in the Bragg scattering or the high-*r* region of the PDF.

Questions may be raised over the validity of describing a local structural deviation in terms of a crystallographic space group and its associated symmetry constraints. However, this approach allows a useful, realistic structural model to be obtained in a simple manner, and was also applied to the structure of γ-Ga_2O_3 in Chapter 3. More thorough alternatives such as PDF refinement of an unconstrained model (*i.e.* using the P1 space group) or modelling a much larger array of atoms (*i.e.* RMC) would require a great deal of computation time and power, and could be extremely difficult to interpret usefully. In the case of the pyrochlore, a structural distortion that has been observed "in bulk" for other pyrochlores, provides the local environment with the necessary flexibility and remains relatively simple to interpret. Describing local structural disorder in the language of crystallography has the additional benefit of being readily understandable to non-experts.

5.4. References

1. Trovarelli, A.; de Leitenburg, C.; Boaro, M.; Dolcetti, G., *Catal. Today* **1999,** *50*, 353.
2. Gorte, R. J., *AlChE J.* **2010,** *56*, 1126.
3. Kaspar, J.; Fornasiero, P.; Graziani, M., *Catal. Today* **1999,** *50*, 285.
4. Hilaire, S.; Wang, X.; Luo, T.; Gorte, R. J.; Wagner, J., *Appl. Catal., A* **2001,** *215*, 271.
5. Kusar, H.; Hocevar, S.; Levec, J., *Appl. Catal., B* **2006,** *63*, 194.
6. Craciun, R.; Shereck, B.; Gorte, R. J., *Catal. Lett.* **1998,** *51*, 149.
7. Wang, D. Y.; Park, D. S.; Griffith, J.; Nowick, A. S., *Solid State Ionics* **1981,** *2*, 95.
8. Balazs, G. B.; Glass, R. S., *Solid State Ionics* **1995,** *76*, 155.
9. Yamashita, K.; Ramanujachary, K. V.; Greenblatt, M., *Solid State Ionics* **1995,** *81*, 53.
10. Baidya, T.; Gayen, A.; Hegde, M. S.; Ravishankar, N.; Dupont, L., *J. Phys. Chem. B* **2006,** *110*, 5262.
11. Li, G. S.; Smith, R. L.; Inomata, H., *J. Am. Chem. Soc.* **2001,** *123*, 11091.
12. Ruedorff, W.; Valet, G., *Z. Anorg. Allg. Chem.* **1953,** *271*, 257.
13. Wright, C. S.; Fisher, J.; Thompsett, D.; Walton, R. I., *Angew. Chem. Int. Ed.* **2006,** *45*, 2442.
14. Playford, H. Y.; Modeshia, D. R.; Barney, E. R.; Hannon, A. C.; Wright, C. S.; Fisher, J. M.; Amieiro-Fonseca, A.; Thompsett, D.; O'Dell, L. A.; Rees, G. J.; Smith, M. E.; Hanna, J. V.; Walton, R. I., *Chem. Mater.* **2011,** *23*, 5464.
15. Sasaki, T.; Ukyo, Y.; Kuroda, K.; Arai, S.; Muto, S.; Saka, H., *J. Ceram. Soc. Jpn.* **2004,** *112*, 440.
16. Dikmen, S.; Shuk, P.; Greenblatt, M., *Solid State Ionics* **1998,** *112*, 299.
17. Li, G. S.; Mao, Y. C.; Li, L. P.; Feng, S. H.; Wang, M. Q.; Yao, X., *Chem. Mater.* **1999,** *11*, 1259.
18. Sears, V. F., *Neutron News* **1992,** *3*, 26.
19. Sardar, K.; Playford, H. Y.; Darton, R. J.; Barney, E. R.; Hannon, A. C.; Tompsett, D.; Fisher, J.; Kashtiban, R. J.; Sloan, J.; Ramos, S.; Cibin, G.; Walton, R. I., *Chem. Mater.* **2010,** *22*, 6191.
20. Harwig, H. A., *Z. Anorg. Allg. Chem.* **1978,** *444*, 151.
21. Hull, S.; Norberg, S. T.; Tucker, M. G.; Eriksson, S. G.; Mohn, C. E.; Stolen, S., *Dalton Trans.* **2009**, 8737.
22. Scavini, M.; Coduri, M.; Allieta, M.; Brunelli, M.; Ferrero, C., *Chem. Mater.* **2012**.
23. Deepa, M.; Rao, P. P.; Sumi, S.; Radhakrishnan, A. N.; Chandran, M. R.; Koshy, P., *Mater. Chem. Phys.* **2011,** *127*, 162.
24. Heremans, C.; Wuensch, B. J.; Stalick, J. K.; Prince, E., *J. Solid State Chem.* **1995,** *117*, 108.
25. Beyerlein, R. A.; Horowitz, H. S.; Longo, J. M.; Leonowicz, M. E.; Jorgensen, J. D.; Rotella, F. J., *J. Solid State Chem.* **1984,** *51*, 253.
26. Ismunandar; Kennedy, B. J.; Hunter, B. A.; Vogt, T., *J. Solid State Chem.* **1997,** *131*, 317.

Chapter 6: Structural Studies of Amorphous Zeolite Precursors

6. Structural Studies of Amorphous Zeolite Precursors

6.1. Introduction

6.1.1. Background

Aluminosilicate zeolites are the archetypal microporous materials: crystalline solids with well-defined framework structures leading to the presence of pores and channels of molecular dimensions. Zeolite frameworks are built from tetrahedral [TO_4] units (where T = Al or Si) which can be arranged in an enormous variety of ways – leading to an enormous variety of different zeolite structures.[1] A large proportion of existing research into zeolites and zeotypes has focussed on the synthesis of new materials, and has been driven by their many industrially and technologically important properties and applications. Zeolites are widely used as catalysts, sorbents and ion-exchangers

Laboratory synthesis of zeolites began in the 1940s – 1950s with the work of Barrer,[2] who studied the effect of strong salt solutions at high temperature on known mineral phases and in some cases produced zeolites that did not have natural analogues. The work of Milton, using freshly prepared aluminosilicate gels as reactive starting materials, led to the synthesis of 20 zeolites, including A and X,[3-4] by 1953 (Figure 6.1).

The early 1960s saw the first use of organic constituents in zeolite synthesis, which expanded the field greatly, and subsequently led to the discovery of pure-silica and high-silica zeolites such as silicalite-1 by Flanigen *et al.*[5] and silicalite-2 by Bibby *et al.*.[6]

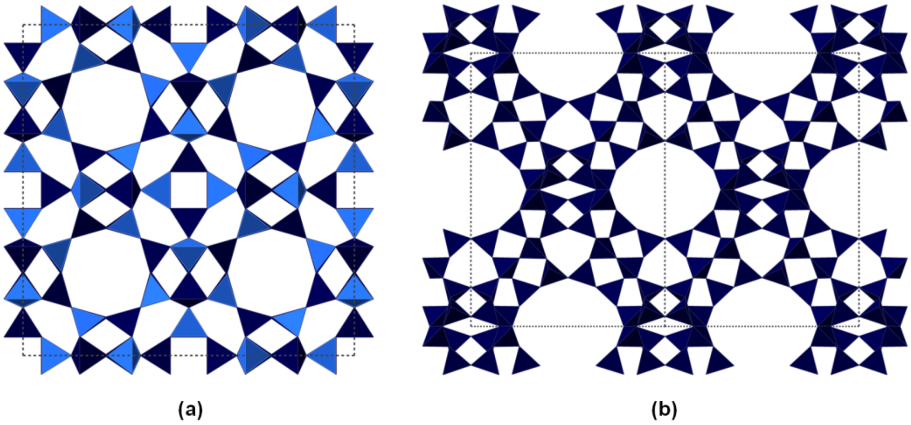
(a)

(b)

Figure 6.1 The structures of (a) zeolite A and (b) zeolite Y. Tetrahedra representing the [TO_4] units are shown without associated water and/or cations.

Since the 1960s, the number of known synthetic zeolites has increased enormously, and research has also expanded to include related materials or “zeotypes” such as aluminophosphates (AlPOs) and gallophosphates (GaPOs).[7-8, 9,10] These materials have a great variety of structures and compositions, many of which are unknown in traditional zeolites. More recently, the synthesis of mesoporous materials with much larger pore sizes has been achieved using surfactant molecules as templates.

It is often the well-defined geometry of zeolitic pores and channels which leads to the shape and size specificity which makes them so useful as adsorbents and catalysts. The ability to target new zeolite structures for a specific application would be enormously valuable, but would require a highly detailed understanding of the mechanisms of their formation.

Research dedicated to understanding the mechanism of zeolite crystallisation has been carried out since the early 1960s. Its progress was discussed in detail in two recent reviews by Cundy and Cox and will be summarised very briefly here.[11-12] Zeolites are typically synthesised by hydrothermal methods: suitable sources of aluminium and silicon are mixed to form reactive aluminosilicate gels which are heated in alkaline, hydrothermal conditions at temperatures of 80 – 200 °C. The formation of the gel is a critical step in the zeolite synthesis, such that gels with different composition will produce different zeolite products on heat treatment, and for this reason the gel phase is commonly referred to, both in the literature and in this thesis, as the zeolite precursor or gel precursor.

It was Barrer, in 1959,[13] who proposed a mechanism for zeolite crytal growth from smaller geometric units made up of multiple silicate/aluminate tetrahedra: the so-called secondary building units (SBUs). These have now been defined by the International Zeolite Association and there are 23 unique types of SBU.[1] Though the existence of complex silicate clusters in solution is well known, particularly through the use of NMR spectroscopy,[14-15] the existence of SBUs in zeolite precursors and their role in the crystallisation mechanism has remained controversial. In 1960, Breck and Flanigen studied the crystallisation of zeolites A and X using X-ray diffraction and electron microscopy.[16] They concluded that the crystallisation occurred by successive ordering of the initial gel phase – the randomly oriented structures in the gel were broken down into TO_4 (T = Si or Al) tetrahedral units by the action of OH^- ions and then new polyhedral structures were formed from these, assisted by the ordering influence of the alkali metal cations (see, for example, Figure 6.2(a)).

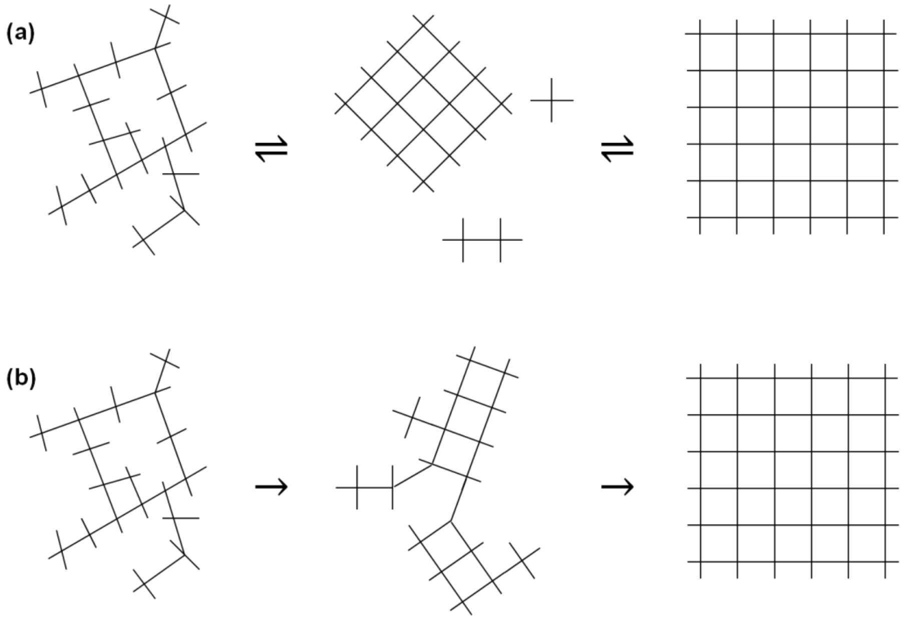

Figure 6.2 Figure illustrating two views of zeolite crystallisation, based on Cundy and Cox,[11] (a) heterogeneous crystallite growth *via* gel releasing reactive species/building units into solution and (b) homogeneous crystallite growth *via* rearrangement and successive ordering of the gel phase.

In contradiction to the work of Breck and Flanigen, subsequent work by Kerr,[17] and Zhdanov provided evidence for solution mediated crystal growth.[18] It was suggested that the initial gel approached equilibrium with the solution through dissolution and re-precipitation and released active species into the solution, wherein nucleation and subsequently crystal growth occurred. This has largely been supported by subsequent research. Angell and Flank reported in the late 1970s that the initial gel that formed on mixing of the reagents was transformed into an “apparently amorphous aluminosilicate intermediate” before the action of heat and base produced active species in solution which initiate crystallisation.[19] A detailed study of the gel isolated from the reaction mixture at different stages during the crystallisation was carried out by Nicolle *et al.* in 1992,[20] and it was found through examination of their compositions and cation exchange capacities that the gels that had been allowed to equilibrate were very different from the initially precipitated ones. The structure of the equilibrated gel, known as the secondary amorphous phase, demonstrated some local ordering of silica and alumina tetrahedra but showed no long range zeolitic order. After the formation of the secondary amorphous phase, zeolite crystallisation proceeds *via* nucleation and then crystal growth, processes which are still far from well-understood.[12] Whether nucleation occurs within the amorphous gel or in solution (or both) is not certain. It is perhaps most plausible, given that crystals are often seen surrounded by a matrix of amorphous material, to assume that the gel, or at least the gel-liquid interface, is the most likely nucleation site. This was the conclusion of a electron microscopy study of zeolite Y by Mintova *et al.*.[21] Using this assumption, nucleation can be thought of as the point at which the regions of order (*i.e.* with structure resembling the crystalline zeolite) in the secondary amorphous phase reach a sufficient size for the order to propagate, forming an ordered lattice. After nucleation, the growth of zeolite crystals occurs either *via* aggregation of crystallites or *via* stepwise addition of smaller units, and it is likely that both of these processes occur to some extent. The rate of zeolite crystal growth tends to be slow compared with that of simpler crystalline materials (*e.g.* NaCl) which highlights the importance of the gel phase in the process. A full discussion of the issues surrounding zeolite nucleation and crystal growth can be found in the latter parts of the aforementioned review by Cundy and Cox.[12] The steps of zeolite crystallisation are summarised in Figure 6.3.

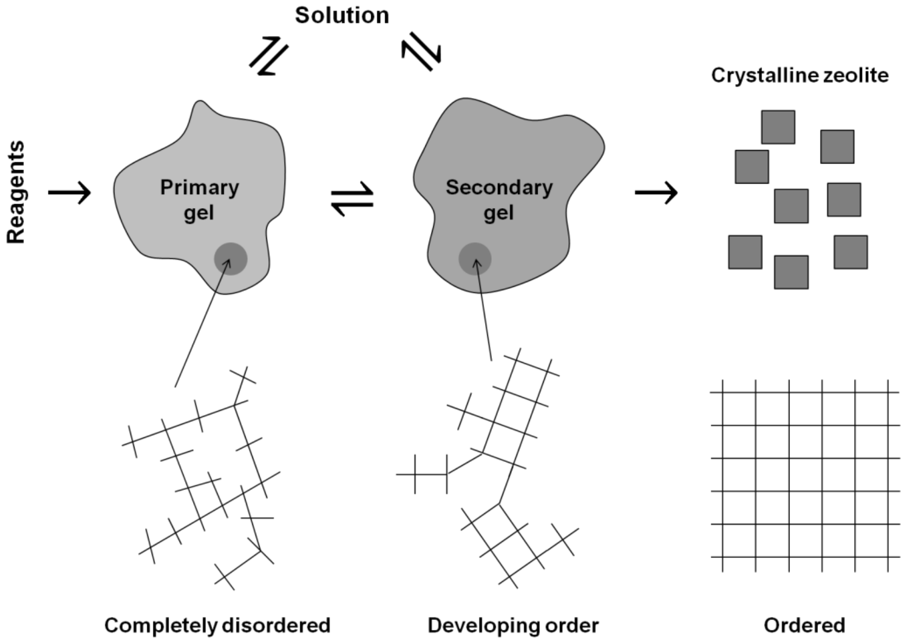

Figure 6.3 Cartoon illustrating a proposed scheme for zeolite crystallisation *via* successive ordering of the gel precursor. Based on Cundy and Cox.[12]

It is generally accepted that the composition of the secondary amorphous phase and the development of order prior to the onset of crystallisation are both hugely important in dictating how the reaction proceeds, and therefore an understanding of these factors is crucial to properly understanding the crystallisation mechanism. A recent review article by Dorset examined the progress made towards structural characterisation of zeolite precursors from the perspective of crystal engineering,[22] *i.e.* the potential for deliberate and targeted construction of zeolitic materials *via* control of their synthesis conditions. In respect of the above discussion, this implies the need for a fuller understanding of the structure of the gel phase and its evolution prior to the formation of zeolite crystals.

Much of the work carried out with the aim of contributing to the understanding of zeolite formation has been carried out on samples of solid removed from the reaction at various times, and are therefore referred to as “quenching” studies. In 2004, Yang *et al.* used solid-state ^{27}Al, ^{29}Si and ^{23}Na magic-angle spinning (MAS) NMR and total neutron scattering to study quenched amorphous zeolite A precursors.[23] It was found from NMR that the local atomic order in the precursors had some similarities with the crystalline zeolite, although there appeared to be a range of T–O distances and T–O–T angles present in the precursors rather than the well-defined structure in the crystalline product. The neutron diffraction data indicated that the medium range order, *i.e.* that beyond the range of the nearest-neighbour interactions, changed with reaction time even before crystallisation occurred. Neutron pair distribution functions (PDFs) extracted from the total scattering data also provided evidence for the evolution of structure prior to crystallisation, revealing that the correlations assigned to T– –T (non-bonded) distances are much less well defined in the amorphous precursors than in the crystalline zeolite, suggesting that a wide range of structural motifs, and not just those which will eventually coalesce to form the zeolite A structure, are present prior to crystallisation.

Studies by Wakihara *et al.*[24-25] used high energy X-ray scattering to examine the structure of a range of crystalline zeolites and their quenched precursors. The local structure of these materials, as revealed by their PDFs, was often strikingly similar between crystalline and amorphous phases, but there was evidence of significant differences in the medium-range order. The PDFs of zeolite A precursors were analysed using Reverse Monte Carlo simulations. The simulations were constrained based on knowledge of the crystalline zeolite structure, such that “reasonable” T–T distances and a connectivity which obeyed Löwenstein’s rule (which states that Al–O–Al bonds should not be formed in zeolite structures)[26] was maintained. The results of the simulations apparently provided evidence for the existence of aluminosilicate rings (up to 6-membered) in the precursors, though how the connectivity of the starting models were determined and then altered by the RMC algorithm is not clear.

A recent synthetic study by Itabashi *et al.*[27] found that different zeolites could be obtained from the same gel precursor depending on the choice of seed crystals. A gel that, under normal, non-seeded, hydrothermal conditions produced zeolite ZSM-5, could be used instead to synthesise zeolite ZSM-12 if zeolite Beta seed crystals were added. This observation was taken as evidence for the presence of secondary building units in the gel, despite the fact that there are no SBUs common to all three structures.

The concern with quenching studies and other *ex situ* analysis techniques is that the quenching and drying process may irreversibly alter the structure of the material, and particularly that the interactions of water molecules and charge-balancing cations in the solution with the emerging zeolite phase are removed by taking the precursor from the reaction solution and studying it in its dry form.

An obvious alternative approach is to study the amorphous phase *in situ*, however this is complicated by the sealed reaction vessels that are often used for zeolite synthesis. Usui and coworkers used an intermediate approach wherein precursor gels were removed from the reaction solution but allowed to remain wet for the duration of the experiment.[28] A laboratory X-ray diffractometer equipped with Mo K_α radiation was used to obtain atomic correlation functions for the precursors and the structural information therein suggested that the most common “building unit” present was a four-membered chain with T– –T distance of 3.2 Å. The broadness of the correlation functions produced from the relatively low energy X-rays prevented detailed analysis, but nevertheless the zeolite structure apparently developed suddenly with no gradual changes in the correlation functions leading up to the point of crystallisation.

Small angle scattering of X-rays or neutrons (SAXS or SANS) is ideally suited to the study of solid materials in the presence of a liquid, and has often been applied to the problem of zeolite formation. Information about particle shape, size and surface structure can be obtained from small-angle scattering data. An *in situ* investigation of the formation of silicalite-1 using SAXS was performed in a specially designed hydrothermal cell by Dokter *et al.*[29] and provided insight into the development of microstructure over the course of the synthesis. Evidence for a significant reorganisation of the gel phase prior to the onset of crystallisation was found in terms of the surface of the particles displaying a varying degree of roughness. SAXS studies on the formation of zeolites from clear solutions have been used to obtain insights into the role of oligomeric silicate species in solution-based crystallisation, although it is unlikely that these results would translate to gel-based syntheses due to the vast differences in the concentrations of reactive species.[30-31]

A combination of X-ray diffraction and Raman spectroscopy was used by Depla *et al.*[32] to study the formation of zeolites A and X. A specially-designed instrument allowed simultaneous measurement of XRD and Raman data and, importantly, samples were studied *in situ* (the solid phases were not removed from the solution). Changes in the vibrational spectra with the onset of crystallinity were observed, but there were also significant changes in the vibrational data before crystallisation occurred, corresponding to the development of different aluminosilicate building units.

Using a Ti/Zr alloy of appropriate composition it is possible to construct a hydrothermal reaction cell that is effectively invisible to neutrons, due to the coherent scattering lengths of Ti and Zr having opposite signs (Ti = -3.438 fm and Zr = 7.16 fm). This vessel was used successfully by Walton *et al.* to study the crystallisation of zeolite A and hydroxosodalite.[33] This study looked at the evolution of the Bragg diffraction peaks over the course of the reaction, and so did not give any information about the amorphous phase(s). A recent total neutron scattering study by White *et al.*,[34] following the formation of a geopolymer cement from metakaolin (an aluminosilicate clay) highlighted the power and potential of neutron scattering to reveal structural information in complex, amorphous, aqueous systems.

6.1.2. Scope of this chapter

This chapter describes the progress made towards carrying out and interpreting the results of *in situ* neutron scattering experiments on zeolite precursor gels.

For the purposes of the *in situ* work, the simple, non-organic-templated zeolite A, chemical formula $[Na_{12}(H_2O)_{27}]_8[Al_{12}Si_{12}O_{48}]_8$ (in its hydrated state) was selected. Due to its industrial significance, its synthesis and structure have been extensively studied and it was considered an ideal model system. Its structure is cubic, space group $Fm\bar{3}c$, a = 24.61 Å and its framework is built from relatively few structural motifs, as shown in Figure 6.4.

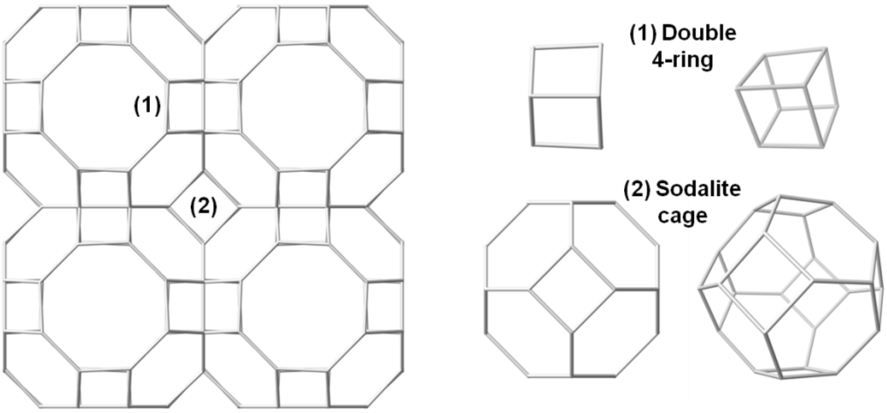

Figure 6.4 The framework structure of zeolite A, showing the structural motifs involved. T atoms lie on the points where the wire “bonds” intersect.

The synthesis of zeolite A from inorganic, anhydrous (and/or deuterated) materials was initially developed by Dr Dorota Madja,[35] using $NaAlO_2$ and Na_2SiO_3 as Al and Si sources, respectively. For the *in situ* studies it was necessary to distinguish between the zeolite precursor gel and its “background” (*i.e.* the synthesis liquid) by allowing the reaction mixture to settle and separate into two layers. To achieve this, excess D_2O was added after an appropriate ageing period had elapsed in order to increase the separation between gel and liquid layers to a point where the neutron beam could be directed at each in turn. The addition of extra D_2O, however, caused the synthesis to deviate from the ideal “real” reaction conditions, and for the work described here it was considered desirable to omit this step. This chapter describes the development of a reliable, reproducible synthesis of well-separated zeolite precursor gels.

The examination of the structure of the gels using total neutron scattering will be described in the second half of this chapter. Since the gels are amorphous, the real-space data contained within the pair distribution functions is of great importance in examining their structures. The structural information about the gels obtained from total neutron scattering and other complementary techniques will be discussed in comparison to similar data from the crystalline zeolite and in the context of previous literature on zeolite crystallisation.

This is a preliminary study designed to investigate any differences between quenched and *in situ* gels, and to evaluate the feasibility of extracting structural information.

6.2. Experimental

6.2.1. Synthesis

A typical synthesis began with the preparation of 1.6 M solutions of $NaAlO_2$ and Na_2SiO_3 in D_2O. The powders of $NaAlO_2$ (Fisher Scientific, technical grade) and Na_2SiO_3 (Alfa Aesar, anhydrous, technical grade) were each dried at 200 °C for 90 minutes prior to addition of D_2O, the solutions were warmed at 70 °C to aid dissolution and were used immediately once prepared. A zeolite precursor gel of total volume 5 ml (see below) was synthesised as follows: To 1 ml of $NaAlO_2$ (1.6 M) in a 10 ml polyethylene bottle was added 1 ml of Na_2SiO_3 (1.6 M) with vigorous stirring. A white gel immediately formed and to this was added 0.8 ml of NaOD (40% in D_2O, ~14.2 M, Sigma-Aldrich) and 2.2 ml D_2O (Sigma-Aldrich) under continued stirring. The bottle was sealed and placed in an oven at the desired ageing temperature (30, 70 or 90 °C) for a chosen period of time.

During the ageing period the reaction mixtures settled into two layers: an opaque gel layer and a clear liquid layer (Figure 6.5). The final height of the gel layer was between 33% and 66% relative to the total height of the mixture.

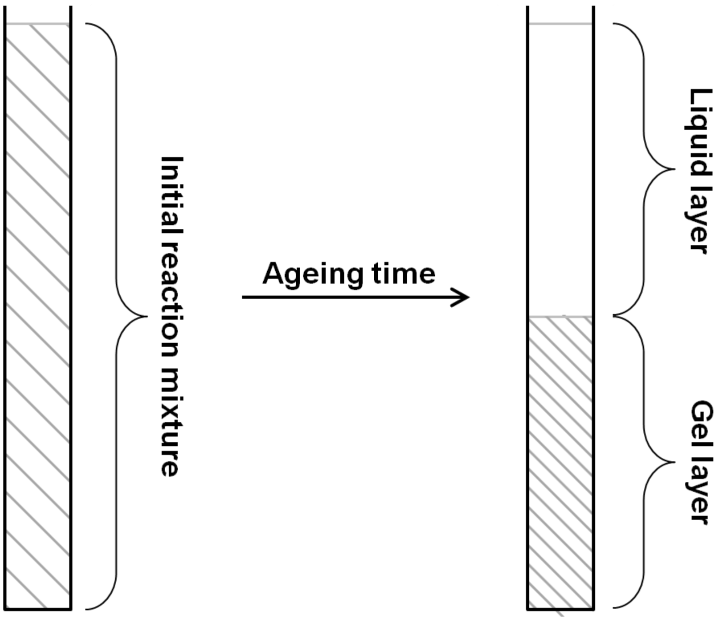

Figure 6.5 Cartoon representation of the separation of zeolite precursor gels.

The sample container for the total neutron scattering experiments was a vanadium can of inner diameter 0.762 cm and length 12.8 cm (volume 5.8 ml) hence a volume of 5 – 5.5 ml for the gels was chosen to appropriately fill the can. After the ageing period had elapsed, the gels were loaded into the vanadium can and immediately sealed. Each gel was prepared in duplicate such that one sample could be placed into a clear plastic tube of the same diameter as the vanadium can so that the progress of its resettling (which generally took no more than 10 minutes) could be observed prior to measurement commencing.

A reference sample of a dried/quenched gel was obtained by collecting the appropriately aged gel by suction filtration, washing with D_2O and drying at 70 °C overnight.

A reference sample of the crystalline zeolite A was obtained by heating a freshly prepared gel at 90 °C for 3 hours, whereupon the solid was obtained by suction filtration, washed with D_2O and dried at 70 °C. The powder X-ray diffraction pattern is shown in Figure 6.6.

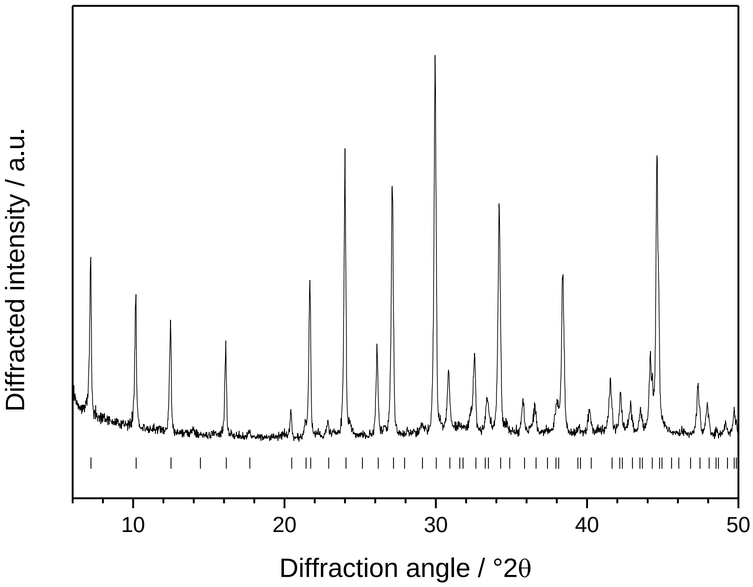

Figure 6.6 The measured X-ray diffraction pattern of crystalline zeolite A, compared with the allowed reflections generated from Ikeda *et al.*[36]

6.2.2. *Neutron scattering measurements*

As noted in the preceding section, the zeolite precursors consisted of two distinct layers (a clear solution and an opaque gel) in a long vanadium can. To facilitate the *in situ* measurements a sample holder with an adjustable-height arm was designed such that the can could be raised or lowered with respect to the neutron beam without disturbing the experimental setup. Data were collected using a square 1.8 × 1.8 cm beam size from both the settled gel layer and the clear liquid layer of the reaction mixture, by altering the height of the can with respect to the neutron beam (Figure 6.7).

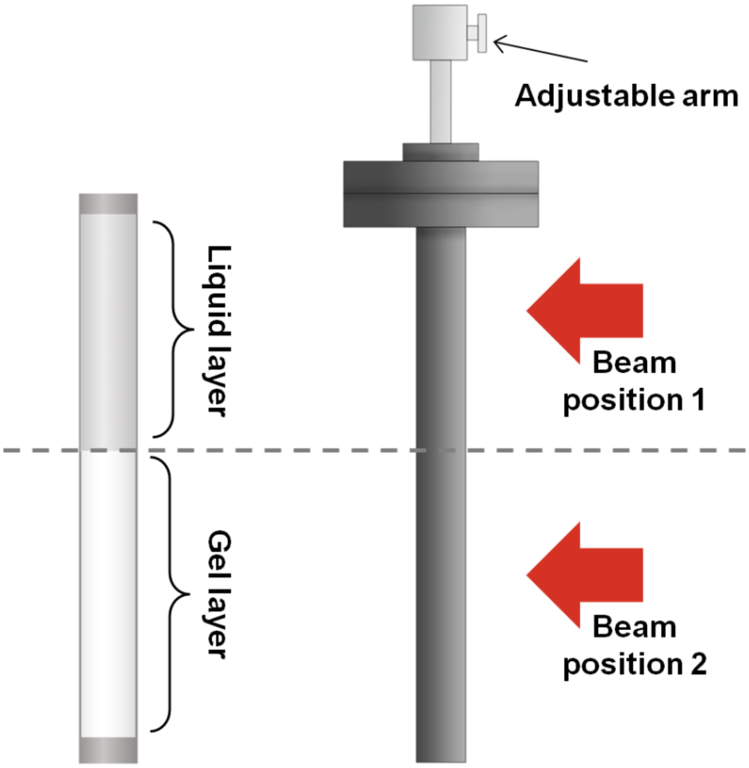

Figure 6.7 A cartoon representation of the zeolite precursor gel and the experimental set-up for neutron diffraction measurements.

The instrument SANDALS[37] was used due to its low-angle detector banks making it ideal for the study of samples containing large amounts of light elements, and the large accessible *Q*-range (0.1 – 50 $Å^{-1}$) suitable for producing high-quality PDFs with good *r*-space resolution.

Datasets of high quality were required for analysis so each layer of each reaction mixture was measured for at least 7 hours. Analysis of the SANDALS data was carried out using the procedures detailed in Chapter 2 to produce corrected *i*(*Q*)s and *D*(*r*)s for each sample. Each measured layer was treated as an independent sample due to the differences in density and composition between the gel and liquid layers and to avoid bias in the final results.

Since the exact composition of each gel and liquid layer was likely to change with reaction time and temperature, it was not possible to retain every measured sample for elemental analysis. Hence, representative samples, prepared separately were studied to obtain chemical compositions for data analysis.

ICP analysis on a representative sample of a gel aged at 30 °C for 3 hours provided the weight percentages as given in Table 6.1.

Table 6.1 Results of ICP analysis of representative zeolite precursor gels.

Sample	Al weight %	Si weight %	Na weight %
Gel layer	1.05	1.31	7.49
Molar ratios:	*1*	*1.2*	*8.35*
Liquid layer	0.28	0.24	6.63
Molar ratios:	*1.1*	*1*	*32.04*
Dried gel	4.22	5.52	10.7
Molar ratios:	*1*	*1.25*	*2.96*

The composition of the entire reaction mixture could be determined from the starting materials, however, the partioning of elements between the settled gel and liquid layers could only be estimated. The liquid layer was carefully decanted and its mass recorded, and likewise the gel layer. The density of the liquid layer was estimated based on its height in a tube of known diameter and its composition was assumed to be purely sodium deuteroxide solution of a concentration appropriate to the weight percentage of Na from the ICP analysis (equivalent to equivalent to a 4.6 times dilution of 40% NaOD in D_2O). Although the liquid was found to contain a small amount of Al and Si, their contribution to its neutron diffraction would be expected to be negligible in the presence of a great excess of D_2O and NaOD, hence for simplicity, it was assumed that all the Al and Si was found in the gel layer. This allowed the ratios of each component of the gel and liquid layers to be estimated (see, for example, Table 6.2)

Table 6.2 The composition of a zeolite precursor gel, as approximated for analysis of neutron scattering data.

Sample		**Al**	**Si**	**Na**	**O**	**D**
Total	**No. moles**	0.0017	0.0016	0.017	0.265	0.490
	Ratio	1.0	1.0	10.3	162.6	300.6
Liquid layer	**No. moles**	-	-	0.006	0.098	0.187
	Ratio	-	-	1.0	17.7	33.6
Gel layer	**No. moles**	0.0017	0.0016	0.011	0.167	0.303
	Ratio	1.1	1.0	7.02	104.1	189.5

SANS data were obtained using the instrument LOQ.[38] In this case, the gel and liquid layers were separately mounted into quartz cuvettes prior to measurement.

The instrument NIMROD[39] was used to obtain $i(Q)$s over an extremely large Q-range (0.02 – 100 Å^{-1}) with the intention of enabling the small-angle scattering to be included in the analysis of the entire range of data. The reaction mixtures were prepared as for SANDALS, however after the aging time had elapsed the liquid and gel layers were decanted and loaded separately into TiZr alloy cans of internal dimensions $4 \times 4 \times 0.2$ cm. The samples completely filled the cans and the beam size was ~3.0 cm square.

6.3. Results and Discussion

6.3.1. NMR

There are several examples of the application of ^{27}Al and ^{29}Si solution NMR to determining the types of aluminosilicate species present in aqueous solution, similar to the reaction liquid in the zeolite A precursor gels described in this thesis.[14-15, 40] Figure 6.8 shows the ^{27}Al and ^{29}Si NMR spectra of the clear liquid layer of a zeolite precursor gel aged at 30 °C for 3 hours.

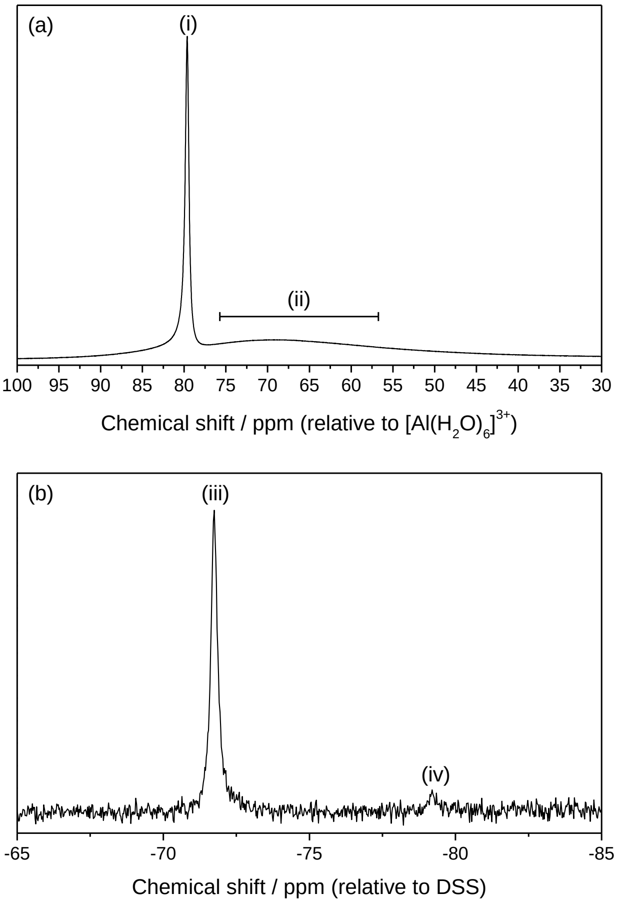

Figure 6.8 (a) The ^{27}Al NMR spectrum of the liquid layer of a zeolite A precursor gel. Features at (i) and (ii) indicate Q^0 monomeric species and Q^1 dimeric species, respectively. (b) ^{29}Si NMR spectrum of the liquid layer of a zeolite A precursor gel. Features at (iii) and (iv) indicate q^0 monomeric and q^1 dimeric species, respectively. Note that DSS is a sodium salt of 2,2-dimethyl-2-silapentane-5-sulfonate, a common NMR standard used in aqueous solution. The Q/q notation is used to represent complex silicate and aluminosilicate species in solution: the superscript represents the number of T–O–T bridges.

In both cases the signal strength was rather low, indicating a low concentration of Al and Si in the liquid layer. This is consistent with the results of ICP analysis which revealed that Al and Si accounted for less that 0.5% by mass of the liquid layer. The majority of Al and Si in the solution exists as monomeric (Q^0) $[Al(OH)_4]^-$ and $[Si(OH)_4]$ species, with a very small amount of silicate or aluminosilicate species with one T–O–T bridge as evidenced by small features at chemical shifts 70 ppm (^{27}Al) and -79 ppm (^{29}Si). The chemical shifts of these features are in agreement with those reported by McCormick *et al.*[40] for dilute aluminosilicate solutions.

6.3.2. IR spectroscopy

Vibrational spectroscopy has been used to characterise zeolitic materials for many years. The vibrational frequencies tend to be sensitive to changes in Al/Si ratio, the number and type of charge balancing cations and the degree of hydration and as such the spectra can be extremely complex.[41]

Figure 6.9 shows the IR spectrum of the zeolite precursor gel with the spectra of the quenched and dried gel and crystalline zeolite A also shown for comparison.

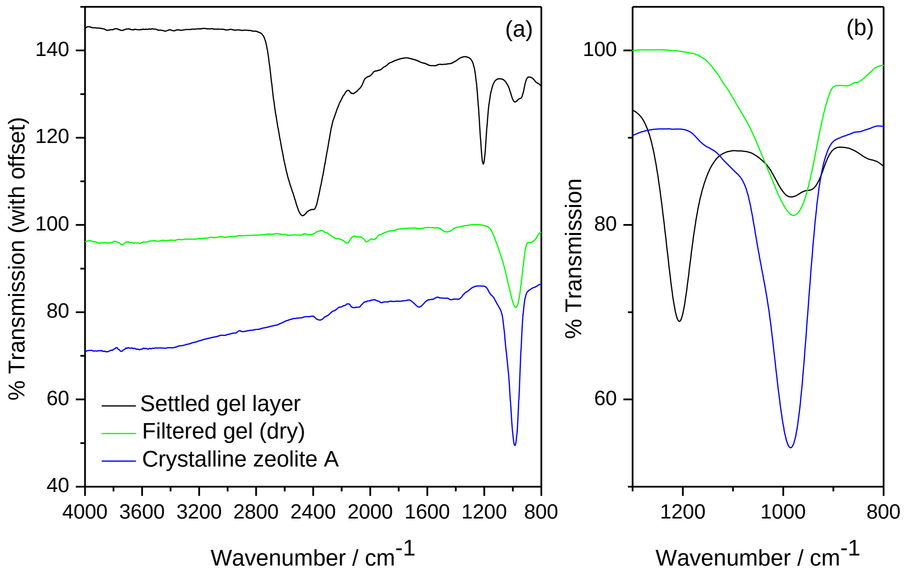

Figure 6.9 Infrared spectra of zeolite samples over the full measured range (a) and over the range incorporating the T–O–T asymmetric stretching frequencies (b).

The gel layer has strong bands due to O–D stretching (2400 cm^{-1}) and D–O–D bending (1200 cm^{-1}) which are clearly absent from the dried samples - although some D (or H) is likely to be present within the pores of the crystalline zeolite detecting it by IR spectroscopy would require a measurement with greater sensitivity. The band at 900 – 1100 cm^{-1} is attributable to the T–O–T asymmetric stretching modes within the tetrahedral network of the zeolites.[41-42] The position of this band is highly sensitive to the Al/Si ratio and the arrangement of the tetrahedral network and its width has been associated with the degree of geometric disorder.[41] In the spectrum of the gel layer this band appears as a doublet, with a shoulder at lower wavenumber relative to the same band in the dried gel layer. The information gained from IR spectroscopy can be summarised thus: the arrangement of the [TO_4] tetrahedral network in the precursor gel is different to that in the crystalline zeolite, and the increased line width of the T–O–T asymetric stretching band in the precursor gel indicates a higher degree of disorder. The doublet observed for this band in the precursor gel may be evidence for the existence of

$Q^{n<4}$ T centres, where tetrahedral units are terminated by one or more –OD groups. It is important to note also that the quenched and dried gel far more closely resembles the crystalline zeolite than does the aqueous gel. This is clear evidence for structural changes occurring during the drying of the gel, despite the fact that it remains amorphous, which highlights the importance of *in situ* studies of these materials.

6.3.3. SEM

The dried zeolite gel and the crystalline zeolite were imaged using SEM. The crystalline zeolite consists of cubic crystallites of 80 - 200 nm in size, whereas the dried gel consists of shapeless particles of less than 50 nm in size (Figure 6.10).

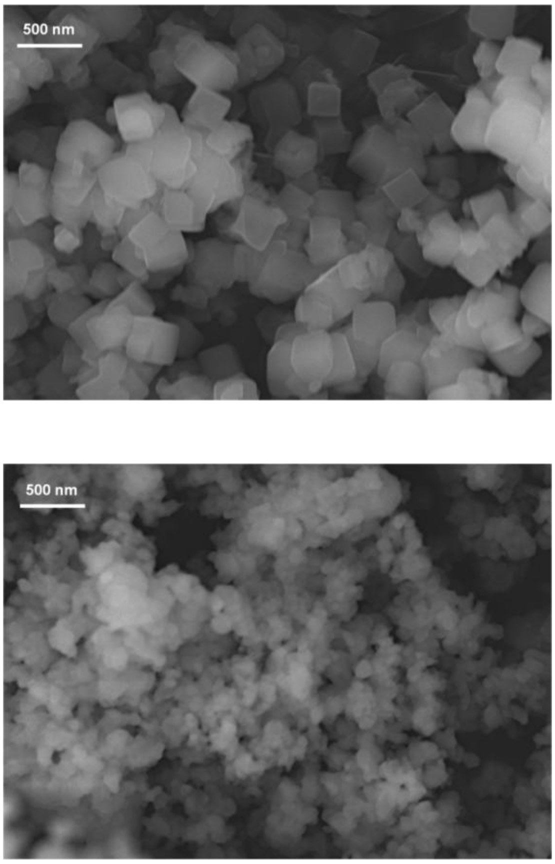

Figure 6.10 Upper: SEM micrograph of crystalline zeolite A. Lower: SEM micrograph of quenched and dried precursor gel.

6.3.4. *Neutron scattering experiments*

6.3.4.1. SANS

Small angle neutron scattering (SANS) was used to examine the microstructure of the zeolite precursor gels. Figure 6.11 shows the SANS plots for corresponding gel and liquid layers measured after ageing at 30 °C for 30 minutes.

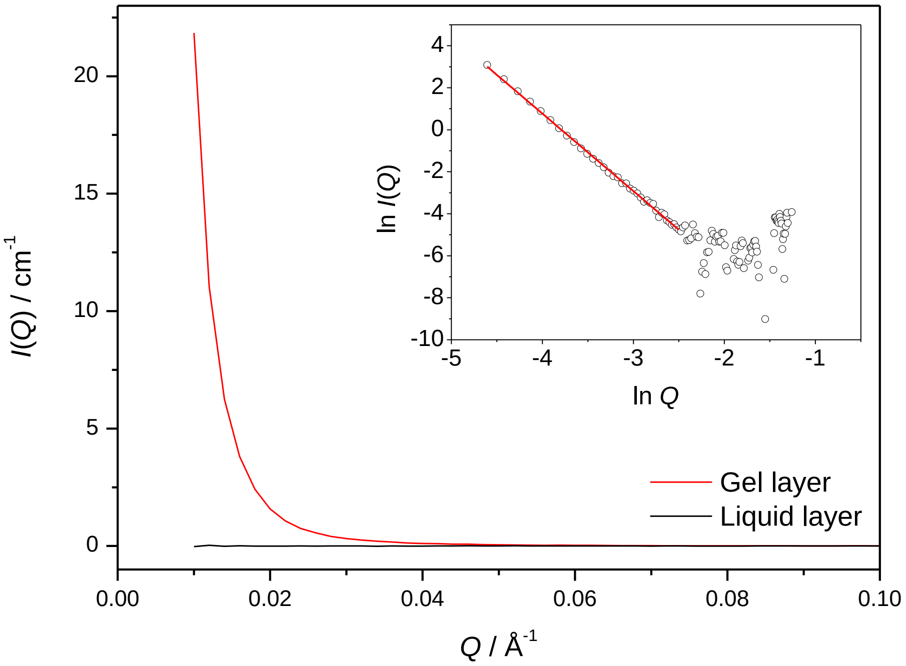

Figure 6.11 SANS plot for a gel and liquid layer pair measured on LOQ at ISIS. Inset: Porod plot of the data from the gel layer.

A common method of analysing small angle scattering data is a so-called Porod plot where the natural logarithm of the scattering intensity, $I(Q)$, is plotted against the natural logarithm of the momentum transfer, Q. The slope of the linear region of the plot provides information about the surface of the scattering object, such that a slope of -4 indicates a smooth object, a slope between -3 and -4 indicates scattering objects with surface fractal geometry (*i.e.* a high degree of surface roughness) and a slope of -2 to -3 indicates a mass fractal.[43-44]

It can be seen from Figure 6.11 that the gel layer exhibits SANS and the liquid layer does not. The Porod plot can be fitted with a linear function of the form y = ax + b, such that:

$$\ln I(Q) = -3.69(\ln Q) - 13.99 \tag{2.24}$$

Which results in an R^2 value of 0.998. The linearity of the Porod plot indicates that the objects in the gel are large compared with $1/Q_{\min}$ and the Porod slope suggests that the gel possesses a surface fractal geometry.

Neutron scattering data from precursor gels of several different "ages" were measured on the instrument NIMROD which is capable of accessing an enormous *Q*-range including the SANS region. The SANS regions of the NIMROD *i*(*Q*) for several gels are shown in Figure 6.12.

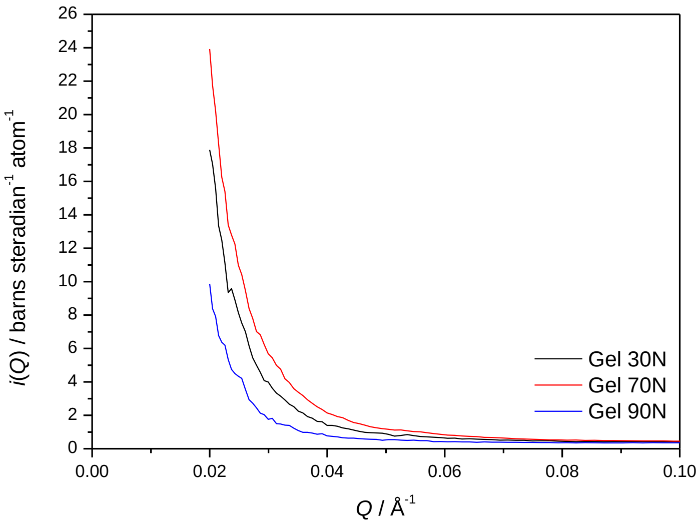

Figure 6.12 SANS plots for zeolite precursor gels aged at different temperatures (30, 70 and 90 °C) for 90 minutes, measured on NIMROD.

The gels are named based on their ageing temperature, and given the N suffix to differentiate them from the similar samples made for SANDALS and discussed in the next section. The gels exhibit slightly different small angle scattering, which is indicative of subtle differences in their microstructure. The equivalent Porod plots (Figure 6.13) further support this.

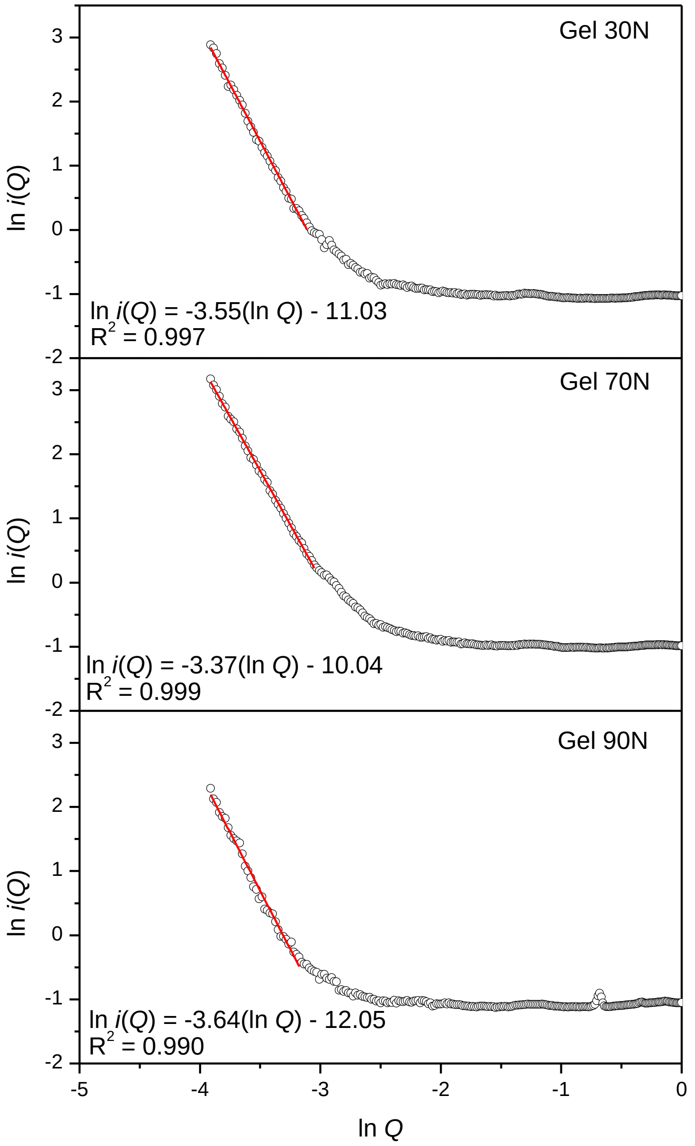

Figure 6.13 Porod plots for the SANS data measured on NIMROD for three differently aged zeolite precursors.

Crystallisation has already begun in the gel aged at 90 °C, and indeed this sample appears somewhat different to the others with the Porod plot appearing less linear (the R^2 value of the linear fit is lower). The Porod slope is always in the region of ~3.5

which implies that the surface roughness remains relatively constant throughout the ageing process. This is in contrast to results of Dokter *et al.*[29] who found a reduction in surface fractal dimension with reaction time in the crystallisation of silicalite.

6.3.4.2. Total scattering

The measured $i(Q)$ and $D(r)$ from crystalline zeolite A are shown in Figure 6.14 and Figure 6.15. The sample was found to be a rather weak scatterer of neutrons, presumably due to its low density, and the data are therefore not of the highest quality (for the Fourier transform, $Q_{\max} = 20$ Å^{-1}). Nevertheless, the agreement between it and the $D(r)$ simulated for "dehydrated" zeolite A (formula $Na_{92.74}Si_{96.96}Al_{95.04}O_{384}.6.92H_2O$) as determined by Ikeda *et al.*[36] is reasonably good. The Ikeda model is the most complete of any of the published work on zeolite A, and includes appropriate ordering of Al and Si as well as the locations of the oxygen atoms of water molecules. No attempt was made to refine this structure in PDFgui due to its large unit cell, its complexity and the limited quality of the data.

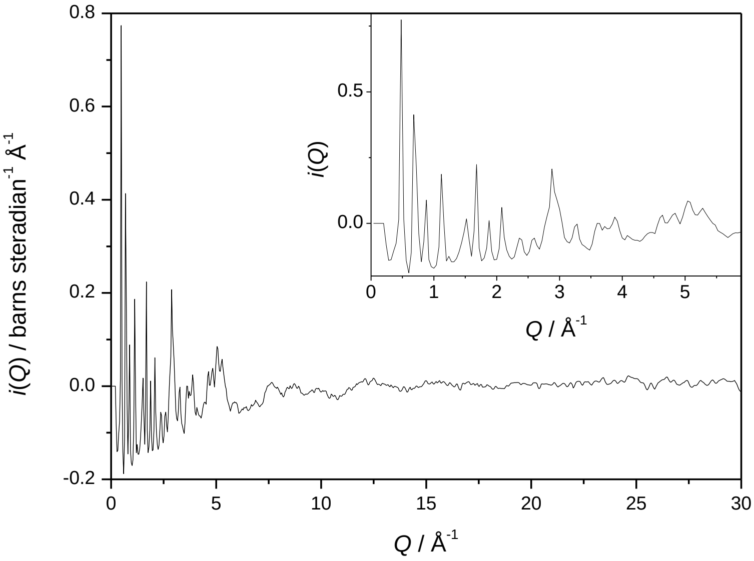

Figure 6.14 The measured *i*(*Q*) for crystalline zeolite A with the inset showing a close-up of the region 0 Å^{-1} ≤ *Q* ≤ 6 Å^{-1}.

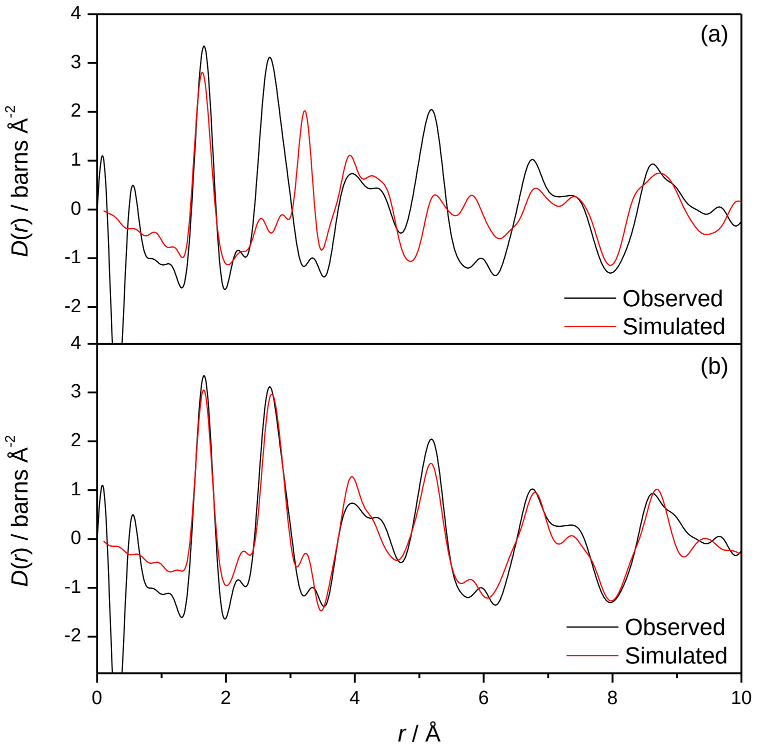

Figure 6.15 (a) The measured *D*(*r*) from a sample of crystalline zeolite A compared with the hydrated model from Ikeda *et al.* and (b) The measured *D*(*r*) compared with the dehydrated model also from Ikeda *et al.*.[36]

The agreement between the "dehydrated" model and the data is surprising given that the positions of hydrogen atoms were not present in the model, however, since there are only 7 H_2O molecules per unit cell their contribution ought to be small. Nevertheless, the lack of an O–D (or O–H) peak in the measured $D(r)$ is unexpected. This can be explained if it is assumed that the sample picked up some atmospheric H_2O whilst being handled prior to measurement, because at a certain ratio of D:H (1:1.78), the scattering lengths of the two isotopes cancel each other out and the mixture becomes null scattering. Support for this conclusion comes from calculation of the expected $T_0(r)$ slopes and comparison with the data. For the "dehydrated" model, assuming full deuteration, $T_0(r) = 0.144$, whereas for a null-scattering mixture of H and D, $T_0(r) =$ 0.137. The measured $D(r)$ has a slope of 0.084, hence the null scattering mixture gives a closer match. Of course, the total amount of water in the sample is likely to be different from the model, which would explain the remaining discrepancy.

The simulated $D(r)$ from the hydrated model of zeolite A is very different, as shown in Figure 6.15(a). Where the framework correlations (*i.e.* T–O and O– –O) dominate in the dehydrated material, (see Table 6.3) the hydrated material contains multiple O– –O_w and O_w– –O_w correlations from the 255 water molecules in the unit cell, which obscure the contributions from the framework. A comparison of partial correlation functions calculated from the hydrated and dehydrated models is shown in Figure 6.16 and the local environments of Na^+ ions in the two models are shown in Figure 6.17.

Table 6.3 A summary of atomic correlations in the crystalline zeolite A, taken from the structure of Ikeda *et al.*[36]

Correlation type	**Distance / Å**	
	Hydrated	**Dehydrated**
Si–O	1.59	1.59
Al–O	1.73	1.74
Na–O	1.98 – 3.4	1.95 – 2.9
Na–O (water)	1.6 – 3.5	1.5 – 2.1
O– –O (tetrahedral framework)	2.6 – 2.75	2.6 – 2.75
O– –O (water-framework)	2.9 – 3.6	3.1 – 3.6
O– –O (water-water)	1.48 – 2.6	1.5 – 2.3
T– –T	3.2 – 3.25	3.2 – 3.25
Na– –T	3.4 – 3.8	2.2 – 3.3

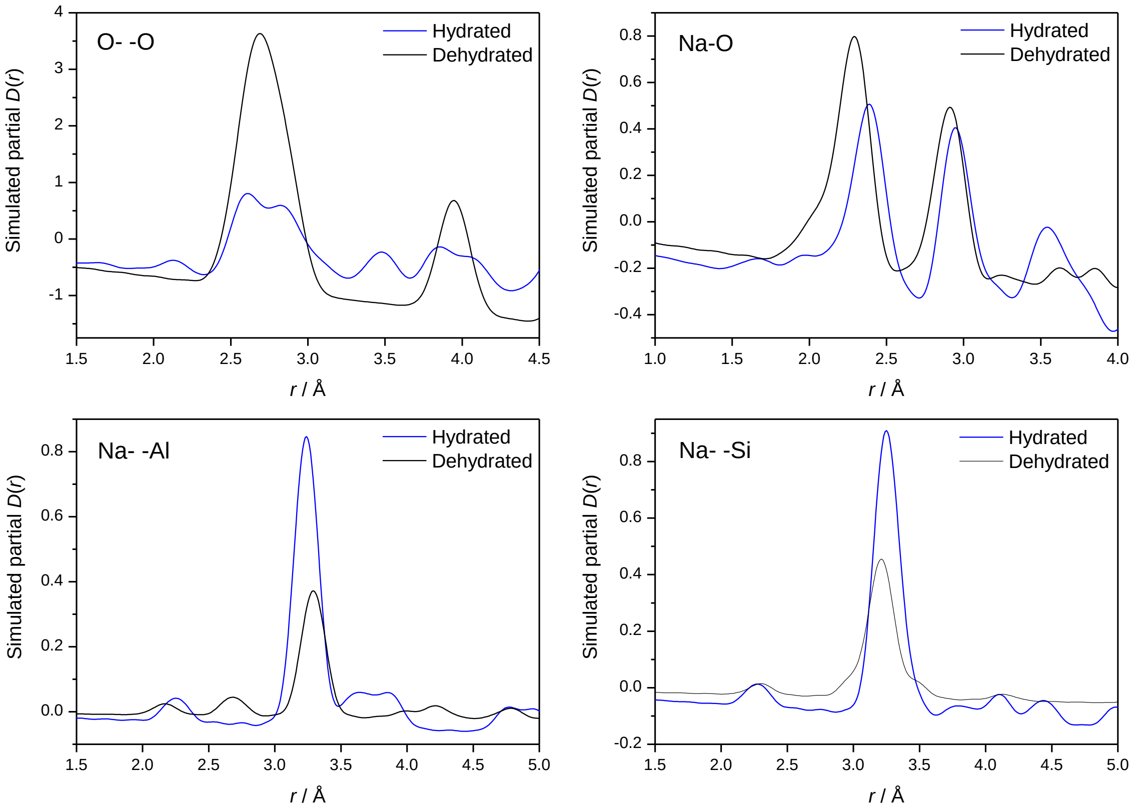

Figure 6.16 Comparison of various partial correlation functions that are significantly different in the hydrated and dehydrated models of zeolite A.[36]

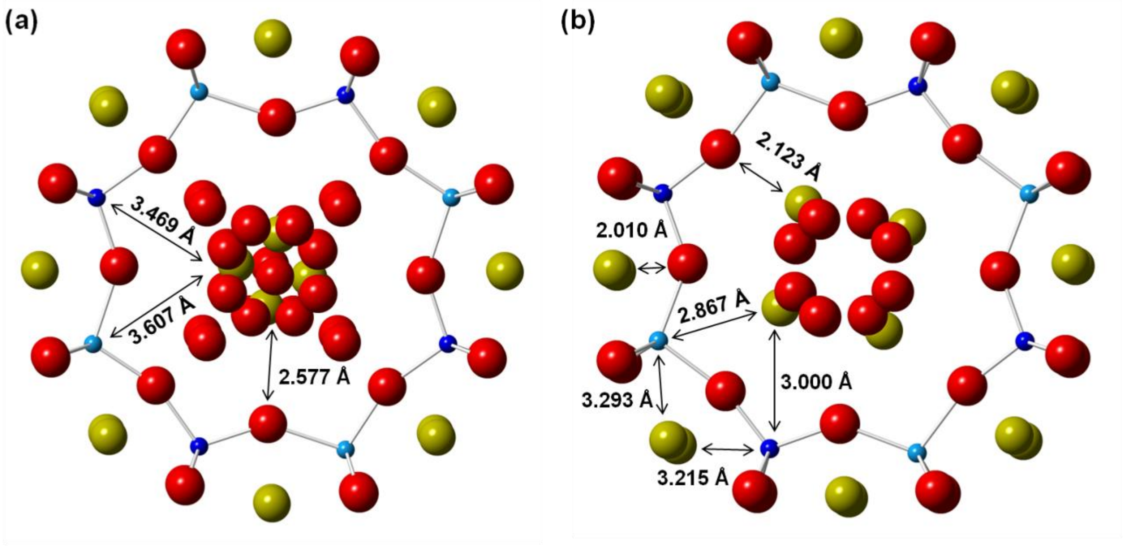
(a)
3.469 Å
3.607 Å
2.577 Å
(b)
2.123 Å
2.010 Å
2.867 Å
3.000 Å
3.293 Å
3.215 Å

Figure 6.17 The local environment of sodium ions in the structure of zeolite A.[36] **Yellow spheres are Na, red oxygen, light blue aluminium and dark blue silicon. (a) the hydrated zeolite A and (b) the dehydrated zeolite A.**

It should be noted from Table 6.3 and Figure 6.16 that the position of Na^+ ions within the structure varies greatly between the hydrated and dehydrated structures. In the hydrated structure, most of the cations apparently sit towards the centre of the pores, whereas in the dehydrated structure a relatively larger number of them are more closely associated with the framework oxygens.

The $i(Q)$ of the dried gel is shown in Figure 6.18 and Figure 6.19 shows the comparison between the $D(r)$ of the crystalline zeolite and the dried gel. It can be seen that the dried gel closely resembles the crystalline zeolite particularly in the region $r < 3$ Å which is in agreement with previous literature,[23] and with the results from infrared spectroscopy (Section 6.3.2) and is due to the rigid nature of the [TO_4] tetrahedral units. In the region 3 – 8 Å, there are some small differences between the two, suggesting differences in the shortto-medium range order. The most noticeable differences at 3.5 – 4.0 Å occur in the region associated mainly with Na– –T correlations in Table 6.3. It is also clear that the dried gel possesses little or no medium-to-long range order, with no obvious correlations visible above 8 Å.

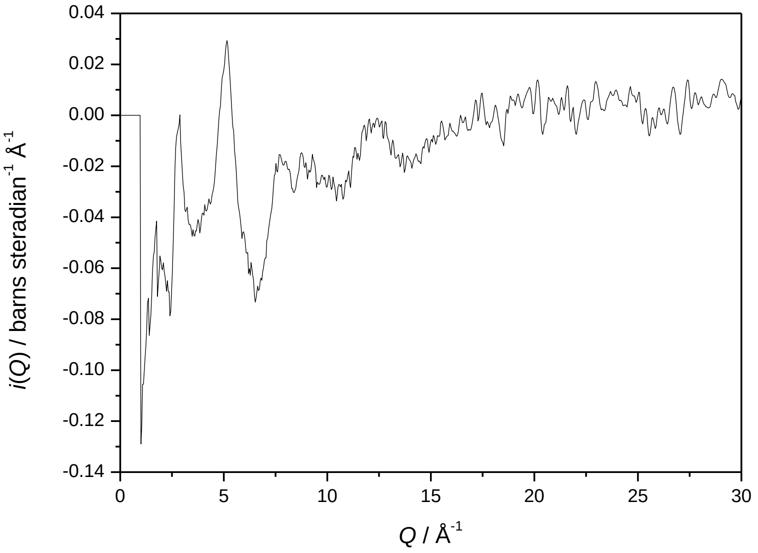

Figure 6.18 The measured *i*(*Q*) for the quenched and dried precursor gel.

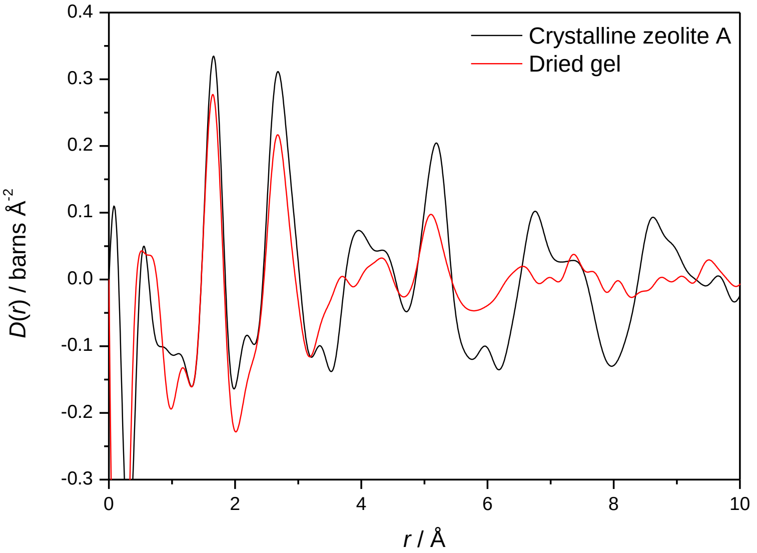

Figure 6.19 The measured *D*(*r*) from crystalline zeolite A and the dried precursor gel.

As well as the dry samples, other complementary measurements were made for comparison with and to provide additional information for the analysis of the zeolite gel data. Figure 6.20 shows the comparison of the *i*(*Q*) measured from D_2O and an NaOD solution of the same concentration as the reaction liquid (ICP analysis revealed that the zeolite precursor liquid layer consisted of 8.79% by mass Na, which is equivalent to a 4.6 times dilution of 40% NaOD in D_2O).

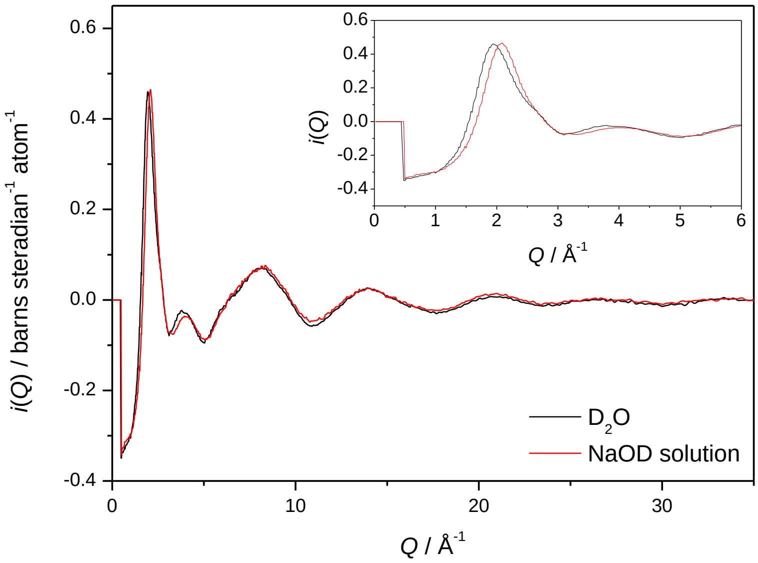

Figure 6.20 The *i*(*Q*)s of D_2O and NaOD solution with an inset showing the low *Q* region.

The most noticeable difference between the *i*(*Q*)s of D_2O and NaOD in D_2O is the position of the first "diffraction peak" at ~2 $Å^{-1}$ which is shifted to lower *Q* in the pure D_2O sample. Figure 6.21 shows the results of Fourier transformation of these datasets (Q_{max} = 35 $Å^{-1}$).

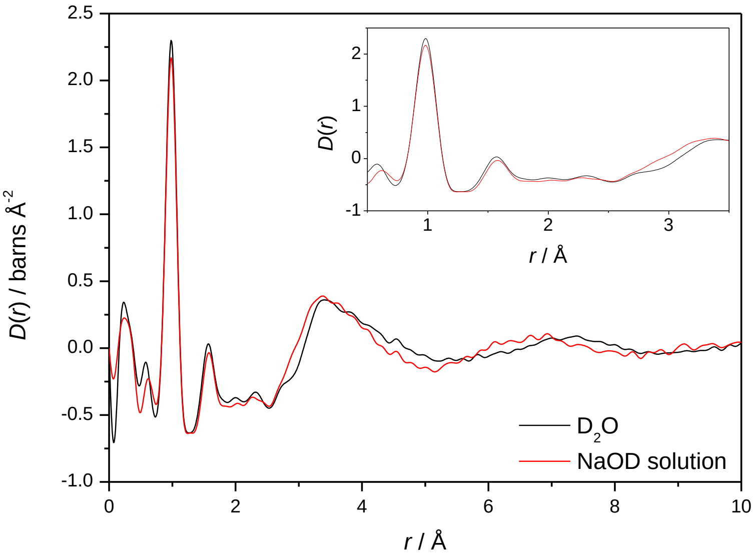

Figure 6.21 The *D*(*r*) of D_2O and NaOD solution with an inset showing the low *r* region.

The O–D peak in the *D*(*r*) is very similar in both D_2O and NaOD, as is the peak at ~1.6 Å due to intramolecular D– –D and intermolecular D–O correlations. The main differences between the two are in the region of 2.8 – 3.5 Å which corresponds to Na– –O_w, Na– –D_w and DO– –O_w correlations according to the work of Soper *et al.*[45] The apparent offset in the features in the *D*(*r*) between the two samples in the region 4 – 8 Å is indicative of disruption caused to the water hydration shells by the presence of NaOD.

Part of the intention of *in situ* measurements is to be able to subtract a background such that the correlations unique to the material of interest (in this case, the gel layer) can be examined more closely. As a model system for this type of subtraction, a previously prepared sample of crystalline zeolite A was added to D_2O and allowed to settle in a way similar to the gels. Figure 6.22 shows the *i*(*Q*) of this sample in comparison with that of pure D_2O.

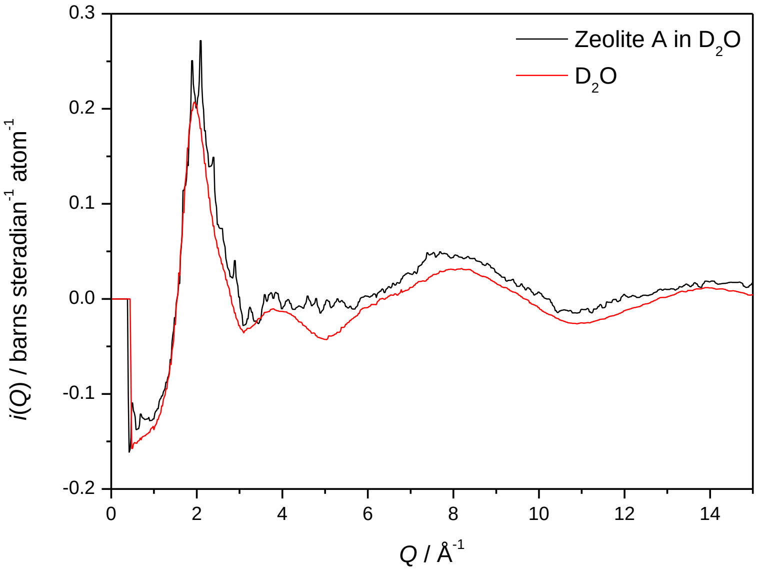

Figure 6.22 The *i*(*Q*) of a sample of zeolite A suspended in D_2O compared with that of pure D_2O.

Bragg peaks from the crystalline zeolite are clearly visible above the D_2O background. The D_2O *i*(*Q*) plotted here has been scaled down to 45% of its original measured value, to best follow the shape of the zeolite data. The D_2O *i*(*Q*) was then subtracted from the zeolite *i*(*Q*) and the result is shown in Figure 6.23.

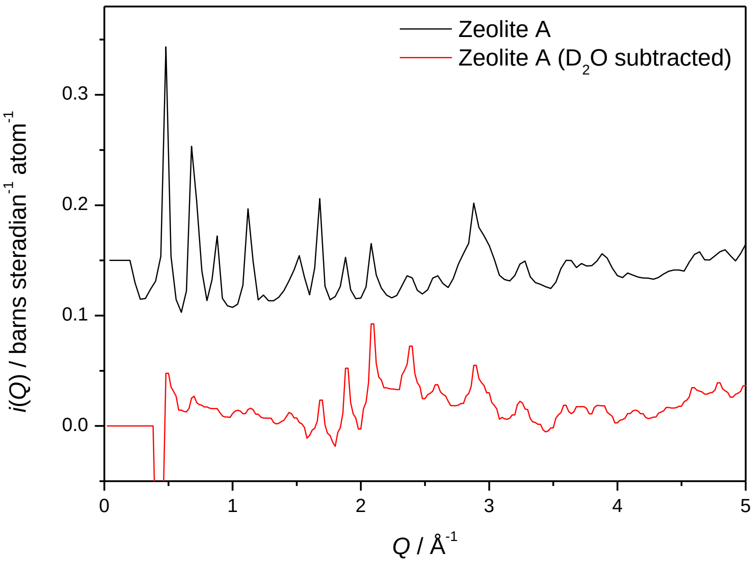

Figure 6.23 Plot showing the *i*(Q) from dry crystalline zeolite A compared with that of the D_2O-subtracted “wet” zeolite A.

In the region above 1.5 Å^{-1} the agreement between the two is reasonably good, with the shape and intensity of the peaks well reproduced. However in the low-*Q* region the Bragg peaks are barely visible in the subtracted dataset. This is likely due to the effect of complex interactions between the D_2O and the zeolite, including the adsorption of D_2O molecules into the pores of the zeolite, and suggests that a simple subtraction of background may not be appropriate for these samples in which the interactions between gel and solution are complex and not well understood.

The neutron scattering lengths of the components of the zeolite precursor gels are shown in Table 6.4. It can be seen that deuterium and oxygen will dominate the scattering from the gels. This combined with the low concentration of the gel relative to the reaction liquid (typical composition in terms of atomic ratios is 1Al:1Si:10.3Na:163O:301D) means that the differences in scattering between the liquid and gel layers are likely to be very small. Therefore, initial experiments were dedicated to establishing that a real difference between the two layers could be measured.

Table 6.4 The coherent neutron scattering lengths of the components of the zeolite gels.

Element	**Neutron scattering length / fm**
Al	3.449
Si	4.153
Na	3.580
O	5.803
D	6.671

Figure 6.24 shows the *i*(*Q*) from a gel-liquid pair aged at 30 °C for 3 hrs. There are small but noticeable differences between them, particularly in the region $0 < Q < 20$ Å^{-1}.

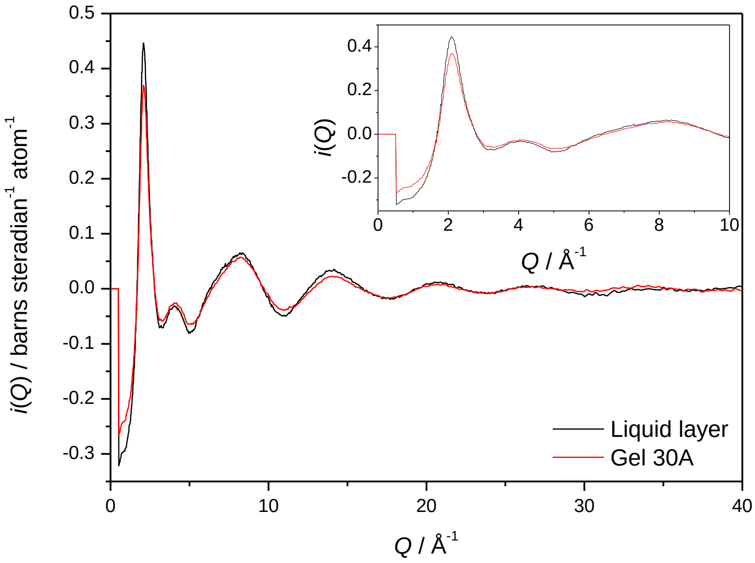

Figure 6.24 A comparison of the *i*(*Q*) for a gel aged at 30 °C for 3 hours and its corresponding liquid layer.

The Fourier transforms of the *i*(*Q*) are shown in Figure 6.25. These reveal the differences in local structure between the liquid and gel layers.

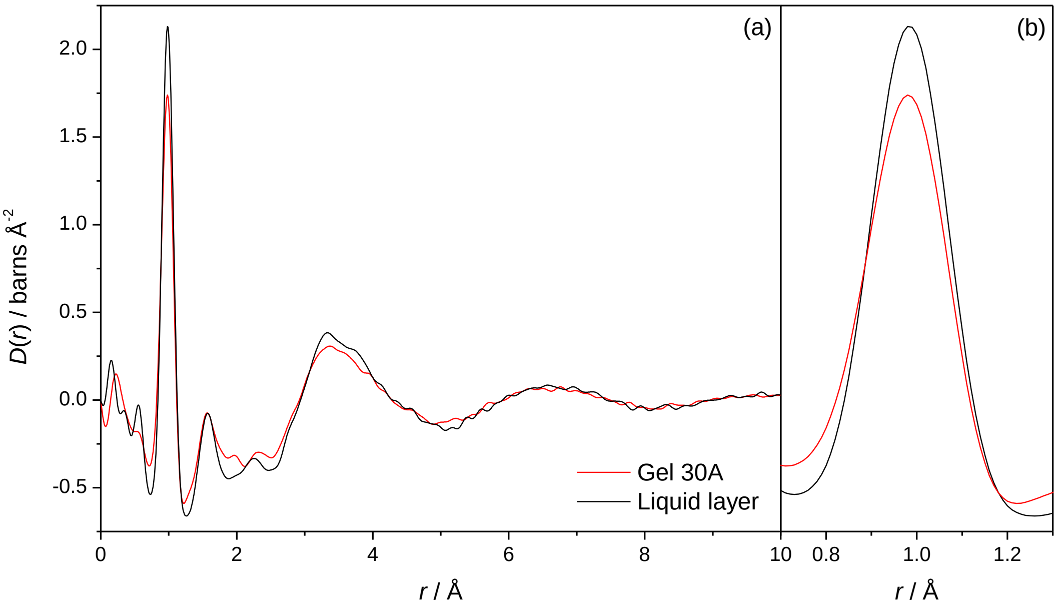

Figure 6.25 (a) A comparison of the *D*(*r*) for a gel aged at 30 °C for 3 hours and its corresponding liquid layer and (b) a close-up of the first peaks of the same two *D*(*r*).

The *D*(*r*) of the gel layer is clearly different to that of the liquid layer, indicating that it is indeed possible to detect structural information from the zeolite precursor gel in the presence of the reaction liquid. The structure of the gel layer is also clearly different from that of the dried gel, as evidenced in Figure 6.26.

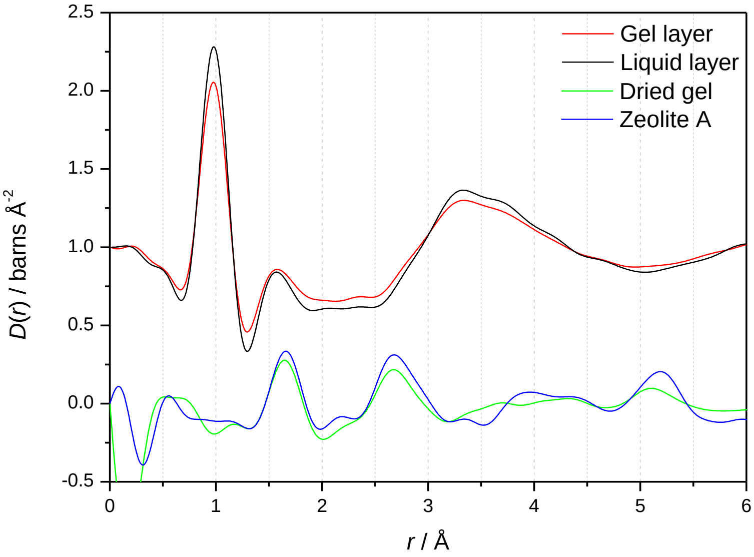

Figure 6.26 A comparison of the *D*(*r*) from the liquid and gel layers with those from the dried gel and crystalline zeolite A. For this plot, all the *i*(*Q*) were Fourier transformed with $Q_{\max}$ = 20 Å^{-1}, to enable direct comparison of the *D*(*r*).

The possibility of extracting structural information specific to the gel by subtracting the scattering from the liquid layer was also examined. Performing the subtraction highlights the positions of the differences and the lack of coincidence of the peaks with those in the dried gel (Figure 6.27).

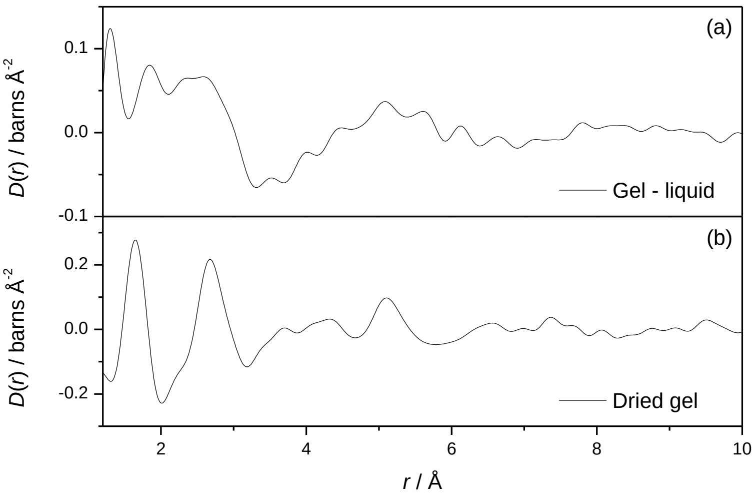

Figure 6.27 (a) The *D*(*r*) obtained after subtracting the *i*(*Q*) from the liquid layer from that of the gel layer and Fourier transforming the result with Q_{max} = 20 Å^{-1}, and (b) the *D*(*r*) measured from the dry gel.

It is illustrative to compare the gel layer *D*(*r*) with the correlations observed in hydrated crystalline zeolite A,[23] which are summarised in Table 6.3. Generally speaking, the significant differences between the PDFs of the gel and liquid layers are in the regions associated with correlations in the structure of zeolite A (Figure 6.28) which would suggest that there are at least some zeolitic motifs in the gel. The O–D peak in the gel layer is less intense and more asymmetrical than that in the liquid layer which may be due to the presence of T–O–D species as part of the amorphous aluminosilicate network in the gel.

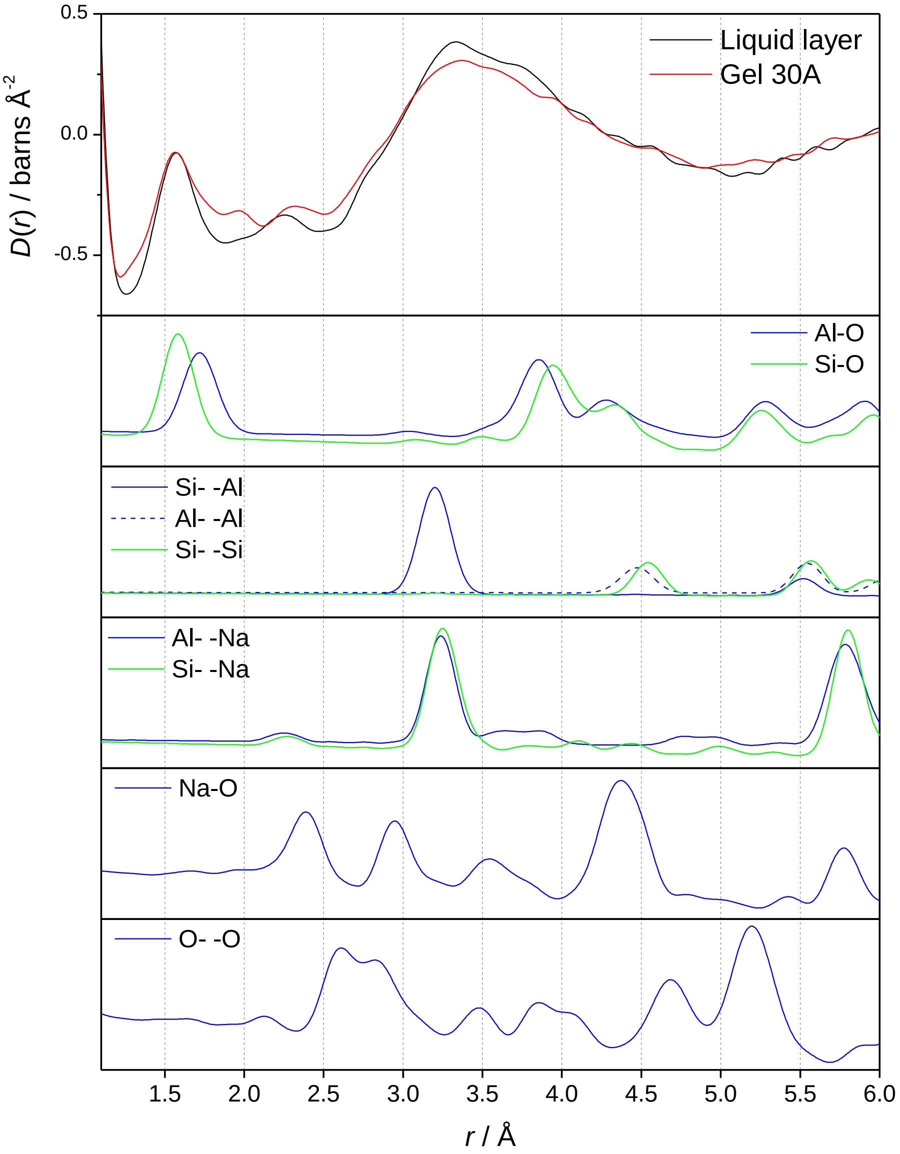

Figure 6.28 The liquid and gel layer *D*(*r*) compared with the calculated partial functions from the hydrated zeolite A model.

That the tetrahedral network in the gel layer is highly disordered is evidenced by the lack of any well-defined features that could be attributed to zeolitic T–O or T– –T correlations. A broadening of the peak at 1.5 – 1.8 Å in the gel relative to the liquid layer is likely due to the presence of T–O pairs in this distance range. Likewise, in the T– –T region there is a broad difference between the gel and liquid layers, perhaps indicating a diffuse range of T– –T distances in the gel. A feature in the gel *D*(*r*) at ~2.0

Å is tentatively related to the interactions of Na^+ cations with the gel, as is the intensity in the region 1.2 – 1.3 Å. Additionally, ICP analysis indicates the gel is sodium rich (Na:Si:Al gel = 8.4:1.2:1.0, zeolite = 1:1:1) and the infrared spectrum of the gel reveals differences in the T–O–T tetrahedral network relative to the crystalline zeolite (Section 6.3.2). These results, when combined, suggest that the gel is a highly disordered aluminosilicate network with, due to the presence of the reaction liquid, a high proportion of its tetrahedral units with the form $[T(OT)_{4-n}(OD)_n]$ and $[T(OT)_{4-n}O_n]^{n-}$, the latter of which would necessitate the inclusion of extra charge balancing Na^+ ions.

To investigate whether the structure of the gel changes with increased ageing but prior to crystallisation beginning, samples aged at 70 °C for 3 hours (Gel 70A) and 90°C for 4 hours (Gel 90A), were also studied. These times and temperatures were found in test experiments to take the gel to just prior to and just after the onset of crystallisation, respectively. The results are shown in Figure 6.29 and Figure 6.30.

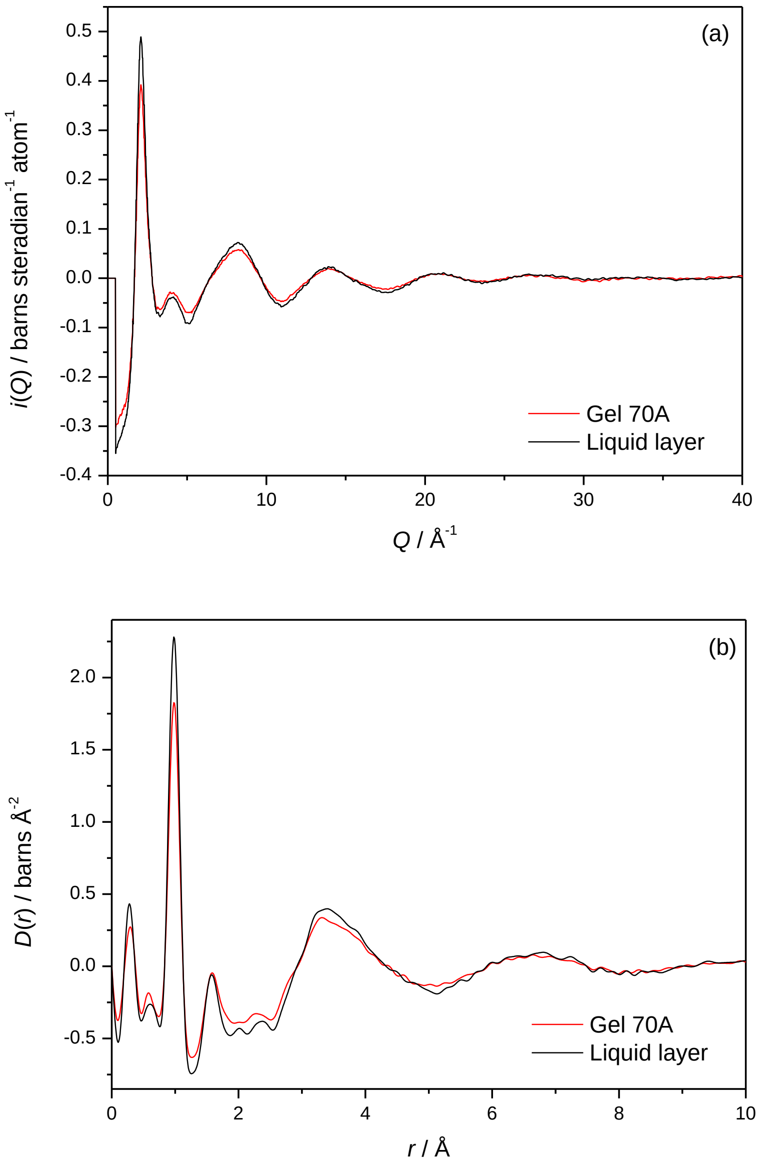

Figure 6.29 (a) *i*(*Q*) for the gel and liquid layers after ageing at 70 °C for 3 hours and (b) *D*(*r*) for the same samples.

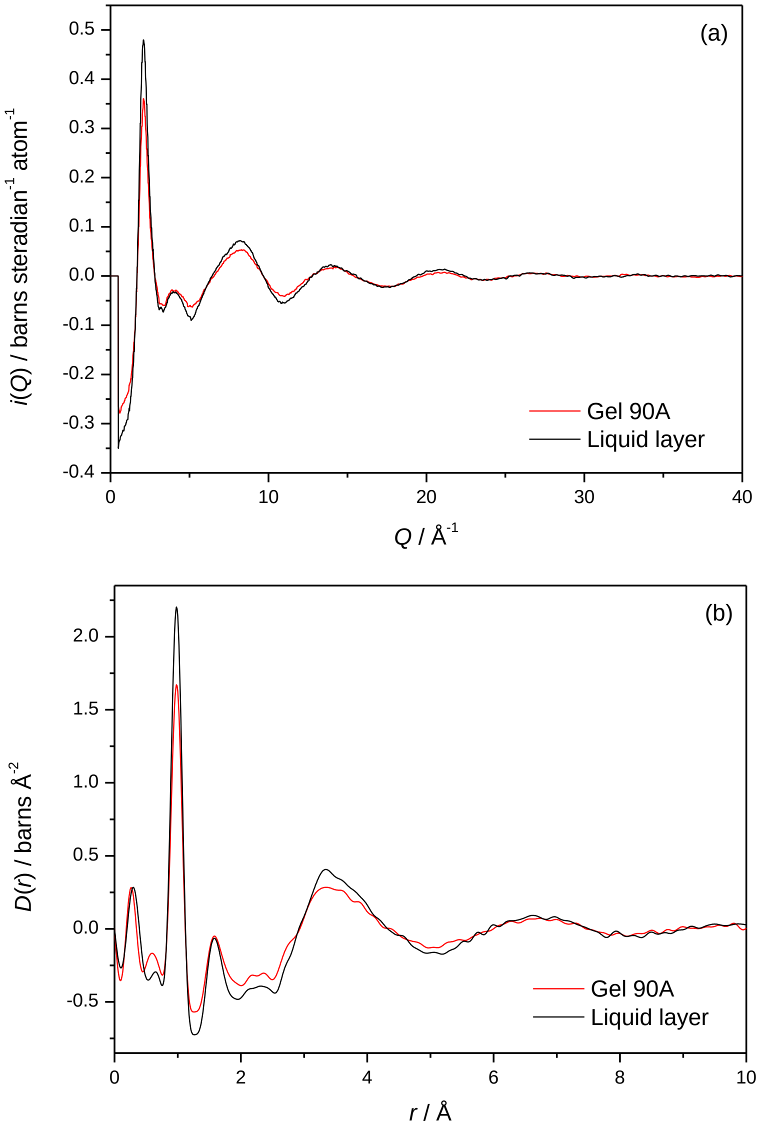

Figure 6.30 (a) *i*(*Q*) for the gel and liquid layers after ageing at 90 °C for 4 hours and (b) *D*(*r*) for the same samples.

The differences between gel and liquid layers in gel 90A are the most pronounced of all the gels: the shoulder at 2.8 – 2.9 Å can be attributed to the O– –O correlation in the crystalline zeolite structure, and similarly a feature attributable to nearest neighbour Na–O pairs is visible at ~2.2 Å. In Figure 6.31, the *D*(*r*) of all the samples are plotted together to aid comparison.

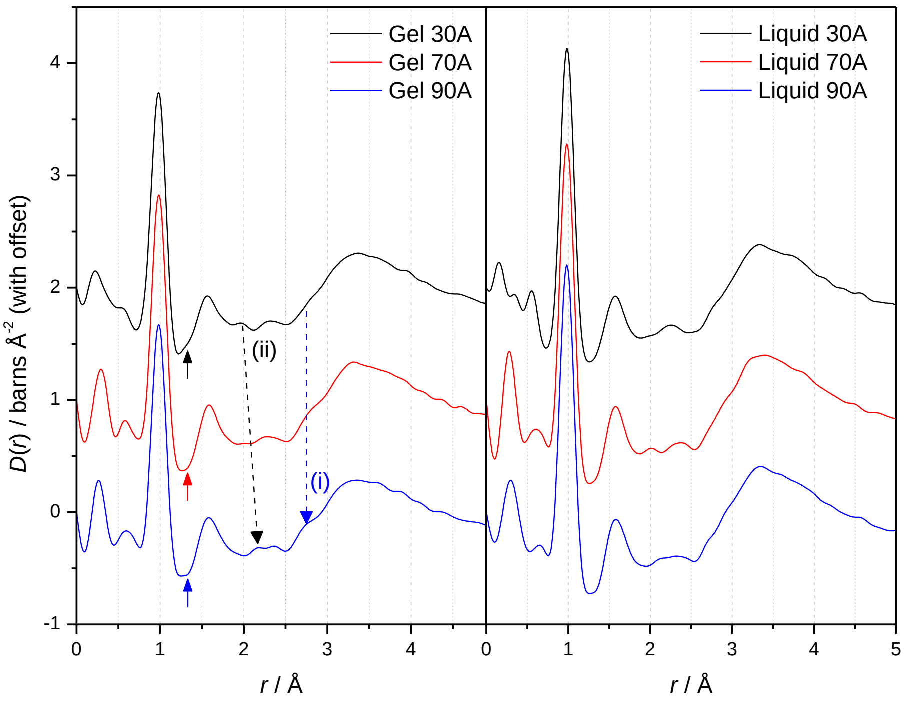

Figure 6.31 A comparison of *D*(*r*) from the gel and liquid layers aged at different times and temperatures. Arrows represent features of note, as explained in the text.

It can be seen that changes are observed both in the gel and the liquid layers, though those in the liquid are rather less obvious. Certain trends are visible in the data from the differently aged gels: namely; that the shoulder at ~2.8 Å (i) grows in intensity with increased ageing; that a feature at ~ 2.0 Å (ii) attributed to the Na–O correlation appears to diminish and shift towards 2.2 Å (nearing its position in the crystalline zeolite) and that the intensity visible in the youngest gel between the D–O peak at ~1.0 Å and the peak at ~1.7 Å disappears over time (see arrows in Figure 6.31). This last observation is likely to be due to the gradual ordering of the tetrahedral network causing the range of T–O distances in the sample to reduce.

Much of the literature discussing zeolite precursors makes a distinction between the primary amorphous phase (the solid/gel-like material formed on the initial mixing of the reagents) and the secondary amorphous phase (the gel after a period of ageing).[12] Using this nomenclature, all the zeolite gels discussed thus far have been examples of secondary amorphous phases. An example of a primary gel was obtained by simply mixing the Al and Si sources without adding NaOD and D_2O and the resulting $i(Q)$ can be seen in Figure 6.32.

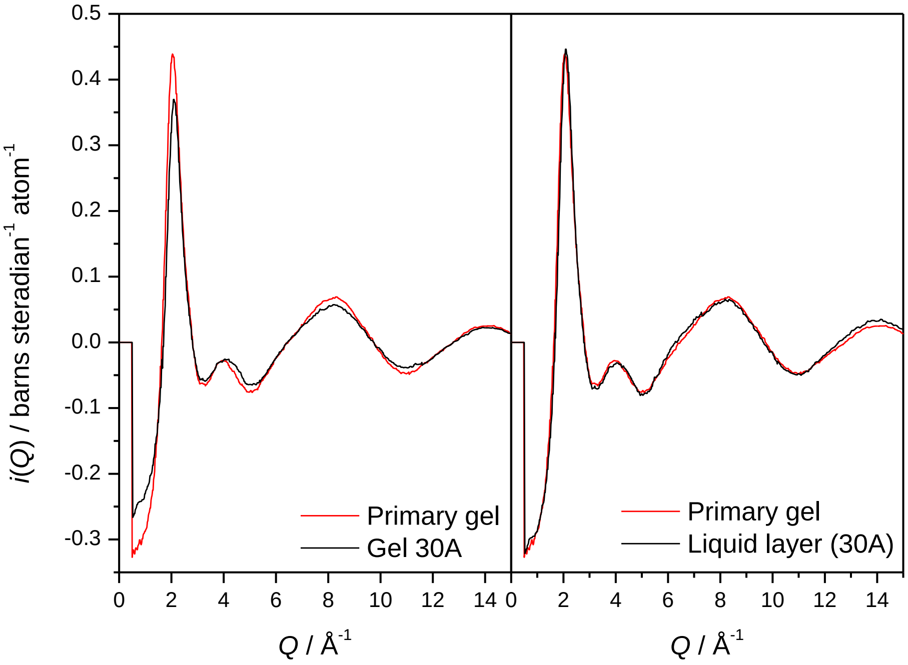

Figure 6.32 Left: comparison between *i*(*Q*) for the primary gel and the gel aged at 30 °C for 3 hours. Right: comparison between *i*(*Q*) for the primary gel and the liquid layer after aging at 30 °C for 3 hours.

It can be seen that the primary gel far more closely resembles the liquid layer than the gel layer, although the position of the first diffraction "peak" in the primary gel is shifted towards lower *Q* (Figure 6.33).

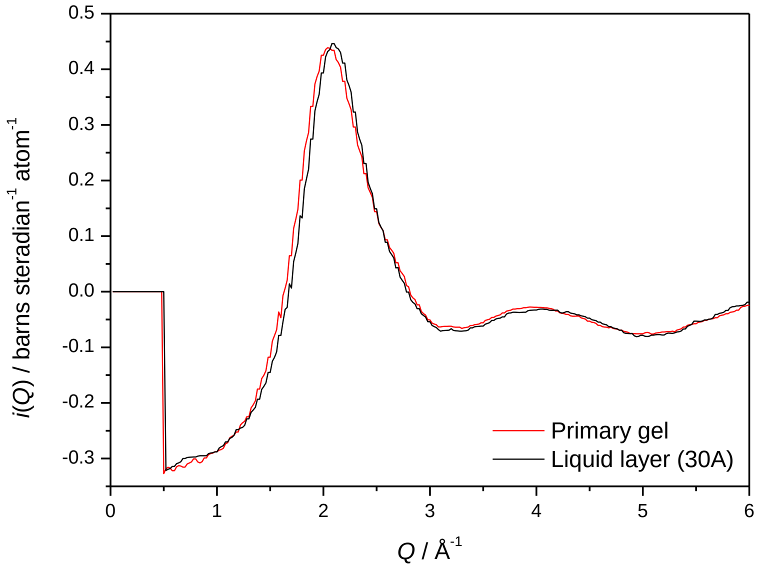

Figure 6.33 The first peak in the *i*(*Q*) of the primary gel and the liquid layer.

In Figure 6.20 we saw that the position of this peak shifted to higher *Q* with the addition of NaOD to D_2O, and since the amount of sodium in the primary gel is significantly lower than that in the liquid layer, this trend appears to continue in Figure 6.33. The position and intensity of this peak is often correlated with changes in the medium range order of amorphous materials and liquids,[24, 46-47] something which may apply here if the Na^+ ions have an ordering effect on the hydration shells surrounding them.

The *D*(*r*) of the primary gel is shown in Figure 6.34. It is clear that its structure is very similar to that of the liquid layer, and is distinct from the aged gel layer. If any zeolitic structural motifs are present in the primary gel, they are not visible in the presence of the reaction liquid.

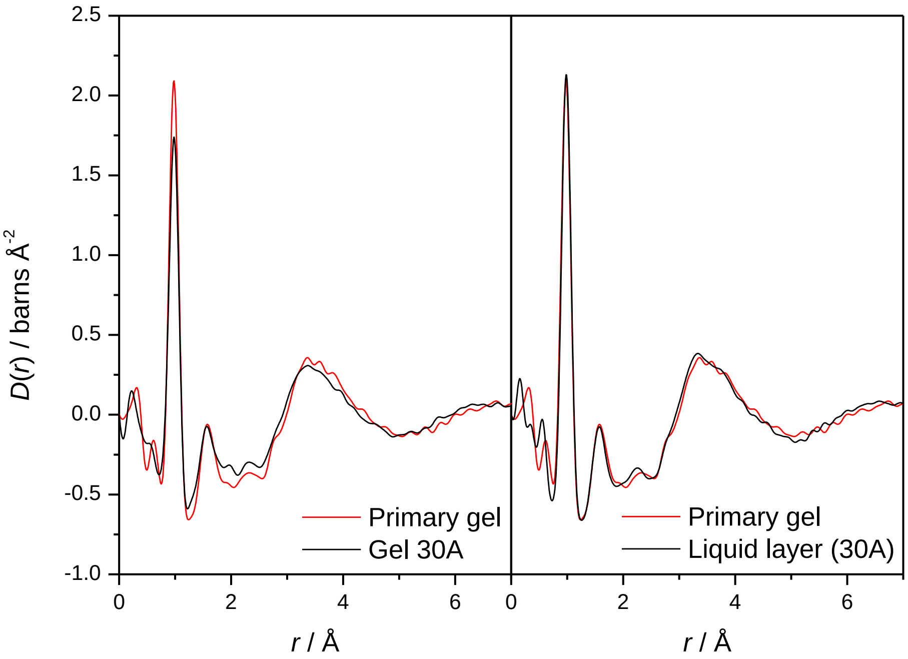

Figure 6.34 Left: comparison between *D*(*r*) for the primary gel and the gel aged at 30 °C for 3 hours. Right: comparison between *D*(*r*) for the primary gel and the liquid layer after aging at 30 °C for 3 hours.

6.3.5. Conclusions

A reliable and reproducible method of preparing amorphous zeolite precursor gels has been developed and their structure studied by *in situ* total neutron scattering. Preliminary results described in this chapter indicate that structural information specific to the gel can be measured in the presence of the reaction liquid, and therefore that neutron scattering is a technique which has great potential for studying zeolite crystallisation *in situ*. Three main conclusions have been reached.

Firstly, an important new observation is that the structure of the dried gel is significantly different to the gel measured *in situ*, and it is not possible to recreate the observed data from the *in situ* gel from a straightforward sum of dried gel and reaction liquid/NaOD solution. This suggests that the reaction liquid has a direct influence on the structure of the gel as the reaction proceeds and that its removal critically alters this structure. This may mean that results from previous studies of quenched gels could be misleading.

Secondly, there is no strong evidence for discrete “building units” in the zeolite precursor gel, as these units would manifest in the *D*(*r*)s as sharp correlations at specific *r* values (particularly at common T– –T distances), and instead the observations are consistent with a disordered, highly hydrated, tetrahedral network. The lack of well-defined T–O correlations in the gel *D*(*r*) implies that a large proportion of the TO_4 units are incomplete and likely to be hydroxyl terminated, a scenario which would explain the changes observed in the IR spectrum and the Na^+ rich nature of the gel, relative to the crystalline zeolite.

Thirdly, the differences in the *D*(*r*) between gel and liquid layers and between gels of different ages suggest that the most significant structural changes are related to the position(s) of the Na^+ ions in relation to the aluminosilicate network. This may be evidence for the cations having a direct influence on the way order develops in the gel.

Subtle differences are visible in the gels aged under different conditions, indicating that the gel structure changes with reaction time, and the primary gel (formed immediately after mixing the reagents) is rather different to the secondary gel (formed after aging). The primary gel exhibits no apparent zeolitic order of any kind.

There is growing interest in the study of the formation of inorganic materials *via* direct observation of reactive species by *in situ* total scattering, with a variety of techniques employed for data analysis. In some cases, as for example Jensen *et al.*[48] on the formation of SnO_2 nanoparticles, and Tyrsted *et al.*[49] on CeO_2, both under hydrothermal conditions. X-ray scattering was used to highlight the contribution from the heavier elements and the scattering from the reaction liquid was simply subtracted away. Although this is an appealing simplification, it relies on the assumption that the composition and structure of the reaction liquid remains constant whether in close proximity to the soluble metal species or not, and neglects the contribution of the solvent to the structure of the nascent oxide particles. An alternative approach was taken by White *et al.*[34, 50] studying the formation of geopolymer cement who used density functional theory based Monte Carlo modelling to simulate the polymerization reaction and provide insight into the molecular origins of the neutron scattering observations.

To achieve a full description of the mechanism of zeolite crystallisation from an amorphous precursor gel would require the employment of a variety of techniques which probe different time- and length-scales and highlight different aspects of the system. Nevertheless, based on the results in this chapter, total neutron scattering clearly should be considered an important part of this investigation.

6.4. References

1. Baerlocher, C.; McCusker, L. B.; Olson, D. H., *Atlas of Zeolite Framework Types*. 6th ed.; Elsevier: Amsterdam, 2007.
2. Barrer, R. M.; Baynham, J. W., *J. Chem. Soc.* **1956**, 2882
3. Milton, R. M.,A. U.S. Patent 2,882,243, 1959.
4. Milton, R. M.,X. U.S. Patent 2,882,244, 1959.
5. Flanigen, E. M.; Bennett, J. M.; Grose, R. W.; Cohen, J. P.; Patton, R. L.; Kirchner, R. M.; Smith, J. V., *Nature* **1978,** *271*, 512.
6. Bibby, D. M.; Milestone, N. B.; Aldridge, L. P., *Nature* **1979,** *280*, 664.
7. Wilson, S. T.; Lok, B. M.; Messina, C. A.; Cannan, T. R.; Flanigen, E. M., *J. Am. Chem. Soc.* **1982,** *104*, 1146.
8. Parise, J. B., *J. Chem. Soc., Chem. Commun.* **1985**, 606.
9. Ferey, G., *C.R. Acad. Sci., Ser. IIc: Chim.* **1998,** *1*, 1.
10. Cheetham, A. K.; Férey, G.; Loiseau, T., *Angew. Chem. Int. Ed.* **1999,** *38*, 3268.
11. Cundy, C. S.; Cox, P. A., *Chem. Rev.* **2003,** *103*, 663.
12. Cundy, C. S.; Cox, P. A., *Microporous Mesoporous Mater.* **2005,** *82*, 1.
13. Barrer, R. M.; Baynham, J. W.; Bultitude, F. W.; Meier, W. M., *J. Chem. Soc.* **1959**, 195.
14. Kinrade, S. D.; Swaddle, T. W., *Inorg. Chem.* **1989,** *28*, 1952.
15. Harris, R. K.; SamadiMaybodi, A.; Smith, W., *Zeolites* **1997,** *19*, 147.
16. Breck, D. W., *J. Chem. Educ.* **1964,** *41*, 678.
17. Kerr, G. T., *J. Phys. Chem.* **1966,** *70*, 1047.
18. Zhdanov, S. P., In *ACS Adv. Chem. Ser.*, Flanigen, E. M.; Sands, L. B., Eds. 1971; Vol. 101, p 20.
19. Angell, C. L.; Flank, W. H., In *ACS Symp. Ser.*, Katzer, J. R., Ed. 1977; Vol. 40, p 194.
20. Nicolle, M. A.; Renzo, F. D.; Fajula, F.; Espiau, P.; Courieres, T. d., In *Proc. 9th Int. Zeolite Conf.*, Ballmoos, R. v.; Higgins, J. B.; Treacy, M. M. J., Eds. Butterworth-Heinemann: Boston, 1993; p 313.
21. Mintova, S.; Olson, N. H.; Bein, T., *Angew. Chem. Int. Ed.* **1999,** *38*, 3201.
22. Dorset, D. L., *Z. Kristallogr.* **2010,** *226*, 18.
23. Yang, H. X.; Walton, R. I.; Antonijevic, S.; Wimperis, S.; Hannon, A. C., *J. Phys. Chem. B* **2004,** *108*, 8208.
24. Wakihara, T.; Kohara, S.; Sankar, G.; Saito, S.; Sanchez-Sanchez, M.; Overweg, A. R.; Fan, W.; Ogura, M.; Okubo, T., *Phys. Chem. Chem. Phys.* **2006,** *8*, 224.
25. Wakihara, T.; Fan, W.; Suzuki, Y.; Ogura, M.; Kohara, S.; Sankar, G.; Okubo, T., In *Stud. Surf. Sci. Catal.*, Ruren Xu, Z. G. J. C.; Wenfu, Y., Eds. Elsevier: 2007; Vol. Volume 170, pp 506.
26. Lowenstein, W., *Am. Mineral.* **1954,** *39*, 92.
27. Itabashi, K.; Kamimura, Y.; Iyoki, K.; Shimojima, A.; Okubo, T., *J. Am. Chem. Soc.* **2012,** *134*, 11542.
28. Usui, K.; Abe, K.; Tokita, T.; Imafuku, S.; Ogawa, M., In *Chemistry of Microporous Crystals*, Inui, T.; Namba, S.; Tatsumi, T., Eds. 1991; Vol. 60, pp 21.
29. Dokter, W. H.; Beelen, T. P. M.; Vangarderen, H. F.; Vansanten, R. A.; Bras, W.; Derbyshire, G. E.; Mant, G. R., *J. Appl. Crystallogr.* **1994,** *27*, 901.

30. Aerts, A.; Follens, L. R. A.; Haouas, M.; Caremans, T. P.; Delsuc, M. A.; Loppinet, B.; Vermant, J.; Goderis, B.; Taulelle, F.; Martens, J. A.; Kirschhock, C. E. A., *Chem. Mater.* **2007,** *19,* 3448.
31. Follens, L. R. A.; Aerts, A.; Haouas, M.; Caremans, T. P.; Loppinet, B.; Goderis, B.; Vermant, J.; Taulelle, F.; Martens, J. A.; Kirschhock, C. E. A., *Phys. Chem. Chem. Phys.* **2008,** *10*, 5574.
32. Depla, A.; Verheyen, E.; Veyfeyken, A.; Gobechiya, E.; Hartmann, T.; Schaefer, R.; Martens, J. A.; Kirschhock, C. E. A., *Phys. Chem. Chem. Phys.* **2011,** *13*, 13730.
33. Walton, R. I.; Smith, R. I.; O'Hare, D., *Microporous Mesoporous Mater.* **2001,** *48*, 79.
34. White, C. E.; Provis, J. L.; Llobet, A.; Proffen, T.; van Deventer, J. S. J., *J. Am. Ceram. Soc.* **2011,** *94*, 3532.
35. Madja, D.; Walton, R. I.; Hannon, A. C., 2006.
36. Ikeda, T.; Izumi, F.; Kodaira, T.; Kamiyama, T., *Chem. Mater.* **1998,** *10*, 3996.
37. Benmore, C. J.; Soper, A. K. *Rutherford Appleton Laboratory Technical Reports, RAL-TR-1998-006*, 1998.
38. Heenan, R. K.; Penfold, J.; King, S. M., *J. Appl. Crystallogr.* **1997,** *30*, 1140.
39. Bowron, D. T.; Soper, A. K.; Jones, K.; Ansell, S.; Birch, S.; Norris, J.; Perrott, L.; Riedel, D.; Rhodes, N. J.; Botti, A.; Ricci, M. A.; Grazzi, F.; Zoppi, M., *Rev. Sci. Instrum.* **2010,** *81*, 033905.
40. McCormick, A. V.; Bell, A. T.; Radke, C. J., *J. Phys. Chem.* **1989,** *93*, 1741.
41. Huang, Y.; Jiang, Z., *Microporous Mater.* **1997,** *12*, 341.
42. Dutta, P. K.; Del Barco, B., *J. Phys. Chem.* **1988,** *92*, 354.
43. Hannon, A. C., PhD. Thesis, University of Reading, 1989.
44. Jarvie, H. P.; King, S. M., *Environ. Sci. Technol.* **2007,** *41*, 2868.
45. McLain, S. E.; Imberti, S.; Soper, A. K.; Botti, A.; Bruni, F.; Ricci, M. A., *Phys. Rev. B* **2006,** *74*.
46. Elliott, S. R., *J. Phys.: Condens. Matter* **1992,** *4*, 7661.
47. Jin, W.; Kalia, R. K.; Vashishta, P.; Rino, J. P., *Phys. Rev. B* **1994,** *50*, 118.
48. Jensen, K. M. O.; Christensen, M.; Juhas, P.; Tyrsted, C.; Bojesen, E. D.; Lock, N.; Billinge, S. J. L.; Iversen, B. B., *J. Am. Chem. Soc.* **2012,** *134*, 6785.
49. Tyrsted, C.; Ørnsbjerg Jensen, K. M.; Bøjesen, E. D.; Lock, N.; Christensen, M.; Billinge, S. J. L.; Brummerstedt Iversen, B., *Angew. Chem. Int. Ed.* **2012,** *51*, 9030.
50. White, C. E.; Provis, J. L.; Proffen, T.; van Deventer, J. S. J., *AlChE J.* **2012,** *58*, 2241.

Chapter 7: Conclusions and Possible Future Work

7. Conclusions and Possible Future Work

The work in this thesis involves the structural characterisation of a diverse range of disordered inorganic materials, with the use of total neutron scattering providing the common link between them.

7.1. The Polymorphism of Gallium Oxide

The synthesis and interconversion of the various previously uncharacterised polymorphs of gallium oxide was investigated in detail. Many new insights into this surprisingly complex system have been obtained, and a paper based on the contents of Chapter 3 has been submitted for publication.[1]

7.1.1. *The structure of γ-Ga_2O_3*

The average structure of γ-Ga_2O_3 was found to be a cubic defect spinel (space group $Fd\bar{3}m$) with four partially occupied cation sites. PDF analysis revealed that the local structure is not well described by this model. In the well-characterised α and β polymorphs the GaO_6 octahedra are rather distorted, and a local structure model for γ-Ga_2O_3 in space group $F\bar{4}3m$ which allows a similar distortion to occur fits the low-*r* region of the PDF much more satisfactorily. That this distortion occurs on a local scale only is evidenced by the lack of any extra diffraction peaks that could be attributed to a lower symmetry space group.

Reverse Monte Carlo modelling confirmed that the average structural model for γ-Ga_2O_3 was consistent with the data (number density, O_h:T_d ratio, and cation distribution). It also offered independent verification of the validity of the symmetry-lowering approach to modelling the local structure: the octahedral Ga environment in the refined configuration was distorted with the Ga–O partial function obviously showing a range of bond lengths, in agreement with the $F\bar{4}3m$ model.

The cation arrangement in γ-Ga_2O_3 was found to depend on particle size and preparation method. Nanocrystalline γ-Ga_2O_3 prepared by a solvothermal method had more gallium in tetrahedral sites and greater occupancy of non-spinel sites than its crystalline counterpart. This trend continued to an extremely nanosized sample prepared by precipitation from ethanolic solution of gallium nitrate: this sample could be modelled using a spinel with five partially occupied sites and a much larger proportion of tetrahedral gallium (although structural refinement was not possible due to the small size of the particles and the presence of a hydrous impurity phase).

RMC refinement of the structures of the nanocrystalline solvothermal and precipitation-method γ-Ga_2O_3 could provide insight into the arrangement of cations and vacancies on the various sites. Unfortunately, this could be made rather difficult by the presence of organic impurities in the former (these could be removed by gentle calcination, though this may also change the structure/cation distribution), and hydrous impurities in the latter.

Solid state $^{69}Ga/^{71}Ga$ NMR could potentially be used as a tool to verify the ratios of octahedral/tetrahedral gallium in the samples and probe the level of disorder in the different environments. To this end, NMR data have been recorded in collaboration with Dr Sharon Ashbrook and analysis is currently in progress.

7.1.2. *The structure of ε-Ga_2O_3 and "δ-Ga_2O_3"*

The hitherto uncharacterised ε-Ga_2O_3 was synthesised from gallium nitrate *via* decomposition at 220 °C followed by prolonged heating at 400 °C. The structure of ε-Ga_2O_3 was found to be hexagonal, space group $P6_3mc$, and analogous to a "disordered" form of ε-Fe_2O_3.

The initial product of thermal decomposition of gallium nitrate at 220 °C, previously designated as a separate polymorph, "δ-Ga_2O_3", was in fact found to be a nanocrystalline modification of ε-Ga_2O_3, rather than a distinct phase. It does not adopt the cubic bixbyite structure, as previously reported.

Neither ε-Ga_2O_3 or its nanocrystalline modification could be prepared without the presence of the β-Ga_2O_3 polymorph, which was found to be an unavoidable by-product of the thermal decomposition of gallium nitrate.

The properties (for example, catalytic or photocatalytic behaviour) of ε-Ga_2O_3 have not as yet been reported, and while it would be problematic to make these types of measurements on the current, mixed-phase sample, it is possible that very careful heating could obtain a pure sample of ε-Ga_2O_3.

7.1.3. *A novel gallium oxyhydroxide and κ-Ga_2O_3*

A novel gallium oxyhydroxide, $Ga_5O_7(OH)$, was synthesised by a solvothermal route. Its structure, determined from neutron diffraction, is analogous to the aluminium oxyhydroxide, a mineral known as tohdite or akdalaite. It has a layered structure, in hexagonal space group $P6_3mc$.

High-resolution powder XRD of the highly crystalline $Ga_5O_7(OH)$ revealed that it exhibits anisotropic peak broadening, presumably due to the plate-like nature of the crystallites. Some of the diffraction peaks were found to be shifted from their predicted positions, which may be attributed to macroscopic strain in the crystallites.

The thermal decomposition of $Ga_5O_7(OH)$ reveals an intermediate phase prior to the complete transformation to β-Ga_2O_3 whose structure was found to be orthorhombic, space group $Pna2_1$, analogous to κ-Al_2O_3 and ε-Fe_2O_3. To avoid confusion with the aforementioned ε-Ga_2O_3, this phase is designated κ-Ga_2O_3. The κ-Ga_2O_3 polymorph was also observed during the thermal decompositon of ε-Ga_2O_3.

$Ga_5O_7(OH)$ is a new material and further analysis of the defects in its structure, for example using electron diffraction, would be beneficial. As it is a precursor to an unusual phase of Ga_2O_3, controlling its thermal decomposition to form a pure sample of κ-Ga_2O_3, and investigating the potential for doping other atoms into the structure are two obvious targets for future work on this material.

7.2. Gallium-containing Mixed Metal Oxides with the Spinel Structure

7.2.1. Synthesis

A simple solvothermal method for the synthesis of gallium-containing mixed metal oxides, involving the reaction of a soluble M^{2+} salt with metallic gallium in an aminoalcohol solvent, was developed. In this manner, spinel-type ternary oxides with general formula $M_xGa_{3-x}O_{4-y}$ (M = Zn, Ni, Co and Fe) were synthesised.

Future work could involve the synthesis of quaternary oxides with a range of compositions, as well as the extension of the method to other metals and/or crystal structures. Quaternary (Cu/Zn and Mn/Co) gallates have been shown to exhibit promising photocatalytic behaviour,[2-3] and therefore these and similar materials could provide initial synthetic targets for the extension of this method.

7.2.2. Cobalt gallium spinel

The average structure of the cobalt gallium spinel was determined from neutron diffraction as a partial defect spinel with chemical formula $Co_{0.973(8)}Ga_{1.767(8)}O_{3.752(8)}$ with approximately 80% of the cobalt in the +2 oxidation state and 20% in the +3 oxidation state. The composition and oxygen deficiency of this material differentiate it from other, previously reported, cobalt gallate spinels. PDF analysis revealed that the local structure of the cobalt gallate material is distorted from the average, similarly to γ-Ga_2O_3. The distortion is likely caused by the preference of both Ga^{3+} and Co^{2+} for distorted octahedral coordination environments, however no simple crystal structure model for this can be described. The cobalt gallate spinel was found from SQUID magnetometry to exhibit ferrimagnetic ordering at temperatures below 18 K.

The structure of this material would be an excellent candidate for RMC modelling as all symmetry constraints could be removed and some insight could be gained into the site geometry and distribution of the two different cations. Further magnetic measurements would be of benefit to examine the magnetic ordering at low temperatures, and low-temperature neutron diffraction could be used to probe the magnetic structure.

7.2.3. Iron gallium spinel

The iron gallium material was found from high resolution powder XRD to consist of two spinel phases with slightly different compositions and lattice parameters. The minority phase appeared to be iron rich, due to its larger unit cell size, while the minority phase appeared to be gallium rich.

Although the presence of the impurity phase and of room-temperature magnetic ordering prevented detailed structure refinement, the structure of the majority phase is consistent with a slightly oxygen-deficient spinel of composition $Ga_{1.8}Fe_{1.2}O_{3.9}$ where all of the iron is in the +2 oxidation state and located on octahedral sites, in line with the XANES results.

Measurements of magnetisation *vs* temperature indicated that the material exhibits ferro- or ferrimagnetic ordering which persists to temperatures above 300 K. Magnetisation vs applied field measurements at 300 K suggest that the sample may be in a superparamagnetic state, though further measurements would be required to confirm this.

In terms of future work, it is possible that the synthesis could be further improved by carefully adjusting the metal ratios or by changing the iron source. Nevertheless, techniques such as high-resolution powder XRD at a different wavelength (to avoid problems with fluorescence of iron) and neutron diffraction at different temperatures could help to resolve the structures of the two constituent phases.

7.3. The Structures of Fluorite-like Cerium Bismuth Oxides and a Cerium Titanate Pyrochlore

7.3.1. Cerium bismuth oxide

A series of cerium bismuth oxides, of general formula $Ce_{1-x}Bi_xO_{2-1/2x}$, were examined using total neutron scattering. Their average structure was found from Rietveld refinement to be described well by the cubic fluorite structure and the lattice parameter was observed to increase with increasing bismuth content. Using PDF analysis, the samples were found to exhibit local structural distortion due to the preference of Bi^{3+} for an asymmetric coordination environment, rather than the regular 8-coordinate environment in the fluorite structure. Modelling the distortion required the introduction of a two-phase (CeO_2 and β-Bi_2O_3) model for the low-*r* (local structure) region only. This model allows the Bi^{3+} to adopt a heavily distorted 5-coordinate environment similar to those in α- and β-Bi_2O_3, and, because the average cubic symmetry is maintained, the distorted sites must be randomly oriented throughout the bulk structure. The work in Chapter 5, Section 5.2.1, formed part of a paper on the structure and properties of the cerium bismuth oxides.[4] Temperature programmed reduction studies revealed a promisingly large hydrogen uptake, however this was later revealed to be due to partial phase separation and attributed to the inherent instability of the highly distorted doped-CeO_2 structure.

Future work would likely involve the development of a non-crystallographic model of the local structure. For example, if a large box fitting regime such as RMC was used it would in theory be possible to model the metal-metal correlations and to “see” effects like clustering, since the atoms would be free to move without symmetry constraints. More data would vastly improve the likelihood of obtaining a useful structural model from RMC, so future work could also include the collection of PDF-quality X-ray scattering data. Information obtained from spectroscopy such as Raman or EXAFS measurements could also be used to gain extra insight into the local order in these materials.

7.3.2. Sodium cerium titanate pyrochlore

A sodium cerium titanate pyrochlore of composition $(Na_{0.33}Ce_{0.53}Ti_{0.14})_2Ti_2O_7$ was found from PDF analysis to adopt the cubic pyrochlore structure with the unusual modification of excess Ti on the A site. The multiple occupancy on the A site was found to cause local distortions in its geometry, which could be modelled if a lower-symmetry pyrochlore in non-centrosymmetric space group $F\bar{4}3m$ was used to fit the low-r region of the PDF only. The work in Chapter 5, Section 5.2.2, formed part of a published study of the structure and properties of the pyrochlore material.[5]

Future work could involve an attempt to model the different coordination environments of each of the A-site metals. This might involve measuring an X-ray PDF which would highlight the Ce and Ti contributions and largely hide the Na and O; and EXAFS measurements at the different absorption edges could highlight differences in the individual local environments. Additional data such as these would permit modelling such as RMC to be undertaken without it being severely underconstrained.

7.4. Structural Studies of Amorphous Zeolite Precursors

7.4.1. Synthesis method and experimental setup

A method for reliably synthesising zeolite A precursor gels using anhydrous and/or deuterated reagents was developed. These reaction mixtures were designed to quickly separate into two layers (an opaque gel and a clear liquid) to allow neutron scattering measurements to be made on both the gel and its “background”.

The compositions of the reaction mixtures were selected carefully so that the transformation of the gel to the crystalline zeolite was extremely slow (crystals not detectable by powder XRD after more than a week) at room temperature so progress of reaction could be considered negligible on the timescales of the neutron experiments.

7.4.2. Neutron scattering results

Preliminary results from the neutron scattering experiments reveal that structural features unique to the gel can be detected in the presence of reaction liquid.

Importantly, it is clear from these results that the structure of the dried gel is significantly different to that of the gel *in situ*. The presence of the reaction liquid clearly influences the structure of the gel, which highlights the importance of *in situ* studies, as results from *ex situ* or quenching studies, as have often been used in the literature, may be misleading.

Another conclusion that can be drawn from these results is that the differences between gel and liquid layers, and between gels aged at different temperatures, are most significant at distances that could be associated with Na–O and Na– –T correlations. The position of the Na^+ ions relative to the developing aluminosilicate network apparently changes as the gel ages, which may be direct evidence for the influence of the cations on the ordering of the gel.

Finally, there is no strong evidence for the presence of discrete building units in the gel (or the solution) as there are no sharp correlations at values of r that could be assigned to common T–O or T– –T distances.

Taken as a whole, these results are consistent with a view of the gel as a disordered, hydrated aluminosilicate network with many of the tetrahedral TO_4 units being incomplete, or hydroxyl terminated, as a result of the presence of the reaction liquid.

Future work will include the full analysis of the wide *Q*-range data collected on NIMROD, which will enable the changes in structure over a range of length scales to be examined simultaneously. Additional information could also be obtained by using a null-scattering mixture of H_2O and D_2O to prepare the gels. This was not possible using the long vanadium can setup used on SANDALS due to the thickness of the sample (the incoherent scattering from the hydrogen would lead to an extremely high background level) but could be done using a different experimental geometry.

The use of X-ray total scattering at a synchrotron source would also provide a great deal of complementary information as it would be strongly weighted towards the contributions of the framework Si and Al atoms. The combination of X-ray and neutron data could enable the modelling of the system in detail, perhaps using Reverse Monte Carlo or the related Empirical Potential Structure Refinement (EPSR) routine.

It would also be extremely interesting to study the formation of other zeolites in this manner, including those that form with the assistance of organic templates.

7.5. General Concluding Remarks

In this thesis, it has been shown that total neutron scattering is a powerful and accessible technique for studying disordered structures. In conjunction with common analytical techniques such as powder X-ray diffraction and electron microscopy, it acts as a cornerstone in the construction of detailed and realistic structural models for highly complex systems which could not be fully characterised by traditional crystallographic methods.

7.6. References

1. Playford, H. Y.; Hannon, A. C.; Barney, E. R.; Walton, R. I., *manuscript submitted for publication*, **2012**.
2. Conrad, F.; Zhou, Y.; Yulikov, M.; Hametner, K.; Weyeneth, S.; Jeschke, G.; Gunther, D.; Grunwaldt, J. D.; Patzke, G. R., *Eur. J. Inorg. Chem.* **2010**, 2036.
3. Conrad, F.; Bauer, M.; Sheptyakov, D.; Weyeneth, S.; Jaeger, D.; Hametner, K.; Car, P. E.; Patscheider, J.; Gunther, D.; Patzke, G. R., *RSC Adv.* **2012,** *2,* 3076.
4. Sardar, K.; Playford, H. Y.; Darton, R. J.; Barney, E. R.; Hannon, A. C.; Tompsett, D.; Fisher, J.; Kashtiban, R. J.; Sloan, J.; Ramos, S.; Cibin, G.; Walton, R. I., *Chem. Mater.* **2010,** *22,* 6191.
5. Playford, H. Y.; Modeshia, D. R.; Barney, E. R.; Hannon, A. C.; Wright, C. S.; Fisher, J. M.; Amieiro-Fonseca, A.; Thompsett, D.; O'Dell, L. A.; Rees, G. J.; Smith, M. E.; Hanna, J. V.; Walton, R. I., *Chem. Mater.* **2011,** *23,* 5464.